Department of Mechanics, Mathematics and Management
MECHANICAL AND MANAGEMENT ENGINEERING
Ph.D. Program
SSD: ING-IND/14–MECHANICAL DESIGN AND MACHINE CONSTRUCTION

Final Dissertation

Acoustic Emission Methods for Mechanical Characterization and Damage Assessment in Structural Materials: Waveforms, Energy based Parameters and Acousto-Ultrasonic Approach

by
Paramsamy Nadar Kannan, Vimalathithan

Supervisors:

Prof. Barile, Claudia

Prof. Casavola, Caterina

Coordinator of Ph.D. Program:
Prof. Demelio Giuseppe Pompeo

Course n°33, 01/11/2018-31/03/2021

Dedicated to my father Kannan...

ABSTRACT

Acoustic Emission technique has grown tremendously over the last few decades. The growth is owing its sensitivity, which is amply supported by the technical advances and the powerful data processing techniques. The engineers, researchers and academicians around the globe has introduced several different techniques for improving the capability of the acoustic emission technique. However, the controversies regarding the usage of this technique for certain applications, usage of certain parameters for specific processes still prevails. The aim of this research work is to explore the advantages of the acoustic emission technique by studying the state of the art and breaks the barriers which limit the usage of this technique. The applications of acoustic emission in the industrial field such as damage monitoring of large structures and bridges, leakage identifications in pipes and pressure vessels and other industrial applications are extremely successful and its thriving. On the other hand, the application of this technique in damage monitoring at micro levels is limited in comparison. In fact, the research gap between the industrial applications of the acoustic emission technique and the micro level damage monitoring is very wide. As a matter of fact, the introduction of this technique is based on its sensitivity to monitor damages at microscopic level in the structural materials. This research work aims in exploring this technique to its full advantage and use it for monitoring damage modes and characterizing the behaviour of structural materials.

In this research work, the state of the art of techniques in this field has been explored. But beyond that, new parameters are also introduced. These novels parameters are based upon one or more different acoustic emission descriptors, which are commonly used. The novel parameters introduced in this research work explore the advantages of their parent descriptors from which they are derived but improve their limitations.

Aside from the new parameters, new methodologies are also used for using the acoustic emission technique. These two form the core of the research work.

Several structural materials, Carbon Fiber Reinforced Plastic (CFRP) composites, with different geometrical and layup configuration and additively manufactured materials are tested during this research work.

The new methodologies used are two: Acousto-Ultrasonic approach, and waveform analysis. The first one is used for assessing the interlaminar fracture strength and the residual strength of CFRP material before and after subjected to a drop-weight impact event. The second methodology used in this research work is a hybrid method of using a wavelet transform and an adaptive transform. The wavelet transform in this work refers to the Wavelet Packet Transform (WPT) and the adaptive transform is the Empirical Mode Decomposition (EMD). This hybrid approach is based on using the advantages of WPT and EMD combinedly, while overcoming their limitations. This hybrid approach is used in analyzing the qualitative damage analysis in the above said CFRP materials.

The new parameters used in this research work are b_{AE}-value and Energy per Count. While both these parameters are based on the acoustic energy and acoustic counts, that are different in many aspects.

The b_{AE}-value is a slope coefficient, which is based on the linear relationship between the cumulative counts and cumulative energy of a series of acoustic events recorded during an entire loading history. This b_{AE}-value is used for characterizing the material behaviour at different stages of loading.

The Energy per Count, on the other hand, is based on the acoustic energy distributed for a single count in an acoustic hit. This is used in two different modes. One, the Energy per Count is directly used for analyzing and identifying the damage modes in CFRP joint specimens which are configured in Single Lap Shear (SLS) configuration. The second mode is using Energy per Count as an identifier for choosing representative waveform from a cluster of acoustic waveforms recorded during the loading history. Then these waveforms are used for identifying the characteristic damage state of the particular stage of loading.

Apart from this, the attenuation of the acoustic wave propagation is also studied in different configurations of CFRP specimens. Moreover, the data clustering technique, which uses k-means++ data clustering, is also used for damage identification and mechanical characterizations. All the aforementioned methodologies and parameters are supported by detailed experimental campaigns, which validates their reliability and usage.

SOMMARIO

Negli ultimi decenni la tecnica delle emissioni acustiche si è evoluta enormemente. La sua crescita è legata essenzialmente alla enorme sensibilità, ampiamente supportata dai progressi tecnici e dalle potenti tecniche di elaborazione dei dati. Ingegneri, ricercatori e accademici di tutto il mondo hanno introdotto diversi approcci per migliorarne le capacità. Tuttavia, prevalgono ancora controversie riguardanti il loro utilizzo e l'utilizzo di alcuni parametri ad esse connessi per processi specifici. Scopo di questa attività di ricerca è quello di esplorare i vantaggi della tecnica delle emissioni acustiche analizzandone lo stato dell'arte e superando i limiti ad esse connessi. L'applicazione delle emissioni acustiche nel settore industriale spazia con enorme successo dal monitoraggio dei danni di grandi strutture e ponti, all'identificazione delle perdite nei tubi e nei recipienti in pressione. Viceversa, la loro applicazione nel monitoraggio dei danni microscopici è ancora molto limitata. Infatti, esiste un ampio divario dal punto di vista della ricerca tra le applicazioni industriali della tecnica e il monitoraggio dei danni a livello microscopico. L'introduzione di questa tecnica sfrutta la sua sensibilità per monitorare i danni tanto a livello microscopico quanto per grandi danneggiamenti nei materiali strutturali. Questo lavoro di ricerca mira ad esplorare questa tecnica in tutti i suoi vantaggi e ad utilizzarla per monitorare i meccanismi di danneggiamento e per caratterizzare in maniera completa il comportamento dei materiali strutturali.

Dapprima è stato esplorato lo stato dell'arte in questo campo; successivamente sono stati introdotti anche nuovi parametri. Questi parametri innovativi si basano su uno o più descrittori comunemente utilizzati nelle emissioni acustiche. I nuovi parametri introdotti esplorano i vantaggi dei descrittori/genitori da cui derivano, ma ne superano i limiti. Oltre ai nuovi parametri, sono state introdotte anche nuove metodologie. Queste innovazioni rappresentano il cuore del presente lavoro di ricerca.

A tal proposito sono stati testati due diversi materiali strutturali: compositi CFRP (Carbon Fiber Reinforced Plastic) con diverse layup e configurazioni, e materiali ottenuti per tecnica additiva.

Sono state utilizzate due nuove metodologie: l'approccio Acousto-Ultrasonico e l'analisi delle forme d'onda. La prima viene utilizzata per valutare la resistenza alla frattura

interlaminare e la resistenza residua dei CFRP prima e dopo essere stati sottoposti ad una prova di impatto di tipo drop-test. La seconda metodologia utilizzata è un metodo ibrido che combina una trasformata wavelet con una trasformata adattativa. La trasformata wavelet impiegata in questo lavoro è la Wavelet Packet Transform (WPT) mentre quella adattativa è la Empirical Mode Decomposition (EMD). Questo approccio ibrido sfrutta la combinazione dei vantaggi di WPT ed EMD, superando al contempo i loro limiti. Questo approccio è stato impiegato nell'analisi qualitativa del danneggiamento nei suddetti materiali CFRP.

I nuovi parametri utilizzati in questo lavoro di ricerca sono il b_{AE}-value e l'Energia per Count. Sebbene entrambi questi parametri siano basati sull'energia e sui count acustici, essi sono per molti aspetti diversi da questi ultimi.

Il b_{AE} value rappresenta la pendenza della relazione lineare tra i count cumulativi e l'energia cumulativa di una serie di eventi acustici registrati durante un'intera storia di carico. Questo valore b_{AE} viene utilizzato per caratterizzare il comportamento del materiale nelle diverse fasi di carico.

L'Energia per Count, al contrario, si basa sull'energia acustica distribuita per un singolo count in un hit acustico ed è applicata in due diverse modalità: nella prima viene utilizzata direttamente per analizzare e identificare le modalità di danneggiamento nei campioni di giunti CFRP nella configurazione SLS (Single Lap Shear), nella seconda si utilizza per individuare la forma d'onda più rappresentativa di un cluster di forme d'onda acustiche registrate durante l'intera storia di carico. Successivamente queste forme d'onda vengono utilizzate per identificare lo stato di danneggiamento caratteristico in una particolare fase di carico.

Nell'analisi dei diversi campioni CFRP, inoltre, è stata studiata l'attenuazione della propagazione delle onde acustiche ed è stata effettuata la caratterizzazione meccanica mediante la tecnica di clustering dei dati, basata sul clustering dei dati k-means.

Tutte le metodologie e i parametri suddetti sono supportati da campagne sperimentali dettagliate, che ne convalidano l'affidabilità e l'utilizzo.

Parole chiave: Emissioni acustiche, Analisi delle forme d'onda, Parametri basati sull'Energia, tecniche di clustering dei dati, Materiali strutturali.

CONTENTS

LIST OF FIGURES

LIST OF TABLES

CHAPTER 1
INTRODUCTION

The material design is an ongoing process throughout the human history, as long as it has existed. The design of materials with new properties, by modifying the existing materials has led to the introduction of more than one hundred thousand materials, which are in commercial use today. These materials are not only used in commercial everyday basis but also in challenging structural engineering problems. To overcome technological limitations and to improve ecological footprints, the properties of the structural materials are being modified on regular basis. Basically, one of the most efficient ways is to introduce spurious dopants into a pure material, thereby improving the desired properties. This has led to the introduction of numerous numbers of metallic alloys, ceramics and composite materials. Akin the introduction of challenging structural materials, the manufacturing methods are being improved over the years. These technological advancements and necessities have led to the introduction of variety of structural materials manufactured using different techniques. The theoretical description of these materials manufactured through different processes is rather amusing and challenging. The description of the failure process, characterization of their behaviour and the damage modes they had to undergo on the course of failure are fascinating, but rather more challenging. Various experimental and numerical methods, starting from the very basic static and dynamic testing to advanced numerical models have been developed over the years, alongside the rise of the structural materials. The complex nature of the material description and the failure processes has compelled the researchers around the world to reinvent adequate testing methods. Various non-destructive evaluation techniques are used over the decades for characterizing the behaviour of the structural materials, predicting the failure occurrences, identifying the critical points of failure and understanding the damage modes. The capabilities of the non-destructive evaluation techniques have been extended beyond their limits with the help of powerful data acquisition system, supported by the technical advancements in

data processing. Acoustic emission technique, which is relatively new in comparison with the other non-destructive evaluation techniques have seen a tremendous growth over the last 4 decades owing to their capability in all the predefined characterizations involving structural materials.

1.1 MOTIVATION OF RESEARCH

Acoustic Emission (AE) technique has been used for structural health monitoring over the last three or four decades. However, several restrictions limit the usage of AE in the mechanical characterization and damage assessment. Particularly, some of the AE parameters are not used to their full potential. Various research groups are actively trying to use the more advanced data processing and signal processing tools for breaking the limiting barrier of AE's potential. Over the years, several data processing tools such as pattern recognition techniques, principle component analysis among the many other are developed and are scrutinized successfully. These data processing tools are seldom used for processing the AE data. Similarly, the signal processing tools such as wavelet transform analysis are also seldom used. Most of the research groups focus on very few AE parameters such as energy and peak amplitude of the AE signals for the mechanical characterization and damage assessment. Besides, some of the techniques such as Acousto-Ultrasonic techniques are often overlooked for mechanical characterization.

The motivation for this research work sprouts from the necessity of using various data processing and signal processing techniques for analysing the AE signals. Moreover, several overlooked approaches, which are limited by the technological limitations during their inception, are explored to their full potential. Not to say the least, new parameters are developed for analyzing the AE data and use them efficiently for mechanical characterization and damage assessment.

1.2 OBJECTIVES OF THE RESEARCH

The main objective of this research work is to use the AE technique for the description of mechanical characteristics and the damage modes in various structural materials. For achieving this objective, the core of this research work is divided into two parts. One is to develop new parameters using the AE information and use them efficiently for the

predefined objective. Second is to introduce innovative ways of using the available AE techniques by incorporating various data processing and signal processing techniques.

The structural materials used for achieving the predefined objectives are Fiber Reinforced Plastic (FRP) composites, particularly the composites with carbon fiber reinforcing the polymeric matrix and the additively manufactured materials. The additively manufactured materials used in this research work are fabricated using Selective Laser Melting (SLM) technique on AlSi10Mg. Various damage modes in these materials under loading are evaluated using the AE technique, aside from using them for the mechanical characterization.

1.3   RESEARCH ACTIVITIES

The research activities are carried out on different configurations of Carbon Fiber Reinforced Plastic (CFRP) composites and SLM material prepared from AlSi10Mg alloy. The research activities, thus, can be divided into two categories: Applications of AE on CFRP and SLM materials.

In the case of CFRP, the different configurations implicate the geometrical configuration, fiber layup configuration, testing methods and application. The acousto-ultrasonic approach, which is used for analyzing the acoustic wave propagation in materials, is tested on CFRP specimens configured for Compression After Impact (CAI) testing. This technique, supported with the Wavelet Packet Transform (WPT), a wavelet analysis technique, is used for studying the interlaminar strength and the residual strength of the CAI specimens after suffering a drop-weight impact. Besides, for studying the AE wave propagation, several configurations of CFRP specimens are tested.

Next, the CFRP adherends bonded together in Single Lap Shear (SLS), Joggled Lap Shear (JLS) and Single Lap Shear with Rivets (SLS-R) are tested for studying the bonding characteristics and damage modes.

Double Cantilever Beam (DCB) specimens prepared from unidirectional CFRP, which are subjected to Mode I delamination are analyzed. Sentry function, a function that relates

the strain energy during the delamination progression and the acoustic information, is used while analyzing the DCB specimens.

In the case of AlSi10Mg specimens prepared using SLM technique, three different configurations are used. These configurations represent the building of the SLM specimens with respect to the axis along which the laser is moved and the building platform. The mechanical characterization of these specimens is obtained using common AE descriptors. For damage assessment, Empirical Mode Decomposition (EMD) and Hilbert-Huang Transform (HHT) is used.

On the course of testing and analyzing the aforementioned specimens with various configurations, two new parameters and several new techniques are introduced. A new AE parameter, which can describe the mechanical characteristics of material under straining, b_{AE}-value is introduced. Another new AE parameter, which is based on the acoustic energy, named Energy per Count, is introduced for analysis. Aside from these new parameters, new algorithms for efficient wavelet analysis is introduced by incorporating EMD/HHT and WPT. Limitations of the attenuation in acoustic wave propagation and various other factors influencing the data processing are explored. Finally, some new methods of using pattern recognition technique are introduced.

All the experimental tests and measurements along with the data processing and signal processing are carried out in Experimental Mechanical Laboratory and in Experimental Mechanics Integrated Laboratory In Aerospace (EMILIA) at the Dipartimento di Meccanica, Matematica and Management (DMMM) of Politecnico di Bari.

CHAPTER 2
ACOUSTIC EMISSION: STATE OF THE ART

Acoustic Emission (AE) technique is based on the detection and interpretation of sound waves, which are generated by rapid internal displacements in a material and are travelling at an ultrasonic velocity. In a structural material, the acoustic source is generated owing to the initiation and propagation of cracks or different damage modes, which are forcing the material to undergo permanent deformation/irreversible changes. In simple words, AE source can be described as spatial crack surface oscillation. This chapter begins with the brief history of the AE technique, followed by the types of AE descriptors which are used for the interpretation of the AE waves. The characterization of the AE technique can be defined by two types of AE descriptors: parameter-based data and signal-based data. Both the types of AE descriptors are discussed in this chapter.

2.1   HISTORY OF ACOUSTIC EMISSION TECHNIQUE

Before the 1960s, the general use of sound waves or acoustic emission signals to characterize any material, ranging from wooden structures, mine shafts, composite pressure vessels, architectural structures, to name a few, under loading has largely been given trivial importance and often neglected by the engineering and scientific community. Within a period of 10 years, the whole scenario has been reversed. A good example for this turnover can be provided by a suitable example: in the year 1971, four major industries had commenced the production and supply of acoustic emission apparatus and instrumentations commercially. The growth of acoustic emission application has been exponential since the beginning of 1970s. Over the years leading to beginning of 1970, the sound waves had been identified as material characterizing parameters, albeit in different names such as clicks, sounds, micro-seismic activity, rock noise, elastic radiation, elastic shock, seismo-acoustical activity, Stress Wave Analysis Technique (SWAT), the term acoustic emission had become household from 1970s.

What leads to this rapid growth? The different terminologies previously used are often used to relate the sound waves arises to different materials, due to different phenomena or based on different applications under different loading conditions. Despite their differences, all these opinions lead to a consensus, and as quoted by Liptai (1972) "Acoustic emission analysis is very sensitive to transient instabilities".

Most of the catastrophic failures in any material system is due to the local instabilities. For instance, the stress concentration accumulating near the local flaw or a micro crack in its structure can result in failure. The local dislocations which can lead to these failures are mostly transient in nature. Acoustic emission is very sensitive to the transient sound waves created by these local failures. However, during the initial booming period of growth, the acoustic emission was commonly related to the dislocation motions. This brought Gillis (1972) to infer that the acoustic emission must be used to describe stress waves or pressure waves arising from different sources owing to different phenomena.

Despite of the great interest in those first years in implementing Acoustic Emission only a countable number of reports can be found on characterizing structural materials, particularly Fiber Reinforced Plastics (FRP), using Acoustic Emission prior to 1970s. Although it has been argued by Liptai that the AE has greater applicability in composites, it has not been implemented efficiently until the beginning of 21st century. This rapid growth in AE technique can be well attributed to the powerful data acquisition systems supported amply by wide range of transducer, amplifiers and data processing techniques. The contributions made by the forerunners of this technique in the early 1970s cannot be foreshadowed either. For instance, Kaiser Effect proposed in 1950s, the AE signals are irreversible in nature has led to the introduction of the terms "characteristic damage state" and Felicity ratio. The number of acoustic events occurring during the initial loading of a composite is always greater in number. This large number of acoustic events can start accumulating as early as 10% of the maximum the ultimate failure stress of a composite material. This is due to the reason that large number of microscopic failures occur on the matrix at the early stages of loading, resulting in uniform stress distribution throughout the material. This uniform damage state during the initial loading of a composite material is known as characteristic damage state.

During the second loading of a composite material after it reaches its characteristic damage state, the material still generates a little acoustic signal even at stress level below the previous damage stage. This occurrence of acoustic signals is known as Felicity Effect. The Felicity ratio is the ratio of load at which the acoustic rate increases to the maximum load of the maximum load of the first cycle. The Felicity ratio has been abundantly used in characterizing the residual strength of a material.

Over the years, several researchers have used several acoustic parameters to characterize the material properties under loading. Conventionally, in metallic materials, the counts are widely being used to characterize the material properties. The acoustic count is the measure of number of times the recorded sensor signals crosses the acquisition threshold of the counter. In composites, however, due to their complex nature, the deformation and fracture becomes complex. Thus, relaying on one acoustic parameter (say acoustic counts) is unreliable. However, with the aid of modern instrumentation of AE technique and multiple acoustic parameters (can collectively be called as AE descriptors) such as peak amplitude, counts, peak energy, rise time, peak frequency, frequency centroid, duration, partial power to name a few, successful characterization of composite material is possible.

It has been eloquently said by Gillis (1972) that the acoustic events recorded using a transducer is predominantly based on the settings selected by individual tester. In addition to that, there are numerous AE descriptors available to characterize the material properties, albeit, each having their inherent advantages and limitations.

Before going further into the AE descriptors, it is essential to understand the types of damage progressions and how it normally is recorded as acoustic events. It has been established nearly 50 years ago by Broutman and Krock (1967) and corroborated by Liptai (1972) in his research work that the AE can be generated in three different modes by straining an FRP composite material. These modes of AE generation are plastic deformation of the matrix, fracture of the fiber and pullout at the interface between matrix and the fiber. Other than these classical damage modes, interlaminar crack growth, sliding of microcracked particles in the matrix, transverse cracks in cross-ply

laminates can also produce both low-frequency symmetric and high-frequency nonsymmetric acoustic signals in different time-frequency domains. Over the years this has been experimentally proved by employing different types of in-situ damage monitoring techniques such as Digital Image Correlation (DIC), Optical Microscopy, Thermography, Thermo-elastic stress analysis and so on.

It is essential to understand the generation of acoustic events in most of the structural materials. According to Hamstad (2000), the initial AE generation occurs even before the material reaches 10% of its maximum failure load. This is highly due to the anisotropic nature of the FRPs which are strong in one direction and generally, but not necessarily, weak in the other. The matrix material, which serves as the load distributing part of an FRP, experiences high stress concentration uniformly throughout the composite. The microcracks in the matrix is the major reason for this uniform stress concentration. Due to the viscoelastic nature of the polymer matrices, the acoustic events generated during this loading period has severe attenuation in high frequency components. An experimental campaign by Awerbuch et. al (1984) shows that the friction between the fractured laminates accumulates a significant amount of acoustic events and in some cases, these accumulated acoustic events are much larger than the AE signals produced by the actual damage progression. Awerbuch and Ghaffari (1988) followed these results by characterizing the AE signals produced by actual damage progression and the friction between the fracture laminates in double-edge notched unidirectional graphite/epoxy composites.

The other basic source of AE signal generation is majorly concentrated on the location close to the local stress concentration and accumulation of damage before the ultimate failure of the material under loading. The location of these AE sources has a small region of origin due to the local stress concentration. However, the damage distribution can alter the elastic properties of the material and consequently, AE signals will be generated from the other locations than the local failure region. Nonetheless, the AE signals concentrated at the region of failure and the other regions vary significantly in terms of frequency, amplitude and duration.

Beyond these, the acoustic signals can be generated due to the rupture of the fibers, pull out of the fibers from the matrix, propagation of crack transversely through the interlaminar plies and so on, in the case of FRP. In metallic materials, the acoustic signals can be generated due to the micro-cracking, dislocation movement, lattice movements, initiation and nucleation of cracks, nucleation of voids and so on. Each of the acoustic event associated with these damage propagations have unique features in terms of frequency, risetime among the other AE descriptors. This makes the AE technique a powerful tool in understanding and characterizing the damage progression and material properties of a structural material.

Most of the researchers in the recent past have been using advanced data acquisition (DAQ) systems to record the piezoelectric transducer signal of the acoustic events. These signals are amplified by amplifiers and filtered through low and high bandpass filters before being converted into the AE descriptors such as peak amplitude, energy, duration, counts and so on. Although these DAQs provide high processing speed and feasibility in recording and interpreting the acoustic signals, they have some limitations. It becomes critical to how to extract the AE descriptors from the transduced sensor signals.

2.2 ACOUSTIC EMISSION DESCRIPTORS

Acoustic Emission signals can be characterized by their descriptors, which can define the characteristics of the signal. The AE descriptors carry the information about the source of the AE signals from which they are originated. Analyzing the AE descriptors and interpreting them forms the basis of the AE technique. For defining the different AE descriptors, it is essential to show a typical AE waveform (refer Figure 2.1). This section is dedicated for describing the basic definitions and the calculation procedure of different AE descriptors.
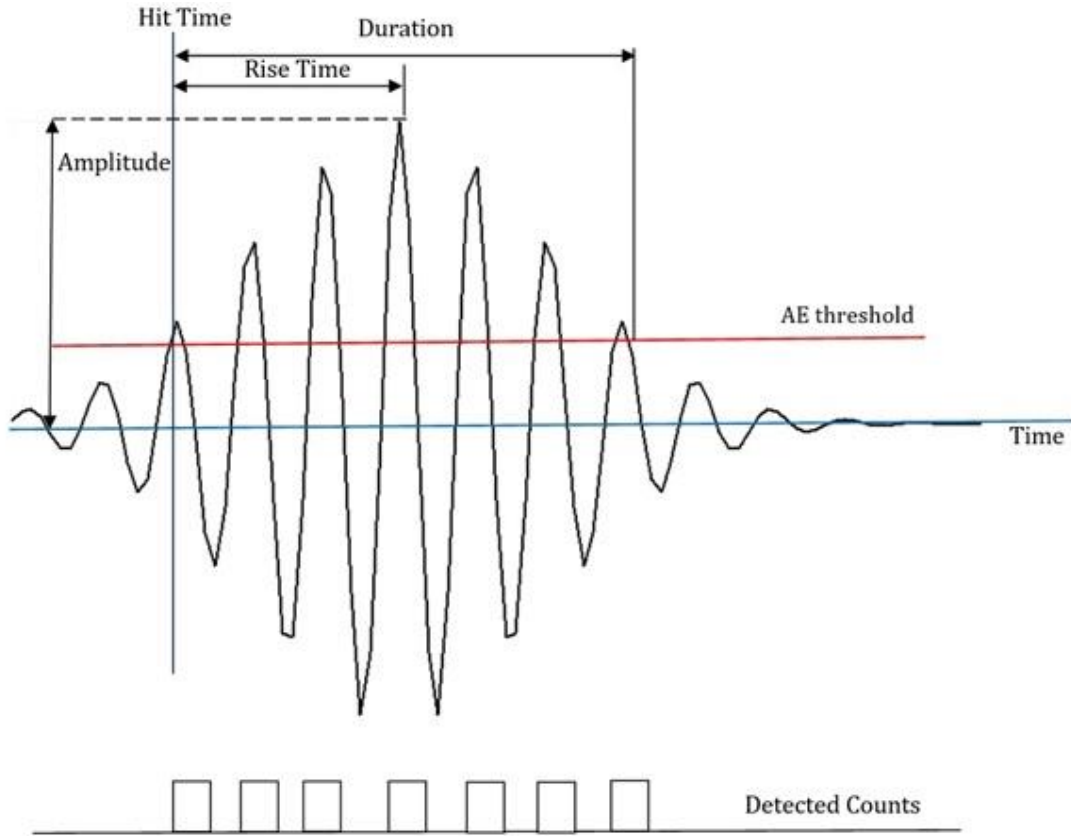
Figure 2.1. Typical Acoustic Emission signal with basic descriptors

2.2.1 Peak Amplitude

Peak amplitude is the most classical, yet, formidable descriptor used for the analysis of AE signals. Till date, it is one of the most reliable parameters for identifying different damage modes, particularly in FRP. It represents the largest voltage peak of the recorded AE signal (U_{max}) with respect to the reference voltage (U_{ref}) set at the pre-amplifier. It is measured in decibels (dB) and it can be expressed as,

$$A = 20 \log \frac{U_{max}}{U_{ref}} \qquad (2.1)$$

The classical way of using peak amplitude for identifying the damage mode is to categorize different levels of amplitudes for different damage modes in FRP. For instance, the AE events with amplitude over 80 dB is mostly correlated with fiber breakage.

2.2.2   Counts

The acoustic counts are the number of times the recorded AE signal crosses the detection threshold. It is also referred to as ringdown counts. It is one of the most commonly used AE descriptors. It has been used since the 1960s, commencing with the detection of failure in FRP pressure vessels, till date. The AE counts have been used commonly at present for detecting the critical points of failure under loading, while some researchers are using the cumulative count rate from the AE events for predicting the crack growth in a structure. Counts have been used for identifying stress corrosion, stress cracking, hydrogen embrittlement, mechanical and fracture behaviour of structural materials.

2.2.3   Energy

Acoustic energy is described as the total energy of the acoustic signal above the detection threshold. It is calculated by integrating the square of the transient voltage of the acoustic signal over the time period of the signal. A separate section in the later chapter has been assigned to explain in detail about the processing of measuring the acoustic energy and its application.

2.2.4   Duration

The total duration of the acoustic signal, which is measured in μs, which can give information about the mode of propagation of the acoustic signal. Typically, acoustic signals propagate in two different modes: lower-order symmetric and higher-order asymmetric. The duration of the AE signal is one of the key factors in understanding the difference between these two modes, which will be explained in the later chapters.

2.2.5   Risetime

Risetime is another parameter, which is used for characterizing the AE signal on whether it has propagated in lower-order symmetric or higher-order asymmetric mode. It is the duration of the AE signal from the point where the signal crosses the detection threshold to the peak amplitude of the signal. It is also measured in μs.

2.2.6　　　　Average Frequency

The average frequency of an acoustic signal is described as the ratio of the total number of counts to the entire duration of the signal above the detection threshold. The average frequency can be represented as,

$$A.\,Freq = \frac{Counts}{Duration} \tag{2.2}$$

2.2.7　　　RMS Value

Root-Mean-Square (Value) is another measure of the AE activity, which measures all the emissions, both positive and negative amplitudes, with equal weight. Unlike AE energy, which is the signal above the signal threshold, the RMS value is the measure of the energy of emission or the area under the total AE signal curve. It can be expressed as,

$$V_{RMS}^2 = \frac{1}{T} \int V_i^2 dt \tag{2.3}$$

where, V_i and T are the transient voltage and the duration of the AE signal.

RMS value is used mostly in operations where the noise level is very low, or it is significant in the measurement of AE signal.

2.2.8　　　Average Signal Level (ASL)

Average signal level is analogous to the RMS voltage but differs only in the sense that the RMS value is measured in mV, whereas, ASL is measured in dB. ASL also differs from peak amplitude in the sense that the peak amplitude represents the peak voltage of the AE signal in dB, whereas, ASL provides the average level of the signal in dB. ASL can be expressed as,

$$ASL_v = \frac{1}{T} \int_{t_0}^{t_0+T} |V_i| dt = \frac{1}{N} \sum_{n=1}^{N} |V_i(n)| \tag{2.4}$$

where, N is the total number of discretized signal points. The ASL in dB can be expressed as,

$$ASL = 20 \log\left(\frac{ASL_v}{1\mu V}\right) \tag{2.5}$$

2.2.9 P-Counts

P-Counts or counts to peak is the total number of counts recorded from the point when the AE signal crosses the detection threshold until it reaches the peak amplitude. This is another identifier for analyzing the propagating mode of the AE signal. Besides, this also gives an indicator of other signal characteristics such as the dispersion level of the signal.

2.2.10 Reverberation Frequency

The dispersion level of the signal during the propagation and the characteristics of the propagating mode can be expressed using the Reverberation Frequency (R-Frequency). Yet, R-Frequency is not commonly used in the damage assessment or mechanical characterization in structural materials. This parameter, although having a great potential, is seldom used even in health monitoring of structures, where AE technique is more prevalent. R-Frequency is the frequency of the part of the signal after it reaches the maximum amplitude. It can be expressed as,

$$F_R = \frac{Counts - P.Counts}{Duration - Risetime}$$ (2.6)

2.2.11 Initiation Frequency

Initiation Frequency (I-Frequency) is another parameter which can describe the characteristics of the AE signal without the necessity of the signal analysis in its time-frequency domain. It is the opposite of the R-frequency as it measures the frequency of the initial part of the signal before the signal reaches the peak amplitude.

$$F_I = \frac{P.Counts}{Risetime}$$ (2.7)

2.2.12 Absolute Energy

Absolute energy of the signal is derived from the integral square of the voltage signal divided by the reference resistance (Ω_{ref}). While monitoring the continuous AE signals, this parameter is very useful as it is independent of the hit based activity. The absolute energy is given in aJ or $10^{-18}J$ and is expressed as,

$$E_{abs} = \frac{\int V_i dt}{\Omega_{ref}}$$ (2.8)

2.2.13   Peak Frequency

Peak frequency of an AE signal is the frequency with the maximum amplitude in the Fast Fourier Transform (FFT). Similar to the peak amplitude, the peak frequency is also used for characterizing the different damage modes. It is also used for identifying the mode of propagation of the AE signal, when compared along with the duration or the risetime. But typically, it is used for categorizing the damage modes. Detailed information about using the peak frequency or frequency of the AE signal in general for categorizing damage modes are given in the later chapters.

2.2.14   Rise Angle

Rise angle (RA) is one of the most successful parameters in relating the mode of propagation of the AE signal with the parameter based data. It is the angle that rises from the point where the signal crosses the AE threshold until it reaches the maximum amplitude. Several researchers have also used RA for characterizing the damage modes, particularly in FRP.

$$RA = \frac{Risetime}{Peak\ Amplitude}$$ (2.9)

2.2.15   MARSE Energy

Measured Area under the Rectified Signal Envelope (MARSE) is one among the seldomly used parameters. It is also known as PAC-Energy. The MARSE is calculated first by creating an envelope of the AE signal $f(t)$ using Hilbert Transform. For the envelope calculated H, the sum of the signal envelope is calculated for the duration of the AE event and converted into counts at $100\ kHz/V$.

$$E_{PAC} = \sum_t |H[S(t)]| . \Delta t. 100.10^6$$ (2.10)

These are the AE parameters which have been used since the inception of this technique till date. Each of these parameters have their advantages and limitation. Nonetheless, they have proven to be efficient tools for monitoring and characterizing damages in structural

materials. It is highly recommended by several researchers with substantial evidences that one AE parameter must not be used as a solitary parameter for damage monitoring as it always leads to anomaly. More than one parameter must be used. For this reason, many researchers used data clustering algorithms or supervised/unsupervised clustering algorithms using pattern recognition approach.

2.3 ACOUSTIC COUNTS AND CRACK GROWTH

While addressing the state of the art of AE technique, the relationship established between the crack growth and the acoustic counts must be included. This theoretical relationship is established based on the assumption that the AE signal is continuous, and the amplified and filtered signal is inserted into the counter for measuring the counts is in the form as described in Equation (2.11).

$$V = V_0 e^{-\beta t} \sin \omega t \tag{2.11}$$

where V_0 is the voltage input received from the AE signal, ω is the frequency of the signal and β is the time constant of exponential decay of the sensor signal.

The minimum voltage required for the trigger counter, V_t is given by

$$V_t = V_0 e^{-\beta t^*} \tag{2.12}$$

If the time t^* is the duration required for the signal to ringdown below the acquisition threshold is compared with the oscillation period of the signal, the total number of counts η can be measured.

$$\eta = \frac{\omega t^*}{2\pi} \tag{2.13}$$

By relating Equations (2.11) and (2.12), the total number of counts can be rewritten as,

$$\eta = \frac{\omega}{2\pi\beta} \ln \frac{V_0}{V_t} \tag{2.14}$$

It is assumed that this continuous acoustic signal is recorded from a crack growth cycle in a specimen, which has a thickness of B and Young's modulus E. When load P is applied

and it stimulated the crack growth at a strain energy release rate of E_R, the energy released by the acoustic event is indicated as U.

Based on the assumption that the energy released by the acoustic event is proportional to the square of the initial voltage resulting from the acoustic event,

$$U \propto V_0^2 \tag{2.15}$$

The initial voltage can be written as,

$$V_0^2 = CG\sqrt{U} \tag{2.16}$$

C is the constant of proportionality and G is the amplifier gain.

The amount of energy released at the maximum load during the crack extension will be,

$$U = E_{Rmax}\Delta A = E_{Rmax}B\Delta a \tag{2.17}$$

where A is the crack length area and a is the crack length. The Equation (2.17) can be rewritten in terms of the stress intensity factor K as,

$$U = \frac{K_{max}^2}{E}B\Delta a = \frac{\widehat{K}^2}{(1-R)^2}\frac{B}{E}\Delta a \tag{2.18}$$

$\widehat{K}^2$ is the stress intensity factor range, which is given as the difference of maximum and minimum stress intensity factors and R is the loading ratio, which can be given by,

$$R = \frac{K_{min}}{K_{max}} \tag{2.19}$$

The theoretical relationship between the acoustic event and the crack growth can be obtained by combining Equations (2.14), (2.16) and (2.18).

$$\eta = \frac{\omega}{2\pi\beta}\ln\frac{CG}{V_t}\frac{\widehat{K}}{(1-R)}\sqrt{\frac{B}{E}}\Delta a \tag{2.20}$$

If the crack growth rate a' for N number of cycles can be given by Equation (2.21),

$$a' = \frac{da}{dN} \tag{2.21}$$

then Equation (2.20) can be rewritten for the total counts per cycle N'.

$$N' = \frac{\omega}{2\pi\beta} \ln \frac{CG}{V_t} \sqrt{\frac{B}{E} \frac{\widehat{K}}{(1-R)}} \sqrt{a'} \qquad (2.22)$$

Equation (2.22) gives the direct relationship between the total number of counts of a continuous signal with the crack growth rate.

This expression has been simplified or used directly for measuring and predicting the crack growth rate of Compact Tension (CT) specimens by many researchers. The simplified version of this theoretical relationship has also been used for predicting the crack growth rate in many structures.

The state of the art of AE technique can be explained further beyond just the comparison of counts and the crack growth rate. In each chapter, the recent trend of using the AE has been highlighted before introducing the novel ideas introduced in this research work. Thus, this chapter will highlight the topics which are not discussed in the subsequent chapters.

2.4 FINITE ELEMENT MODELLING

The Finite Element Modelling (FEM) on the acoustic emission wave propagation has been growing over this last decade, thanks to the powerful FEM software programmes and the numerous researches on numerical modelling by the researchers. The main application of the FEM is to understand the propagation and the attenuation of the AE waves during the course of propagation. A detailed chapter about the experimental investigation on the attenuation of wave propagation is provided in this work. So, the details about the FEM is highlighted in this section.

Acoustic emission can be described as the result of transient oscillatory movements within the solid. The AE waves have to propagate through the solid before being transduced at the receiving end by a piezoelectric sensor. However, during the propagation, the AE waves are subjected to dispersion and geometric spreading. It is also affected by the attenuation effects due to the dissipative mechanisms in the material and the formation of different wave modes at the finite geometrical boundaries.

The source model of AE must be clearly depicted to understand this attenuation. Considering a FRP medium, the AE source can be the formation of cracks in the matrix, or fibers or the interface between them. The system under the crack progress moves from one equilibrium stage to another equilibrium stage due to the formation of this crack. The energy released during this equilibrium shift is consumed by plastic deformation of the material, heat generation and the generation of the oscillating elastic waves in the solid. The heat formation in the deformed zone fluctuates in space and time. In the case of spatial heat propagation is slower than the elastic wave formation and propagation, the processes can be assumed to be adiabatic.

By the principle of virtual work W, the FEM program solves the dynamic equations of the equilibrium, expressed in global or local stress and strain vector components, $\vec{\sigma}$ and $\vec{\varepsilon}$ for an external stimulation. The acoustic waveforms are then recorded by the $\vec{\varepsilon}$ strain components at the surface of the model in the area of detection.

The principle of virtual work states that the variations in the virtual work W induced by the forces F_i and virtual displacements δu_i in an equilibrium state is equal to zero.

$$\delta W = \sum_i F_i . \delta u_i = 0 \tag{2.23}$$

The external applied virtual work equals to the internal virtual work of the body. The deformed body with a volume V and surface area S results in the new deformed state with internal stress and strain components.

$$\iint \delta \vec{u}.\overrightarrow{F_S} dS + \iiint \delta \vec{u}.\overrightarrow{F_V} dV = \iiint \delta \vec{\varepsilon}.\vec{\sigma} dV \tag{2.24}$$

The external applied force on the surface and the volume are represented as $\overrightarrow{F_S}$ and $\overrightarrow{F_V}$, respectively. Since the work due to the heat formation is considered negligible, the only source for stress is due to the formation of strain resulting from the crack progress. For a linear elastic media, the Hook's law is valid.

$$\vec{\sigma} = \overleftrightarrow{D} . \vec{\varepsilon} \tag{2.25}$$

The elastic tensor defined in Equation (2.25) has the elastic tensor for an anisotropic material is a 6×6 matrix with 12 independent components. The stress vector $\vec{\sigma}$ comprises of 6 components, composed of normal σ and shear stress τ components.

18

Similarly, the strain vector $\vec{\varepsilon}$ comprises of 6 components, composed of normal ε and shear strain γ components.

$$
\begin{bmatrix}
\sigma_x \\
\sigma_y \\
\sigma_z \\
\tau_{xy} \\
\tau_{yz} \\
\tau_{zx}
\end{bmatrix}
=
\begin{bmatrix}
D_{11} & D_{12} & D_{13} & 0 & 0 & 0 \\
D_{21} & D_{22} & D_{23} & 0 & 0 & 0 \\
D_{31} & D_{32} & D_{31} & 0 & 0 & 0 \\
0 & 0 & 0 & D_{44} & 0 & 0 \\
0 & 0 & 0 & 0 & D_{55} & 0 \\
0 & 0 & 0 & 0 & 0 & D_{66}
\end{bmatrix}
\cdot
\begin{bmatrix}
\varepsilon_x \\
\varepsilon_y \\
\varepsilon_z \\
\gamma_{xy} \\
\gamma_{yz} \\
\gamma_{zx}
\end{bmatrix}
\tag{2.26}
$$

If the material is isotropic, the stress tensor is completed with the Young's modulus and the Poisson's ratio.

The principle of virtual work can be extended to the dynamic systems by adding the mass accelerations in Equation (2.24). Considering the material density ρ and by taking into account the dynamic systems, the equilibrium equation can be written as,

$$
\iint \delta\vec{u}.\overrightarrow{F_S}dS + \iiint \delta\vec{u}.\overrightarrow{F_V}dV = \iiint \delta\vec{\varepsilon}.\vec{\sigma}dV + \iiint \rho\frac{d^2\vec{u}}{dt^2}.\delta\vec{u}dV \tag{2.27}
$$

This defines the basic differential equations solved inside the FEM tools for each of the finite element. By giving the displacement as the displacement of the piezoelectric crystal which simulates the source of the acoustic signal, the structural response can be recorded at any point on the material surface. This forms the basis of the FEM modelling.

2.5   LIMITATIONS OF ACOUSTIC EMISSION TESTING

This entire work is encompassed with the different applications, advantages and novel ideas of the acoustic emission testing methods. Thus, it is important to highlight the limitations of the AE technique. This section is dedicated to brief about the limitations of the AE technique.

2.5.1   Repeatability

It was mentioned in Section 2.1 that, according to Gillis (1972), the acoustic events recorded using a transducer is predominantly based on the settings selected by individual tester. This means that the AE transducing is based on the skill of the individual tester. Besides, the holding pressure of the sensor, the thickness of the couplant between the transducing crystal and the surface of the specimen and the surface defects and

impurities are all responsible for the low repeatability in AE technique. Two specimens tested after one another using AE technique cannot be compared in terms of the numerical specific AE energy values. The problems with the holding pressure of the sensor can be rectified by using mounting mechanisms for the sensors, where the pressure can be controlled. For maintaining an uniform thickness of the couplant, KAPTON tapes can be used, however, the silicone gel is highly recommended.

2.5.2   Attenuation

The attenuation of the acoustic wave is unavoidable due to the dispersion effects of the propagating medium. This limitation can be addressed by using understanding the attenuation of the signal. For instance, in some Data Acquisition Systems (DAQ), the attenuation of the AE signal can be calibrated by the velocity of the sound waves in the testing medium and the attenuation of the peak amplitude with respect to the distance between the source and the sensor. This may reduce the errors arising due to the attenuation, but is not completely unavoidable.

2.5.3   Noise

AE technique is very sensitive to transient signals with very low energy levels. Thus, the problem of noise is inevitable. Various methods have been used by several researcher to address the problems of this noise. Filtering the AE signals through low bandpass and high bandpass filters, selecting appropriate acquisition threshold for different applications are done at the input side for controlling the noise. While analysing the AE data, the denoising techniques are commonly used. Or the parameters which is unaffected by the noise signals are also used.

This concludes the introduction about the Acoustic Emission techniques and its state of art. The following chapter contains the newly developed parameters for this research work, which are supported by a detailed experimental campaign. Before introducing the newly developed parameters or techniques in each chapter, the basis of the methods or parameters, their state of art is explained. In many cases, the experimental campaign is

conducted for understanding the popular methods based upon which the new parameters or methods or devised.

CHAPTER 3
PROCESSING OF ACOUSTIC WAVEFORMS

Acoustic Emission (AE) signals are essentially sound waves released during the sudden outburst of energy in a material under deformation or loading. These sound waves travel at ultrasonic velocity through the structure of the material before being transduced at the receiving end of the piezoelectric sensor. It is essential to analyze these acoustic waveforms in their time frequency domain. Normally, Fast Fourier Transform (FFT) is popularly used for this purpose. However, FFT deduces the frequency content and its magnitude using sinusoidal wave. Acoustic waves released in materials are sometimes decaying sinusoidal in nature but most of the times are complex. This puts FFT in disadvantage. Wavelet analysis such as Continuous Wavelet Transform (CWT), Discrete Wavelet Transform (DWT) and Wavelet Packet Transform (WPT) have advantage over FFT. Besides that, the Empirical Mode Decomposition (EMD), which does not rely on wavelets can also be used. This chapter gives brief introductions about the different waveform processing techniques and the application of each of them in different acoustic signals released from different materials.

3.1 INTRODUCTION TO ACOUSTIC WAVEFORM AND WAVELET ANALYSIS

Acoustic waveform is created by the sudden release of energy in a material when it is strained or damaged. This sudden release of energy generates waves which propagate through the material by adiabatic compression and decompression of the material. The acoustic waves propagate through the material at an ultrasonic velocity, which can be described by the stiffness or modulus of the material. The most general form of acoustic waveform has been given by Feynman (1965) as:

$$\frac{\partial^2 p}{\partial x^2} - \frac{1}{c^2} \frac{\partial^2 p}{\partial t^2} = 0 \tag{3.1}$$

where p is pressure of the sound and x is the position of the wave in its propagating direction, c is the velocity of the sound in the particular medium and t is the time period.

The acoustic waves can be analyzed in their time frequency domain. The magnitude of the frequency at which the acoustic wave, that has been generated. has been calculated through FFT for many years. However, the FFT decomposes the original acoustic wave or any signals into infinite lengths of sines and cosines. By doing so, they lose the time localization information. The FFT provides information about the magnitude and frequency of the waveform. In AE study, the time localization of the waveform is very critical. Because the acoustic wave in a material propagates through two different modes: low-frequency symmetric and high-frequency asymmetric modes. The low-frequency symmetric has a very short risetime but the acoustic wave has longer duration with the energy distributed throughout the duration of the wave. On the other hand, high-frequency asymmetric waves have shorter duration with high energy content concentrated within that shorter duration. For instance, in a CFRP material which is under strain, both the matrix cracking and the delamination release acoustic signals that propagate under low-frequency symmetric mode. While, the damages such as fiber breakage or interlaminar crack growth release acoustic signals which propagate in high-frequency asymmetric mode. Thus, it is essential to analyze the acoustic waveforms in their time-frequency domain, which is not possible in FFT.

There is another limitation of the FFT when it comes to analyze acoustic waves. Acoustic waves are generally decaying in nature and sometimes it may take the form of decaying sinusoidal. But mostly, the AE signals are unstable and nonstationary. By decomposing these waves into infinite sine and cosine waves using FFT is not suitable.
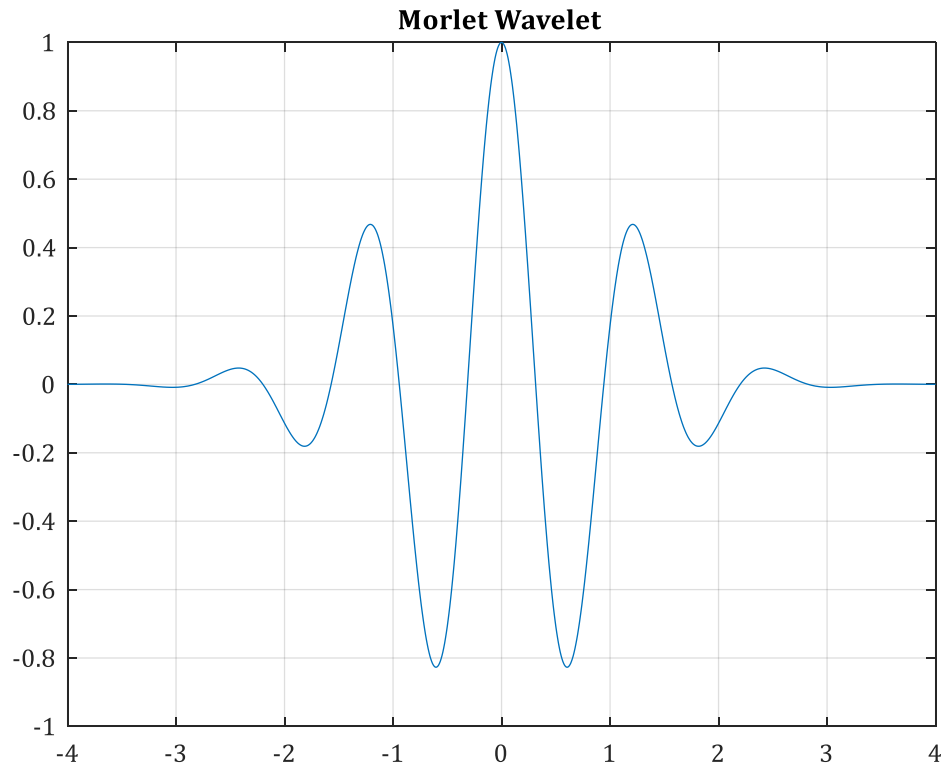
Figure 3.1. The mother wavelet used for wavelet analysis: Morlet Wavelet

Wavelet analysis decomposes the original signal into a set of basic functions of defined contractions, expansions and translations of the mother function, which is essentially called as wavelet. Wavelets are small oscillations that are highly localized in time. The most commonly used wavelet is Morlet wavelet, which is presented in Figure 3.1. Instead of decomposing the signal into sine and cosines, it is decomposed into different sets of function defined wavelet. This gives the independence to choose the type of wavelet to be used any type of unstable or nonstationary waves. For instance, MATLAB® provides 16 different wavelet families to choose wavelet from. Moreover, user defined wavelets or adaptive wavelet can be also be used for the analysis. This makes the wavelet analysis superior to the FFT. Below is the list of few commonly used wavelet families for analysing acoustic signals.

- Haar
- Daubechies

- Symlets
- Coiflets
- BiorSplines
- ReverseBior
- Meyer
- DMeyer
- Gaussian
- Mexican Hat
- Morlet
- Complex Gaussian
- Shannon
- Frequency B-Spline
- Complex Morlet
- Fejer-Korovkin

In this chapter, a waveform propagated through a Carbon Fiber Reinforced Plastic (CFRP) specimen is taken for analysis and given as an example for all the types of wavelet analysis and processing of the waveforms. This constitutes half of the chapter. The second half of the chapter provides the experimental results of different wavelets used for the analysis purpose in damage characterization of the material using acoustic waveforms.

3.2 CONTINUOUS WAVELET TRANSFORM

Generally, a wavelet transform is a decomposition of the original signal $f(x)$ into a set of elementary waveforms and analyze the original signal into their wavelet coefficients. Then by studying the wavelet coefficients, the signal can be analyzed in its time-frequency domain.

The continuous wavelet transform (CWT) can be defined as:

$$CWT_f(a,b) = \int_{-\infty}^{\infty} f(x)\overline{\zeta_{a,b}(x)dx}, a > 0, b \in \mathbb{R} \tag{3.2}$$

where the mother wavelet is defined as,

$$\zeta_{a,b}(x) = \frac{1}{\sqrt{a}} \zeta\left(\frac{x-b}{a}\right) \tag{3.3}$$

The complex conjugate of the mother wavelet is $\bar{\zeta}$, a is the scaling factor with which the mother wavelet is dilated or compressed and b is the translation factor, which is the time shift. It also obliges to the condition $\zeta = L^2(\mathbb{R})$

The CWT is the convolution of data sequence with a scaled and translation of the mother wavelet ζ. An example of a mother wavelet, Morlet wavelet, which is the most commonly used wavelet in the CWT (refer Figure 3.1) can be given by the equation,

$$\zeta(x) = e^{-\pi x^2} e^{10i\pi x} \tag{3.4}$$

In this similar way, adaptive wavelets based on the original signal can be devised and used in the CWT. This gives an advantage over the FFT, which only uses sine or cosine waves for convolution.

A typical acoustic waveform generated in a CFRP material, which is subjected to mode I delamination is presented in Figure 3.2. The material used for this study is a double cantilever beam (DCB) specimen made from 12 layers of unidirectional CFRP laminate, each having a ply thickness of 0.152 mm. This waveform will be used as example for all the wavelet analysis in the subsequent sections.
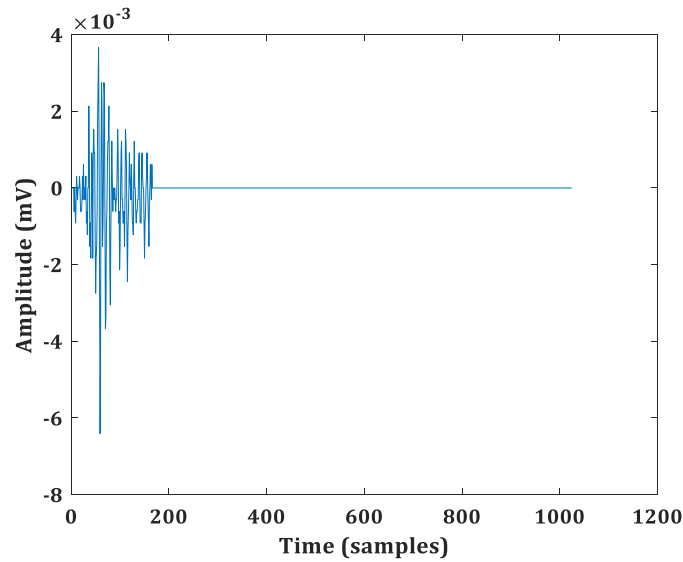
Figure 3.2. Example of Acoustic Waveform generated during the mode I delamination of CFRP laminates
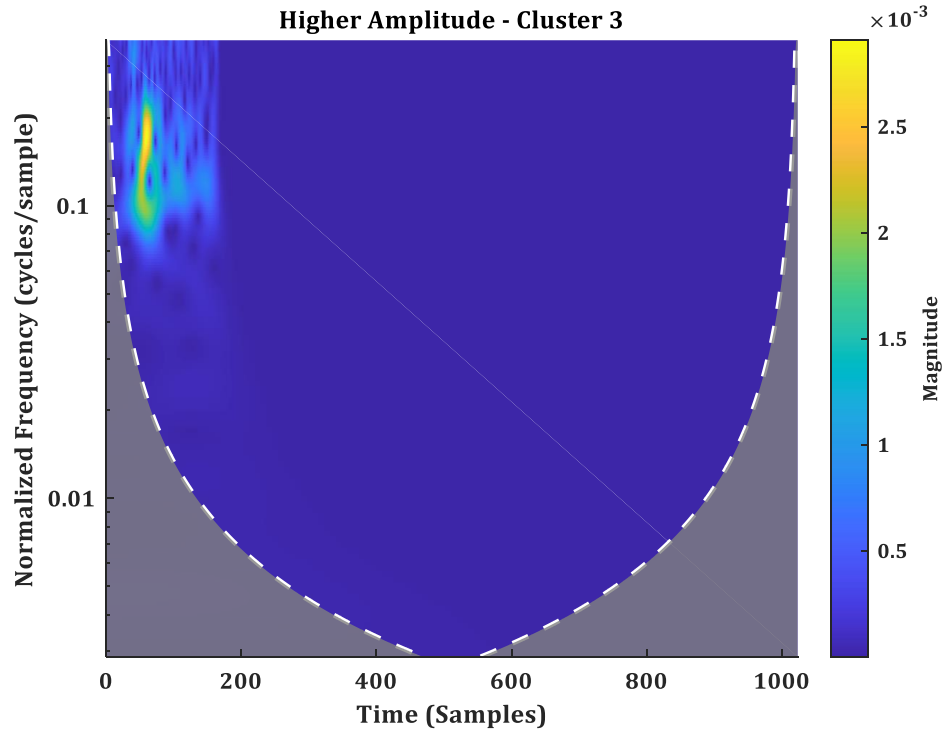
Figure 3.3. CWT results of the acoustic waveform generated during the mode I delamination of CFRP laminate

The CWT of this waveform is performed using the analytical Morlet wavelet and the results are presented in Figure 3.3. Number of octaves used for this analysis is 7, while the number of voices per octave is 32. The presented result shows the frequency localization in the time domain. It also expresses the maximum magnitude of the frequency localized. Unlike FFT, which loses the time-localization information, CWT provides both the time localization and the magnitude of the waveform.

3.3 DISCRETE WAVELET TRANSFORM

The Discrete Wavelet Transform (DWT) has a different application with respect to the other wavelet analysis. DWT is mostly used for denoising and compressing a signal. By using the mother wavelet, DWT discretises the original signal based on the scaling and translation factors.

DWT decomposes the signal into certain number of user defined levels into their approximation and details. The approximations are the low pass sub-bands in the

decomposition level and the details are the high pass sub-bands. In some cases, the noises may also carry some useful information and the DWT enables to analyze the noise separately.

DWT for a waveform $f(x)$ can be defined as:

$$DWT_\varphi(j_0, k) = \frac{1}{\sqrt{M}} \sum_x f(x)\varphi_{j_0,k}(x) \tag{3.5}$$

$$DWT_\psi(j, k) = \frac{1}{\sqrt{M}} \sum_x f(x)\psi_{j,k}(x) \tag{3.6}$$

where, $\varphi_{j_0,k}$ is the convolution function for devolution/compression and scaling. $\psi_{j,k}$ is the mother wavelet. Both $\varphi_{j_0,k}$ and $\psi_{j,k}$ are the functions of the discrete variable x. Typically, j_0 is left as 0 and $M = 2^j$.

Besides, the inverse of discrete wavelet transform, which essentially means reconstruction of the signal back to the original form is also possible. This is known as Inverse Discrete Wavelet Transform (IDWT). The original waveform can be reconstructed through the following equation.

$$f(x) = \frac{1}{\sqrt{M}} \sum_k DWT_\varphi(j_0, k)\, \varphi_{j_0,k}(x) + \frac{1}{\sqrt{M}} \sum_{j=j_0}^{\infty} \sum_k DWT_\psi(j, k)\psi_{j,k}(x) \tag{3.7}$$

DWT decomposition tree is presented in Figure 3.4.

The signal presented in Figure 3.2 is decomposed into single level decomposition using DWT. The approximation and detail parts of the decomposed signal are presented in Figure 3.5. The reconstructed signal using IDWT along with original acoustic waveform is presented in Figure 3.6. The wavelet used for the DWT and IDWT processes is Haar wavelet.
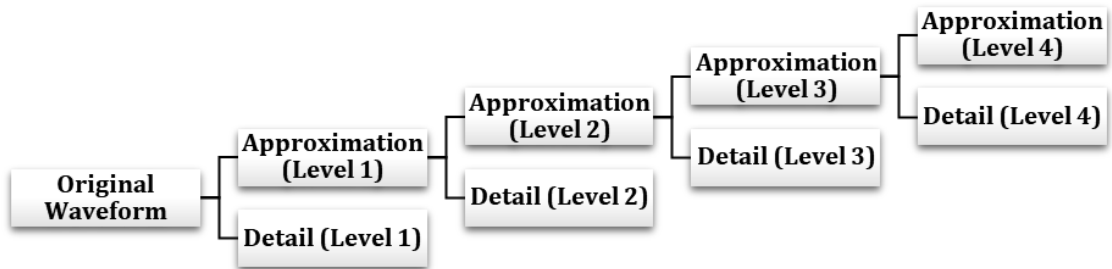
Figure 3.4. Discrete Wavelet Transform – Decomposition Tree
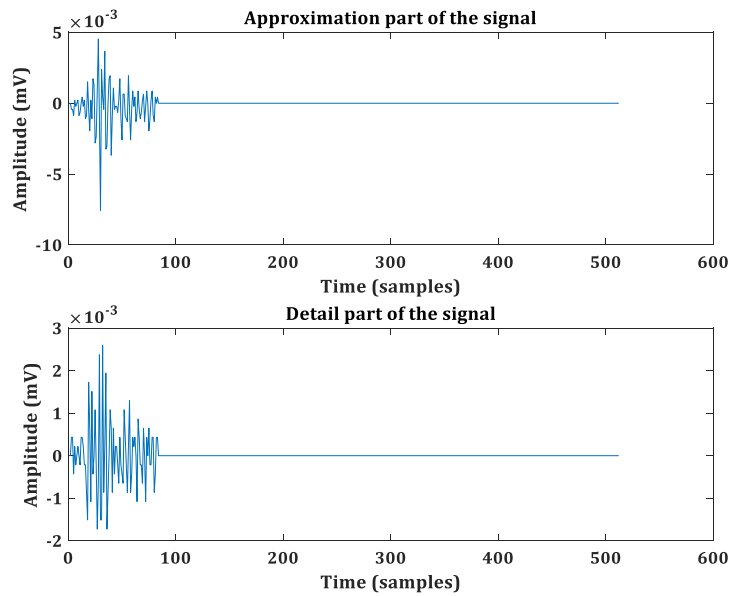
Figure 3.5. Approximation and Detail part of single level decomposed acoustic waveform generated during the mode I delamination test using DWT
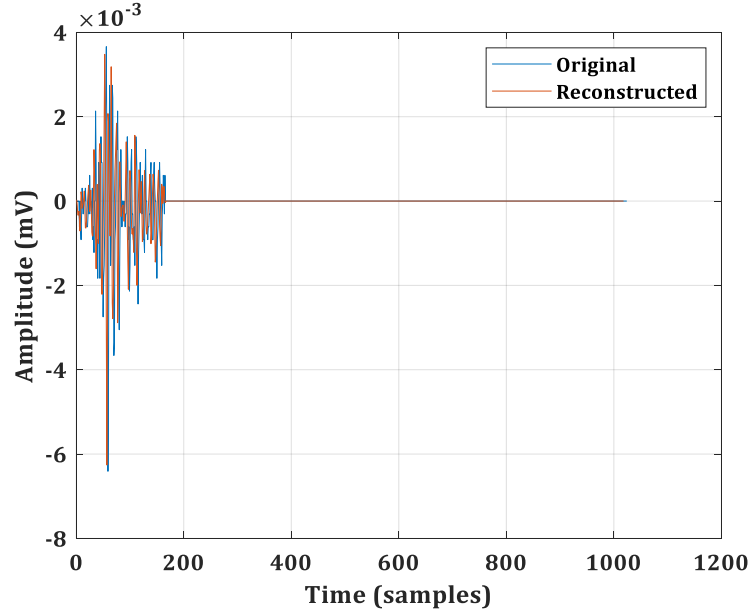
Figure 3.6. Original and Reconstructed signal from the approximation content of the acoustic waveform generated during mode I delamination

The original signal is decomposed into 3 levels and 5 levels, respectively and the decomposed parts are presented in Figures 3.7 and 3.8, respectively.
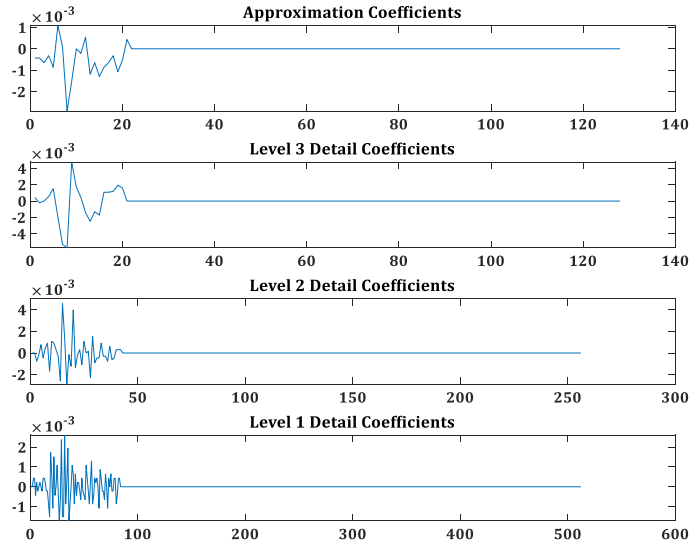
Figure 3.7. Decomposition of the signal generated during the mode I delamination into 3 levels using DWT

30
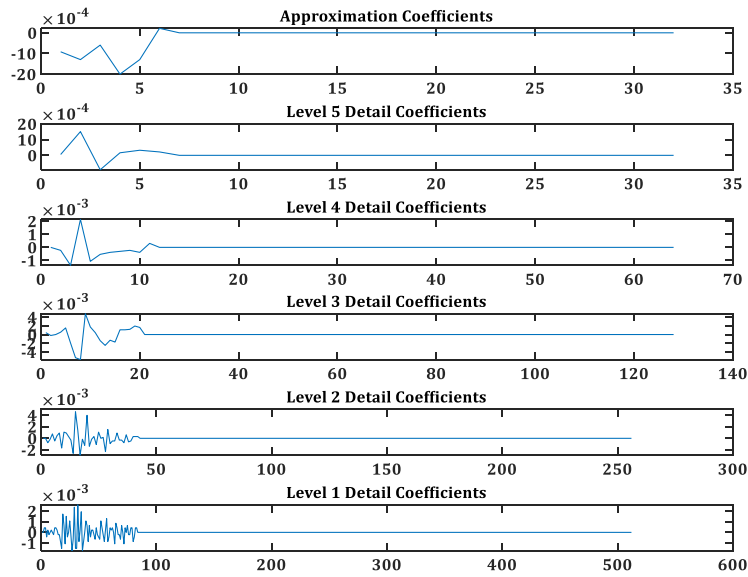
Figure 3.8. Decomposition of the signal generated during the mode I delamination into 5 levels using DWT

This is the advantage that DWT presents over the FFT. The denoising of the signal is performed by scaling and translating user defined wavelets and thereby the frequency localization information is not lost. Besides, the DWT varies also from CWT in terms of the applications in which it is used. CWT is a powerful tool for frequency localization in time domain, whereas DWT is more suited for denoising a signal into different levels. DWT also retains the original features of the signal.

3.4   WAVELET PACKET TRANSFORM

Wavelet Packet Transform (WPT) overcomes the limitations of CWT and DWT, while retaining their advantages over FFT. The major problem with the DWT is that it decomposes the signals into approximations and details, retaining all the levels of details but only one level of approximation. This means that DWT discards the low sub-band content post denoising. In some cases, it is crucial to also study the low sub-band frequency content and DWT limits the analysis. WPT, on the other hand, decomposes the original waveforms into predefined number of levels, while retaining both the

31

approximation and detail content of both the low sub-band and high sub-band for the predefined levels.

Wavelet packets are linear combinations or superpositions of wavelets which retains the orthogonality, smoothness and localization properties of their parent. WPT, as indicated earlier, decomposes the original signal with the mother Wavelet into a low-frequency component (called Approximation) and a high-frequency component (called Detail). Each of these components is again decomposed into Approximation and Detail until the desired level of decomposition is achieved. The Wavelet Packet Tree of decomposition is provided in Figure 3.9.
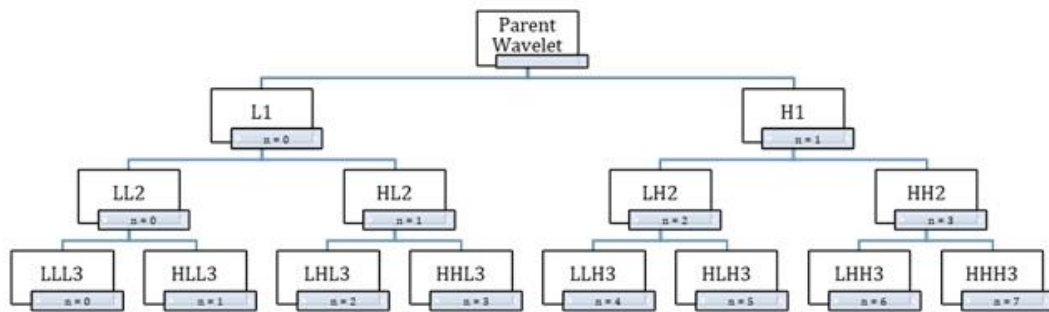
Figure 3.9. Wavelet Packet Tree of Decomposition Levels

The low frequency levels are mentioned as L and the high frequency levels as H in Figure 3.9. The provided wavelet packet tree shows the decomposition to level 3. Clearly, at each level, both the low sub-band L and high sub-band H are being decomposed into LH and HL. The process continues until the predefined number of levels. The number of components (n) for each level is given by 2^i, where i is the decomposition level. The energy of each component in the specific decomposition level can be calculated by,

$$E_i^n = \sum_{T=t_0^n}^{t_1^n} f_i^n(T) \tag{3.8}$$

where, E_i^n is the Energy of each component, f_i^n is the WPT component and t_0^n and t_1^n is the time period. The Energy Percentage ($\%_i^n$) of each component of the original signal can be calculated using,

$$\%_i^n = \frac{E_i^n}{\sum_n \sum_1^{2^n} E_i^n} \tag{3.9}$$

Similar to the previous sections, the acoustic waveform presented in Figure 3.2 is decomposed into 3 levels using WPT and the result is presented in Figure 3.10.
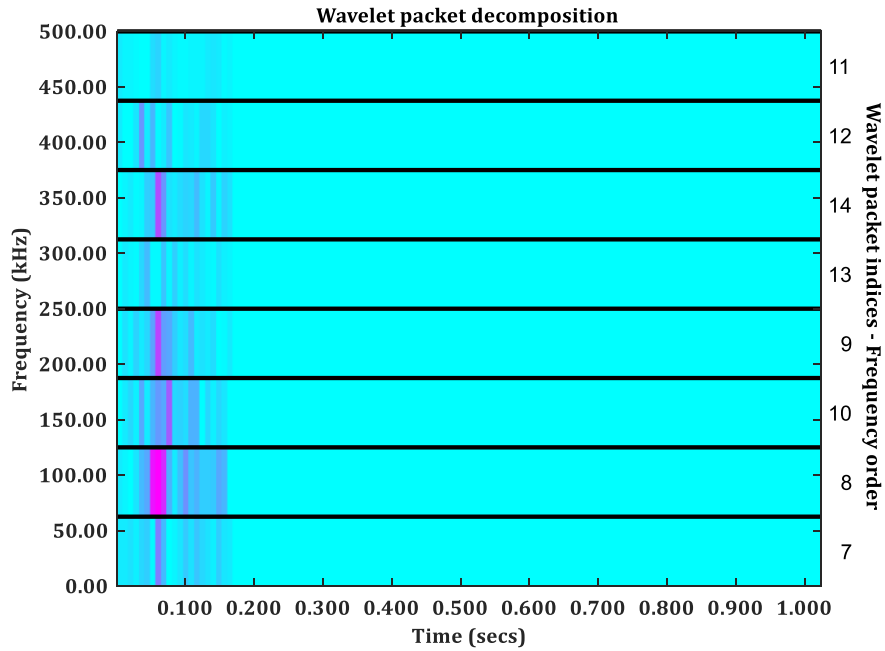
Figure 3.10. WPT results of Acoustic Waveform generated during the mode I delamination

The wavelet energy coefficients at each level are calculated using Equation (3.7), which is followed by the percentage of energy distributed each level/frequency band is presented in Table 3.1.

Table 3.1. Percentage of Energy distributed for the signal decomposed using WPT

Energy percentage (%) distributed in each Frequency Band (kHz)							
0-62.5	62.5-125	125-187.5	187.5-250	250-312.5	312.5-375	375-437.5	437.5-500
7.47	42.58	14.73	14.17	2.99	12.08	4.87	1.09

This proves the efficiency of WPT and its advantages over CWT and DWT. An obvious question that may arise on why simply WPT can be preferred over CWT and DWT since it has the advantage. Not for all the applications, the energy distribution of the frequency

band must be essentially calculated. In most of the cases, it is suffcient to localize the frequency band in the time domain. Besides, one of the limitations of WPT is that it involves post processing of data to calculate the energy bands and it requires more computation time and space. Nonetheless, it has certain advantages over the CWT and DWT, not to mention the FFT as well.

3.5 EMPIRICAL MODE DECOMPOSITION AND HILBERT-HUANG TRANSFORM

Unlike the previous 3 methods of waveform analysis, Empirical Mode Decomposition (EMD) and Hilbert-Huang Transform (HHT) are not wavelet analysis. Because these methods do not convolute the waveforms into infinite number of sine/cosine waves or into infinite number of wavelets with different scaling and shifting parameters. In fact, EMD does not rely on any wavelets. Since AE waveforms are unstable and nonstationary, there are occasions where any of the wavelets cannot be properly assigned for time-frequency analysis. At this point, the adapted wavelet technique is preferred. The adapted wavelet technique is based on creating an user-defined wavelet based on the original waveform.

This has some practical limitation when it comes to damage monitor using AE. A material releases hundreds/thousands of acoustic waves while deforming or undergoing damage progression. It is not certain that one user-defined wavelet can be assigned to all these acoustic waves. At the same time, the task becomes tedious and consumes lots of memory in the data acquisition system if an unique wavelet is adapted for all the hundreds/thousands of acoustic waves.

EMD can overcome these limitations. It works very well for any type of nonlinear and nonstationary signals. EMD can work with any complicated data by decomposing them into finite or often small number of Intrinsic Mode functions (IMF), which can provide instantaneous frequency in the Hilbert Transforms.

By the sifting process, the EMD decomposes the given signal $F(t)$ into a specified number of Intrinsic Mode Functions (IMF) (k) and residual $r_k(t)$. The intrinsic mode functions are created using shifting process. The decomposition is based on three assumptions.

34

1. The signal $F(t)$ has at least two extrema: a maximum and a minimum
2. The characteristic time scale is defined by the time lapse between the maximum and the minimum
3. If the data were totally devoid of extrema but contained only inflection points, then it can be differentiated once or more times to reveal the extrema

Once the extrema are identified, all the local maxima are connected by a cubic spline line as the upper envelope $S_u(t)$. The procedure is repeated for local minima to produce the lower envelope $S_l(t)$. The upper and lower envelopes should cover all the data between them. Then a first temporary IMF component h_1 is calculated by calculating the mean of the envelopes m_1.

$$F(t) - m_1 = h_1 \tag{3.10}$$

where, $m_1 = [S_u(t) + S_l(t)]/2$

The h_1 is considered as a temporary IMF because overshoots and undershoots are common, which can also generate new extrema, and shift or exaggerate the existing ones. Besides, the spline fitting can occur near the ends, where the cubic spline fitting can have large swings. Left by themselves, the end swings can eventually propagate inward and corrupt the whole data span especially in the low-frequency components.

For eliminating the riding waves and for creating wave profiles more symmetric, the sifting process is followed. The second sifting process gives,

$$h_1 - m_{11} = h_{11} \tag{3.11}$$

where h_{11} is the new temporary IMF and m_{11} is the new average of the envelope. By repeating the sifting process for k number of times,

$$h_{k-1} - m_{1k} = h_{1k} \tag{3.12}$$

$$IMF_1 = h_{1k} \tag{3.13}$$

The first IMF is taken after iterating the sifting process for k number of times.

The next step in EMD is the creation of an envelope over the given signal by connecting the points of local minima and maxima, respectively. The envelope connecting the local maxima forms the upper envelope $S_u(t)$ and the envelope connecting the local minima

forms the lower envelope $S_l(t)$. Then the mean envelope $m_{k,i}(t)$ is calculated by taking the average of upper and lower envelopes.

After assigning the first IMF, the algorithm will check the condition for the IMF to be valid. The conditions are as follows:

1. The number of maxima and minima and the number of zero-crossing points of the given data set must be equal, if not, they should differ at most by one.
2. At any point, the mean value of the upper envelope and the lower envelope must be zero.

This simply means that each IMF function in which the given signal $F(t)$ will be decomposed into, must be in oscillatory mode with same the number of maxima, minima, zero-crossings and that its envelope is symmetric with respect to zero.

Once these conditions are satisfied, the remaining predefined numbers of IMF are calculated following the same procedure. All these calculated IMF and residual signals $r_n(t)$ must be a function of the given signal $F(t)$ as follows:

$$F(t) = \sum_{i}^{k} IMF_i(t) + r_n(t) \tag{3.14}$$

The instantaneous frequency of the IMF or the original signal can be calculated using Hilbert Transform. The Hilbert Transform $Y(t)$ can be calculated as:

$$Y(t) = \frac{1}{\pi} P \int_{-\infty}^{\infty} \frac{F(t')}{t - t'} dt' \tag{3.15}$$

Similar to the previous sections, the signal from Figure 3.11 is taken as an example and decomposed into 5 IMFs and its residual.

In the next section of this chapter, the experimental campaign in which the different waveform processing methods are used for material characterization or assessing damage modes are explained. CWT, WPT and EMD/HHT has been used in this study. DWT is not used in any of the experimental campaign because WPT is preferred over it. As indicated in the previous sections, the only limitation WPT has over the DWT is the processing time and consumption of space. Since these two restrictions did not limit the performance of the experimental campaign, WPT is preferred over DWT.
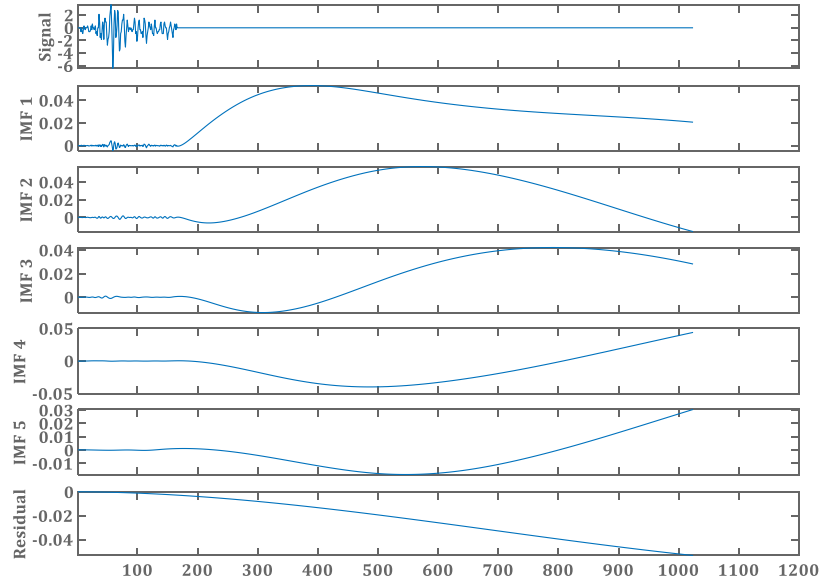
Figure 3.11. Decomposition of Acoustic Waveform into Intrinsic Mode Functions using EMD

3.6 EXPERIMENTAL RESULTS AND DISCUSSION ON THE APPLICATIONS OF WAVEFORM ANALYSIS

3.6.1 Analysis of Wave Propagation using CWT

During the course of the research work, it is identified that there is an attenuation of acoustic waves during its propagation in material. This is common, however, the extent of this propagation can affect the proper acquisition of data during damage monitoring. During damage monitoring, one or more AE sensors are mounted on the specimen and the load is applied to the specimen. When the specimen is strained or goes through irreversible change, it releases acoustic waves. These waves have to propagate a distance from their origin to the sensor. To understand how the geometry and the configuration of the structural material affect the propagation, Fiber Reinforced Polymer (FRP) composites have been studied.

Four different CFRP specimens with varying geometry and lay-up configuration are taken for this study. The details about the specimen geometry and lay-up configurations are presented in Table 3.2. The sensors used for this study is R30α – General purpose sensor

with an operating frequency of 150 kHz to 400 kHz. The signal which is generated for understanding the propagation acquisition is a 28 V voltage spike by the piezoelectric crystal, which is excited through Auto Sensor Testing – Self Testing Mode (AST-STM) of PAC PCI II AE systems. The distance between the source and the receiver is 75 mm. The details about this testing mode is explained in the subsequent section, where the same specimens are used for understanding the attenuation of wave propagation through parameter approach. In this section, only the signal-based, that is the acoustic waveforms are analyzed and explained.

Table 3.2. Specimen configuration used for studying the attenuation of Wave Propagation

Specimen Name	Layup Configuration	Length mm	Breath mm	Thickness mm
C1	[0/90]$_{12}$	150	100	2.76
C2	[45F/0T/0T/45F/0T/0T/0F/ 0T/0T/0F/0T/0T/45F/0T]$_S$	250	25	2.08
C3	[0/90]$_{12}$	300	30	2.73
C4	[0]$_{11}$	155	10	2.94

The CWT results of the signal sent, which corresponds to the voltage excitation with 28 V burst signal is presented in Figure 3.12. The CWT results of the signals received at the receiving end of all the four specimens are presented in Figure 3.13.
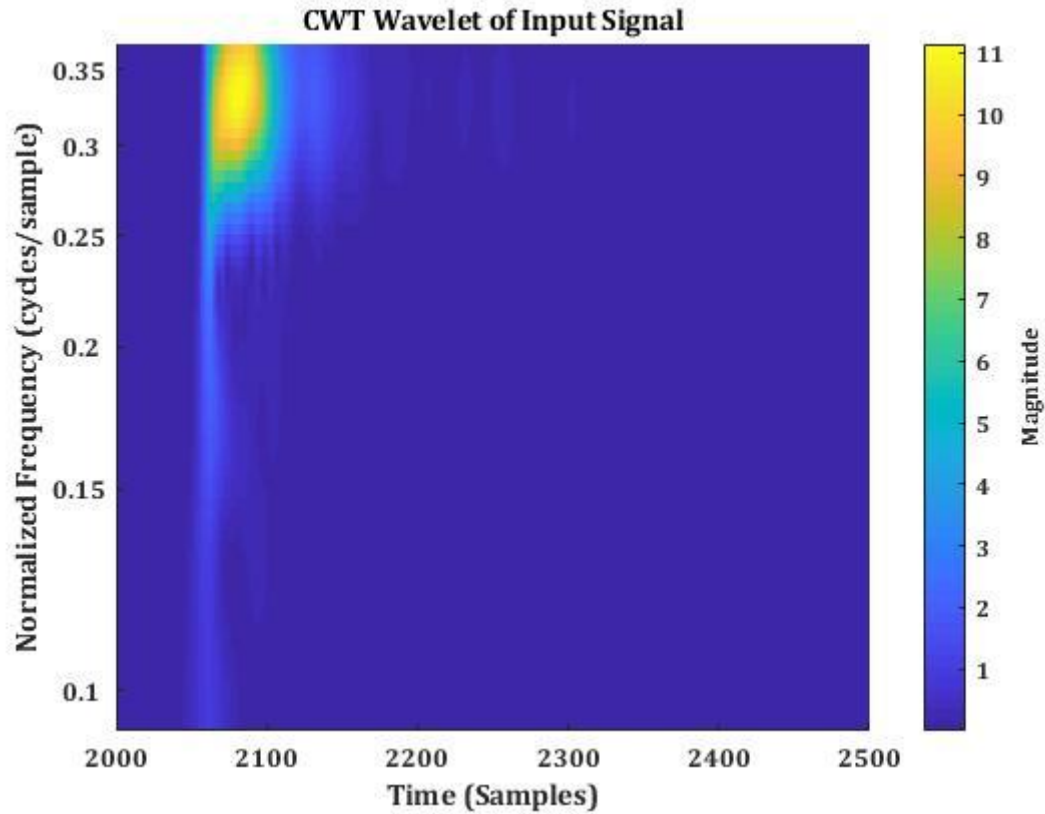
Figure 3.12. CWT results of the signal sent

Figure 3.12 indicates that the sent signal is highly modulated in amplitude (spectral magnitude ranges from 2 to 11 in the frequency domain) over a very short time interval. Conversely, Figure 3.13 shows that received signals are modulated over relatively longer time intervals. As mentioned above, the distance between the source and the receiver is 75 mm. The acoustic signals are decaying in nature and they tend to disperse in the propagating medium by losing their energy before reaching the receiver.
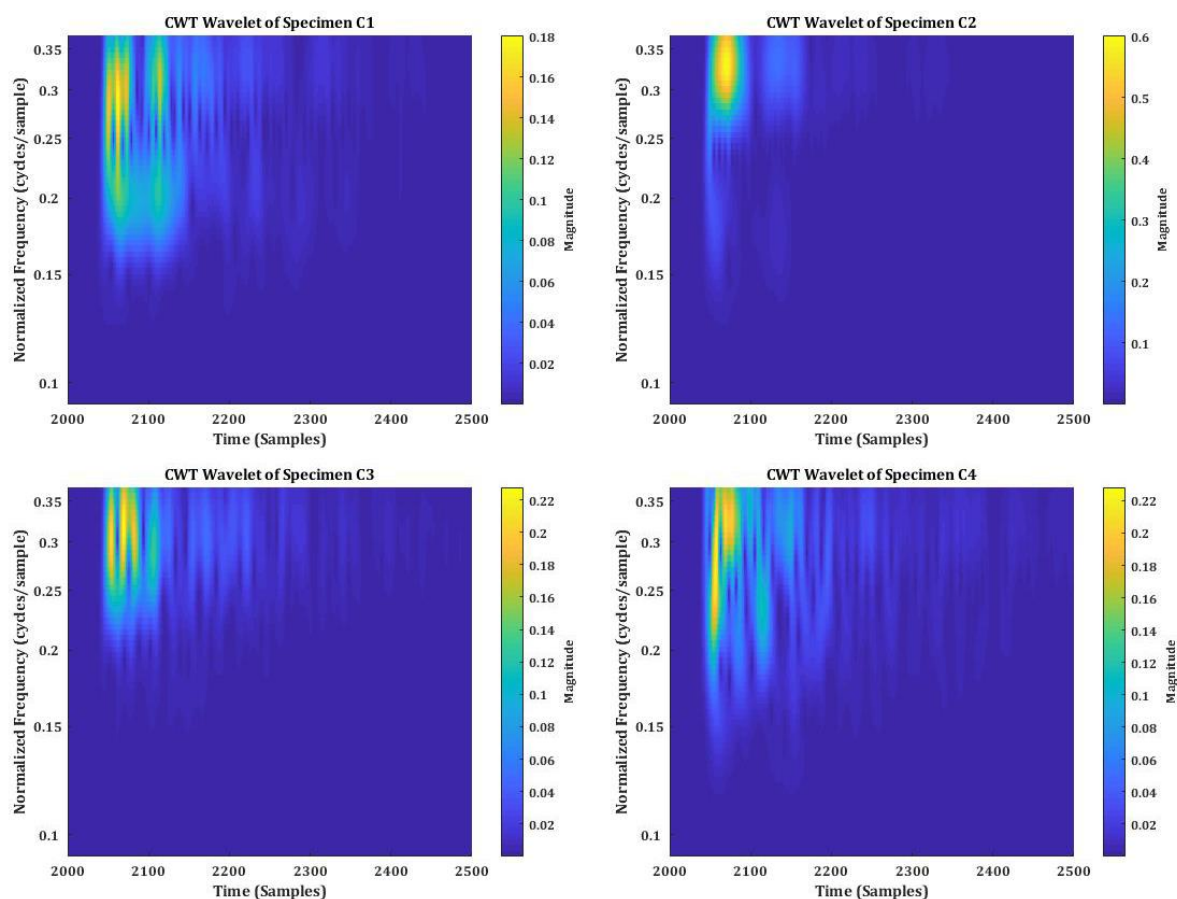
Figure 3.13. CWT results of signals received by the sensor in specimens C1, C2, C3 and C4

In specimens C1 and C4, the waveform can be observed in two different frequency domains. The frequency spectrum in the specimens C1 and C4, for the same sample value in the initial stages, shows two frequency domains separated very narrowly. Moreover, two distinct frequency domains can be observed in specimen C2, even if not so clearly as in the previous ones. The two frequency domains in the specimen C2 have different magnitude values for each domain. Moreover, the frequency pattern of the specimen C2 is almost identical to the Input signal. In addition, specimen C2 exhibited the minimum loss in AE descriptors. On the other hand, the wavelet transform on the specimen C3 is completely different. Although frequency domains of C1 and C3 above the normalised frequency 0.25 cycles/sample are very similar, the entire wavelet is not identical.

Thus, it can be inferred that the different material properties, geometry of the material and the thickness of the couplant play an important role in the acoustic signal transmission.

Besides, the major point which can be considered through this analysis is the minimum distance between the sensor and the damage source can be analyzed using this CWT analysis. This is the major application. In large composite structures, a grid of AE sensors is used for structural health monitoring. By analyzing the wave attenuation in the propagating medium in their time-frequency domain using CWT can help in assessing the minimum and maximum number of sensors required in the grid for accurate health monitoring.

3.6.2 Analysis of Damage modes during Mode I delamination using WPT

Damage modes during the mode I delamination of CFRP unidirectional laminate specimens are studied using WPT. The specimens used this study has a Double Cantilever Beam (DCB) configuration.

3.6.2.1 Materials used for DCB Mode I delamination testing

The DCB specimens are prepared as per ASTM D5528 standard: the length and breadth of each specimen are 125 mm and 25 mm, respectively and the thickness is 3 mm. The specimens are prepared by Resin Film Infusion (RFI) process. The CFRP system has 35 % resin content and the carbon fibers in 0° horizontal direction along the delamination direction. The specimens were fabricated with an even number of unidirectional plies with a ply thickness of 0.152 mm. A non-adhesive insert of 45 mm long and thickness 13 μm (approx.) is inserted during the curing process, located at the middle of the sample through its thickness to initiate the Mode I delamination. A couple of Piano Hinges are adhered to the surface of the specimen, near the edge of the surface where the insert is positioned, through a strong adhesive. The delamination propagation was along the 0° direction. The schematic of the DCB Specimen tested is given in Figure 3.13. The DCB test is carried out at room temperature (~23 °C) on an INSTRON (Servo-Hydraulic) testing machine. The test is carried out in displacement-controlled mode at a constant

displacement rate of 1 mm/min. Three DCB specimens (named A, B and C) are taken for this study.
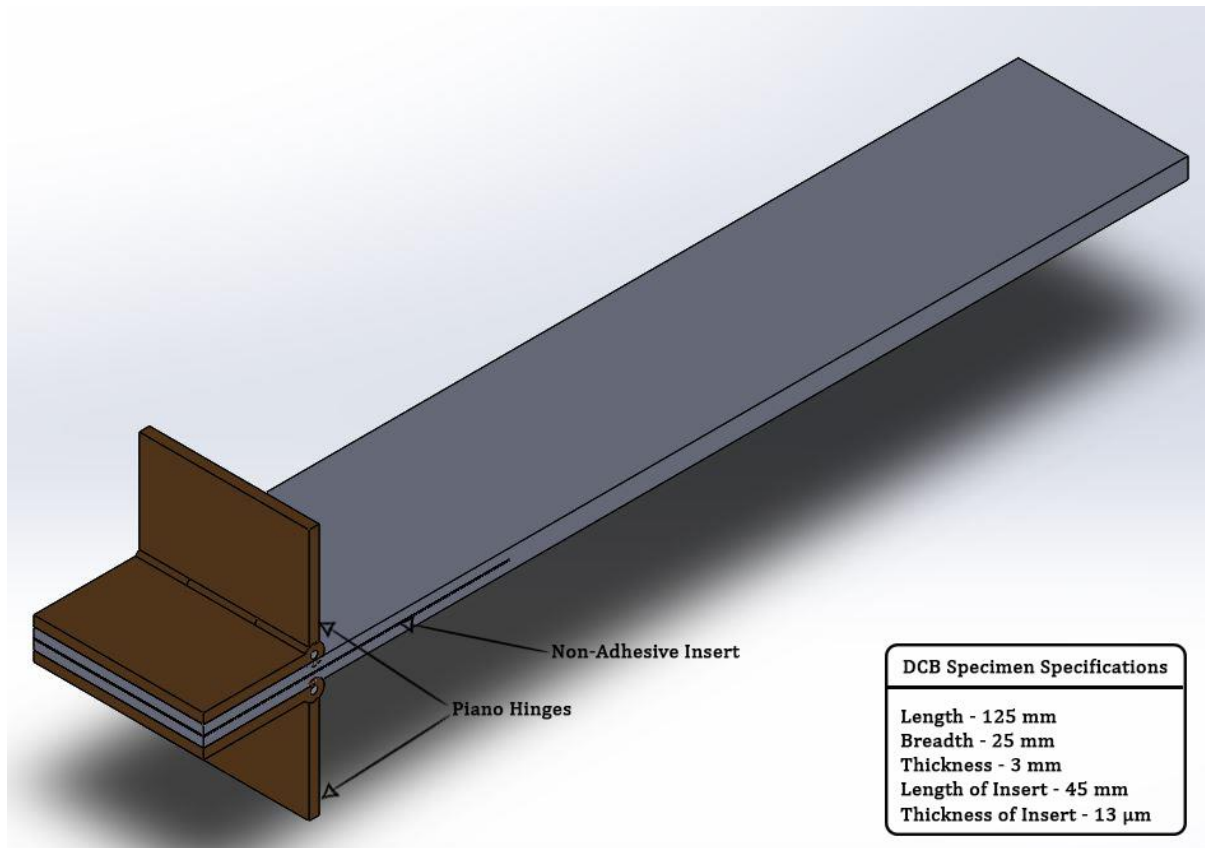
Figure 3.14. Schematic of DCB specimen with piano hinges

3.6.2.2   Acoustic Emission Setup for testing

To record the Acoustic Events during the test, a piezoelectric sensor is coupled to the surface of the specimen through silica gel. Since the surface roughness of the specimen affects the sensor performance in recording the resonances and reverberations, it is necessary to couple the sensor through a suitable couplant (in this case, silica gel). The sensor used in this study is R30α, supplied by Mistras, Physical Acoustics Corporation (PAC). It is a high sensitivity hybrid sensor with a peak sensitivity of 54 dB and an operating frequency ranging between 150 kHz and 400 kHz. The sensor is connected to the PCI-2 data acquisition board not before pre-amplifying the signal by 40 dB through 20/40/60 AE Preamplifier. The signals are filtered through low-pass and high-pass band

filters of frequencies 1 kHz and 3 MHz, respectively. The wavelets of the acoustic signals are recorded at a sampling rate of 1 MSPS and length of 1K.

3.6.2.3   DCB Mode I delamination Results

From the Load-Displacement curve in Figure 3.15, it is possible to observe that the damage did not progress in the same way for all 3 specimens, despite their similar geometrical and material similarities. Specimen A exhibits a peak load of 96.26 N, while Specimen B and Specimen C have 97.80 N and 115.70 N, respectively.
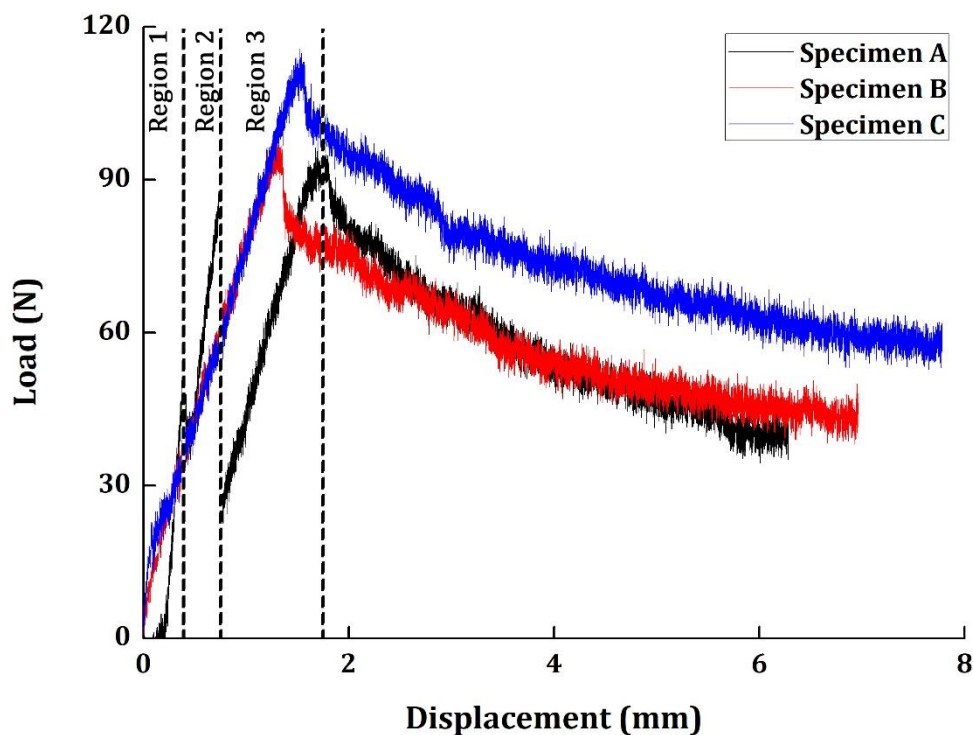
Figure 3.15. Load response of DCB specimen A, B and C

The non-adhesive insert inside the specimen, its dimension and the ply where it is placed between possibly could affect the Mode I delamination. Another factor that can be attributed to the variation in the Load-Displacement curve is the attachment of piano hinges to the upper and lower plies. The adhesive force with which the hinges are attached to the specimen surface and the curing conditions of the adhesive also plays a

significant role in the Mode I Delamination properties of the specimen. Moreover, the fiber pull-out from the adjacent ply during the delamination, the initiation and the propagation of the crack also play a major role in determining the delamination strength. Thus, the variation in the Peak Load and different peaks observed in the Load-Displacement curve can be justified.

3.6.2.4 *Wavelet Packet Transform Results and Discussions*

The signal-based acoustic parameter, the waveform, carries information about the type of damage progression. Many researchers have reported the different frequency bands in the waveform that can be attributed to the different damage mechanisms. For instance, the Peak Frequency associated with Matrix Cracking is 125 kHz, Debonding is 200 kHz and Fiber Breakage can be associated with the Peak Frequency above 250 kHz.

It is quite impossible to present the Waveform Analysis for each Hit acquired during the Acoustic Events. For instance, in Specimen A, the total number of Acoustic Hits recorded during the DCB test is close to 20000. It means, necessarily there are almost 20000 waveforms recorded. Thus, based on the Load vs Time results, the region of damage progression in all the specimens was separated into three zones named Region 1, 2 and 3. From each Region, three hits were taken for WPT analysis. These Hits were not taken in random, nevertheless. The Hits taken for WPT analysis from each region represents the Peak Load in that specific region. However, in Specimen C there is no specific peak in Region 3. For this reason, 3 random hits at different time intervals from Region 3 were taken for analysis. The Cumulative Hits results were plotted over the DCB test results. For each specimen, a total of 9 Hits were taken for WPT analysis.

The WPT analysis is performed at the decomposition level $i = 3$, thus obtaining a total of $2^i = 8$ components. The decomposed WPT results for Specimen A, B and C are presented in Figures 3.16, 3.17 and 3.18, respectively.

The Energy content in each Wavelet Packet Level is an important parameter to be considered in the Frequency Analysis. To discriminate the different frequency band associated with the type of damage progression, the Energy content of each Frequency Band becomes an essential tool in damage characterization. The Energy Content and the

Percentage of Each Energy Component has been calculated by Equations 3.8 and 3.9. Accordingly, for each region, there are 3 hits with a total of 9 hits for a Specimen. The Energy Content of each component in each specific hit for Specimen A, B and C has been provided in Tables 3.3, 3.4 and 3.5, respectively.

Table 3.3. *WPT Energy Content for Specimen A*

Region	Hit	Energy Content (%)			
		Frequency (kHz)			
		0-100	150	200-250	> 250
	1	8.64	65.33	18.92	7.11
1	2	27.11	27.18	40.13	5.58
	3	26.52	54.31	9.98	9.18
	4	7.73	74.58	11.44	6.26
2	5	5.69	82.61	8.33	3.37
	6	11.1	15.4	69.33	4.17
	7	36.06	24.6	26.17	13.17
3	8	27.36	32.78	16.47	23.39
	9	6.68	22.23	34.44	36.65
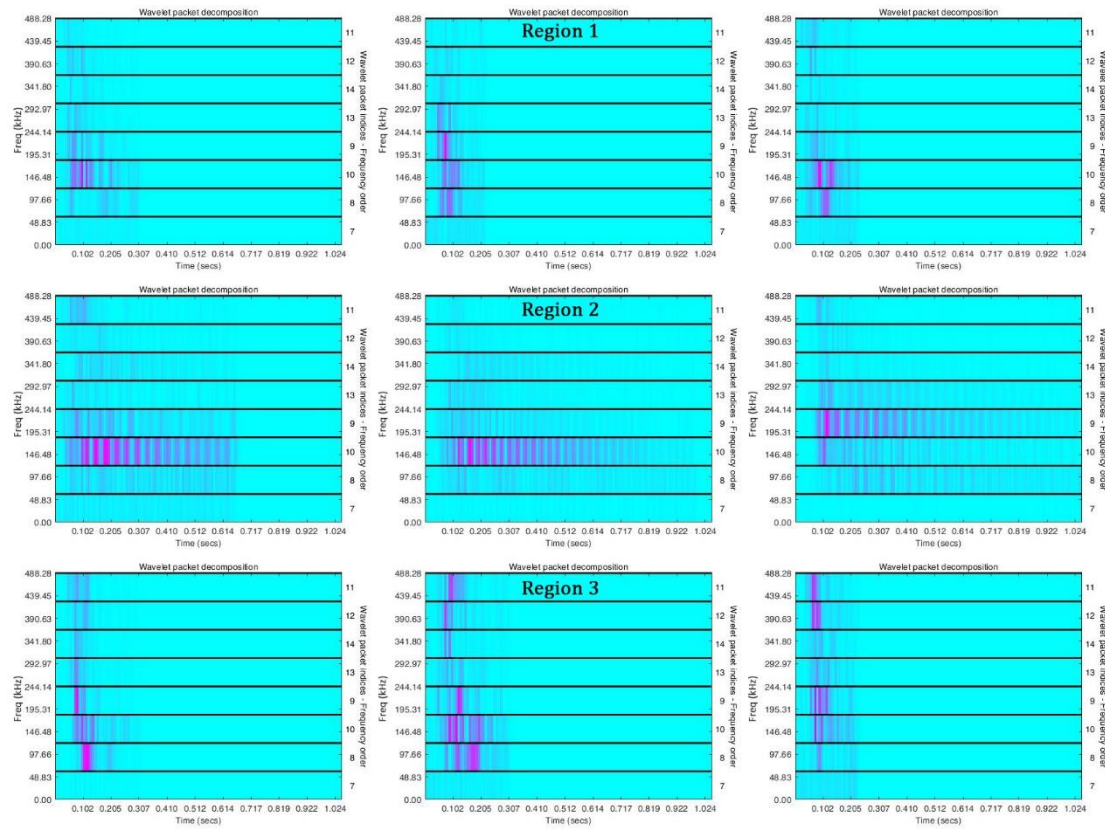
Figure 3.16. WPT analysis of AE hits in specimen A

In Figure 3.16, the frequency band is predominantly between 150 kHz and 200 kHz region, thus, implying that the damage mechanism in Region 1 is predominantly due to Matrix Cracking and Debonding. In Region 2, again the frequency band is around 150 kHz however, the duration of the waveforms is rather longer. In Region 3, a different number of the short-ranged frequency band can be observed. This implies that in Region 3, the damage mechanism is an accumulation of Matrix Cracking, Debonding and Fiber Breakage. The exact percentage of the Energy Content in each Frequency Band can be evaluated and understood from Table 3.3. While looking at the Region 2 in Figure 3.16, the waveform with uncharacteristic longer duration can be seen. This indicates that the acoustic activity at that point is different from the other instances. From which, we can confer that the longer duration signal represents the cracking in the adhesive holding the piano hinges. The frequency band in that region also around 150 kHz indicating that the damage propagation can be attributed only to matrix cracking.
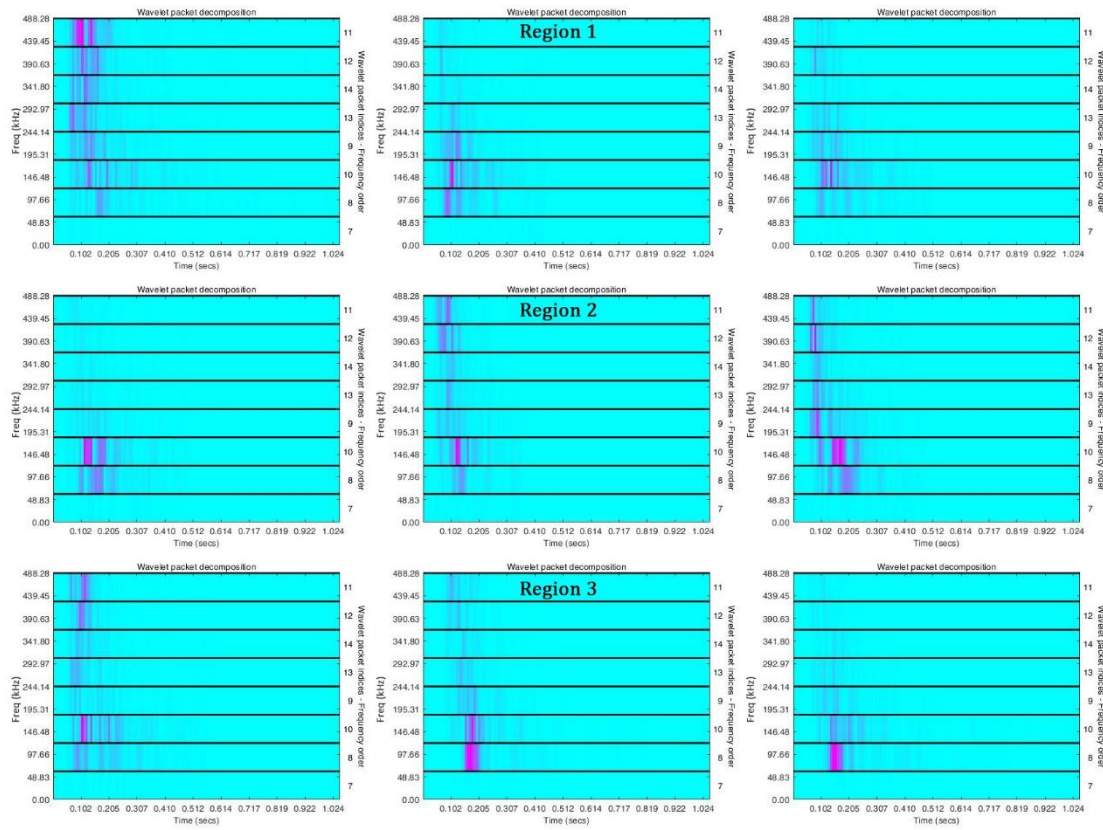
Figure 3.17. WPT analysis of AE hits in specimen B

Similarly, from Figure 3.16 and Table 3.4, the Energy Content of Specimen B can be seen. The majority of the Energy content lies above 400 kHz. Normally, only the Fiber Breakage occurs above the frequency of 250 kHz. It can be understood that some major damage propagation, possible, fiber breakage has occurred at a very early stage in Specimen B. This can also be confirmed by the lower Peak load and earlier stage of deterioration in Specimen B.

For Specimen C, from Figure 3.18 and Table 3.5, in Region 1 and 2, most of the Energy content lies within the two Frequency bands, 150 kHz and 200–250 kHz. However, in Region 3, about 27%–35% of the Energy Content lies above 250 kHz. It can be observed in Region 3 the different short-ranged frequency bands. This confirms that the several damage mechanisms at Region 3 accumulated to the true failure of the material.

47

Table 3.4. *WPT Energy Content for Specimen B*

Region	Hit	Energy Content (%)			
		Frequency (kHz)			
		0-100	150	200-250	> 250
	1	4.26	12.19	20.10	63.45
1	2	27.23	44.33	24.43	4.01
	3	10.01	61.64	18.65	9.70
	4	28.47	67.03	3.09	1.41
2	5	9.97	42.85	10.36	36.82
	6	15.23	42.88	19.39	22.51
	7	12.55	42.78	8.45	36.21
3	8	54.52	29.80	8.56	7.12
	9	72.38	19.57	6.37	1.68
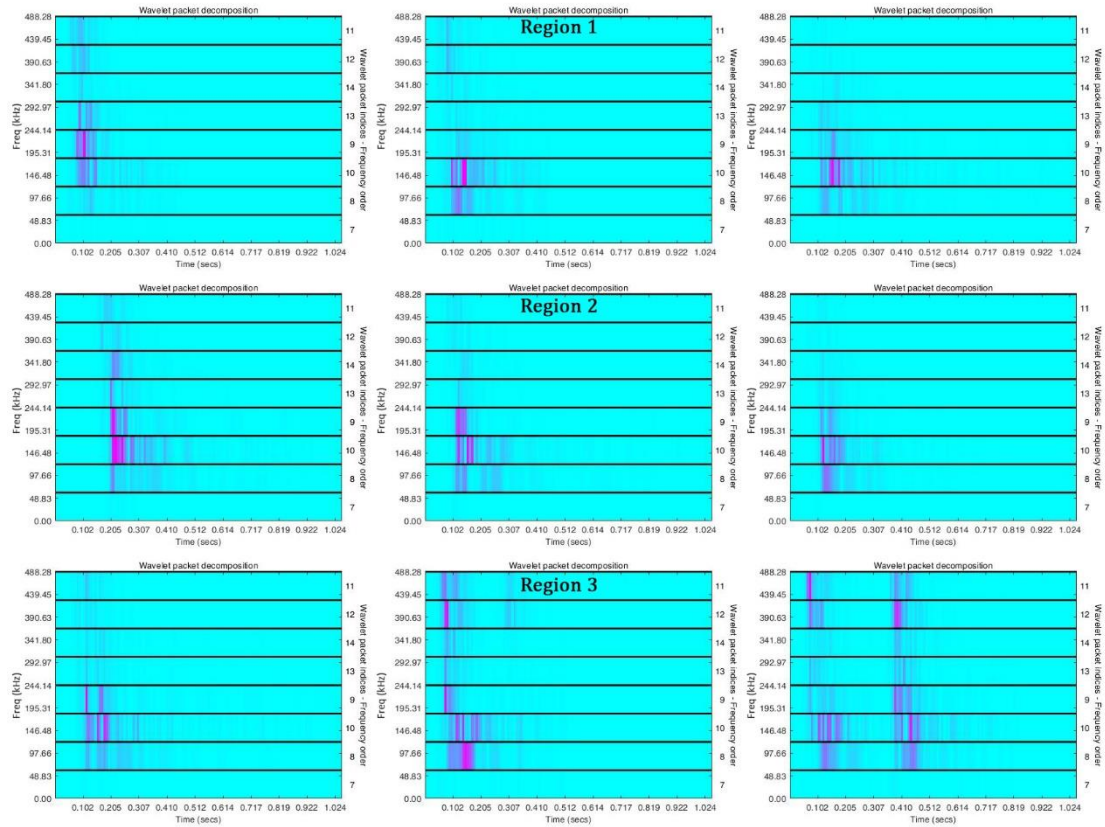
Figure 3.18. WPT analysis of AE hits in specimen C

From the above observations, it can be inferred that the WPT provides information on the Material characteristics not only at the critical point but also during the entire load

history. It truly serves the purpose of the preventive monitoring of a Material. It provides very simple decomposition plots from which the initiation or propagation of damage can be easily identified. Apart from that, the false signals and critical stages of failure can also be monitored using WPT results. By categorizing the frequency band and time domain for each type of damage propagation, the false alarms can be easily identified.

Table 3.5. *WPT Energy Content for Specimen C*

Region	Hit	Energy Content (%)			
		Frequency (kHz)			
		0-100	100-150	200-250	> 250
	1	2.61	26.92	59.14	11.33
1	2	22.61	65.93	4.53	6.93
	3	11.69	73.60	13.67	1.04
	4	6.84	55.77	28.19	9.20
2	5	14.92	51.24	31.65	2.19
	6	29.05	56.29	13.83	0.83
	7	13.13	52.86	29.87	4.14
3	8	33.37	24.93	14.91	26.79
	9	16.24	33.08	15.74	34.94

3.6.3 Analysis of Damage characterization in Selective Laser Melted Specimens using EMD/HHT

The damage modes in Selective Laser Melted (SLM) – additively manufactured materials from AlSi10Mg is tested under static tensile loading. The damage modes in the material under loading is studied using acoustic emission. The acoustic signals are analyzed in their time-frequency domain using Empirical Mode Decomposition (EMD) and the instantaneous frequency of the acoustic signals are analyzed in Hilbert-Huang Transform (HHT).

3.6.3.1 Materials and Testing Methods

Three different configurations of specimens built in the SLM process, which are classified based on the direction of building with respect to the building platform. The three configurations are named as T_X, T_Y and T_{45}. All the specimens are prepared as per ASTM E8 standard with rectangular cross-section.

All specimens are prepared using an industrial additive manufacturing system. The SLM process is carried out by a Nd:YAG laser with a maximum output power of 400 W and a wavelength of 1.064 μm. The laser is scanned along the X-direction, while the AlSi10Mg powder is recoated along the Y-direction. The powder is scanned at a velocity of 100 mm/s. The spot diameter of the laser target is 200 μm for achieving a single-track energy density of 2 J/mm². The layer thickness is selected to be 20 μm. The stress is relieved by post processing treatment in air-cooled conditions at 300 °C ± 10 °C for 2 h.

The test is carried out under displacement-controlled mode with a crosshead displacement of 1 mm/min. The test is carried out in INSTON 1342-Servohydraulic testing machine with a maximum load capability of 10 kN.

For monitoring the AE signals, a piezoelectric sensor with a frequency band (200 kHz - 750 kHz) is mounted on the mid position of the specimen. Detailed information about the AE sensor and preamplifier used in this study are presented in Table 3.6. A thin layer of silicone gel and Kapton tape is applied between the sensor and the surface of the specimen for providing better acquisition of the AE signals. The silicone gel helps in avoiding the reverberated frequencies from being recorded. The threshold frequency of the AE signal acquisition is set to 35 dB. The recorded signals overcoming the threshold frequency are pre-amplified by 40 dB through a 2/4/6 AE preamplifier. The waveforms are recorded at a sampling rate of 1 mega sample per second (1 MSPs).

Table 3.6. AE Sensor and Preamplifier Characteristics

Characteristics of the AE system	
Sensor	PICO Sensor
Operating Frequency	200 kHz – 750 kHz
Resonant Frequency, Ref V/(m/s)	250 kHz
Peak Sensitivity, Ref V/(m/s)	54 dB
Dimensions	$\emptyset 5\ mm \times 4\ mm$
Preamplifier	2/4/6 Preamplifier
Gain Selectable	20 dB/40 dB/60 dB
Input Impedance	10 kΩ
Bandwidth for 40 dB*	10 kHz – 2 MHz

*Bandwidth is provided only for 40 dB since the gain selected for this study is 40 dB

3.6.3.2　　　　Selection of AE waveforms for EMD/HHT analysis

As indicated in the section 3.6.2.3, it is not possible to analyze all the waveforms generated by the material in their time-frequency domain. A selection criterion has been used in this section for choosing the acoustic waveform, which can be the representative of the region. The peak amplitude distribution of the AE events recorded during the history of the loading has been taken as the selection criterion. The peak amplitude recorded for all the three specimens are presented in Figure 3.19.

It is noted that there is an acoustic gap, which is a period where there is no acoustic emission recorded in the loading history, in all three specimens. This acoustic gap represents the incubation of the damage in the specimen before a major damage is about to occur.
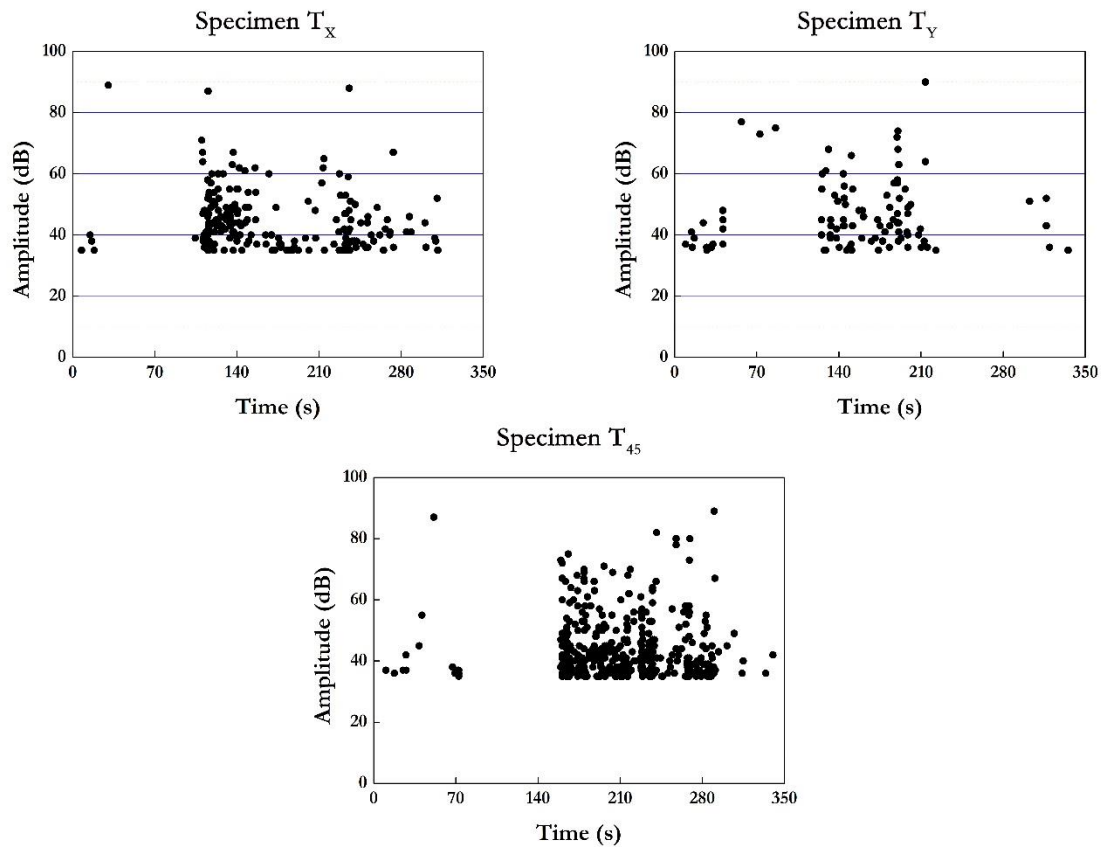
Figure 3.19. Peak Amplitude distribution for all three specimens T_X, T_Y and T_{45}

In all three specimens, there is the presence of an acoustic gap before the major failure starts. In the specimen T_X, an acoustic activity with very high amplitude is recorded around 35 s and after that, there is a period of acoustic gap until 100 s. Similarly, in the specimen T_{45}, an acoustic activity with higher amplitude is recorded around 65 s, following that there are 4 low amplitude acoustic activities. There is an acoustic gap following that low amplitude activities. However, in the specimen T_Y, the acoustic gap is very narrow. There are no low amplitude signals recorded between 50 s and 120 s, nonetheless, there are 3 distinguishable higher amplitude signals recorded during this time. This possibly could represent the strain relaxation at the boundaries where grain cohesion is poor. This can be explained by the direction of the laser during the preparation of the specimen T_Y. The laser is scanned along the X-axis while recoater moves along Y-axis. Thus, it is foreseeable that these two specimens will have not the same microstructure near the boundaries. Because the direction of the melt pool and the density of the borderline porosity differs between the T_X and T_Y specimens due to the direction of laser scan and recoater movement. In all the specimens, the first cluster of acoustic activity could possibly represent the microcracking and sliding of the grain which normally exhibits lower amplitude. During the period of yielding, there is no acoustic activity, which can be explained by the acoustic gap. Subsequently, the crack starts to develop and propagate through the volumetric and surface pores and a number of acoustic events is recorded after this acoustic gap.

Table 3.7. Selection of Signals for EMD and Hilbert Spectrum Analysis

Signal Number	Category	
1	Cluster 1* of Amplitude Distribution	Amplitude <50 dB
2		Amplitude >50 dB
3	Cluster 2** of Amplitude Distribution	Amplitude <50 dB
4		Amplitude >50 dB
5	Random Signal	
6	Random Signal	

*Cluster 1 – AE signals recorded before the acoustic gap
**Cluster 2 – AE signals recorded after the acoustic gap

Using this peak amplitude distribution, the acoustic waveforms are selected for time-frequency analysis. The selection criterion is presented in Table 3.7.

3.6.3.3 *Empirical Mode Decomposition and Hilbert-Huang Transform Results and Discussions*

Figure 3.20 shows a general decomposition of the acoustic waveform into 5 levels of Intrinsic Mode Functions (IMF) using EMD. It can be observed that the amplitude levels of IMF 4 and IMF 5 are very low. They possibly can be identified as unnecessary noise signals, which is added to the original signal. Therefore, while reconstructing the signal and calculating its instantaneous frequency using HHT, the IMF 4 and IMF 5 are removed from the signal.

A total of 6 signals for each specimen are selected, based on the selection criterion presented in Table 3.7.
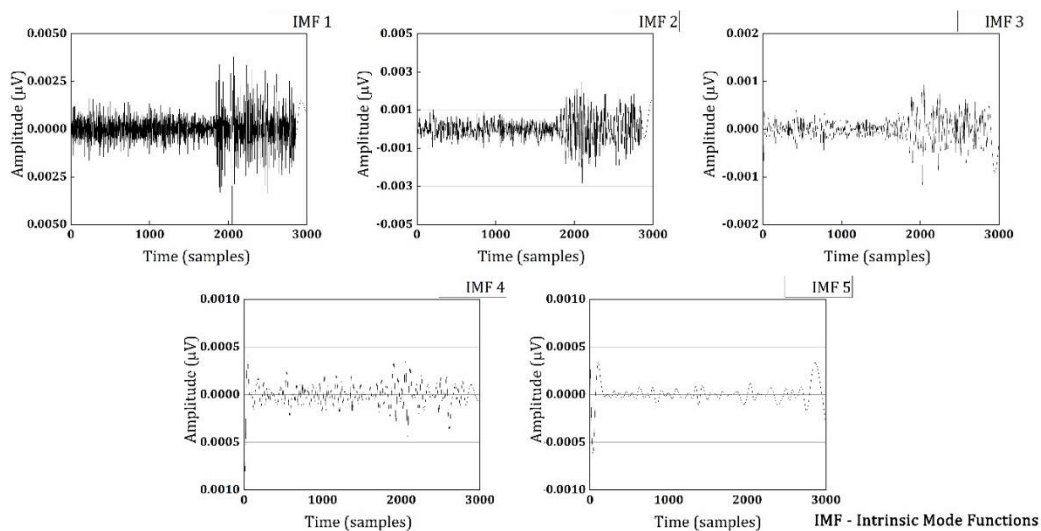
Figure 3.20. Decomposition of original signal into intrinsic mode functions IMF 1, IMF 2, IMF 3, IMF 4 and IMF 5 using empirical mode decomposition

Associating frequency spectrum of the AE results with the damage progression in metals has been a central point of debate over the years. The reason behind this debate is due to the inability to identify exactly the source of the acoustic events during a material deformation under loading. For instance, Raj et al. (1989) investigated the deformation of AISI 316 Steel at different strain rates to understand the frequency spectrum of

different damage modes. Some authors have tried to identify the primary source of acoustic events, whether it is due to the dislocation motions, movement of grain boundaries or local yielding around inclusions (Vinogradov et al. (2000), Akbari and Ahmadi (2010), Rouby and Flieschmann (1978), Kiesewetter and Schiller (1976)). Abkari and Ahmadi (2010) associated the plastic deformation with the 280 kHz–310 kHz frequency band. Raj et al. (1989) associated crack growth through micro-void coalescences to 140 kHz frequency band and yielding from 470 kHz–660 kHz. However, these research works have used FFT to analyze the frequency band, which is a major limitation. As indicated at the beginning of the chapter, the AE signals are transient, unstable, nonstationary and decomposing in nature. So, using the FFT will not provide accurate information about the frequency spectrum. For this reason, EMD is used in this research work and the HHT results are used for analyzing the instantaneous frequency band.

The AE signals for the frequency analysis are taken as per the procedure indicated in Table 3.7. The Hilbert Spectrum of specimens built along X-direction T_X is provided in Figures 3.21, 3.22 and 3.23. Figure 3.21 shows the Hilbert Spectrum of the AE signal taken from the first cluster, Figure 3.22 the Hilbert Spectrum of AE signal from the second cluster and Figure 3.23 couples of random signals. The magnitude identification is indicated in the right-hand side of all the figures and the line covering the shaded mountains indicates the instantaneous frequency results.
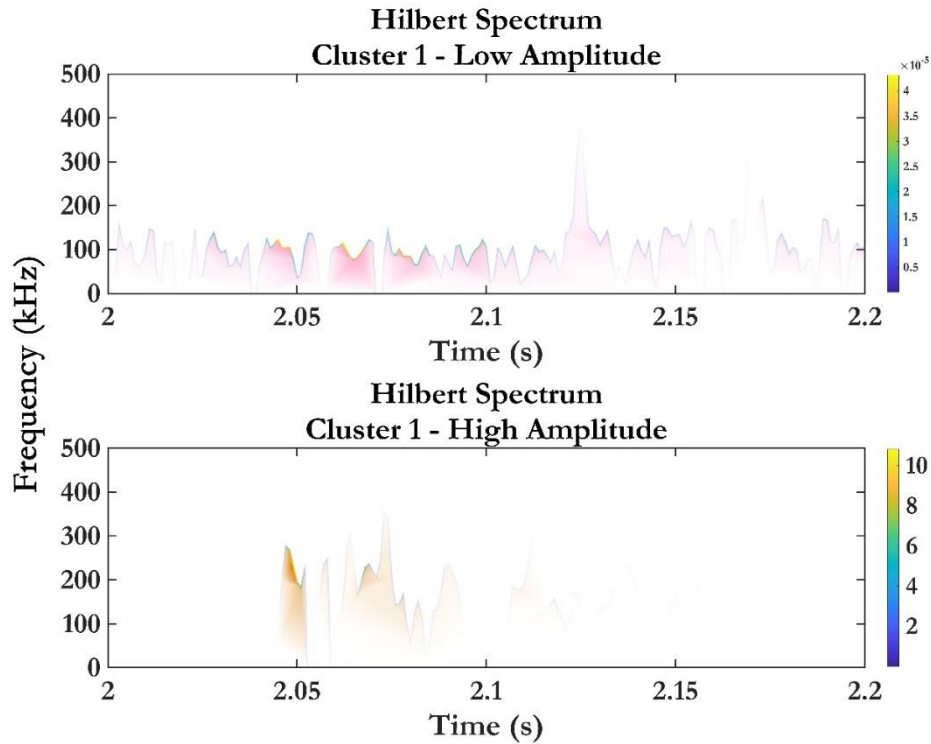
Figure 3.21. Instantaneous frequency from Hilbert Spectrum of the specimen T_X – AE signal taken from Cluster 1

In Figure 3.21, the low amplitude (<50 dB) signal of cluster 1 has an instantaneous frequency of 100 kHz–150 kHz. In the meanwhile, the high amplitude signal (>50 dB) of cluster 1 has an instantaneous frequency of 200 kHz. Similarly, while looking at the low amplitude signals of cluster 2, the frequency is 200 kHz – 250 kHz but the higher amplitude has the frequency of 150 kHz–200 kHz. This implies that the frequencies below 150 kHz only have a very low magnitude and are observed at the very early stage of loading (since it is in the cluster 1). So probably, the frequencies below 150 kHz are noise and it can be associated with the friction of extensometer which is unavoidable in this case. The higher amplitude signals of the first cluster (Figure 3.21) represents the grain boundary movement and dislocations since it is the major damage progression mode at the early stages of loading. Thus, the AE signals generated due to the grain boundary movement and dislocations may be associated with 200 kHz.
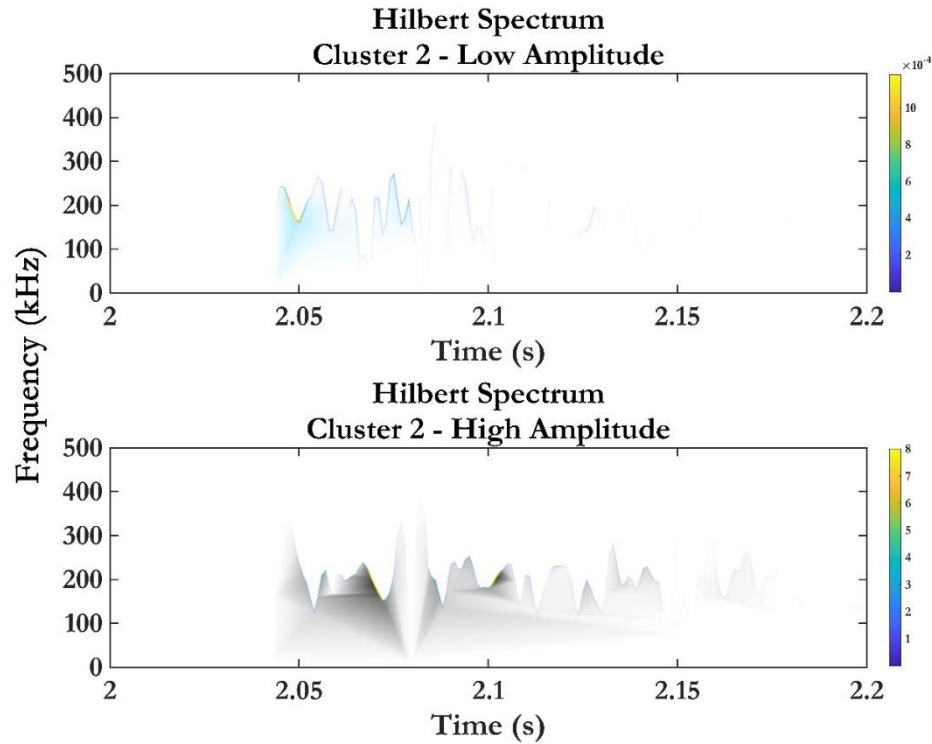
Figure 3.22. Instantaneous frequency from Hilbert Spectrum of the specimen T_X – AE signal taken from Cluster 2

The frequency band between 150 kHz–200 kHz is very important because it is associated with the crack growth or damage progression through micro-voids, as indicated by Raj et al. (1989) That frequency band is observed only in the higher amplitude signals of Figure 3.22. This means that the signals with higher amplitude and has the instantaneous frequency centered at 150 kHz – 200 kHz can very possibly represent micro-cracking or void opening.
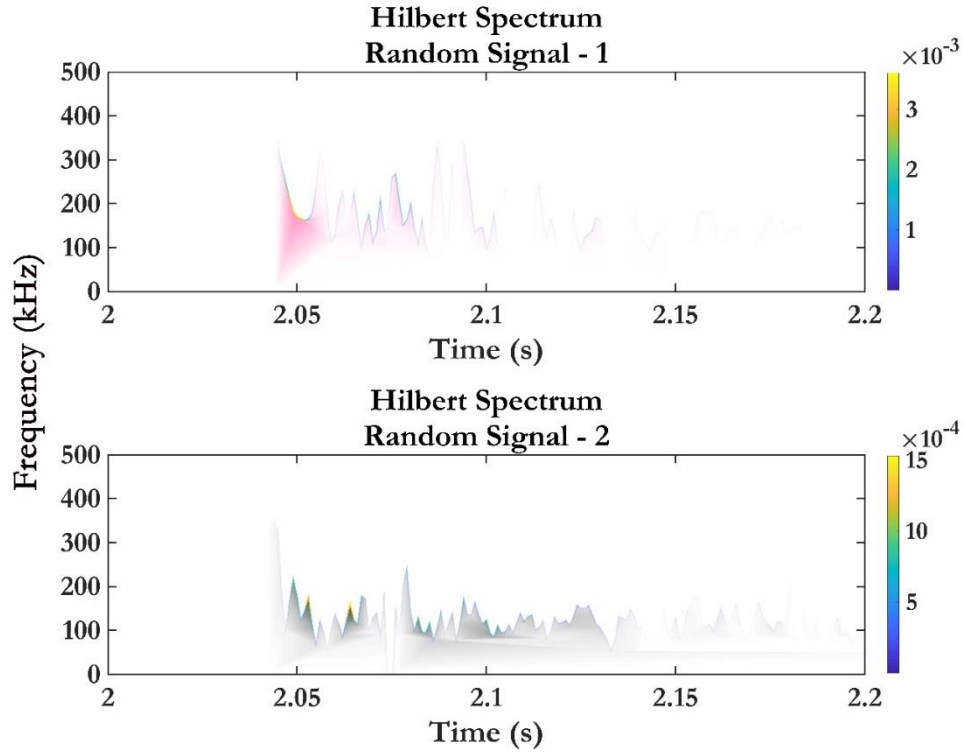
Figure 3.23. Instantaneous frequency from Hilbert Spectrum of the specimen T$_X$ – Random Signals

The random signals in Figure 3.23 have lower magnitude but again the frequency band is associated with 200 kHz and 150 kHz – 200 kHz, for signal 1 and signal 2 respectively. Again, here the 150 kHz – 200 kHz frequency band can be associated with crack growth and the 200 kHz can be associated with the yielding of the material. This is very difficult to concur with since there is no previous research work which can be used for comparison. However, while comparing with the available research works, these results are compelling.

Similarly, for specimen T$_Y$, the Hilbert Spectrums are presented in Figures 3.24, 3.25 and 3.26. The results of specimen T$_Y$ are very intriguing because the frequency band 150 kHz – 200 kHz is observed in higher amplitude first cluster signal in Figure 3.24. Does this mean this signal still represents the crack growth or micro-void opening? If so, why is it occurring in the very early stage (in the first cluster)? Fortunately, the answer has already been established in section 3.6.3.2. The high porosity in specimen T$_Y$, with respect to the other specimens, due to the melt pool boundaries distributed normally to the loading

57

direction. In the same Figure 3.24, the frequency pattern of low amplitude signal is quite nonstationary. However, as indicated earlier, lower magnitude represents around 150 kHz–200 kHz represents noise signal and hence it does not affect the analysis. This is just an indication of how to identify the noise signals.
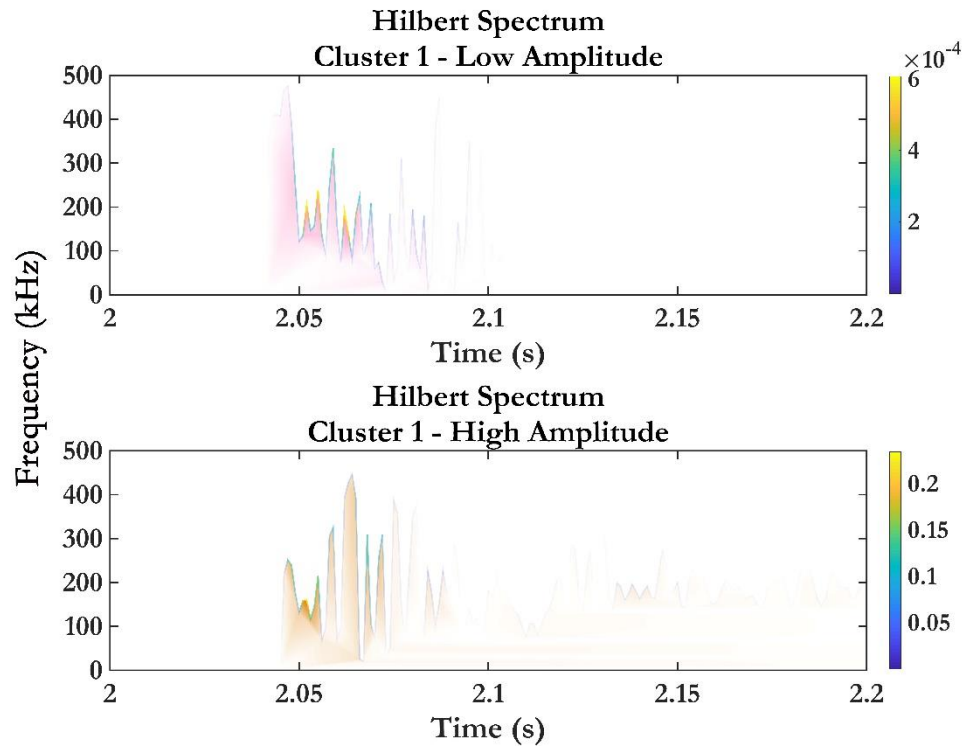
Figure 3.24. Instantaneous frequency from Hilbert Spectrum of the specimen T_Y – AE signal taken from Cluster 1

In Figure 3.25, the frequency bands are also associated with 150 kHz–200 kHz frequency band. This necessarily means that most of the AE signals recorded in the specimen T_Y represent the opening of micro-voids. This again proves the high porosity in specimen T_Y. The random signals of Figure 3.25 represent the frequency bands 200 kHz and 250 kHz which most probably represents the yielding or grain boundary movements.
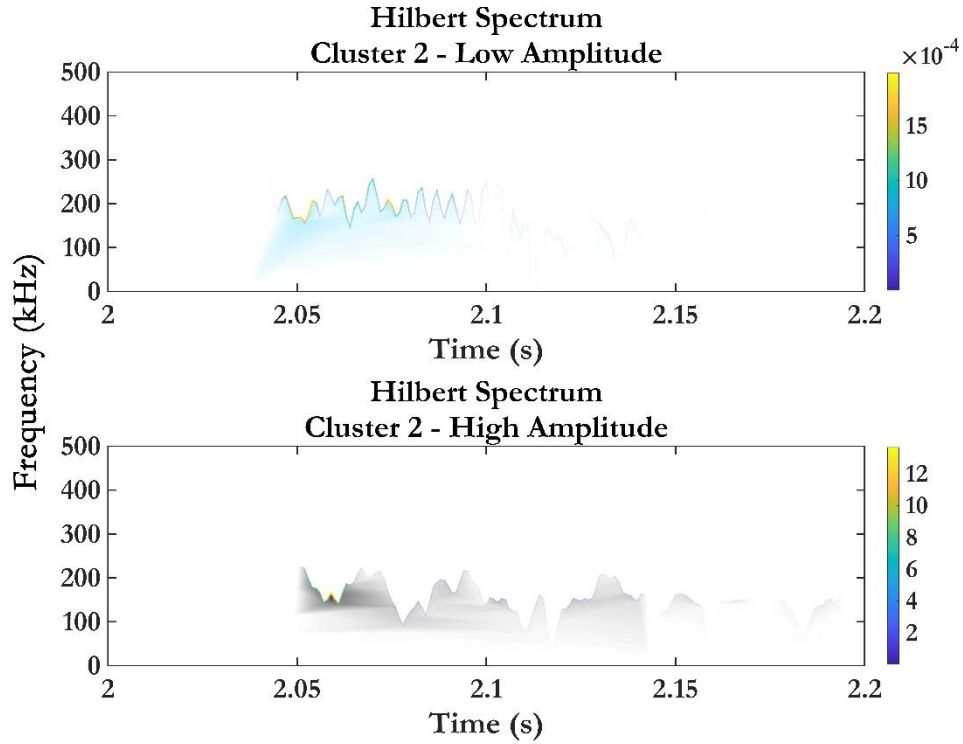
Figure 3.25. Instantaneous frequency from Hilbert Spectrum of the specimen T_Y – AE signal taken from Cluster 2

Similarly, the frequency analysis of specimen T_{45} is presented in Figures 3.26, 3.27 and 3.28. The Hilbert spectrum results of specimen T_{45} are almost identical to the specimen T_X proving that the association of damage progression with the different frequency bands is agreeable with the available research activities. The instantaneous frequency of the grain boundary movement or dislocations can be identified at 200 kHz and 250 kHz in Figures 3.26 and 3.28. The instantaneous frequency of the micro-void opening can be observed in Figure 3.27. This again agrees with the previously issued statements.
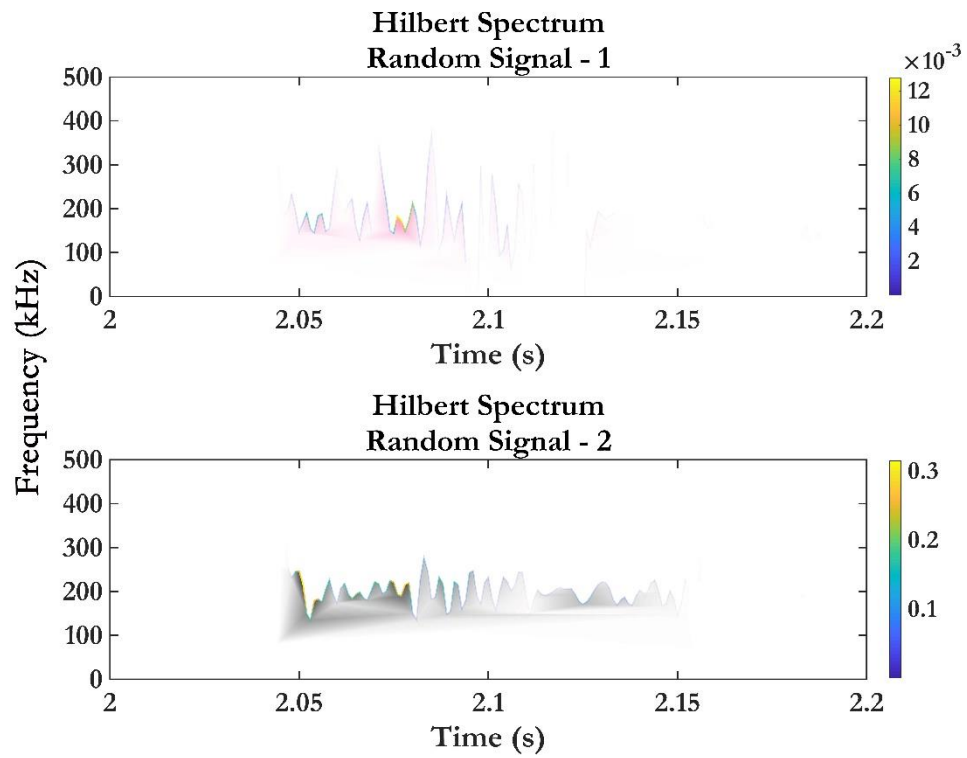
Figure 3.26. Instantaneous frequency from Hilbert Spectrum of the specimen T$_Y$ –

Random Signals
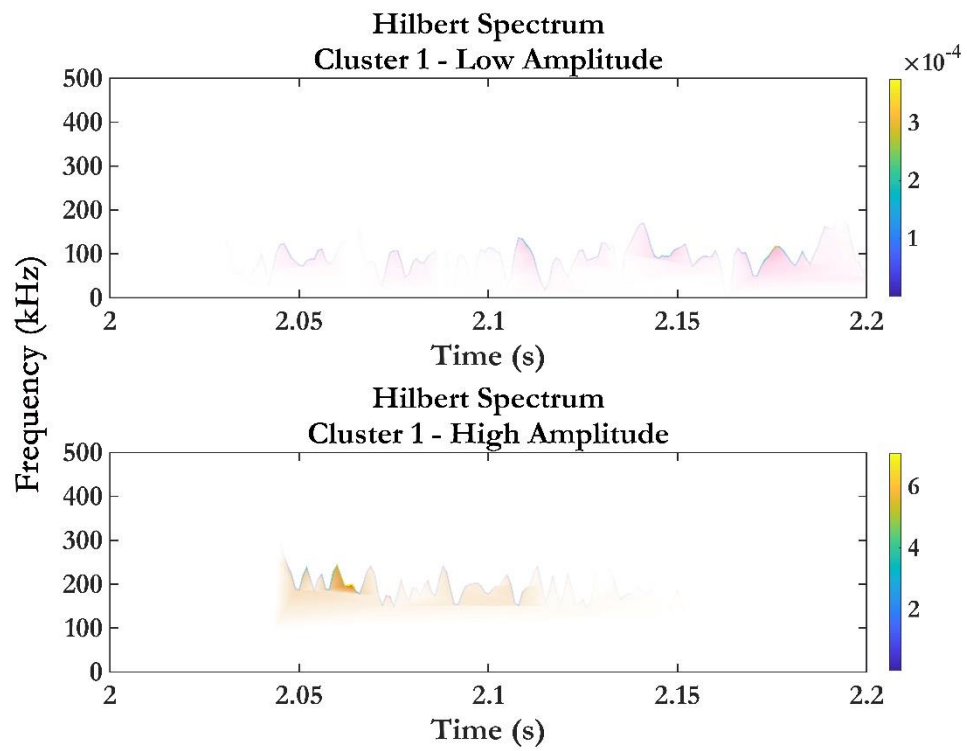
Figure 3.27. Instantaneous frequency from Hilbert Spectrum of the specimen T_{45} – AE signal taken from Cluster 1
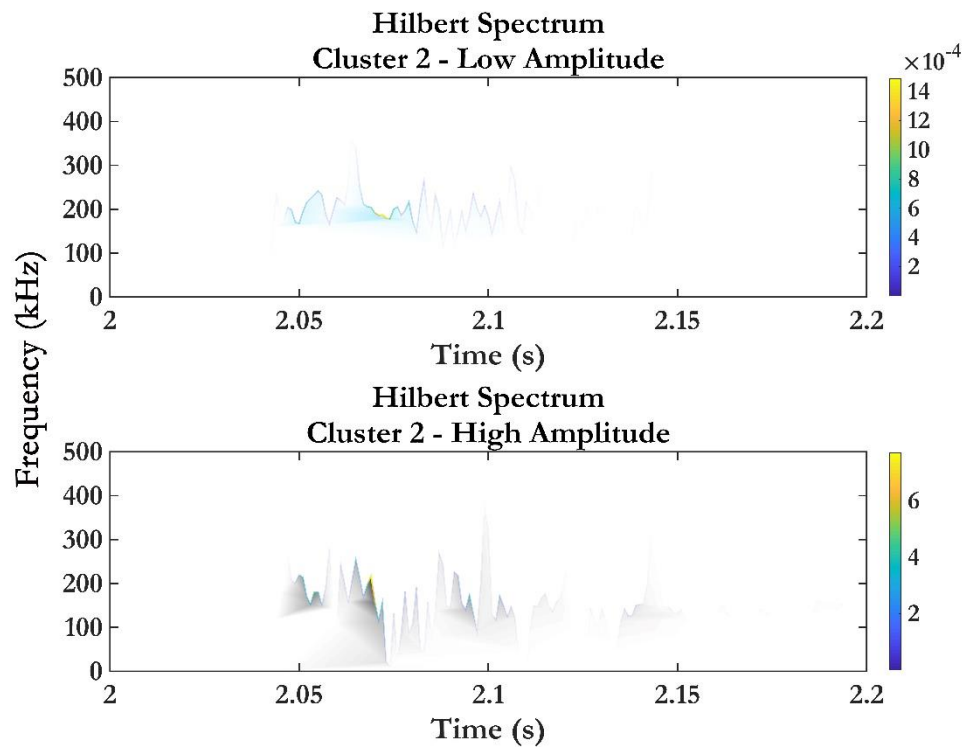
Figure 3.28. Instantaneous frequency from Hilbert Spectrum of the specimen T_{45} – AE signal taken from Cluster 2
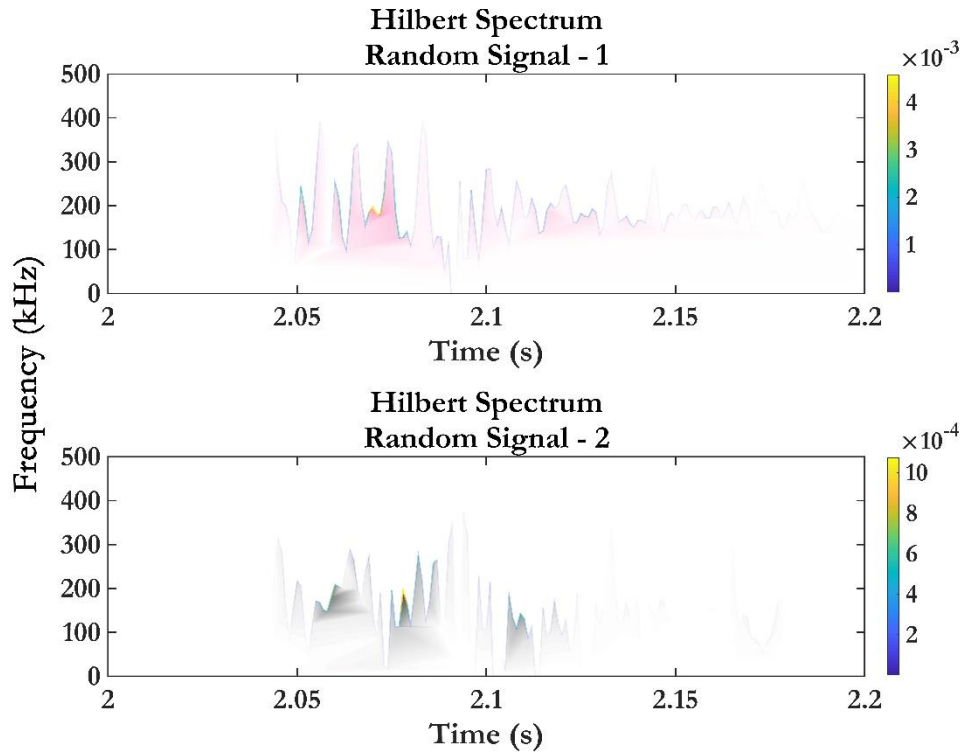
Figure 3.29. Instantaneous frequency from Hilbert Spectrum of the specimen T_{45} – Random Signals

To summarize, the frequency band associated with grain boundary movement is around 200 kHz, yielding of material and dislocations motion or development of new dislocation motions are associated with 200 kHz and 250 kHz frequency bands. Finally, the crack growth or micro-void opening are associated with 150 kHz–200 kHz.

The result shows that the EMD/HHT provides very accurate information about the damage modes and their instantaneous frequencies. A question may arise, why the EMD/HHT cannot be used for all types of waveform analysis over the WPT, CWT and DWT. The CWT and DWT has definite wavelets to be chosen for the time-frequency analysis. In some cases, the AE waves are completely nonstationary that provides us with no option but to go to adapted wavelet analysis. At that time, the EMD/HHT can be preferred over the wavelet analysis. Besides, the EMD/HHT provides instantaneous frequency results but the CWT, DWT and WPT provides the entire information in the time-frequency domain.

3.7   CONCLUSION

This chapter summarizes the different types of waveforms used in this research work. the chapter begins with the introduction of the different waveform analysis and their major advantages and limitations. Each of these sections about the different waveform analysis also includes an example waveform being analyzed by each type of analysis. This also provides a visual explanation on the advantages and limitations of each method.

Continuous Wavelet Transform (CWT) is used for understanding the wave propagation attenuation in materials having different geometries and configurations. The frequency analysis in the time domain indicates clearly how the geometry of a Carbon Fiber Reinforced Plastic (FRP) material affects the wave propagation.

Wavelet Packet Transform (WPT) is used for identifying the damage modes in CFRP laminates which are delaminated in mode I delamination. It also gives the measure of the spectral energy distributed in each frequency band, there by identifying the damage mode. The damage modes are identified by mapping the frequency bands with the damage progressions such as matrix cracking, fiber breakage, debonding or interlaminar crack growth.

Finally, the Empirical Mode Decomposition (EMD) with the support of Hibert-Huang Transform (HHT) gives instantaneous frequencies of the different damage modes in additively manufactured material under static loading. EMD removes the noise by decomposing the acoustic signals into different levels of Intrinsic Mode Functions (IMF) and reconstructing them by eliminating the noise. Similar to the WPT, the HHT gives instantaneous frequencies for different damage modes such as yielding, strain hardening, micro-void cleavage and crack initiation/propagation.

In a nutshell, the different waveform methods used in this section for analyzing the acoustic signals are summarized in this chapter. Each waveform analysis method has their inherent advantages and limitations, which are explored to its full extent.

CHAPTER 4
NEW METHOD FOR USING ACOUSTIC EMISSION TECHNIQUE: A HYBRID ACOUSTO-ULTRASONIC APPROACH

Acousto-Ultrasonic is a powerful, nonetheless, often overlooked approach of using Acoustic Emission (AE). The ultrasonic wave velocities can be used for measuring material properties such as yield strength and Young's modulus. This is due to the velocity attenuation of the ultrasonic waves in a material due to their inherent mechanical properties. This forms the basis of the Acousto-Ultrasonic approach. Because this velocity attenuation of the ultrasonic waves is very sensitive to the micro-voids, fiber orientation direction, interlaminar properties and so on. However, this technique has been rarely used in composite materials. In this research work, a hybrid approach is used while implementing Acousto-Ultrasonic approach. This method is used for identifying the damage in Carbon Fiber Reinforced Polymer (CFRP) composites. Moreover, this method is used for quantifying the interlaminar strength of the CFRP composites.

4.1 INTRODUCTION TO ACOUSTO-ULTRASONIC APPROACH

Conventional Non-destructive Evaluation (NDE) techniques can identify the flaws in a material. They can provide information about the position and the extent of the damage in a material. In composite materials, particularly the Fiber Reinforced Polymer (FRP) composites, the conventional NDE can identify the delamination, discontinuities, fiber breakage, etc. Nonetheless, the overall properties may not be affected by small discontinuities or minor flaws owing to their laminated structures.

The acousto-ultrasonic approach does not concern about these minor flaws or the identification of the flaws, nevertheless, provides a quantified information about the overall strength/property of the material. The acousto-ultrasonic assess the combined

effects of all the defects present in a material and evaluates the variations of the tensile, shear or flexural properties of the material due to these defects.

The elastic properties of a material can be calculated from the measurement of the ultrasonic velocity in the material. For an isotropic material, the longitudinal wave velocity (C_L) can be given by Eqn. 4.1.

$$C_L = \sqrt{\frac{E}{\rho}} \tag{4.1}$$

where, E is the Young's modulus of the material and ρ is its density. This forms the basic principle of the acousto-ultrasonic approach.

The term acousto-ultrasonic is coined by Alex Vary (1979), who describes this as a contraction of "Acoustic Emission simulation with Ultrasonic sources". Just as the name implies, this simulates stress waves in a material, which resembles the acoustic emission waves and records them using piezoelectric sensors. The stress waves are simulated without disrupting the physical characteristics of the material. These waves are stochastically modified inside the material depending on the interlaminar or directional properties of the material. Now by analyzing the waves transduced at the receiving end, the properties of the material can be analyzed. Unlike the ultrasonic approach, this technique does not concern about the location of the flow, instead, it concerns the position of the sensor. The positions of the pulsar and the receiver are predefined and the acousto-ultrasonic approach can characterize the strength of the material between the sensors.

The stress wave in the acousto-ultrasonic approach can be simulated by various sources. For example, in the past only the piezoelectric sources were used for simulating the stress waves. In the recent years, Laser source, water jet, out-of-plane mechanical impact, pencil lead break test and even electromagnetic sources are being used for simulating the stress wave. In this research work, a new innovative method is utilized for simulating the stress waves.

In AE technique, for verifying the proper contact between the transducer surface of the sensor and the surface of the specimen, a pencil lead break test has been recommended by ASTM E976 - Standard Guide for Determining the Reproducibility of Acoustic Emission Sensor Response. This process not only verifies the contact between the sensor and surface but also verifies the overall system performance. This is performed by breaking a pencil lead at a fixed distance from the sensor, creating a transient mechanical excitation. The stress wave is simulated through this mechanical excitation and it propagates through the specimen, which inevitably is recorded by the sensor.

In 2000, the Physical Acoustics Corporation incorporated a new method for this overall system performance, which is known as Auto Sensor Test-Self Test Mode (AST-STM). When this mode is activated, the sensor crystal is excited by a voltage spike of 28 V. The consequent displacement of the sensor crystal simulates pressure waves into the material through the surface. These simulated pressure waves are converted into structural stress waves inside the material structure. The resulting stress waves are similar to the acoustic emission waves and are influenced by the material characteristics such as geometry, resonance and other material properties. The PAC-PCI 2 system allows recording the amplitude, energy and duration of the simulated structural waves in the material. By verifying the amplitude, energy and duration of the of the recorded waves, the overall performance of the system can be validated.

In this research work, the concept of AST-STM is taken and used in the simulation of stress waves for the acousto-ultrasonic approach. Two piezoelectric sensors, both acting as pulsar and receiver simultaneously are fixed to a known distance on the surface of the material to be tested. Normally, both the sensors are fixed on the same surface of the material, however, the sensors can also be affixed on the opposite sides of the surface plane of the material.

At the beginning of the test, both the sensors act as the pulsar. A series of pressure waves are simulated by the sensor crystals through the couplant. When the pressure wave

reflects back from the structure, which is the first structural response, the sensor reverts its role into a receiver. Thus, both the sensor acts as pulsar and receiver simultaneously.

The following chapter explains the experimental investigation conducted to validate the AST-STM procedure for the acousto-ultrasonic approach and how the wave propagation is affected by the material properties.

4.3 ATTENUATION OF WAVE PROPAGATION IN COMPOSITE MATERIALS

For evaluating the attenuation of wave propagation in FRP composite materials, due to their geometry, fiber orientation direction, laminate layup and other parameters, the following experiments are proceeded.

Four different CFRP specimens with varying geometry and lay-up configuration are taken for this study. The details about the specimen geometry and lay-up configurations are presented in Table 4.1. Two general purpose piezoelectric sensors are taken for the AST-STM of acousto-ultrasonic testing. The gate time of acquisition is very important in AST-STM because it prevents the ricocheting signal from the pulsar to be recorded back in its own node. For this purpose, the gate time of acquisition is set as 10 ms.

Table 4.1. Specimen configuration used for the Acousto-Ultrasonic Testing

Specimen Name	Layup Configuration	Length mm	Breath mm	Thickness mm
C1	$[0/90]_{12}$	150	100	2.76
C2	$[45F/0T/0T/45F/0T/0T/0F/$ $0T/0T/0F/0T/0T/45F/0T]_S$	250	25	2.08
C3	$[0/90]_{12}$	300	30	2.73
C4	$[0]_{11}$	155	10	2.94

Figure 4.1. Schematic of the Acousto-Ultrasonic test set-up using AST-STM

Since the AST-STM module works on a fixed 28 V spike, it cannot be modified in the system module. However, the characteristics of the pulse can be defined. The characteristics of the pulse used in this study are presented in Table 4.2.

Table 4.2 Characteristics of the pulse used for Acousto-Ultrasonic approach

Characteristics of the Pulse	
Spike Voltage of the Pulse	28 V
Pulse Width	5 µs
Number of Pulses	10
Time between each Pulse	100 ms
Gate Time of Acquisition	10 ms

The sensor used for this study is a pair of R30α general purpose sensor with an operating frequency of 150 kHz to 400 kHz. The sensor has a resonant frequency of 250 kHz. All the simulated waves are recorded at a sampling rate of 1 mega samples per second (1 MSps). A total of 10 pulses are recorded at the receiving side of the system. The sensors are positioned along the longitudinal axis with a constant distance of 75 mm between them,

regardless of the geometry of the specimen. All the experiments are conducted at a room temperature of 22 ℃. The test set-up is presented in Figure 4.1.

4.3.1   Results of Wave Propagation Attenuation

For the purpose of comparison, the first structural response received by the sensors as the input waveform. Although it is not definitively the representation of the 28 V spike by the piezoelectric crystal response, it is considered as the signal sent for comparison purposes. The wave parameters such as amplitude, energy, duration and counts are measured directly with the data acquisition system.

The simulated waveform signals were recorded by the two sensors S1 and S2, respectively. Both the sent signals and the received signals were recorded and the average value of the signal descriptors (Peak Amplitude, Energy, Duration and Counts) for each specimen is provided in Table 4.3.

The descriptors of the waveforms can be observed in Table 4.3. The variation between the sent and the received signal is due to the loss of energy in the simulated acoustic waves before it reaches the receiver.

The peak amplitude, which corresponds to the voltage spike of 28 V, recorded for all the sent signals is 99 dB (∼100 dB), while the received signals have lower values. The simulated acoustic signal must pass through the material, which acts as the transmission medium, before reaching the receiving end. It is expected that the medium of transmission affects the acoustic signal, which results in the loss of Amplitude, Acoustic Energy and Duration when the signal reaches the receiver. The relative loss of amplitude is significantly smaller than the loss of Acoustic Energy and Duration. This is because the amplitude is recorded mostly as a structural response, which is dominated by the 28 V excitation of the sensor crystal. Thus, it is valid to use the acoustic energy or duration for the validation of the results.

Table 4.3. Descriptors of the simulated structural waves recorded for all the Specimens

Specimen Name	AE Signal	Amplitude *dB*	Acoustic Energy *au*	Duration *ms*	Count
C1	Sent	99	1015.1	5463.4	53
	Received	69.1	15.6	379	90
C2	Sent	99	1060	5491.3	66
	Received	76.4	32.8	390.6	104
C3	Sent	99	1030	5467.5	60
	Received	68.8	17.5	431.8	105
C4	Sent	99	1011.5	5474	69
	Received	71.5	19.6	517.9	126
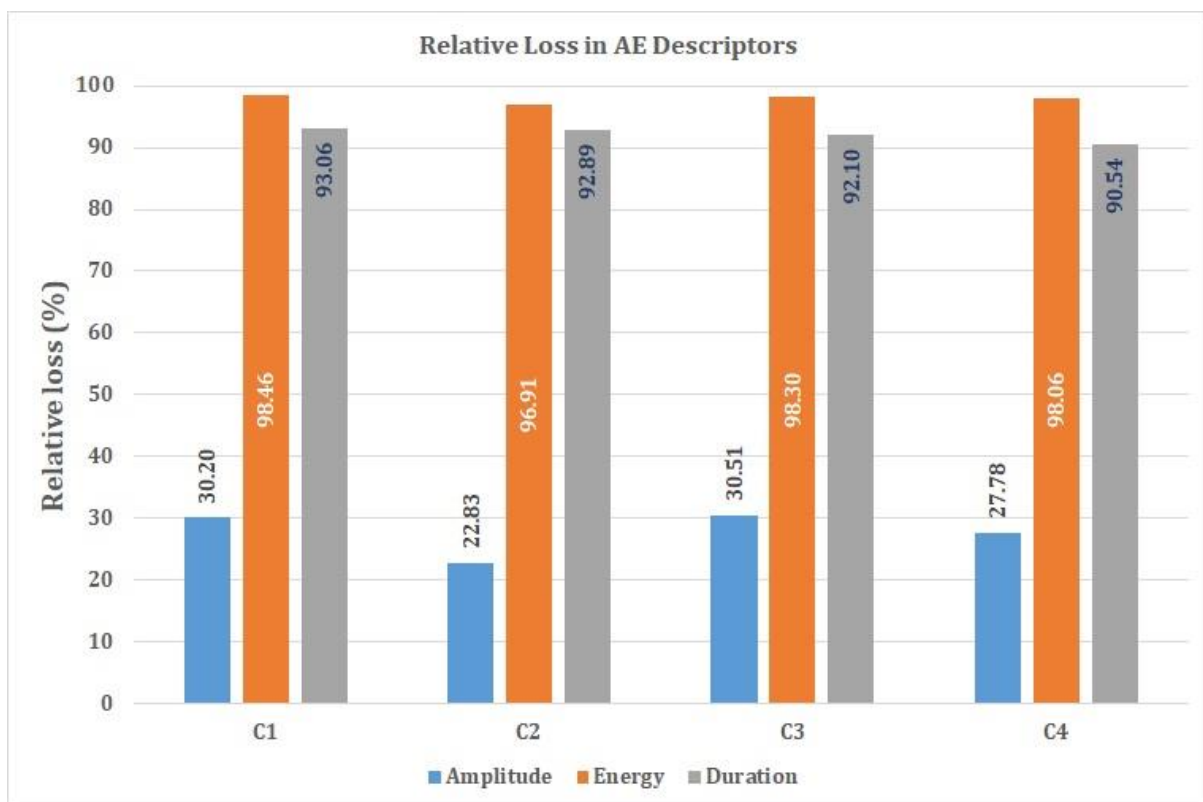
Figure 4.2. Relative loss of the simulated Acoustic Emission signal descriptors at the receiving end of the sensor

A graphical representation of the percentage loss in the signal descriptors are presented in Figure 4.2. Combining data of Table 4.3 and Figure 4.2, a correlation between the material properties and its adverse effects on the acoustic signal can be found. Specimens C1 and C3 have very close material geometry (thickness 2.76 and 2.73 mm, respectively) and same fiber layup. The number of plies in both the specimens are 12 and their fiber orientations are similar. The relative loss in the Amplitude and Energy of the acoustic signals in specimens C1 and C3 have closer values. The relative loss of Amplitude for C1 and C3 are 30.20 and 30.51%, respectively. Similarly, the loss of acoustic energy is 98.46 and 98.30%, respectively. Although the length and the breath of the specimens may vary, when the sensor is placed along the fiber direction of the specimen with a close proximity between them (75 mm), the relative loss has very similar values. While looking at the AE descriptors of the other two specimens, C2 and C4, which have different fiber orientation, thickness and the ply number, it can be inferred that the material properties play an important role in the transmitted acoustic signal.

Specimen C2, 2.08 mm thick, exhibits the lowest relative loss in all the AE descriptors. The Amplitude loss is 22.83% in C2, while the other specimens have relatively higher loss. This begs the question, whether only the thickness plays a major role in the acoustic signal transmission. Is it possible the lower specimen thickness can result in lower loss in AE descriptors during transmission? The results for the specimen C4 suggest otherwise. C4 is the thickest specimen but variations of AE descriptors are smaller than for C1 and C3. However, C4 is unidirectional laminate including 11 plies. It was experimentally proved by Alex Vary (1979), the forerunner of the acousto-ultrasonic approach, that the acoustic wave can run in the direction parallel to the fiber direction. This can be related to the fact that the fiber orientation provides the feasibility of acoustic signal transmission.

The loss in energy, amplitude and duration in all the specimens are accounted for more than 90%, which can be attributed to the non-isotropic nature of the composites. Since the composite specimens used in this test do have similar fiber orientation or physical properties in transverse and longitudinal directions, the non-isotropic nature and the

phase difference between the epoxy matrix and the reinforcement, carbon fiber might have played a major role in the relative loss.

The waveforms of the signals are also analyzed. The waveform of the signal sent is presented in Figure 4.3., while the waveforms of the signals received by all the specimens are presented in Figure 4.4. A total of 10 waveforms are recorded for each signal, since 10 pulses are excited in each specimen. Only a representative waveform of the signal received is presented in Figure 4.4 for all the specimens.
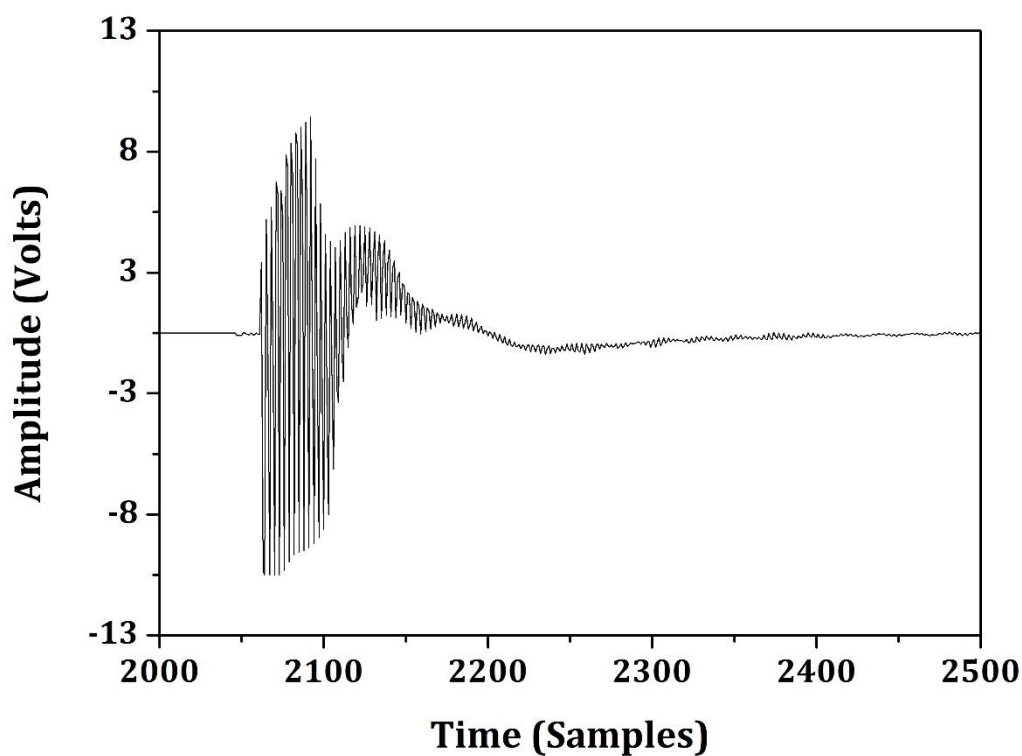
Figure 4.3. Waveform of the Signal Sent

There is an obvious loss in amplitude in the received waveforms while comparing with the first structural response, which is considered as the sent signal. Although the peak amplitude of the waveforms of specimens C1 and C3 are similar, the second section of the waveform (after 2100 samples) is different in each case. This shows that the length and width of the waveform does affect the wave propagation even between the sensors in closer proximity. However, it is not enough to affect the loss in total acoustic energy or

the make variations in the duration of the signal. This is because the simulated acoustic signal propagates in two different modes, symmetric and asymmetric, each having different wave velocity.

The waveforms of signals received in C2 and C4 are entirely different. The signal received in the specimen C4 is decaying in its entire duration, while C2 shows an entirely different trend.
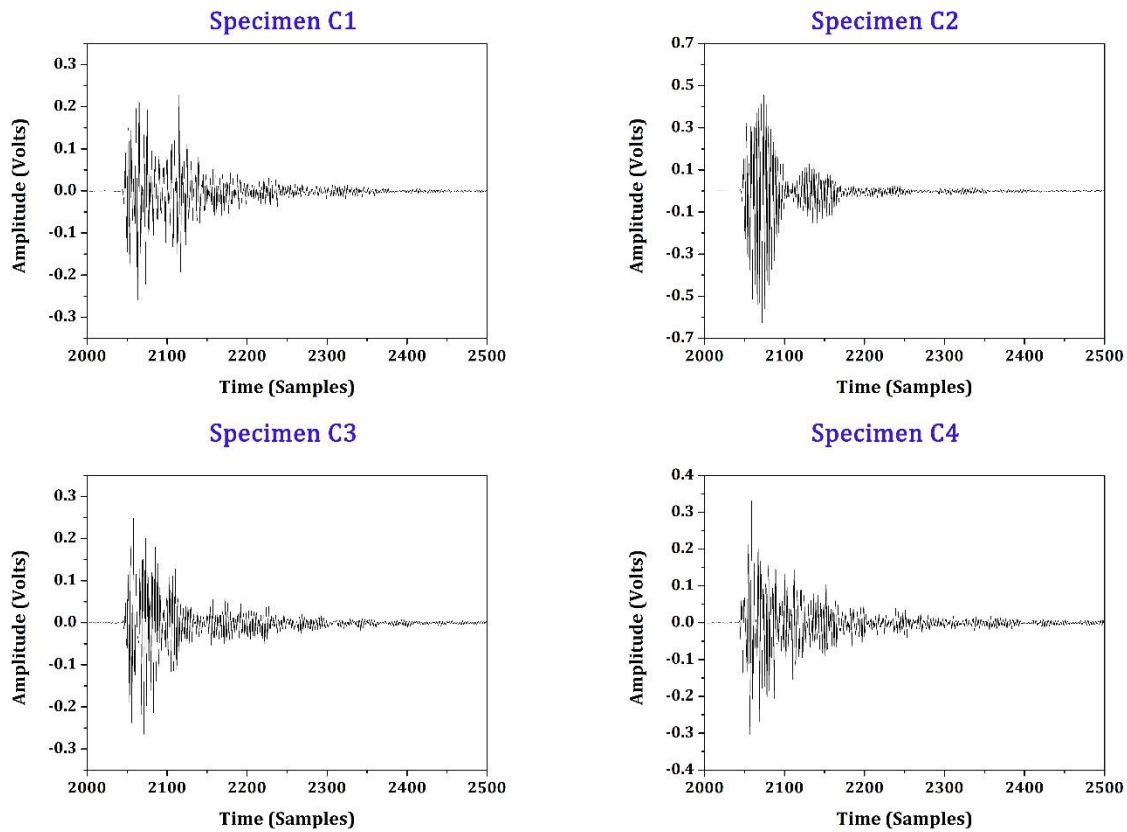
Figure 4.4. Waveforms of signals received by all the four specimens

This section is dedicated only to show the attenuation in wave propagation due to the different material characteristics such as geometry and fiber orientation direction. The next section briefs the new hybrid procedure used for analyzing the waveform and the experimental procedure followed for quantifying the interlaminar strength of the CFRP specimens using the acousto-ultrasonic approach.

4.4   A HYBRID APPROACH FOR WAVEFORM ANALYSIS

The waveform analysis is the basis for understanding the acoustic waves in their time-frequency domain. Although there are so many waveform analyses, which are explained in the previous chapters, such as FFT, CWT, DWT and WPT, each of them have their own limitation. To overcome this limitation, a very simple yet compelling approach is introduced in this research work. The wavelet transform analysis is combined with an adaptive wavelet technique for analysis.

The waveforms are processed by using two different techniques: Wavelet Packet Transform (WPT) and Empirical Mode Decomposition (EMD). The WPT is a wavelet transform technique, which decomposes the parent waveform into low-frequency (approximation) and high-frequency (detail) contents. The wavelet packets are the combination or superposition of the parent waveform, which retain the orthogonality, smoothness and localization properties of the parent waveform. On the other hand, the EMD is similar to an adaptive wavelet technique, which decomposes the parent waveform into functional modes called Intrinsic Mode Functions (IMF). A simple model is created to use both these waveform processing methods to overcome the specific limitations of these techniques by exploiting their advantages.

WPT can decompose the signal into the frequency domains and can measure the energy content of the frequency spectrum in each of these domains. However, it is not capable of reconstructing the signal back to its original form. By decomposing the signal, the frequency and the energy content of the noise level can be identified but cannot be removed entirely from the parent waveform.

On the other hand, the EMD can decompose the signal into IMF and residual (which essentially is the unnecessary noise or reverberated signal modulated over the actual signal) and then enables the reconstruction of the signal from the IMF by discarding the residual. More importantly, it allows the reconstruction of the parent waveform just by selecting the user-defined IMF. Since EMD decomposes the signal into functional modes, the energy of the frequency spectrum cannot be measured.

For this reason, a simple model is created to use both the WPT and EMD for analysing the recorded waveforms.

In this model, WPT decomposes the input waveform $f(T)$ into a predefined number of decomposition level i. The total number of WPT components n can be defined as 2^i. The model enables the calculation of the energy content in each frequency domain E_i^n within the time period t_0^n and t_1^n.

$$E_i^n = \sum_{T=t_0^n}^{t_1^n} [f_i^n(T)]^2 \tag{4.2}$$

Then the percentage of each energy component ($\%_i^n$) with respect to the parent waveform is calculated using Eqn. (4.3).

$$\%_i^n = {E_i^n} \Big/ {\sum_i \sum_{n=1}^{2^i} E_i^n} \tag{4.3}$$

Input Signal

Decompose Waveform using WPT into predefined number of levels 'i'

Calculate the Energy component of each Frequency Domain

$$E_i^n = \sum_{T=t_0^n}^{t_1^n} [f_i^n(T)]^2 \qquad \%_i^n = E_i^n \Big/ \sum_i \sum_{n=1}^{2^i} E_i^n$$

Decompose the signal into IMFs using EMD and Reconstruct the Signal without Residual

Decompose using WPT and Calculate

$$E_{i+k=1,2,\dots,5}^n \qquad \%_{i+k=1+2,\dots,5}^n$$

If $E_i^n <$ 0.2% E_{i+k}^n

No

Yes

Loop Conditions

Until the Looping condition is satisfied, otherwise Maximum Number of Iterations – 5

End the Program

76

Figure 4.5. Flowchart for the Hybrid model created for Waveform processing

Then the input signal is again decomposed using EMD into different IMF functional modes. The IMF are reconstructed by discarding the residual signal. Now the newly reconstructed signal is again decomposed using WPT. The energy content of each frequency domain is again calculated as $E^n_{i+k=1,2,...,5}$ and $\%^n_{i+k=1+2,...,5}$. The percentage of the energy in each frequency domain is compared with the previously decomposed data. If the difference in the percentage of energy is more than 2%, the signals are decomposed again into IMF and residual. The value 2% is selected because if a higher percentage of variation is selected, the EMD will decompose the signal further and further and will deteriorate the parent waveform. This looping is terminated, however, once the signal is decomposed and reconstructed for 5 instances. Again this 5 time is selected to avoid the deterioration of the parent signal. In this way, the low-level noise signals in the residual signal can be removed and at the same time, the energy content of each frequency domain can be calculated. The flowchart for this model is presented in Figure 4.5. Thus, this model compensates the limitations of EMD and WPT by using their advantages together.

4.5 EXPERIMENTAL CAMPAIGN FOR IMPLEMENTING THE HYBRID APPROACH
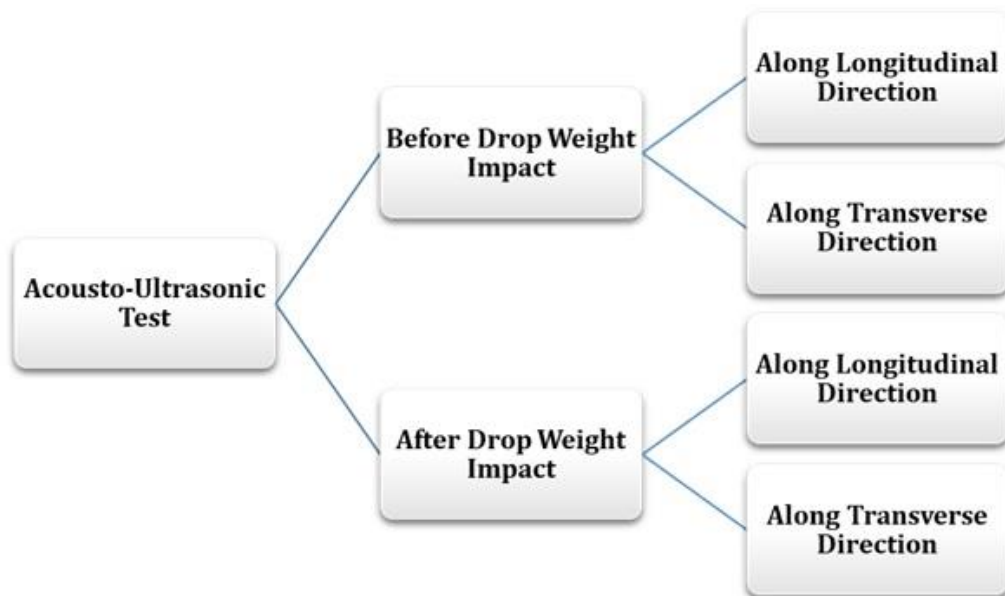
Figure 4.6. Schematic of testing modes used for the experimental campaign

An experimental campaign is carried out for implementing the hybrid approach for analyzing the AE waveforms simulated during the acousto-ultrasonic testing. The CFRP laminates are used for this experimental campaign. First, the acousto-ultrasonic test was conducted on five CFRP laminates having similar geometry and lay-up configurations. Following the testing, Barely Visible Impact Damage (BVID) is induced on these specimens using drop-weight impact/out-of-plane impact. The specimens are tested again using acouso-ultrasonic approach. Then the hybrid waveform analysis approach is used for studying the waveforms simulated in the CFRP laminates before and after the impact event. A schematic showing the mode of testing used in this experimental campaign is presented in Figure 4.6.

4.5.1 Testing Materials and Methods

The material used for this testing is CFRP laminate plates with the dimension of $100 \times 150 \times 10 \ mm^3$. The specimen dimensions are as per the ASTM D7136 Standard Test Method for Measuring the Damage Resistance of a Fiber-Reinforced Polymer Matrix Composite to a Drop-Weight Impact Event, since the specimens will be subjected to drop weight impact event to create the BVID. The details of the Fabric (F) and Tape (T) related to the layup and fiber orientation is as follows: [45F/0T/0T/45F/0T/0T/0F/0T/0T/0F/0T/0T/45F/0T]s.

For performing the acousto-ultrasonic test, two general purpose piezoelectric sensors R30α with an operating frequency of 150 kHz to 400 kHz is selected. To avoid recording any unnecessary noise signals, the low band-pass filter is selected as 100 kHz. This is because during the acousto-ultrasonic testing, both the sensors act as a pulsar and they revert their role into a receiver upon receiving the first structural response. This means that the sensors can revert their role even by receiving noise signals. For avoiding this problem, the low band-pass filter is selected as 100 kHz. The sensors are placed exactly 30 mm from the geometric centre of the specimen, during both the instances of longitudinal and transverse testing.

The specimen dimensions, the longitudinal and transverse directions, the positions of the sensors and all the details are presented schematically in Figure 4.7. For the acousto-

ultrasonic testing, the voltage spike of 28 V and other procedures explained in section 4.3 is followed. The number of pulses, the pulse width and the time interval between each pulse is given in Table 4.2.
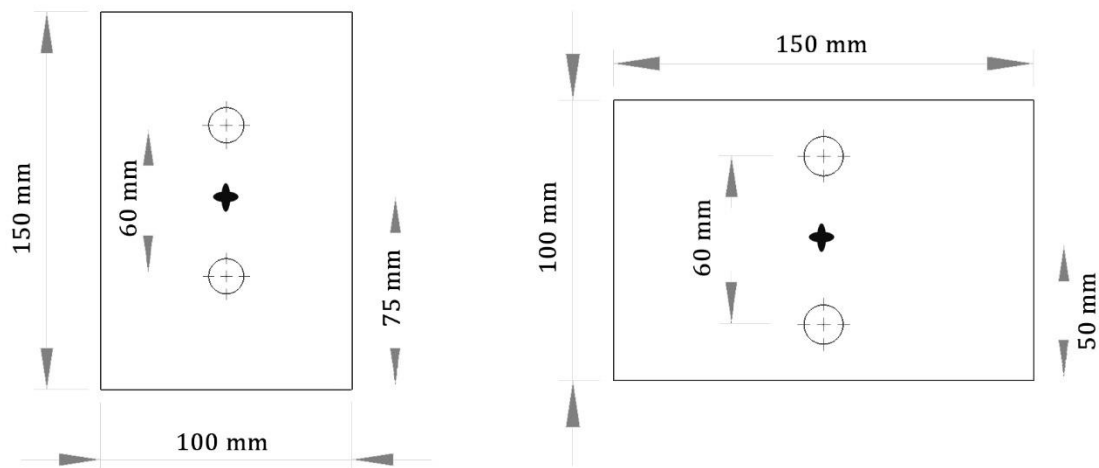
Figure 4.7. Schematic describing the longitudinal and transverse positioning of the sensors and the location of the BVID

For creating the BVID, an out-of-plane impact event is created in the INSTRON CEAST 9350 Drop Tower Impactor. An impact event of 50 J is created by dropping a hemispherical tipped intender with a mass of 2.781 kg. The impact event is a low-velocity impact event: the intender is dropped from a height of 1835.50 mm at a velocity of 7.151 ms^{-1}. When the impactor drops on the specimen, the specimen absorbs the energy. The peak force and energy absorbed by the specimen during the event are recorded. Then, the residual indentation produced by the impactor at the BVID location is measured using digital depth gauge.

For measuring the residual strength of the specimens post the drop-weight impact event and the acousto-ultrasonic testing, Compression after Impact (CaI) is conducted. The compression test is conducted for the impacted specimens in accordance with ASTM D7137 – Standard Test Method for Compressive Residual Strength Properties of Damaged Polymer Matrix Composite Plates. The test is carried out in SCHENK servo-hydraulic testing machine (250 ms−1kN load capacity) at a crosshead movement of

1.25 $mm\ min^{-1}$. The fixture used is as recommended by ASTM D7137, supporting upper and lower edges of the specimen and also holding the specimen rigidly on its sides.

4.5.2   Results and Discussions

Totally 5 specimens are tested in this study, each of them along both longitudinal and transverse directions. The specimens are named from AU1 through AU5. The relative loss between the acoustic descriptors, peak amplitude, energy and duration of the signal between the sent and received signal are analyzed. The recorded descriptors for each specimen along the longitudinal and transverse directions, respectively, before the impact event are presented in Tables 4.4 and 4.5.

Table 4.4. Acousto-Ultrasonic Results along Longitudinal Direction before the Impact Event

Specimen Name	Signal Sent				Signal Received			
	Amplitude	Energy	Duration	Count	Amplitude	Energy	Duration	Count
	dB	au	ms		dB	au	ms	
AU1	99	940.50	5443.40	82	80.50	61.20	798.30	137
AU2	99	934.10	5448.50	68	81.30	107.80	957.10	151
AU3	99	921.00	5440.30	60	84.10	104.10	1104.10	162
AU4	99	930.17	5444.67	73	81.33	71.00	922.83	142
AU5	99	944.20	5440.70	72	81.10	66.13	818.73	136

Table 4.5. Acousto-Ultrasonic Results along Transverse Direction before the Impact Event

Specimen Name	Signal Sent				Signal Received			
	Amplitude	Energy	Duration	Count	Amplitude	Energy	Duration	Count
	dB	*au*	*ms*		*dB*	*au*	*ms*	
AU1	99	961.60	5475.70	66	88.50	195.50	1317.30	1401
AU2	99	912.50	5446.40	70	86.40	142.00	1191.40	173
AU3	99	917.90	5441.10	75	87.20	135.90	1196.00	146
AU4	99	982.80	5455.10	61	85.50	104.80	1023.80	137
AU5	99	892.70	5424.90	63	86.50	169.80	1279.80	145

The relative loss between the signals are provided in Figure 4.8. The first major question that arises while looking at the results is, why the relative loss in amplitude is very much lower when compared to the other AE descriptors? While observing the results from Section 4.3., it is established that the peak amplitude represents the structural signal propagated along the surface of the specimen.
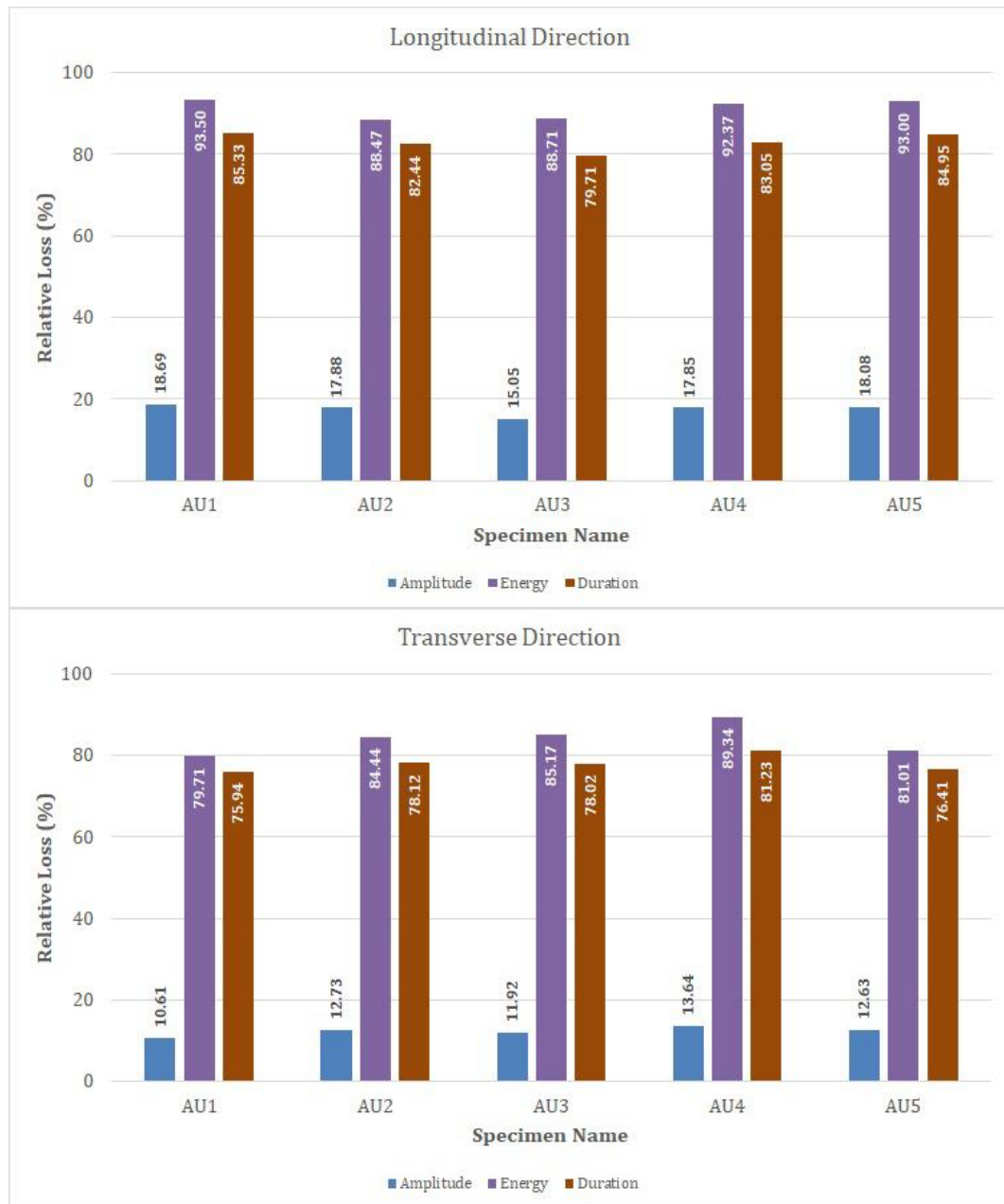
Figure 4.8. Relative loss of AE descriptors for all specimens before the impact event

The second important observation is the differences between the AE descriptors along longitudinal and transverse directions. In specimen AU1, along the longitudinal direction, the relative loss of AE energy is 93.5%, while it is 79.71% along the transverse direction. Similarly, in all the other specimens the relative loss in AE energy and duration along longitudinal direction is more than the transverse direction. This result, when compared with the specimens after the drop weight impact, becomes even more intriguing.
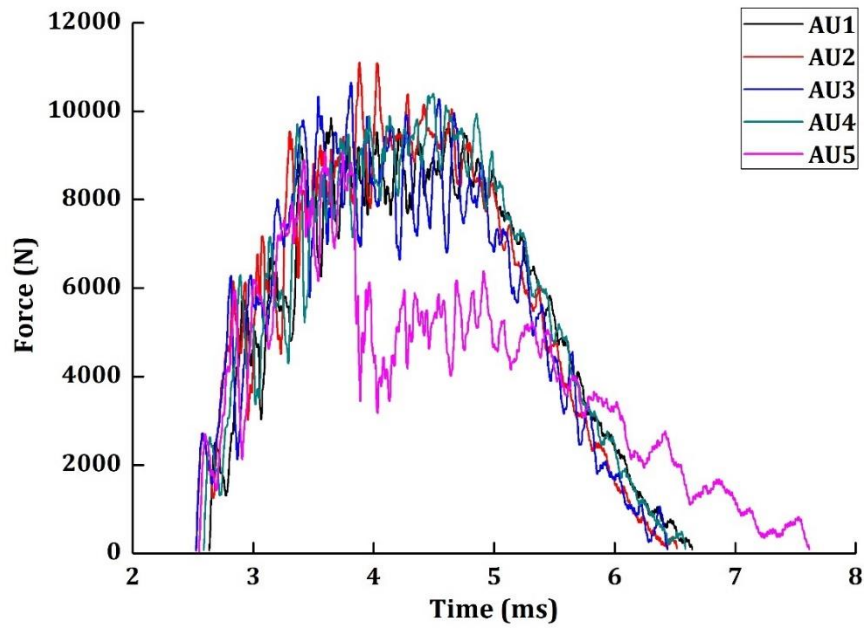
Figure 4.9. Load Response of all the specimens during drop-weight impact event

Table 4.6. Drop-Weight Impact and CAI Test results with the Residual indention measured for all specimens

Specimen Denomination	Residual Indention	Drop Weight Impact		CAI	
		Peak Force	Peak Energy	CAI Force	CAI Strength
	mm	*N*	*J*	*kN*	*MPa*
AU1	-0.59	9849.16	26.84	110.52	1539.22
AU2	-0.41	11095.55	37.57	113.55	1581.42
AU3	-0.46	10652.33	36.23	111.56	1553.74
AU4	-0.39	10393.53	47.72	119.80	1668.58
AU5	-1.74	9090.62	32.20	104.90	1461.02

The load response of all the specimens during the drop-weight impact event is presented in Figure 4.9. From the data, the peak force, energy at peak force during the impact event, residual indentation and the results from the CAI tests are all presented in Table 4.6. Besides, the load response of all the specimens during the CAI tests are also presented in Figure 4.10.
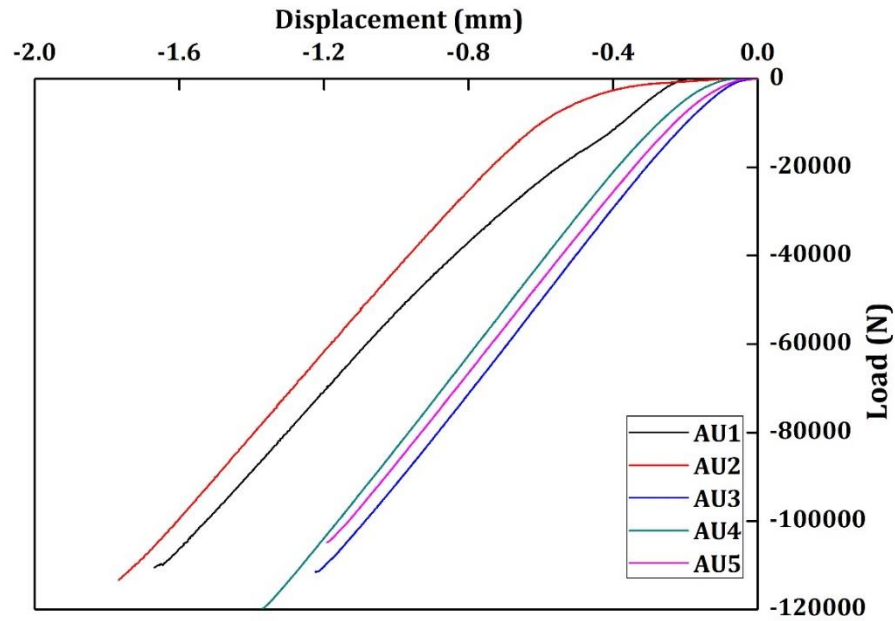
Figure 4.10. Load response of all specimens during the CAI test

It can be observed that a residual indentation is formed on the top surface of specimen; while the impact energy has transmitted through the surface and severe damage can be seen at the bottom surface. In all the specimens, the fibers along the transverse direction has been broken by the impact. Although the extent of interlaminar damage cannot be observed through visual inspection, it can be explained through the results obtained (Refer Figure 4.11).

After the drop weight event, the fibers in the transverse direction have broken. This shows that the drop weight impact energy did not transmit symmetrically through the specimen. The fiber breakage in the transverse direction represents that the interlaminar strength along the transverse direction is low and it is responsible for the fiber breakage along that specific direction.

The phase direction of the material along which the interlaminar strength is low also has the lowest acoustic energy (Figure 4.8). Supposedly, an assumption can be made to understand the relation between the structural response and the acoustic signal transmission. The phase direction of the material which has the lowest interlaminar

84

strength permits the easy propagation of the acoustic signal. This maybe the reason why the AE descriptor loss along the transverse direction is less than the longitudinal direction.
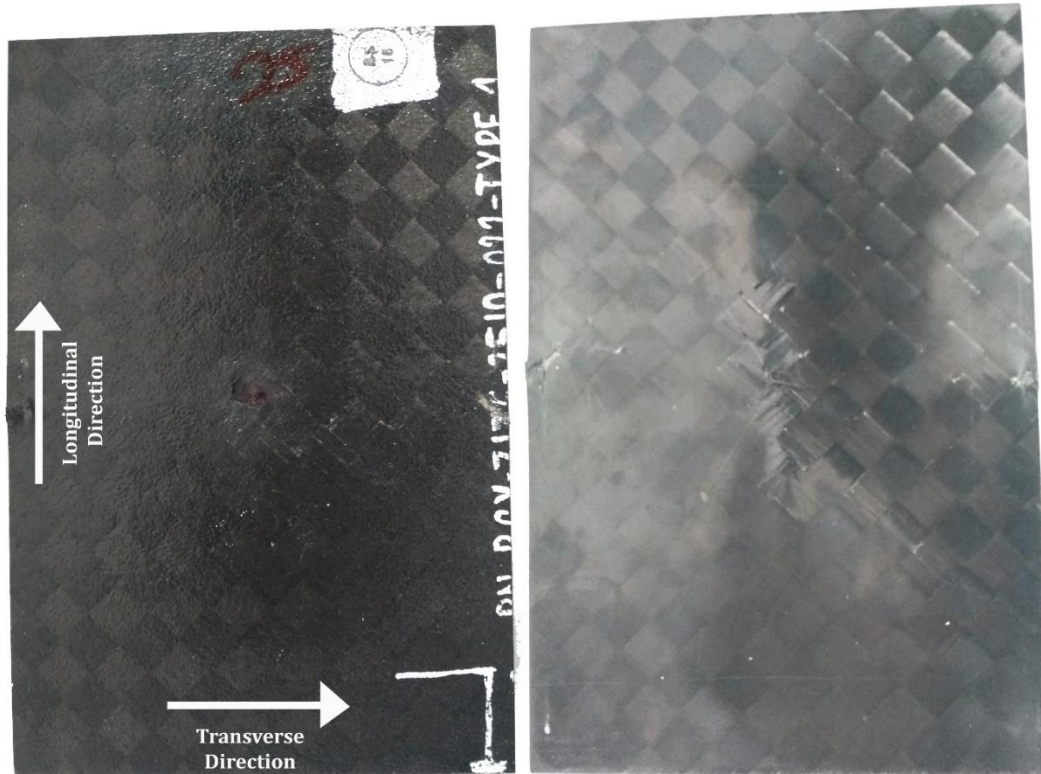
Figure 4.11. Top and Bottom surface of the specimen after Drop Weight and CAI tests

However, this is just an assumption made. To verify the credibility of the assumption made, the AE descriptor loss along the transverse direction in different materials is compared with the mechanical experimental results.

After the drop weight impact, the residual indentation of all the specimens were measured using digital depth gauge. The specimen AU1 and AU5 have the residual indentation of -0.59 mm and -1.74 mm, respectively, which is by far more when compared to the other specimens. The peak force absorbed by AU1 and AU5 are 9849.16 N and 9090.62 N, respectively. The peak force and energy absorbed by the aforementioned specimens are also very low when compared with AU2, AU3 and AU4 (Table 4.6). In the similar way, after the compression test, the specimens AU1 and AU5

also have the lowest CAI force and CAI strength. Now, this clearly shows that the interlaminar integrity of the material AU1 and AU5 is comparatively lower than the other specimens. AU1 and AU5 have the highest residual indentation and absorbed low impact energy and have shown poor CAI strength.

Considering the relative loss of AE in transverse direction (Figure 4.8) between the different specimens, AU1 and AU5 have the lowest AE energy loss (79.71% and 81.01%, respectively) when compared to the other specimens. Expectedly, these two specimens have the lowest mechanical properties (interlaminar properties). The assumption initially made for understanding the relation between the AE descriptors and the interlaminar property of the material seems to hold true.

A general hypothesis can be created following these observations. The direction along which the AE descriptor loss is low, has the lowest interlaminar strength. The hypothesis can be verified by comparing the results from Figure 4.8 and the experimental drop weight impact and CAI results from Table 4.6. Figure 4.9 also shows the lowest energy absorbed by AU5 during the drop weight impact event. Although AU1 seems to follow the same Force vs Time curve as the other specimens, the peak force and energy absorbed by AU1 is also very low. If this hypothesis holds true, the interlaminar strength of the material can be characterized by the acousto-ultrasonic approach.

The hybrid approach is used for analyzing the signals in their time-frequency domain. The decomposition level for this study is $i = 3$, which gives a total of 8 WPT components. The decomposition level is chosen based on the requirements of the frequency bands of interest. By decomposing the waveform which is in the frequency domain 0 kHz to 500 kHz into 8 components will provide necessary information about all the frequency bands of interest. Going beyond this decomposition level will create complications in measuring the energy of the decomposed waveform. The decomposed waveform of the sent signal is presented in Figure 4.12. It is a pictorial representation of how the energy of the simulated pressure wave is distributed among different frequency bands. All waveforms are decomposed into IMFs and reconstructed using EMD.
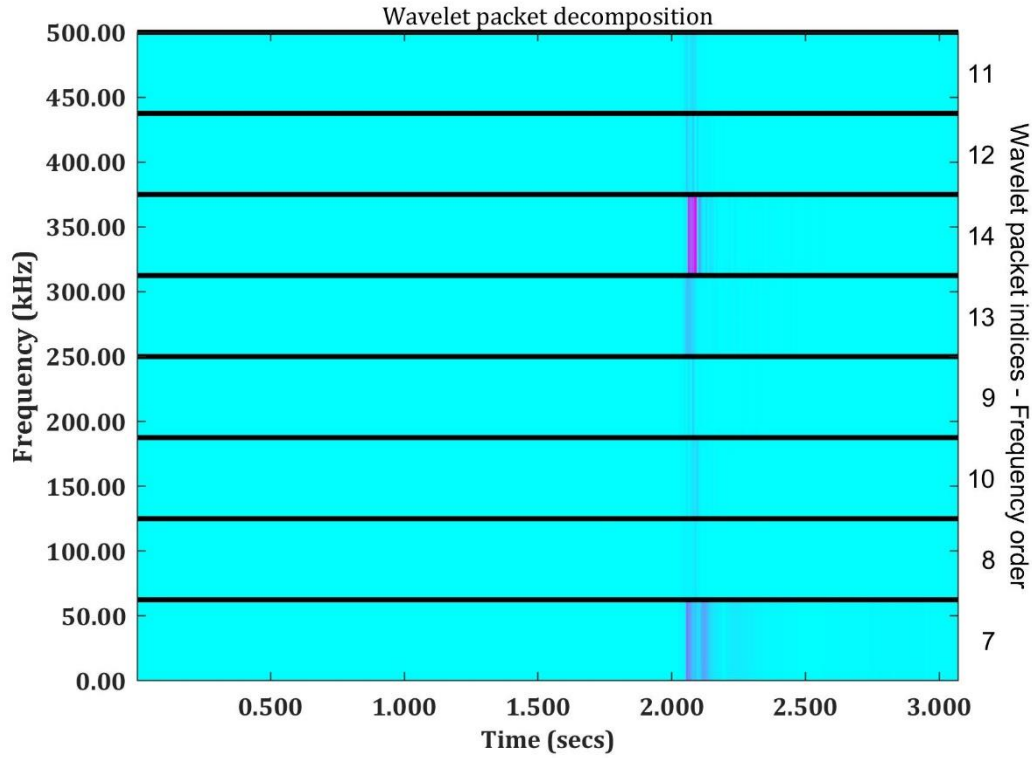
Figure 4.12. WPT Decomposition of the signal sent

Figure 4.13 shows the waveform being decomposed into five intrinsic mode functions (IMF) and also its residual. From the amplitudes of the IMF, residual and sent signal, it can be observed that the sent signal has a maximum amplitude close to 0.2 *(au)* and the IMF modes 1, 2 and 3 also has the maximum amplitude close to 0.2 *(au)*. The residual, however, has a range between -6×10^{-3} *(au)* to -0.1×10^{-3} *(au)*. This clearly indicates that the residual signal contributes nothing but low amplitude signals, which very well maybe noise, to the frequency spectrum.

The applied signals are received by the sensors and their waveforms are analysed using the hybrid method introduced in Section 4.4. The arbitrary energies of each frequency spectrum are calculated using Eqn. (4.2). The percentage of the spectral energies are also calculated using Eqn. (4.3). The percentage of spectral energies recorded along the longitudinal and transverse directions before the impact event are presented in Tables 4.7 and 4.8, respectively.
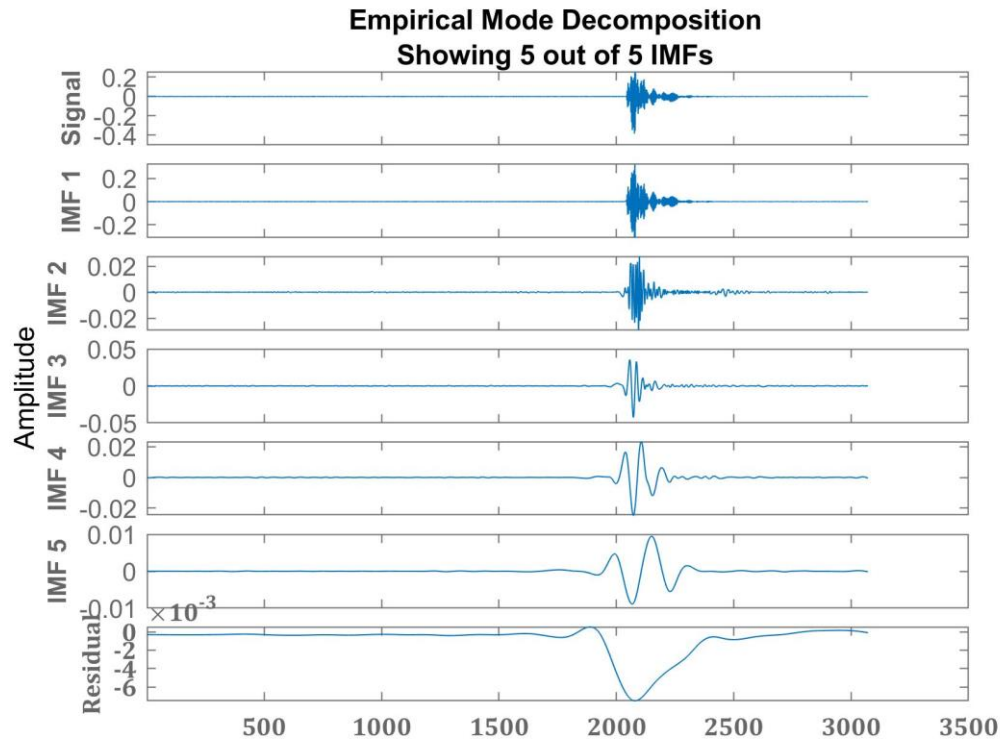
Figure 4.13. Decomposition of the sent signal into 5 IMF using EMD

Table 4.7. Percentage of Spectral Energy in each frequency band of the waveforms recorded along longitudinal direction before BVID

Specimen Name	Percentage of Spectral Energy in Frequency Band (kHz)							
	437.5-500	375-437.5	312.5-375	250-312.5	187.5-250	125-187.5	62.5-135	0-62.5
AU1	0.02	1.77	76.59	16.48	2.11	2.45	0.38	0.20
AU2	0.03	2.00	90.04	2.82	0.45	2.64	0.55	1.45
AU3	0.05	2.26	87.44	5.69	1.13	2.85	0.47	0.11
AU4	0.04	2.14	85.28	5.75	1.10	3.46	0.48	1.75
AU5	0.07	3.14	81.18	11.15	0.41	2.84	0.28	0.93

These energies are calculated from the decomposed waveforms at the final iteration of the predefined model using WPT. The WPT results of all the specimens before BVID along longitudinal and transverse directions are presented in Figures 4.14 and 4.15, respectively. Despite the energies being presented in Tables 4.7 and 4.8, the WPT figures are required. Because the energy percentage requires post-processing of the data. The

Figures 4.14 and 4.15, on the other hand, gives the pictorial representation of the frequency bands which carries most of the spectral energy. While processing a large number of signal-based data simultaneously, the pictorial representations reduce the tardiness in working with large datasets.

Table 4.8. Percentage of Spectral Energy in each frequency band of the waveforms recorded along transverse direction before BVID

Specimen Name	Percentage of Spectral Energy in Frequency Band (kHz)							
	437.5-500	375-437.5	312.5-375	250-312.5	187.5-250	125-187.5	62.5-135	0-62.5
AU1	0.05	1.83	86.59	4.51	0.05	3.30	0.41	3.26
AU2	0.04	1.80	88.39	5.69	0.11	2.99	0.36	0.62
AU3	0.04	1.76	85.42	9.01	0.40	2.83	0.38	0.16
AU4	0.04	2.54	74.15	10.30	0.25	9.80	2.28	0.64
AU5	0.04	1.89	89.51	4.32	0.18	3.02	0.47	0.57
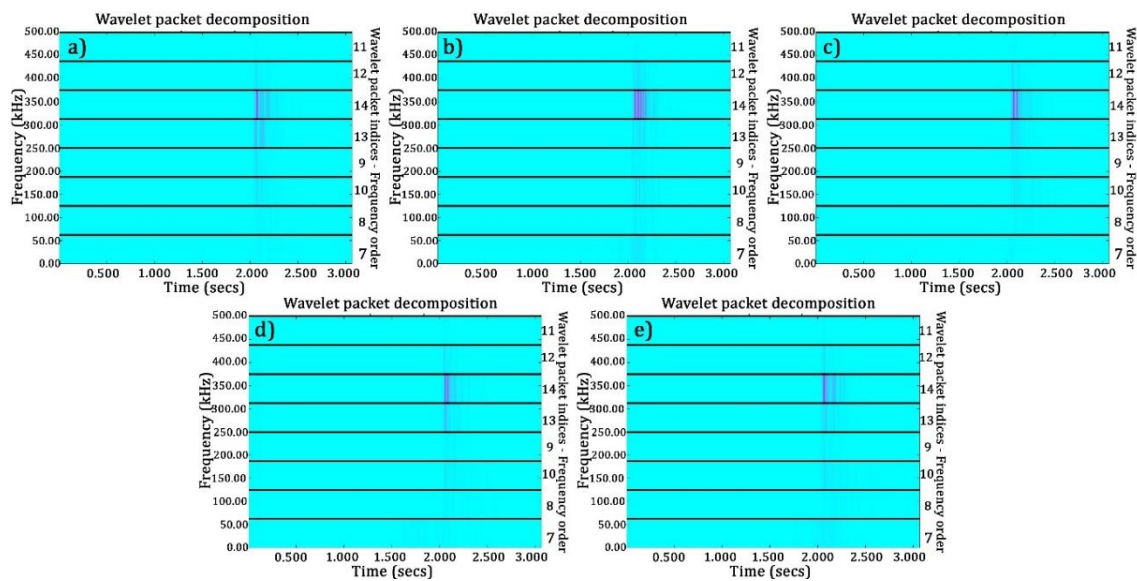
Figure 4.14. WPT results of specimens **a**) AU1, **b**) AU2, **c**) AU3, **d**) AU4, **e**) AU5 before BVID along Longitudinal Direction

From Tables 4.8 and 4.9, it is clear that most of the spectral energies are associated with three major frequency bands: 125 kHz – 187.5 kHz, 250 kHz – 312.5 kHz and 312.5 kHz – 375 kHz. For the sake of simplicity in mentioning, these bands will be named as Band-I, Band-II and Band-III, respectively. On average, these three frequency bands have

89

cumulative spectral energy of above 93%. Therefore, the applied pressure waves are transformed into elastic waves associated with these three frequency bands. As indicated by Vary (1979), Vary and Bowels (1979) and Finkel et. al (2000), the pressure waves carry the characteristics of the propagating medium. Therefore, for any further analysis of the waveforms recorded before the BVID event, the spectral energies associated with only three frequency bands of interest will be considered.
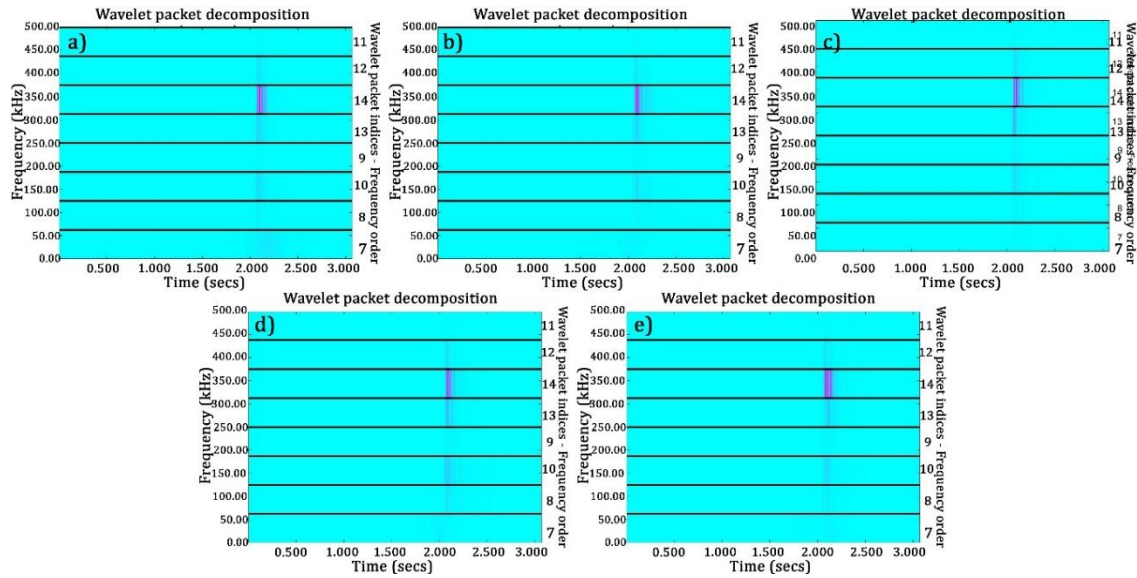
Figure 4.15. WPT results of specimens **a**) AU1, **b**) AU2, **c**) AU3, **d**) AU4, **e**) AU5 before BVID along Transverse Direction

The waveform loses its energy during the propagation and, besides material, also the geometry of the propagating medium plays a significant role in affecting its energy loss. Moreover, the propagating acoustic waveforms are generally dispersive in nature. Typically, about 90% of the energy will be dissipated before reaching the receiver, as reported earlier in Section 4.3.1. The calculated spectral energies in the aforementioned frequency bands are compared with the spectral energies of the same bands in the sent signal using Eqn. (4.4 and 4.5). The percentage of energy recovered after the transmission is presented in Table 4.9.

$$\% \ of \ Energy \ recovered = \left. E_i^n \middle/ E_{sent-i}^n \right. \times 100 \qquad (4.4)$$

90

$$\% \ of \ Energy \ recovered = {(E_{rec})_n^i} \Big/ {(E_{sent})_n^i} \times 100 \qquad (4.5)$$

The term E_{sent} represents the energy measured from the WPT of the signal sent through the specimen. The terms E_{sent-i}^n represents the energy associated with frequency band 'i' of the signal sent.

Table 4.9. Percentage of energy recovered after transmission before BVID

Specimen Name		% of Energy Recovered			Specimen Name		% of Energy Recovered		
		Band III	Band II	Band I			Band III	Band II	Band I
Longitudinal Direction	AU1	7.60	6.45	24.01	Transverse Direction	AU1	0.53	1.86	1.41
	AU2	3.70	3.88	10.37		AU2	1.71	0.87	4.17
	AU3	3.83	6.59	10.54		AU3	1.80	1.91	4.87
	AU4	1.72	3.89	18.84		AU4	0.90	0.98	3.01
	AU5	5.58	4.39	15.64		AU5	0.61	1.36	1.77

In Table 9, the percentage of spectral energies recovered from the signal sent is presented for both longitudinal and transverse directions. There is a huge difference in the percentage of energy recovered between the two directions. For instance, the percentage of energy recovered in Band-I for AU2 is 10.37% along longitudinal direction but is only 4.17% along the transverse direction. This difference can be attributed to two major factors: boundaries of the specimen geometry with respect to the signal source is not the same in these two directions (since the length > width of the specimens referring to Figure 4.7.). More importantly, the wave propagation relies very much on the interlaminar toughness of the specimen in that particular direction. There were several contradicting reports regarding the propagation of the simulated acoustic signals. Vary and Pollard observed that the simulated acoustic signals transmit with less energy loss along the direction of the fiber in a composite laminate. This is due to the high rigidity of the fiber in the composite laminate. However, Moon et al. observed the simulated acoustic signals transmit with less energy loss along the direction opposite to the fiber orientation. Despite these contradicting reports, the consensus is the interlaminar properties of the specimen is the key contributor in the energy loss across the propagating medium. The

overall energy recovered along the longitudinal direction is larger than the energy recovered along the transverse direction in Table 4.9. This clearly indicates the non-isotropic nature of the specimen and the signal propagation is affected by the properties of the specimen in the longitudinal and transverse directions.

It can be observed from Figure 4.11 that the damage propagates along the longitudinal direction of the specimen, while the fibers along the transverse directions have broken by the impact. This damage indicates that during the formation of BVID, the fibers along the transverse direction of the specimen carried most of the load and suffered the fiber breakage.

Specimens AU1 and AU5 have recovered only about 0.53% and 0.61% in Band-III, and 1.41% and 1.77% in Band-I, respectively along the transverse direction. This indicates that the stiffness of the fibers along the transverse direction or the interlaminar strength of the specimens AU1 and AU5 along the transverse direction is quite low compared to the other specimens. This leads to the less recovery of the spectral energy along these directions and consequently, during the impact event, they suffered more damage. However, the same specimens recovered more energy along the longitudinal direction. This means that AU1 and AU5 carry most of their strength along the longitudinal direction and not in the transverse direction.

Nevertheless, it is debatable why the energy recovered is higher along the longitudinal direction than the transverse direction. When the pulsar and receiver are placed along the longitudinal direction of the specimen, the boundaries of the geometry for wave propagation is shorter along the width of the specimen. This leads to less dispersion of the applied stress waves along the width and consequently, more energy is recovered along this direction. This is probably the reason why the energy recovered along the longitudinal direction is higher.

Table 4.10. Percentage of Spectral Energy in each frequency band of the waveforms recorded along longitudinal direction after BVID

| Specimen Name	Percentage of Spectral Energy in Frequency Band (kHz)							
	437.5-500	375-437.5	312.5-375	250-312.5	187.5-250	125-187.5	62.5-135	0-62.5
AU1	0.08	1.79	79.34	13.46	3.74	1.17	0.03	0.38
AU2	0.15	2.55	87.10	5.73	1.05	1.57	0.07	1.78
AU3	0.06	1.73	79.40	14.06	0.65	2.99	0.05	1.08
AU4	0.04	3.97	86.28	6.23	0.64	1.69	0.13	1.02
AU5	1.64	16.99	73.69	0.67	5.19	0.73	1.03	1.64

After the impact event creating the BVID, the acousto-ultrasonic test is again conducted for all the specimens. The percentage of energies recovered in each band along the longitudinal and transverse directions are calculated and presented in Tables 4.10 and 4.11, respectively. Similar to Figures 4.14 and 4.15, the pictorial representations of where the spectral energy is dispersed on the frequency spectrum in the specimens after impact, along longitudinal and transverse directions are presented in Figures 4.16 and 4.17, respectively.

Table 4.11. Percentage of Spectral Energy in each frequency band of the waveforms recorded along transverse direction after BVID

Specimen Name	Percentage of Spectral Energy in Frequency Band (kHz)							
	437.5-500	375-437.5	312.5-375	250-312.5	187.5-250	125-187.5	62.5-135	0-62.5
AU1	0.03	2.71	86.71	5.00	0.45	3.91	0.43	0.75
AU2	0.03	1.37	50.34	11.75	2.15	25.40	8.45	0.52
AU3	0.03	1.44	74.53	10.58	0.36	9.41	3.46	0.18
AU4	0.04	1.25	87.52	5.89	0.34	4.07	0.83	0.06
AU5	0.04	1.81	79.82	7.46	0.29	6.35	3.27	0.96
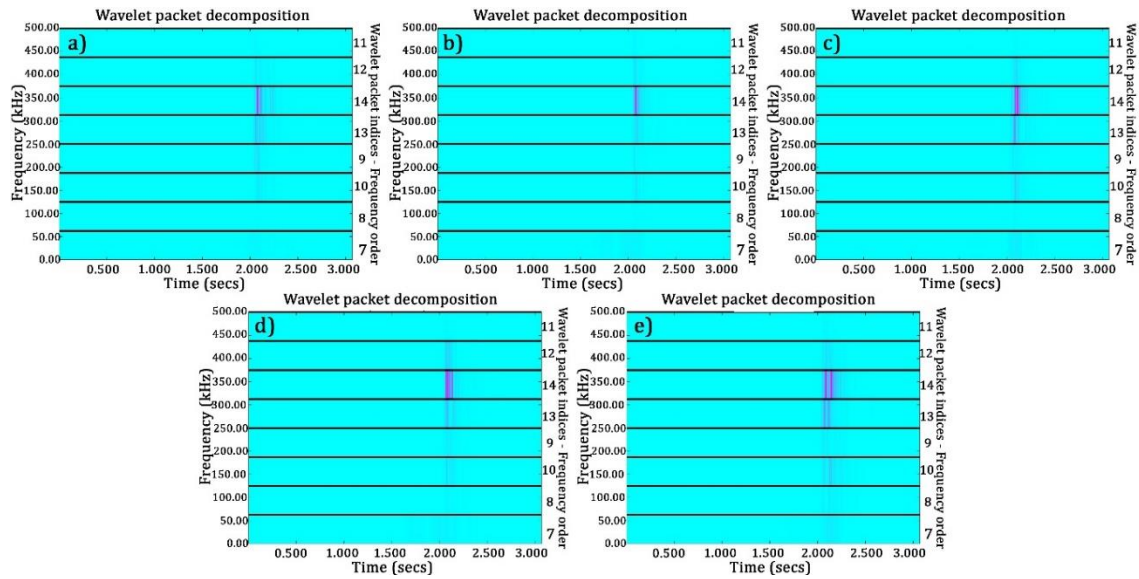
Figure 4.16. WPT results of specimens **a**) AU1, **b**) AU2, **c**) AU3, **d**) AU4, **e**) AU5 after BVID along Longitudinal Direction

Similar to the results before BVID, the significant frequency bands which carried more than 90% of the total spectral energies are Band-I (125 kHz – 187.5 kHz), Band-II (250 kHz – 312.5 kHz) and Band-III (312.5 kHz – 375 kHz). So, these bands will be considered for further analysis. The spectral energy recovered in the bands with respect to the spectral energy of the sent signal is presented in Table 4.12.

Expectedly, the percentage of energy recovered is significantly lower when compared to the results before BVID. This is because the BVID created interlaminar damage to the specimens. Moreover, the fibers along the transverse direction have been broken and the damage has also propagated along the longitudinal direction. Necessarily, the propagation path of the simulated acoustic signals from the pulsar to the receiver is damaged.

Previous studies indicate that the high-frequency signals simulated as a result of pressure waves correspond to the signals propagating along the fibers. Similarly, the low-frequency signals correspond to the matri4. However, no experimental evidence on the frequency bands were directly associated with the damages in those studies.
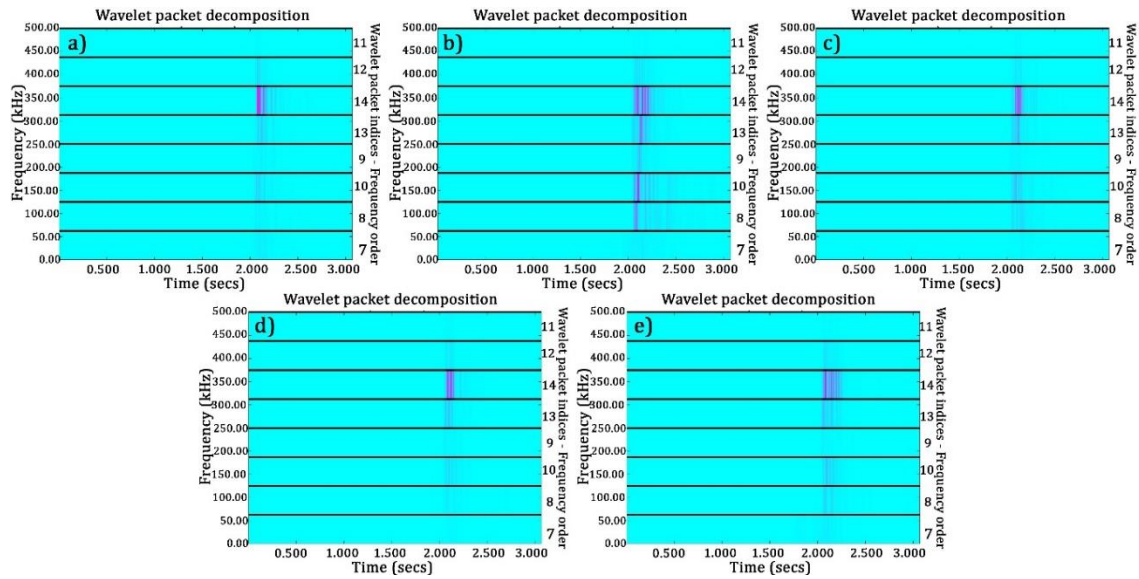
Figure 4.17. WPT results of specimens **a**) AU1, **b**) AU2, **c**) AU3, **d**) AU4, **e**) AU5 after BVID along Transverse Direction

In the presented research work, it can be observed that the energy recovered in longitudinal directions of Band-I, Band-II and Band-III are less than 1% of the sent signal. Particularly, specimen AU1 has recovered 0.09%, 0.20% and 0.07% of the sent signal along longitudinal direction in Band-I, Band-II and Band-III, respectively. Specimen AU5, although recovering 0.51% and 0.33% of the spectral energy in Band-I and Band-II, respectively, recovered only 0.09% of energy in Band-III. However, the other three specimens have recovered a comparatively larger percentage of spectral energy in the longitudinal direction. This is because the sensors are placed along the line of damage in the longitudinal axis (Refer to Figures 4.7 and 4.12). Due to the directionality of the sensors, the most energy of the signals sent normally propagate along the longitudinal axis before reaching the receiver. Since the propagating axis is deteriorated, the recovery of the signal is affected considerably.

The same cannot be explained for the percentage of recovered energy along the transverse direction. The signals in Band-II and Band-III are reduced. As indicated earlier, the lower frequency signals normally represent the signals simulated along the matri4. Although the fibers along the transverse direction are broken, probably the interlaminar matrix layers remain largely unaffected. Thus, the simulated signal found a propagation

95

path along these layers to reach the receiver. This probably is the reason why the percentage of recovered spectral energy is higher in Band-I for all the specimens.

Table 4.12. Percentage of energy recovered after transmission after BVID

	Specimen Name	% of Energy Recovered			Specimen Name	% of Energy Recovered		
		Band III	Band II	Band I		Band III	Band II	Band I
Longitudinal Direction	AU1	0.07	0.20	0.09	AU1	0.22	0.21	0.82
	AU2	0.40	0.43	0.60	AU2	0.10	0.37	4.09
	AU3	0.15	0.42	0.46	AU3	0.49	1.14	5.16
	AU4	0.15	0.17	0.24	AU4	0.44	0.48	1.69
	AU5	0.09	0.33	0.51	AU5	0.16	0.25	1.07

(Second Specimen Name group header: Transverse Direction)

Nonetheless, this waveform analysis of acousto-ultrasonic testing method must be studied carefully. If used properly, the extent of interlaminar damage and also the interlaminar strength of a material/structure can be predicted easily. The results presented show that the non-isotropic properties of a composite structure affect the propagation of the simulated acoustic waves. The extent of the interlaminar damage, qualitatively, can be assessed using this testing method. In addition, the interlaminar strength and other properties such as compression after impact (CAI) can be compared and assessed using this technique. With proper understanding of the wave propagation and energy loss in a damaged medium, the location, shape and size of the damage can also be identified using this testing method.

4.6   CONCLUSION

A new method for using acoustic emission technique has been introduced in this research work. A hybrid approach is followed for using this new acousto-ultrasonic approach. The waveforms, normally studied under time-frequency domain, are studied using Wavelet Packet Transform (WPT). But this hybrid approach allows to denoise the signal and reconstruct them before analyzing them on WPT. For denoising, the Empirical Mode Decomposition (EMD) is used. The EMD decomposes the signal into Intrinsic Mode Functions, rather than wavelets and the reconstruct the original signal by removing the residual noise. For validating this new approach, the interlaminar strength of the material is studied for CFRP specimens.

The acousto-ultrasonic approach is tested for CFRP specimens subjected to low velocity drop weight impact. The specimen is tested along both its longitudinal and transverse axes, before and after the drop weight impact event. Compression after impact test is also performed on the specimen to characterize its strength with the presence of BVID. The acousto-ultrasonic results are used to characterize the interlaminar strength of the material along both the longitudinal and transverse directions. A conditional hypothesis is made to evaluate the results: the direction along which the relative loss of AE descriptors is low, possess the higher interlaminar strength. However, after the material is subjected to damage/flaw, the lower relative loss is attributed to the lower interlaminar strength. Nonetheless, this intricating phenomenon can be simplified with the hybrid analysis. Using the hybrid approach, it is possible to discriminate the lower interlaminar strength and the presence of damage/flaw in the material.

By analysing the percentage of energy recovered in these frequency bands before and after the formation of BVID, the extent of damage in the specimens can be identified. The residual indention recorded after the BVID does not explicitly show the interlaminar damage extent in the materials. However, the acousto-ultrasonic approach can detect the same. Even if findings should be limited to the specific CFRP studied and to the specific geometrical configuration and much more extensive experimental campaign would be required to assess feasibility in other experimental conditions and as a function of the relative damage extension, nevertheless this work gives a first proof of capability of the approach of detecting BVID damage in CFRP composite.

Using the acousto-ultrasonic approach, it seems relatively easy to characterize the material properties. Along with the proper evaluation tools and techniques, this approach has a greater scope in discriminating the types of defects and the position of the flaws in the material.

CHAPTER 5
CLUSTERING OF ACOUSTIC EMISSION DATA FOR DAMAGE MONITORING

The Acoustic Emission data recorded during an entire loading history of a material or a structure is enormous in number. Sometimes, it is difficult to use all the data contemporarily for analysis. For this reason, different types of data processing techniques are being used. The purpose of these tools is to process the AE data effectively and assign them to different damage mode, thereby identifying the critical points of failure. In this research work, the data processing technique called data clustering or pattern recognition technique is used for a different purpose. The data clustering tool is used in this research work to comprehend the relationship between different AE descriptors, thereby simplifying the damage monitoring process using AE. This chapter briefs the introduction on the statistical pattern recognition technique, which is followed by a detail explanation of an unsupervised pattern recognition technique called k-means++ clustering. The k-means++ clustering technique is used in this work for analyzing the AE data. The application of this technique is explained with an experimental evaluation and the results are discussed in this chapter.

5.1 INTRODUCTION

Pattern recognition is a statistical tool for classifying information in a dataset. Essentially, it is one of the tools used for decision making process. The aim of the pattern recognition tools is to simplify the complicated mechanisms of decision making process and automate the process.

For understanding the basics of pattern recognition technique, a time-sampled value of a waveform can be considered. The most basic way to describe all the datapoints in the time-sampled waveform in Figure 5.1 is to identify all the grey valued pixels. The datapoints of the time-sampled waveform can be expressed as $x(t_1), x(t_2), \dots, x(t_n)$. The

n number of datapoints form the vector X. The datapoints in the vector X are randomly distributed in the dataset, so $x(t_i)$ can be described as a random variable. This makes the vector X a random vector, which is comprised of random variables.
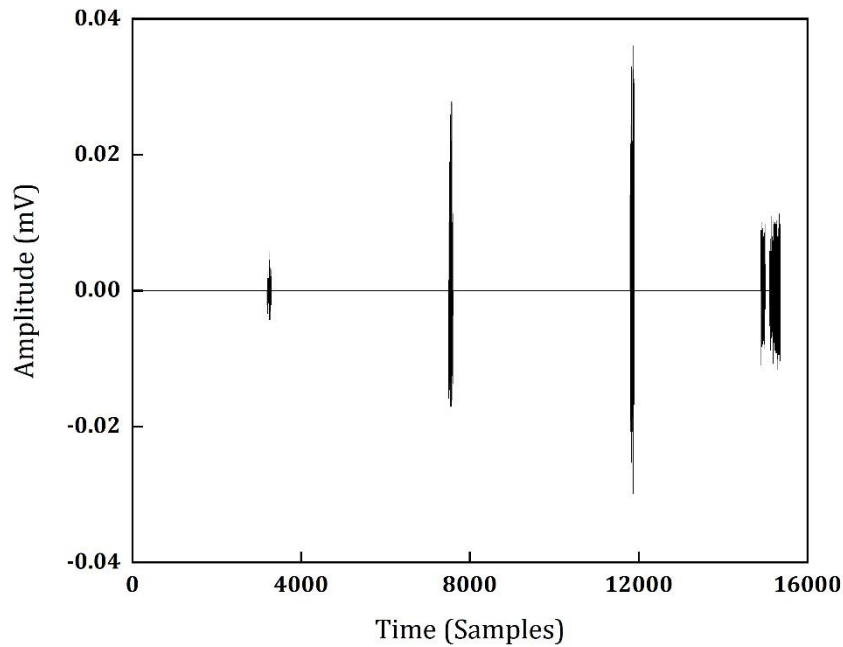
Figure 5.1. An example time-sampled waveform

If a boundary is selected to classify the random variables into different classes or categories, a discriminant function which classifies these random variables must be used. The pattern recognition technique is the function which classifies the random variables into a different classes or categories. Normally, there are two types of classifiers that can be used in the pattern recognition techniques: parametric classifier and nonparametric classifier. Parametric classifiers are based on the mathematic forms of the random variables or its density functions such as linear, quadratic or piecewise classifiers. When no parametric structure is used, Parzen or k-nearest neighbour approach is used.

In this work, the k-nearest neighbour approach is used for the classification of data clusters. Nonetheless, a brief introduction on the parametric classifier is presented in this

chapter. The reason for selecting a nonparametric pattern recognition technique is also provided in the subsequent sections.

5.2 INTRODUCTION TO PARAMETRIC PATTERN RECOGNITION TECHNIQUE

As indicated in the previous section, the parametric pattern recognition technique is based on the simple mathematic forms of random variables. A parametric random vector X with n number of random variables can be expressed as,

$$X = [x_1 x_2 \dots x_n]^T \tag{5.1}$$

where, T denotes the transpose of the vector X.

The random variables are often characterized by a distributed function. For instance, if the random vector maybe characterized by the probability distribution function, it can be described as,

$$P(x_1, x_2, \dots, x_n) = \Pr\{X_1 \leq x_1, X_2 \leq x_2, \dots, X_n \leq x_n\} \tag{5.2}$$

where, $P(A)$ is the probability of an event A. In general terms, Equation (5.2) is written as,

$$P(X) = \Pr\{X \leq x\} \tag{5.3}$$

In case, the random variables are characterized by the density function, it can be described as,

$$p(X) = \lim_{\Delta x_1 \to 0, \dots, \Delta x_n \to 0} \frac{\Pr\{x_1 < X_1 \leq x_1 + \Delta x_1, \dots, x_n < X_n \leq x_n + \Delta x_n\}}{\Delta x_1 \dots \Delta x_n} \tag{5.4}$$

In general terms, the density function can be expressed as,

$$p(X) = \frac{\partial^n P(X)}{\partial x_1 \dots \partial x_n} \tag{5.5}$$

Similarly, the random vectors can also be characterized by the normal distribution as,

$$N_X(M.\Sigma) = \frac{1}{(2\pi)^{n/2}|\Sigma|^{0.5}} \, exp\,[-0.5\,d^2(X)] \tag{5.6}$$

where, N_X is the normal distribution with the expanded vector M and the covariance Σ.

$$d^2(X) = (X - M)^T \textstyle\sum^{-1}(X - M) \; = \; tr[\textstyle\sum^{-1}(X - M)(X - M)^T] \tag{5.7}$$

In Equation (5.7), the tr represents the trace of the matri5. For instance, if A is a matrix, then $tr(A)$ is the trace of the matrix A, which is equal to the summation of the diagonal components of the matrix A.

The normal distribution is commonly used in the parametric pattern recognition technique because of the parameters that characterize the distribution. First, the moment vector M and the covariance $\sum$ are sufficient to characterize the normal distribution. Secondly, the marginal densities and the conditional densities of the normal distribution are normal. Besides, the condition of normality is a reasonable approximation for many datasets. These are some of the reasons why the normal distribution is preferred over densities and probability distribution functions.
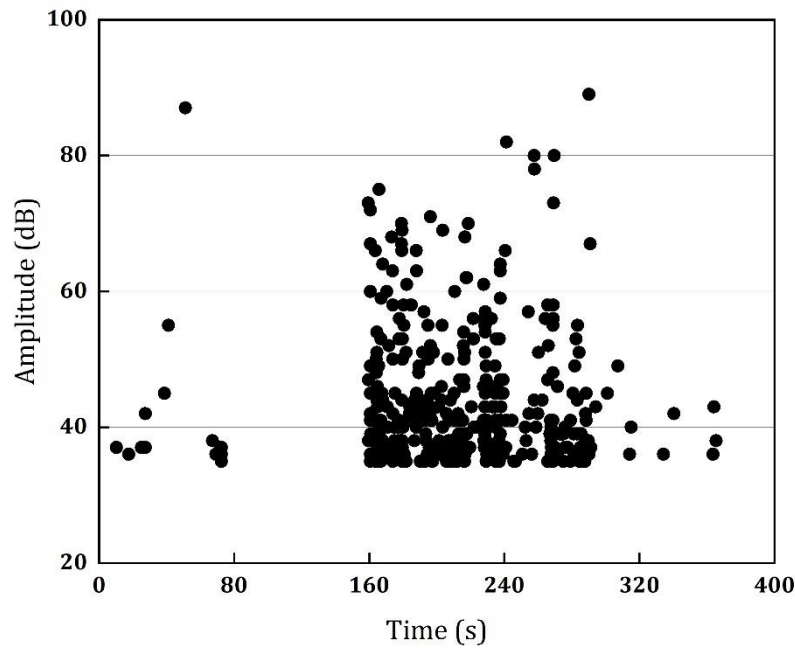
Figure 5.2. Peak Amplitude distribution of AE events recorded during static Tensile Test on AlSi10Mg specimens

However, the dataset of the AE cannot be characterized by any conventional mathematical approximations such as linear, quadratic or any other basic forms. For

instance, the peak amplitude of the recorded AE events during a static tensile test of AlSi10Mg specimens is presented in Figure 5.2. The dataset cannot be characterized in terms of parametric pattern recognition technique.

This is the reason why the nonparametric pattern recognition technique such as k-nearest neighbour is used for classification of data. In this work, the k-means++ algorithm is used. In the next section, the function with which the k-means++ classifies the data into different clusters is explained.

5.3 NONPARAMETRIC PATTERN RECOGNITION TECHNIQUE

As mentioned in the previous section, when the variables in a dataset are characterized by a mathematical form, the parametric pattern recognition technique can be used. In other cases, when the density functions of the random variables cannot be characterized by these types of classifiers, the nonparametric approach is used. In nonparametric classification, the random variables are classified based on the density functions, which are classified based on the small number of neighbouring variables. The estimation of the density function based on the neighbouring values is far less reliable with large covariance when compared to the parametric recognition techniques. Nonetheless, the nonparametric technique is not about obtaining accurate results, but is more focussed on the classification and the performance of these classifications. In that context, the nonparametric classifiers serve the purpose. In this research work, k-means++ clustering technique is used, which is explained in the next section.

5.3.1 k-means++ Clustering Technique

The Lloyd's algorithm or k-means algorithm, as it is known popularly, classifies the data into a defined number of clusters. The various steps in this pattern recognition technique are explained, which is followed by a brief description supported by a self-explanatory flowchart (Figure 5.3).

The dataset to be clustered into predefined number of classes 'k' is taken as X.

Step 1: Select a random point from the input dataset X. This random datapoint is considered as the first centroid (c_1).

Step 2: Compute the distance of all the datapoints from the centroid c_1. The distance between the centroid c_j and each datapoint m is stored as $d(x_m, c_j)$.

Step 3: The next centroid is selected with the following probability in random from the dataset X, using Equation (5.8).

$$\frac{d^2(x_m, c_1)}{\sum_{j=1}^{m} d^2(x_j, c_1)} \tag{5.8}$$

Step 4: Choose center j by computing the distance between each datapoint of each dataset and the respective centroid.

Step 5: Assign each datapoint to the closest centroid.

Step 6: Repeat Steps 4 and 5 until all centroids k are chosen.

Step 7: Calculate datapoint to cluster centroid distance for all the datapoints with respect to their assigned centroid.

Step 8: Calculate the average of the datapoints in each cluster to obtain new (or optimal) centroid locations.

Step 9: Repeat Steps 7 and 8 until the cluster assignments do not change (or the maximum number of iterations is reached).
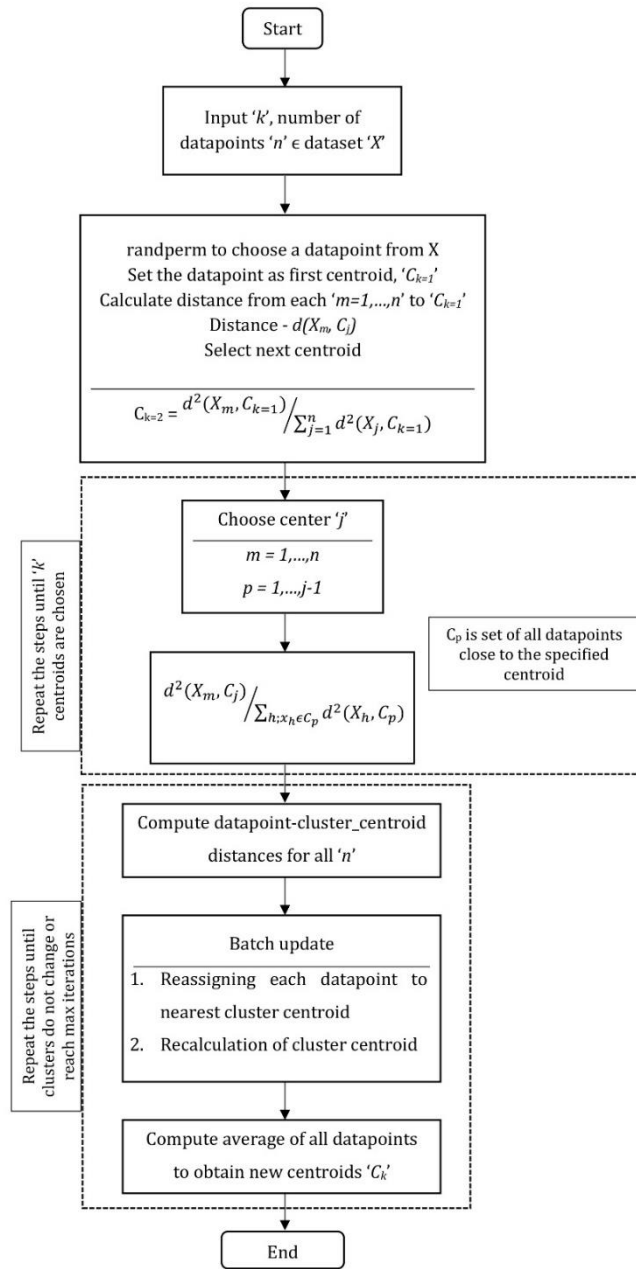
Figure 5.3. Self-explanatory Flowchart for k-means++ algorithm

A datapoint is assigned to a cluster based on the minimum distance between that data point and the centroid of the cluster. Then the algorithm will compute the average distance among all the datapoints in each cluster to calculate the new centroid. These steps are iterated until the optimum centroid is obtained and all the datapoints are assigned to their respective clusters. The k-means++ algorithm improves the running

time of k-means by using a heuristic approach to find the centroids. A self-explanatory flow chart has been provided in Figure 5.3 for a better understanding of the algorithm. The batch update is faster than the online update but at times, it does not converge the solution to the minimum distance from the cluster centroid. However, for this research work, the batch update is used because the algorithm could minimize all datapoints to the local minima, thus avoiding the necessity of online update.

5.3.2 Davies-Bouldin Index for Optimal Number of Clusters

The Davies-Bouldin Index (DBI) is a metric used for calculating the optimal number of clusters, a particular data can be clustered. It is based on the ratio of distance of the datapoints within the cluster and the distance between the datapoints in different clusters. DBI can be expressed as,

$$DB = \frac{1}{k} \sum_{i=1}^{k} max_{j \neq i} \{D_{i,j}\} \tag{5.9}$$

$$D_{i,j} = \frac{\overline{d_i} + \overline{d_j}}{d_{i,j}} \tag{5.10}$$

$\overline{d_i}$ is the average distance between each point in the ith cluster and the centroid of the ith cluster. $\overline{d_j}$ is the average distance between each point in the jth cluster and the centroid of the jth cluster. $d_{i,j}$ is the Euclidean distance between the centroids of the ith and jth clusters. The maximum value of $D_{i,j}$ represents the worst-case within-to-between cluster ratio for cluster i. The optimal clustering solution has the smallest Davies-Bouldin index value.

5.4 EXPERIMENTAL VALIDATION OF K-MEANS++ CLUSTERING FOR ACOUSTIC EMISSION DATA

Various researchers have used different pattern recognition techniques such as k-means, k-means++, k-nearest neighbour, Kohenen's Self Organizing Maps (SOM), Artificial Neural Networks (ANN) and Fuzzy C-means algorithms. However, in each of those research work, a similar trend has been followed, which is the traditional way of using the pattern recognition technique. The AE descriptors, mostly 1 or 2, are selected and are

classified into 3 clusters. Each cluster is assigned to a damage mode. For instance, for AE descriptors recorded from the mode I delamination of CFRP, the peak frequency during the entire loading history is clustered. The cluster which covers the data between frequencies 50 kHz to 150 kHz are associated with matrix cracking, 150 kHz to 250 kHz are associated with delamination/debonding and the cluster which covers the dataset above 250 kHz is associated with fiber breakage. This is the common trend followed by all the researchers, who have used the pattern recognition technique. Some researchers have classified the data into 4 clusters, and some have classified into 2 clusters. Nonetheless, the method of classification remains the same.

In this work, the k-means clustering technique is used for analyzing the damage mode in Carbon Fiber Reinforced Plastic (CFRP) composites under the mode I delamination. Unlike the traditional method of classifying, in this research work, the relation between different AE descriptors for a particular damage mode is discussed.

5.4.1 Materials and Methods

Three DCB specimens (named as MI-1, MI-2 and MI-3) are prepared as per ASTM D5528 standard. The CFRP prepreg used in the preparation of DCB utilizes high strength carbon fibers of filament diameter 5-7 µm while the epoxy resin system used has a density of 1.31 g/cm^3. Each ply has a thickness of 0.25 mm. The DCB specimen was prepared by curing the first half of the plate, followed by placing a non-adhesive insert, which serves as the crack initiator and the noncured second half of the plate. The final curing was done in an autoclave under a pressure of 6 bar at 180 °C. The total length of each specimen is 125 mm and a width of 25 mm. The thickness of each specimen is 3 mm, which constitutes 12 number of plies. The non-adhesive insert has a length of 45 mm and has a very low thickness, lower than 13 µm according to the standard. A pair of piano hinges are attached by a strong adhesive to both the sides of the specimen, near the edge where the non-adhesive insert is placed.

The DCB tests are carried out in a INSTRON 1342 testing machine under displacement-controlled mode at a crosshead displacement rate of 1 mm/min.

5.4.2 Acoustic Emission Setup

The acoustic activities are recorded during the entire load history of the DCB tests using a general-purpose, 300 kHz resonant frequency acoustic emission sensor, MISTRAS R30α. The sensor has an operating frequency of 150-400 kHz and a peak sensitivity at 52 dB. The sensors are coupled to the surface of the specimen using silicone gel, to ensure better acoustic coupling between the sensor and the surface of the specimen. The sensor signals are amplified by 40 dB using a 2/4/6-AE preamplifier. The amplified signals are filtered through bandpass filters and recorded by the PAC PCI-2 data acquisition system. The waveforms of the recorded acoustic signals are sampled at 1 MSPS. The PCI-2 system performs automatically the FFT analysis and provides the peak frequency and frequency centroid of the recorded AE events during the acquisition. The AE descriptors peak amplitude, duration, counts and energy are recorded for all the acoustic events along with the signal-based data, peak frequency and frequency centroid.

5.5 EXPERIMENTAL RESULTS AND DISCUSSIONS OF THE CLUSTERED ACOUSTIC DATA

The test is carried out for three different DCB specimens, which are named as MI-1, MI-2 and MI-3. The names MI represents the delamination mode (mode I), in which the test is carried out. In this work, five different AE descriptors are classified into different clusters using k-means++ algorithm. The descriptors used in this study are peak amplitude, frequency centroid, counts, duration and risetime. The definitions and significance of each AE descriptor classified in this study are explained in the previous chapters.

Initially, the DBI is calculated for each dataset. Three specimens are tested in this work, five descriptors from each specimen is taken for analysis. Naturally, each of these datasets must be classified based on the optimal cluster value calculated from each dataset. This means that, there will be a total of 15 DBI calculated from all the datasets. However, it is not easier to compare these datasets with different number of clusters. Therefore, the DBI is calculated for each dataset and the most repeated cluster is taken as k, the number of cluster. From the analysis, the optimal number of cluster is calculated to be 3. So each AE descriptor is classified into 3 clusters and analyzed in this section.
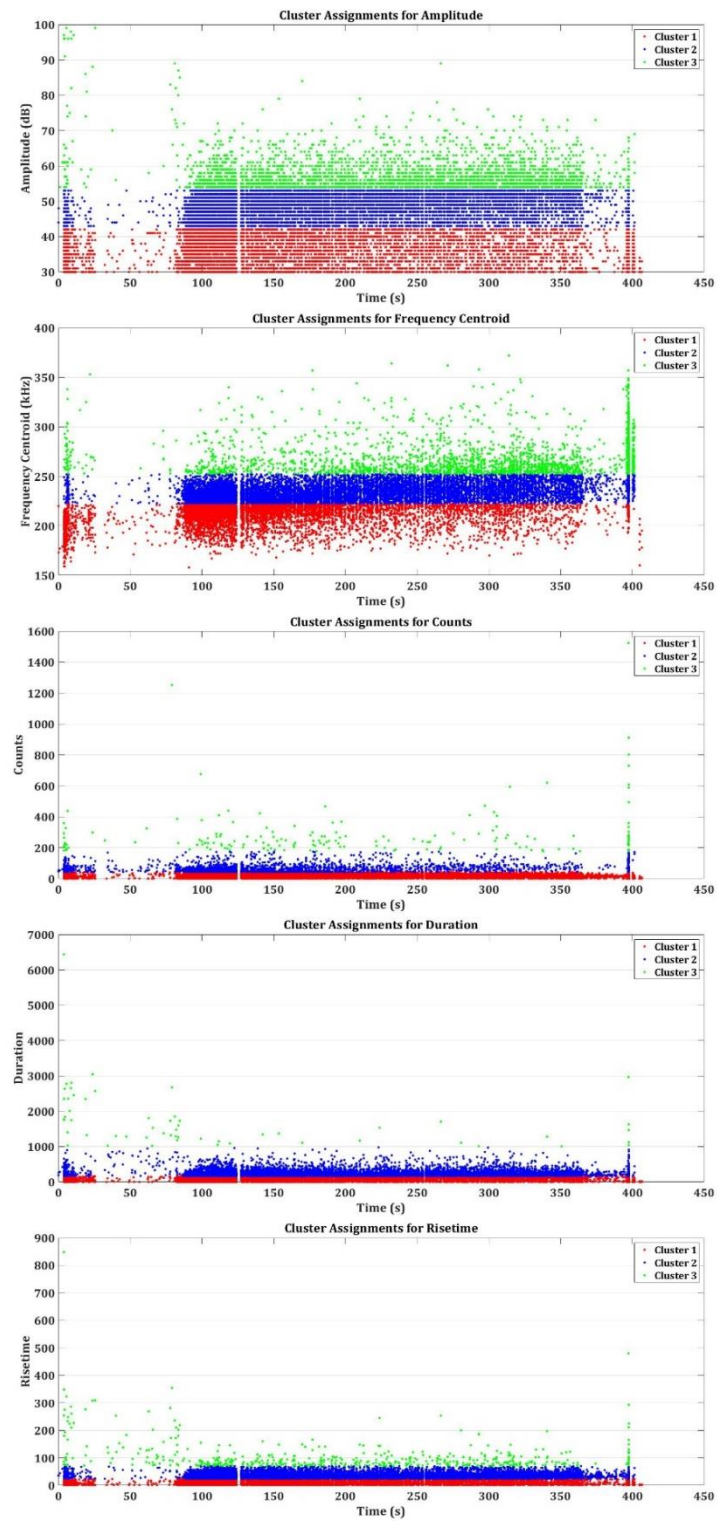
Figure 5.4. Clustered AE descriptors of specimen MI-1

Figure 5.4 shows the clustered AE descriptors of specimen MI-1. Before the duration of 10 s, quite a significant number of AE signals with higher amplitude are recorded. These signals lie in cluster 3. Moreover, more than 10 signals were recorded above 90 dB in the first 10 s duration at the beginning of the test. It has been indicated by many researchers that only fibers breakage emits AE signals above 80 dB. However, the specimen tested for this study is unidirectional and during the first 10 s of the test, the already initiated crack was opening through the non-adhesive insert. No visible fiber cracking is observed or is possible at that instant. While looking at the frequency centroid, a considerable amount of AE data was categorized in cluster 3, nonetheless, only 3 signals were recorded above 300 kHz. The number of AE events in cluster 3 of frequency centroid is not comparable with the cluster 3 of peak amplitude. Supposedly, the same number of AE events should be recorded in cluster 3 of frequency centroid and peak amplitude. This difference indicates that the misconception of AE descriptor is possible when it is used individually or when it is assisted by one another descriptor. It is essential to use multiple AE descriptors to identify the different damage mechanisms.

The amplitude, when compared along with the frequency centroid, counts, risetime and duration of the AE data, gives more information regarding the damage mode. Moreover, it has been indicated by Aggelis et. al. (2012) and Kalteremidou et. al. (2018) that the high risetime normally represent interlaminar debonding/crack growth. Considering the counts, there are plenty of AE signals with a large number of counts were recorded and accumulated at the end of the test in cluster 3. Comparing the peak amplitude and counts in cluster 3, one can clearly infer that there are large number of weak signals recorded, which is the reason why the counts are larger whereas the number of higher amplitude signals are small in that specific region. This can also be observed in the larger risetime in cluster 3.

Typically, acoustic waves propagate in two modes: lower order symmetric and higher order asymmetric. The lower order symmetric has high frequency but low speed and are mostly formed due to the interlaminar crack propagation in the thin CFRP plies. Conversely, the higher order asymmetric has low frequency but high speed and has the tendency to disperse before reaching the sensor. It mostly represents the matrix cracking

or microcracking. Considering these possibilities, it can be inferred that the large counts number, low amplitude, higher risetime of the signals in cluster 3 represents the interlaminar crack propagation. Thus, during both the initial and final stages of loading, specimen MI-1 has suffered damages which are related to the matrix cracking and interlaminar debonding/crack growth. This is also an indication that the delamination occurred vigorously at the final stages of loading resulting in the failure of the specimen MI-1.

For specimen MI-2, the clustered AE descriptors are provided in Figure 5.5. Unlike the MI-1, there are no high amplitudes in cluster 3 at the early stages of the loading. However, around 25 s duration, AE events have accumulated. For instance, approximately 10 events are observed in cluster 3 of the amplitude at 25 s, however, only one event has been recorded in cluster 3 of frequency centroid. Similar observations can also be found in counts, duration and risetime. Following this, there is an idle period where no AE events were observed. This idle period can be termed as an acoustic gap.

The acoustic gap is the period of no acoustic activity before the occurrence of a major acoustic events. This has commonly been observed in earthquakes and quasi-brittle structures such as concrete. However, in the recent years, this phenomenon has also been observed in metals and CFRPs. Thus, the specimen MI-2 has sustained a major damage after 25 s duration. This can be observed from the fact that a significant amount of AE signals is accumulated in cluster 3 of amplitude and frequency centroid, throughout the loading time beyond the 50 s duration. A significant number of events with a duration of 500 μs to 1800 μs can be identified in cluster 3 of specimen MI-2. This indicates the number of lower order asymmetric AE events are recorded (which represents interlaminar debonding, rather than interlaminar crack growth) during the loading of the specimen. Similar observation can also be made in counts, as specimen MI-1 had highest counts only at the initial and final stages of loading, while MI-2 has highest counts throughout the entire loading. It is clear from these observations that the microcracking and interlaminar debonding has occurred vigorously at the initial and final stages of MI-1 but it is observed consistently in MI-2 after 50 s duration.
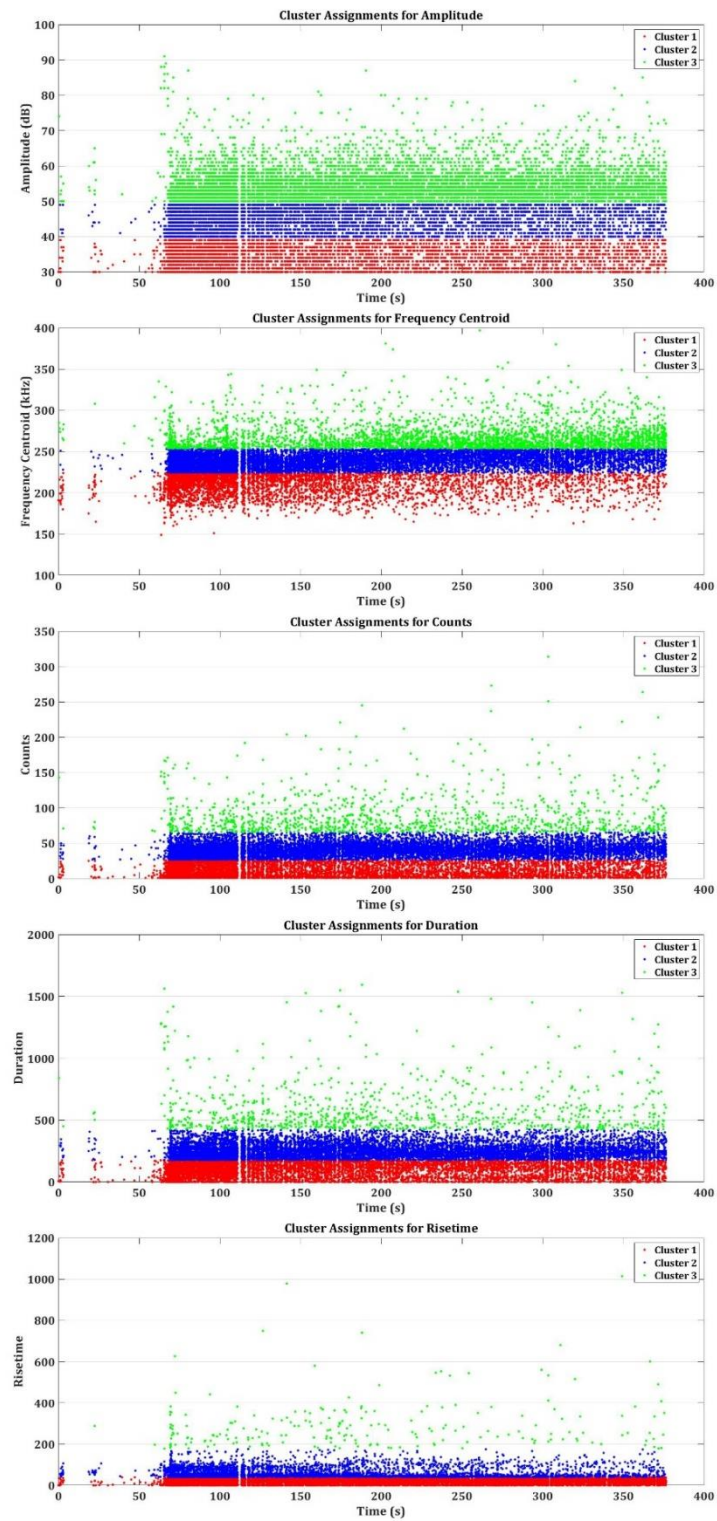
Figure 5.5. Clustered AE descriptors of specimen MI-2
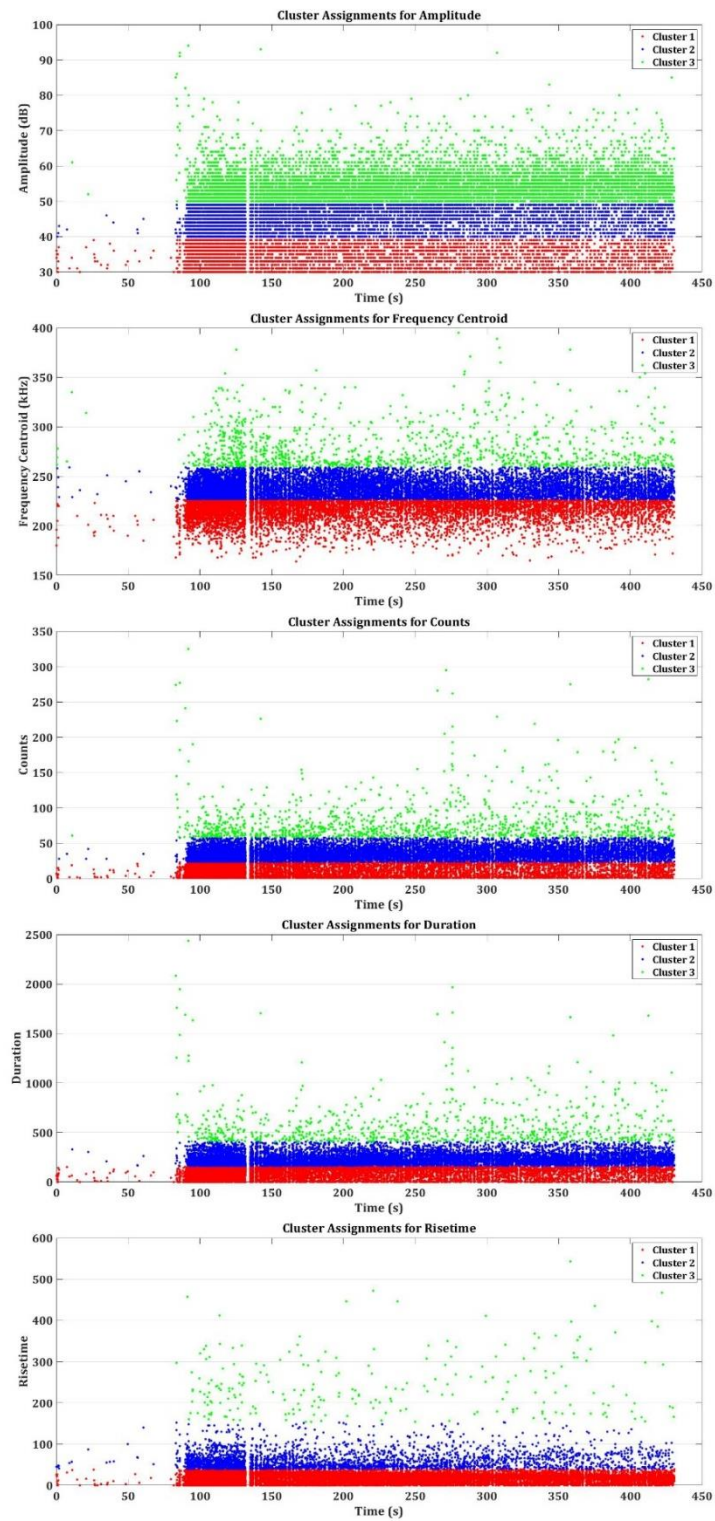
Figure 5.6. Clustered AE descriptors of specimen MI-3

Specimen MI-3 has unique characteristics in AE results, which can be observed in Figure 5.6. During the initial stages of loading, there are no AE signals recorded in cluster 3 of all AE descriptors. Besides, the general acoustic activity during the initial stages of loading (up to 70 s) is very few to none. As mentioned earlier, by observing the amplitude, counts and risetime, it can be inferred that the few AE events recorded at the early stages of loading can be attributed only to the microcracking in the matri5. Because the high order asymmetric waves carry low frequency but at a higher speed. That is why there is no higher risetime in cluster 3 at the early stage. Moreover, the counts are also very low at that duration. It makes us to believe that the AE events occurred during the early stages of loading is purely attributed to matrix cracking. Similar to MI-2, after a period of the acoustic gap, a large number of acoustic events can be observed just before the 100 s duration. These events have high counts, high-frequency centroid, high amplitude, whereas low risetime. This infers that the damage propagation at that duration is because of the low order symmetric waves propagated due to interlaminar crack growth.

It can be assumed that the major crack growth started just before the 100 s duration and beyond that point, the material started to lose its load-bearing property gradually. Since there are no major damage accumulated in cluster 3 and very few AE events recorded in cluster 1 and 2, the material did not suffer any severe micro-damages.

Thus, in this work each cluster is not related with specific damage mechanisms but rather used as a model tool to characterize the material properties and damage propagation. The above observations clearly indicate that the material characterization using AE results cannot be achieved through a single or two AE parameters. A set of AE parameters are required to be analysed simultaneously, and more preferably using clustering to characterize the material under loading.

Apart from this, the k-means clustering is also used in another application, where a new parameter called Energy per Count is introduced. Since the parameter is explained in detail in a separate chapter (Chapter 7), the application of the k-means++ clustering or in general the pattern recognition technique is also validated experimentally in the subsequent chapters (Chapters 5 and 7).

5.6   CONCLUSION

The introduction about the statistical pattern recognition technique is presented in this chapter. The possibility of classifying data using parametric and nonparametric approaches is introduced. The parametric pattern recognition can be used for the variables or dataset which are characterized by some mathematical forms such as linear, quadratic or piecewise classifiers. Since the AE data is not distributed in the mathematical form, the nonparametric pattern recognition technique has been used. The k-means++ algorithm, which is one of the most powerful classification type of nonparametric technique has been used in this work. For experimental validation of this technique, the AE descriptors recorded from the mode I delamination of three DCB specimens are analyzed. The traditional method of classifying the AE descriptors is not followed in this research work. Instead, the relationship between different AE descriptors in a damage mode has been analyzed using this technique. Particularly, the amplitude, risetime and counts are used simultaneously to identify the type of acoustic wave propagated during different damage modes. A formidable conclusion has been brought that more than one AE descriptor is always essential for characterizing the damage modes in a material. k-means++ pattern recognition technique paves way for using multiple AE parameters contemporarily, which serves the purpose mentioned.

CHAPTER 6
NEW ACOUSTIC EMISSION
PARAMETER b$_{AE}$-VALUE

An innovative way of utilizing acoustic energy is introduced in this chapter. Over the years, researchers have formulated several methods for utilizing acoustic energy. Particular interest has been provided for introducing a direct relationship between the mechanical results and the acoustic energy. In this chapter, a new acoustic emission function, called b$_{AE}$, is introduced. This function is based on the relationship between the cumulative acoustic energy and counts recorded during the straining of a material. In the first part of the chapter, the introduction and the evolution of this parameter is presented. In the second part of the chapter, the results and discussions of the mechanical tests carried out to validate the parameter is presented.

6.1 INTRODUCTION TO b-VALUE

The origin of the relationship between the acoustic energy and counts can be dated back to the empirical formula proposed by Gutenberg and Richter (1949), which quantifies the magnitude-frequency relationship in an earthquake event.

$$\log N = a - bM_L \tag{6.1}$$

In Eqn. (6.1), N is the incremental frequency, M_L is the Richter magnitude of events and 'a' and 'b' are empirical constants. The Richter magnitude M_L is proportional to the logarithm of the maximum amplitude A_{max} corrected for the attenuation in amplitude due to the wave propagating distance and the inelastic absorption. The magnitude is also proportional to the logarithm of source rupture area S.

$$M_L \propto \frac{2}{3} c \log A_{max} \propto \frac{2}{3} c \log S \tag{6.2}$$

where the value of c varies depending on the type of transducer used for recording the event.

This is the empirical formula proposed by Gutenberg and Richter (1949) for earthquake seismology, where the events with larger magnitudes occur seldom than the events with smaller magnitude. Henceforth, this empirical formula cannot be directly used for the AE events. Nonetheless, the same principle can be used for studying the amplitude distribution during AE events in quasi-brittle materials such as concrete or other brittle structures.

The linear relationship in Eqn. (6.1) provides the negative slope gradient b-value from the magnitude-frequency plot. The gradient of the b-value changes with the different stages of fracture growth. For instance, the b-value is high when the microcracks are distributed in the early stages and it is low when the macrocracks begins to localize. The Gutenberg-Richter relationship has been modified for the AE technique as follows:

$$\log N = a - b' A_{dB} \tag{6.3}$$

where A_{dB} is the peak amplitude of the AE events in decibels. It can be written in equation form as,

$$A_{dB} = 10 \log A_{max}^2 = 20 \log A_{max} \tag{6.4}$$

The b-value gradient in Eqn. (6.3) is very powerful in understanding the fracture growth in quasi-brittle materials such as concrete and/or other civil structures. This is due to the fact that the amplitude of these events is larger in comparison with the transient low frequency AE signals generated when commercial materials such as metals, additively manufactured materials or FRPs.

For this reason, a new parameter has been developed for this study and is named as b_{AE}-value. The detailed explanation about this new developed slope gradient is presented in the subsequent sections.

6.2   RELATIONSHIP BETWEEN ACOUSTIC ENERGY AND ACOUSTIC COUNTS

Upon an extensive literature survey and data analysis, an observation has been made upon the relationship between the acoustic energy and counts. When different commercial materials are strained or when they undergo a fracture process, the natural

logarithm of the cumulative number of counts is always proportional to the natural logarithm of the cumulative energy of the acoustic events recorded during the process. This phenomenon was first observed by Botvina and Tyutin (2019), upon which they established a power-law relationship between the AE events and the amplitude of the events.

$$\sum N = C_{AE} A^{-b_s} \tag{6.5}$$

where, b_s is the slope coefficient and C_{AE} is the constant relating the amplitude distributed in the AE events.

Developing the Eqn. (6.5), Botvina and Tyutin developed an equation to relate the total number of AE signals with the high amplitude signals.

$$20 \log N = const - b_s A_{AE} \tag{6.6}$$

Using this b_s value, Botvina and Tyutin (2019) investigated the fracture mode of low carbon and medium carbon steel under cyclic loading. Based on the intensity of the AE events generated by the materials under tension cyclic loading and the b_s value, they distinguished the different stages of the material change.

For instance, there is an intensive AE activity and growth in total number of AE signals, which occurred at the elastic deformation stage. During the next stage, which is the strain hardening, there is an abrupt decrease in AE intensity and b_s value. When the maximum load is reached, there are very few AE events, which is followed by their complete absence. At the end of this stage, the fracture appears.

This hypothesis is based on the AE events with higher amplitude similar to Eqns. (6.3 & 6.4) and is not empirical in that sense.

To establish an empirical formula to relate the linear relationship between the cumulative counts N_{AE} and cumulative energy E_{AE} of the AE events generated by commercial materials under loading, the following equation is proposed in this thesis work.

$$\ln N_{AE} = b_{AE} \ln E_{AE} + a \tag{6.7}$$

The b_{AE} in Eqn. (6.7) is the new slope gradient introduced in this research work. This b_{AE}-value considers the total number of AE counts above the threshold of acquisition and the total AE energy. Without considering the high amplitude or low amplitude signals, this relationship is based upon all the AE events generated under loading.

The hypothesis formed for relating this newly developed b_{AE}-value and the validation of it with the experimental results is presented in the subsequent sections.

6.3 THE b_{AE}-VALUE AND HYPOTHESIS FOR IDENTIFYING THE DAMAGE MODES

As mentioned in the previous subsection, there exists a linear relationship between the natural logarithms of cumulative counts and cumulative energy generated during acoustic events, which is explained by Eqn. (6.7).

Due to this strict correlation between the cumulative count and cumulative energy of the acoustic signals, whenever there is a rapid increase in either the counts or the energy, the linearity is affected. For instance, as long as the acoustic energy generation is uniform and stable, the linearity existing between these two parameters are not affected. However, when there is a rapid energy release, such as due to a crack initiation or crack nucleation in a metallic specimens or a fiber breakage in a FRPs, this linearity is affected.

Since AE technique is sensitive even for recording transient elastic signals, this rapid release of energy tends to affect the linearity explicably. Thus, by considering the slope gradient in Eqn. (6.6), 'b_{AE}', this shift is linearity can be identified. This forms the basis of the b_{AE}-value, which when plotted over the strain or the duration of the test can identify the invariabilities in the cumulative counts and energy of the recorded AE signals. A set of hypotheses is formed based on the trend of the b_{AE}-value under loading is established and is presented in Table 6.1.

The hypotheses are based on the literature surveys made on how the AE descriptors behave to each of the damage mode in materials. By relating these variations in AE counts and energy with the b_{AE}-value, the hypotheses are made. To validate the hypotheses, a series of tensile tests are performed on AlSi10Mg additively manufactured samples and

the test is monitored by AE technique. Further details are presented in the subsequent sections.

Table 6.1 Hypotheses for damage characterization using b_{AE}-value

b_{AE}-value Trend	Acoustic Emission Characteristics	Damage Characteristics
Sudden Increase	Larger Number of Acoustic Events Recorded with Low Energy	Microcracking or dislocation movements under straining
Gradual Increase	Number of Acoustic Events (Counts) are larger, nonetheless, the energy is also slightly higher than it is for microcracking	Yielding stage in Metal or Crack nucleation
Rapid Decrease	Fewer Acoustic Events but with Higher Acoustic Energy	Cracks propagating through Surface Pores/Volumetric Pores or Defects Interlaminar crack growth in FRP
Remains Constant	Number of Acoustic Events and Acoustic Energy increases constantly indicating the failure path	Material progressing towards Failure

6.4   VALIDATION OF b_{AE}-VALUE

As indicated in the previous section, the validation of the hypotheses presented is done by monitoring AE activity of tensile tests of AlSi10Mg specimens. This section comprises of 'Materials and Methods' employed for the tensile tests and acquisition of AE data, 'Results' from the tensile tests and the b_{AE}-value and finally 'Validation' through analysing the AE waveforms in their time-frequency domain.

6.4.1   Materials and Methods

6.4.1.1   *Preparation of Materials for Testing*

The samples used for the tensile tests are prepared using Selective Laser Melting (SLM) process. The material used for the tests is AlSi10Mg alloy. This alloy is selected for its best casting property due to the presence of 11% Silicon (Si) in the hypoeutectic alloy near the eutectoid composition. The best casting property of this alloy is more desirable for

the SLM process. This alloys also has a good hardenability, which can be attributed to the presence of Magnesium (Mg) up to 0.45% and the Si. The natural improvement of strength and hardness by the addition of Si and Mg can be attributed to the formation of Mg2Si precipitate. This alloy has also a good corrosion resistance due to the natural formation of the oxygen layer on its surface. The major chemical constituents of AlSi10Mg are presented in Table 6.2. The density of the AlSi10Mg alloy is 2.68 g/cc and has a melting range from 570 °C to 590 °C.

Table 6.2 Chemical constituents and their composition in AlSi10Mg alloy

Element	Al	Si	Mg	Fe	N	O	Ti	Zn	Mn	Ni	Cu	Pb	Sn
Mass (%)	Bal*	11	0.45	<0.25	<0.2	<0.2	<0.15	<0.1	<0.1	<0.05	<0.05	<0.02	<0.02

Balance percentage is Aluminium

Three different configurations of SLM specimens are prepared for this study. The specimens are prepared in the configurations as recommended by ASTM E8M – Standard Test Methods for Tension Testing of Metallic Materials. The specimens are prepared in the SLM process in three different orientations with respect to the processing bed. The schematic of the specimens prepared is presented in Figure 6.1. The three configurations built respectively along X-axis, Y-axis and 45° with respect to the X-Y plane are named as T_X, T_Y and T_{45}.
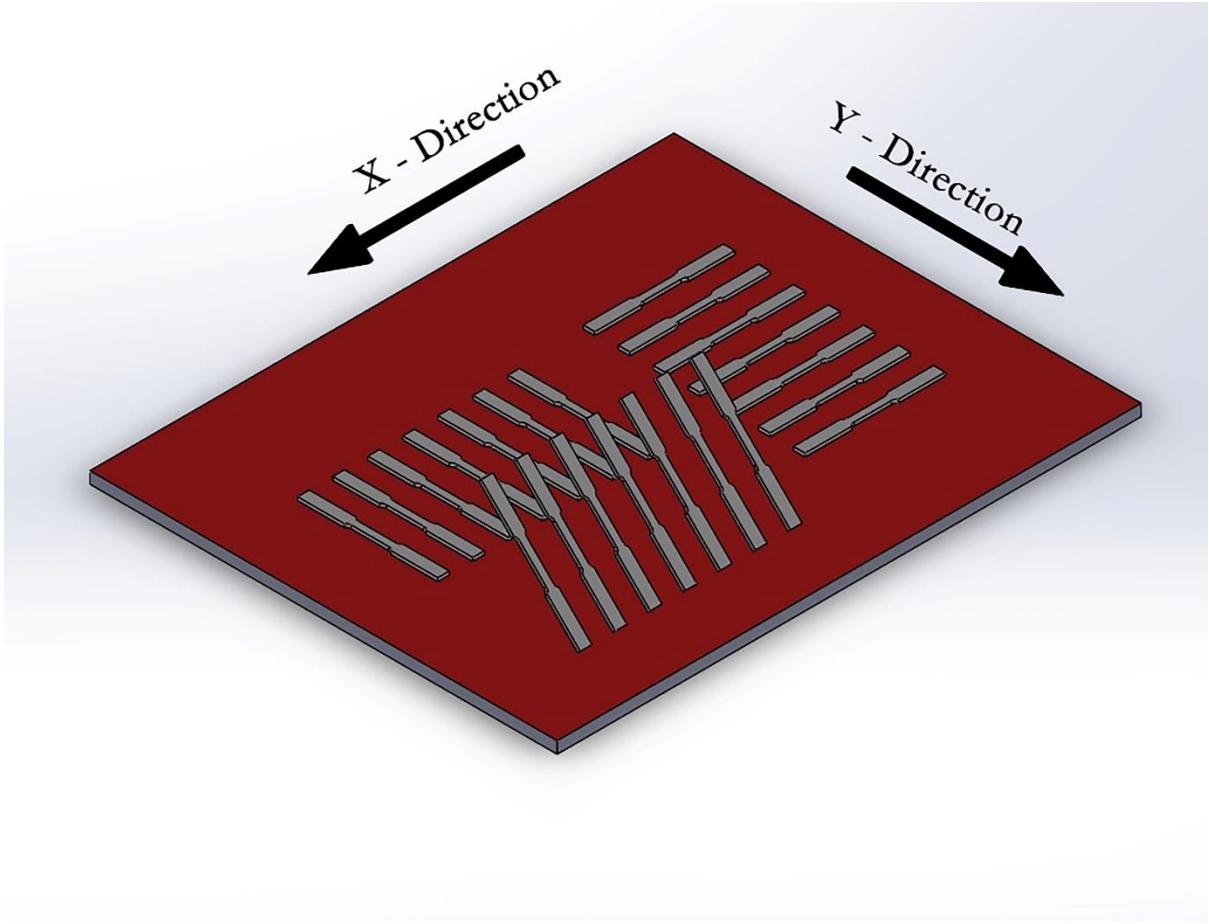
Figure 6.1. Building Configurations of SLM specimens with respect to the Building Plane

All the specimens are prepared in RenAM 500 M System. The laser used for melting the raw AlSi10Mg is Nd:YAg laser, which has a maximum power output of 400 W and a wavelength of 1064 nm. The processing parameters used for the SLM process in preparation of the specimens are presented in Table 6.3. To calculate the desired energy density and the scanning speed of the laser during the SLM process, Campenelli et. al (2014) has provided a generalized equation, Eqn. (6.8).

$$E_{laser} = \frac{P_{laser}}{v_{laser}.d_{laser}} \qquad (6.8)$$

The required energy density (E_{laser}) can be calculated by controlling the power output (P_{laser}), scanning velocity (v_{laser}) and the spot diameter (d_{laser}).

121

Table 6.3. Selective Laser Melting process parameters set for building AlSi10Mg specimens

Parameter	Details
SLM System	RenAM 500M Industrial additive manufacturing system (Renishaw plc, Staffordshire, United Kingdom)
Laser type	Nd-YAG Solid-state
Power Output	400 W
Wavelength	1.064 μm
Spot Diameter	200 μm
Scanning Velocity of Laser	11 mm/s
Energy Density	2 J/mm²
Thickness of Layer	20 μm

During the SLM process, the recoater is moved along the Y-axis, while the laser traced the samples along the X-axis at the velocity of 11 mm/s. The specimens are built in three different orientations with respect to the building platform by rotating the platform. The laser scanning direction and the recoater direction is kept the same throughout the process. Once the specimens are built, the specimens are air cooled and the stress is relieved by keeping the specimens inside the building environment at a constant temperature of 300 °C $\pm$ 10 °C for about 2 hours.

All dimensions are in mm
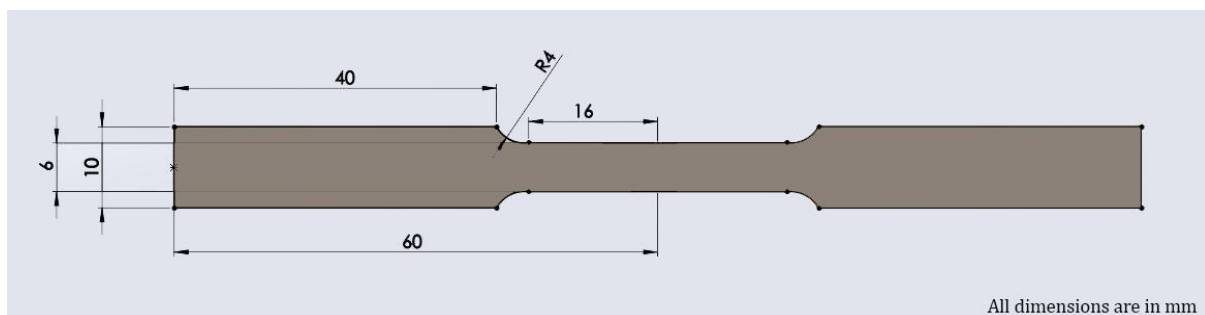
Figure 6.2. Specimen dimensions selected as per ASTM standards

The dimensions of the specimen, which is prepared as per ASTM E8M standard is presented in Figure 6.2. The specimens are standard plate type specimens with a rectangular cross section. The nominal thickness of all the specimens is 3 mm.

6.4.1.2   Test Setup with Acoustic Emission Sensors

The tensile test is carried out in INSTRON 1342 Servo-hydraulic testing machine with a maximum load capacity of 10 kN. The tests are carried out under displacement-controlled mode with a crosshead displacement rate of 1 mm/min. An uniaxial strain gauge is attached to the surface of the specimen, approximately at the midspan of the gauge length.

For monitoring the acoustic activity, a piezoelectric sensor is attached to the specimen during the testing. The characteristics of the sensor used in this study are presented in Table 6.4. A thin layer of silicone and a Kapton tape is used to separate the surface of the specimen and the transducing layer of the sensor. The Kapton tape is provided for maintaining an uniform surface roughness between the sensor layer and the specimen surface. In addition to that, the Kapton tape also prevents the interference of the signals from the strain gauge to affect the acoustic emission acquisition. The silicone layer generally acts as a protective layer by preventing the reverberating signals from being transduced.

Table 6.4. Acoustic Emission sensor/system characteristics used for the study

Characteristics	
Sensor	PICO Sensor – Physical Acoustics Corporation
Operating Frequency	200 kHz – 750 kHz
Resonant Frequency, Ref V/(m/s)	250 kHz
Peak Sensitivity, Ref V/(m/s)	54 dB
Dimensions	Ø5 mm x 4 mm
Preamplifier	2/4/6 AE Preamplifier
Gain Selectable	20 dB/40 dB/60 dB
Input Impedance	10 kΩ
Bandwidth	10 kHz – 2 MHz

The AE signals above the threshold amplitude of 35 dB are recorded. The signals are pre-amplified by 40 dB through a 2/4/6 AE Pre-amplifier. To avoid the acquisition of noise signals arising from the testing rigs and the electric interferences, the signals are filtered through a low-bandpass and high-bandpass filter. The frequency window of acquisition

is set as 10 kHz and 2 MHz. All the waveforms of the signals are recorded at a sampling rate of 1 mega samples per second.

6.4.2 Results

6.4.2.1 Tensile Test Results

A total of 7 specimens from each group are tested for obtaining the nominal tensile properties. The Yield Strength, Young's Modulus, Ultimate Tensile Strength and Elongation at break are presented in Table 6.5. From Table 6.5., it can be observed that the yield strength, ultimate tensile strength and Young's modulus of the specimen groups T_x and T_y are significantly greater than the specimen group T_{45}.

Table 6.5. Tensile Test results of all three configurations of Specimens tested

Orientation	Specimen Name	Yield Strength σ_y	Ultimate Tensile Strength σ_{UTS}	Young's Modulus E	Elongation at break ε
		MPa	MPa	GPa	%
x - direction	T_x1	137.4	214.9	65.4	12.3
	T_x2	135.4	217.5	67.7	12.2
	T_x3	137.8	214.7	66.1	12.1
	T_x4	136.7	216.1	73.5	14.2
	T_x5	132.5	209.0	63.1	12.4
	T_x6	131.7	207.9	64.9	10.8
	T_x7	134.5	209.2	63.7	11.0
	Mean	*135.1*	*212.8*	*66.3*	*12.2*
	Std. Dev.	*2.4*	*3.9*	*3.5*	*1.1*
y - direction	T_y1	135.2	211.1	67.6	12.9
	T_y2	138.0	217.0	67.6	15.0
	T_y3	142.1	216.6	68.0	11.1
	T_y4	137.5	215.7	74.3	12.7
	T_y5	141.3	215.9	67.3	11.6
	T_y6	136.9	214.5	65.8	12.6
	T_y7	140.9	217.1	68.4	13.0
	Mean	*138.8*	*215.4*	*68.4*	*12.7*
	Std. Dev.	*2.7*	*2.2*	*3.0*	*4.6*
4 5 °	$T_{45}1$	121.0	208.9	61.9	10.8

$T_{45}2$	127.2	213.6	64.9	10.8
$T_{45}3$	123.7	209.9	64.4	7.5
$T_{45}4$	125.8	214.1	66.0	10.1
$T_{45}5$	126.1	213.0	65.2	8.0
$T_{45}6$	124.5	214.2	63.5	10.7
$T_{45}7$	128.2	216.0	64.1	9.2
Mean	*125.2*	*212.8*	*64.3*	*9.6*
Std. Dev.	*2.4*	*2.5*	*1.3*	*1.4*

Generally, specimens show an orthotropic mechanical behaviour. In particular, according with Analysis of Variance (ANOVA), both the ultimate tensile strength (p = 0.004), yield strength (p << 0.00001) and elongation at break (p << 0.00001) show strong correlation with building direction whereas a lower correlation is found for the Young's modulus (p = 0.057).

The Tensile properties of the specimen groups T_x and T_y do not vary widely, rather lie in a comparable limit. However, the specimen T_{45} is built at 45 degrees with respect to the building plane. Moreover, the slenderness ratio of the specimen with respect to the XY plane, where the specimen is built, in T_{45} specimen is considerably low. This means that the height of the specimen built along the 45 degree direction could lead to some micro-distortion. Moreover, the borderline porosity in the T_{45} specimens is quite higher due to the continuous beginning/ending of the scan vector near the edges. This possibly could lead to an unidentifiable distortion in the material, which might have affected the tensile properties. This could be one of the reasons why the properties of T_{45} specimens are low when compared to specimen T_x and T_y.

The orientation of the building with respect to the building platform is a crucial factor which attributes to the properties of a material based on its geometry.

The most significant results drawn out are the mechanical properties of the material before and after the yield point. The stress-strain graph of all the specimen groups is presented in Figure 6.3. It can be observed from Figure 6.3 that all the specimens have higher elongation beyond the yield point, before breaking. Unless the AlSi10Mg specimens, which are manufactured using additive manufacturing techniques being

tested at elevated temperatures, the elongation at break normally lies around 3.5% to 5.5%. During this study, the elongation at break for the SLM specimens are clearly above 7.5%, which falls outside of the value found in the literatures. Normally, SLM specimens are post-treated by placing them in an elevated temperature or subjected to aging or compression before being tested. After the post-processing of SLM specimens, they become more rigid, significantly less porous and possess better mechanical properties. This improves the Ultimate Tensile Strength of the material.

No post-processing of the SLM specimens are used in this present study. The specimens are only air-cooled and kept in the SLM building environmental temperature of 300 °C for 2 hours, which is a standard procedure SLM process built on the said building equipment. Consequently, the specimens tested in this study have higher elongation before breaking and also have significantly lower Ultimate tensile strength.
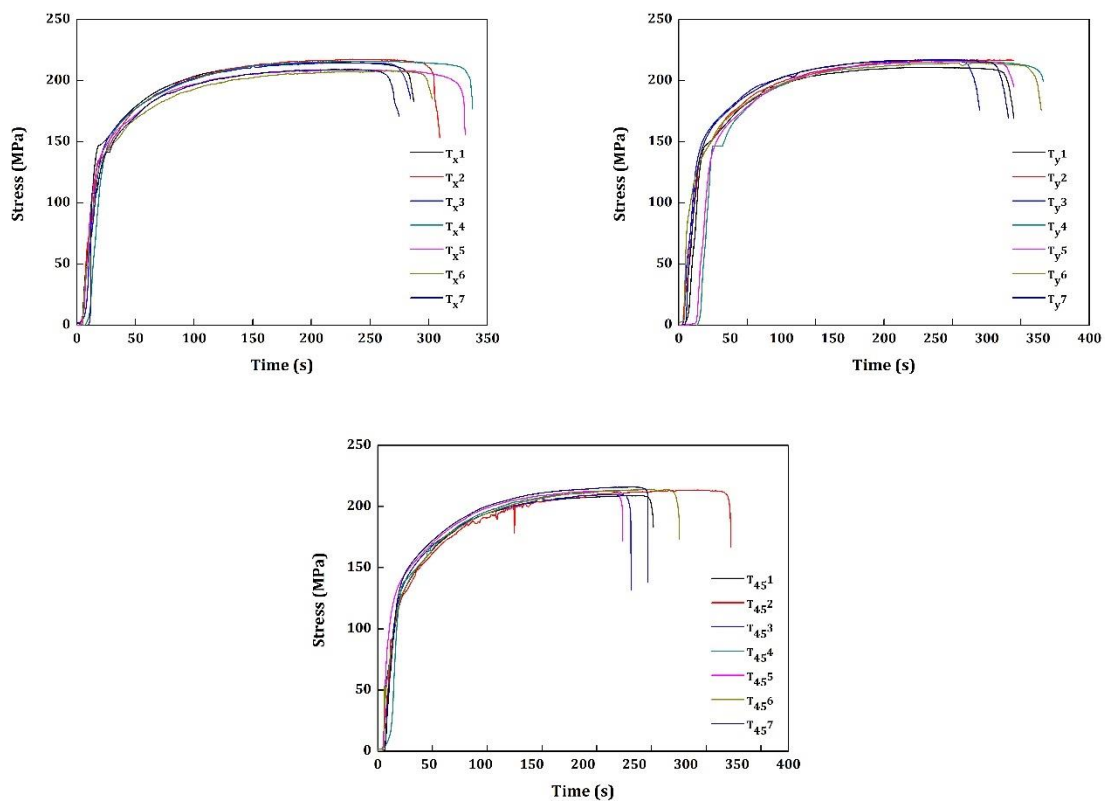
Figure 6.3. Stress-Strain curves of all the Specimens tested

Regardless of the post-processing of the SLM specimens used for this study, they exhibit very good tensile properties. For instance, the Young's modulus and the Yield Strength of the SLM specimens presented in Table 6.5 are comparable with the previous researcher works. In most of the research works, the Yield strength has been reported between 200 MPa to 250 MPa and in the present work, the average Yield strength is 215 MPa. Similarly, Young's Modulus reported in the previous research works were 68 GPa and it is also comparable with the presented results in Table 6.5.

However, the specimen T_{45} has the lowest elongation before failure (9.6±1.4%). One of the probable reasons was explained above. Nonetheless, more concrete reasons can be provided upon inspecting the elongation before failure and compare the results with the previous research works. The percentage of porosity is one of the main factors deteriorating the properties of SLM and has been a prevailing problem over the years. However, the porosity can be reduced by post-processing, as explained earlier. While building the T_{45} specimen, the cross-sectional is along the cutting plane X-Y is very low compared to the cross-sectional area of T_x and T_y specimen groups. Therefore, the number of voids present in the smaller cross section of the built sample along 45 degree direction is apparently higher than the other groups of specimens. This obviously would have resulted in higher porosity in the specimen group T_{45} (Figure 6.4) especially near the borderline. According to Kempen et al. (2012) and Tridello et al. (2019), the presence of borderline porosity at the beginning/end of every scan vector is due to the reduction of scan velocity near the borderline, at constant laser power density, that increase the local temperature. As illustrated in Figure 6.5, these borderline pores are higher in parts produced in the 45 degree direction, compared to parts produced in the X and Y directions. Consequently, the specimen has experienced lower elongation before failure, due to the simultaneous local microcrack propagation through the voids, resulting in early failure and poor Ultimate Tensile Strength.
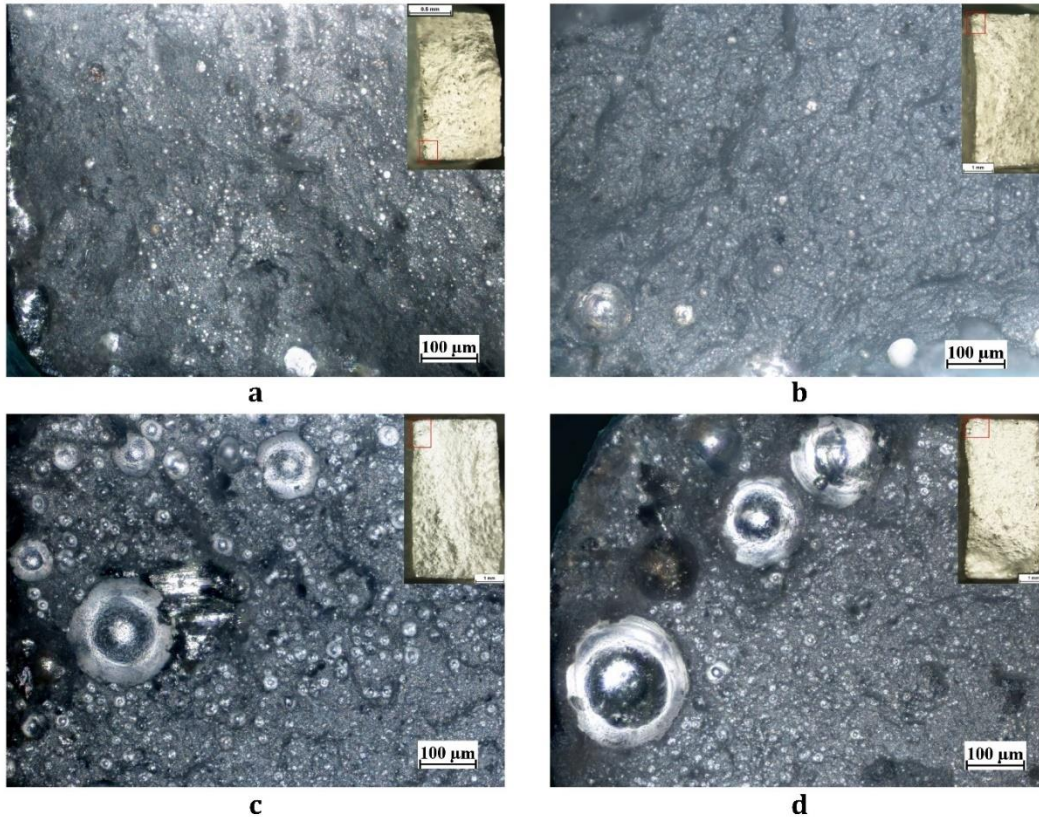
Figure 6.4. Examples of the porosity relieved on the fracture surfaces

This summarizes the tensile properties of the SLM specimens built along X, Y and 45 degree orientation with respect to the building plane. In the next subsection, the mechanical properties, critical points of failure, the crack initiation zones, and other details are deliberated using the newly developed AE parameter, the b_{AE}-value.

6.4.2.2 b_{AE}-value Results

The basis of the b_{AE}-value is taken from the linear relationship between the cumulative counts and the cumulative energy of the recorded AE signals. The discrepancies in the linearity are affected by the variation in the b_{AE}-value. The existing linear relationship between the cumulative counts and cumulative energy is presented in Figure 6.5.
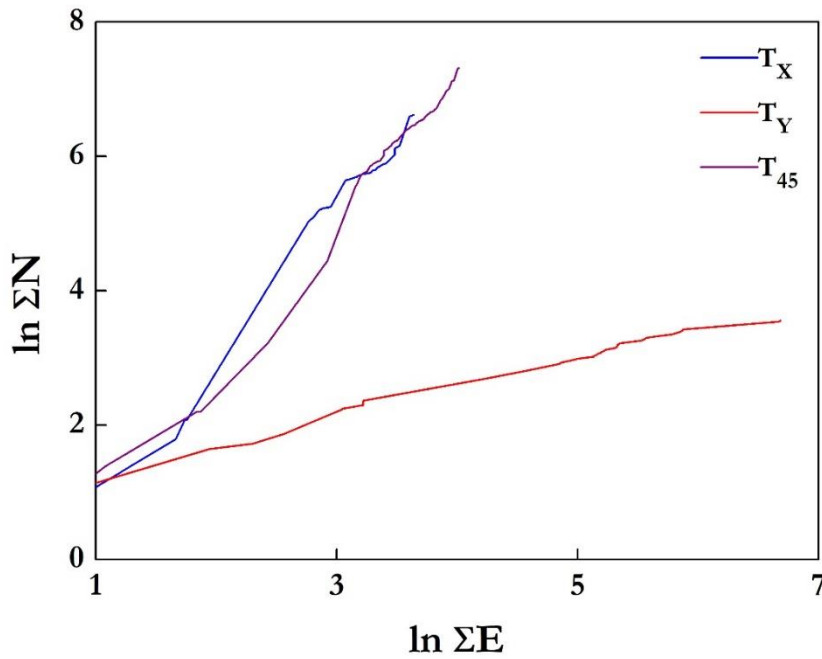
Figure 6.5. Plot between Cumulative Counts and Cumulative Energy for all three specimen groups displaying a linear relationship

The cumulative energy/cumulative counts recorded in a specimen is not only depended on its properties/fracture modes but also on how the sensor is attached to the surface of the specimen. Therefore, comparing specific values of the counts and energy between different tests is not right. This means that, a specific value cannot be assigned for the b_{AE}-value at this moment. Although the traditional b-value, which is used for monitoring the damage modes in large concrete structures has specific values for each damage modes, this has not been established in this study for the b_{AE}-value. This is because the amplitude of the recorded signal in damage modes of a metallic specimen is far lower in comparison with the AE signals generated in the concrete structures.

In this study, the linear relationship between the natural logarithms of the cumulative counts and cumulative energy is considered. Any discrepancy in the linearity could reflect in the b_{AE}-value characteristics and through the hypotheses provided in Table 6.1, the damage mechanisms can be predicted.

Using this linearity as the basic reference and from Equation (6.7), the slope coefficient b_{AE} values for the specimens are plotted and presented in Figure 6.6.
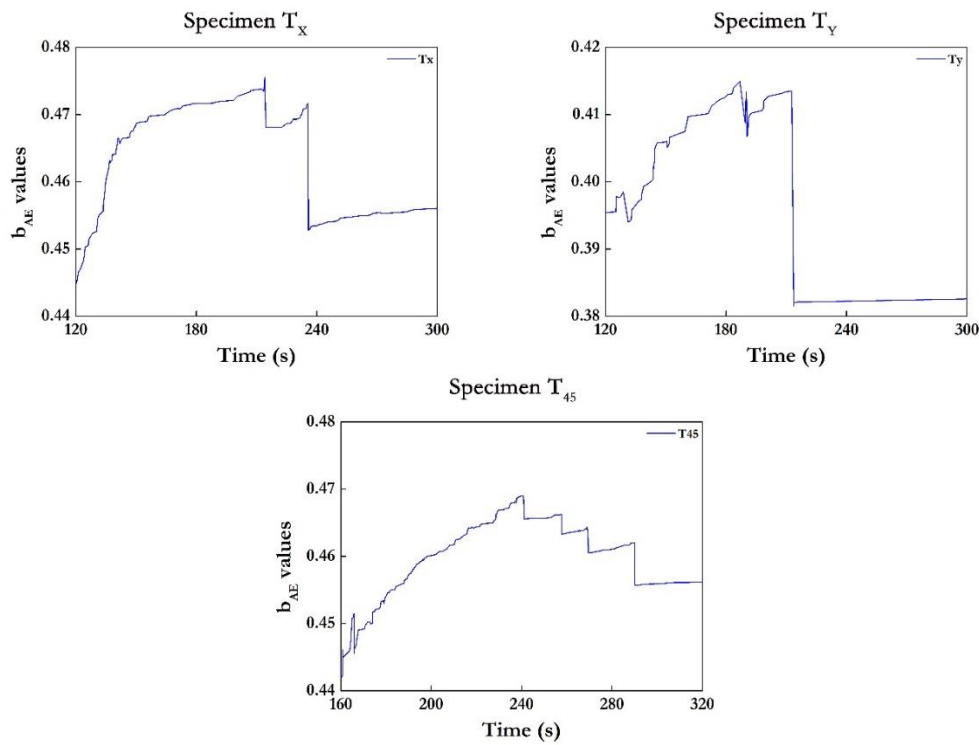
Figure 6.6. The characteristics plot of b_{AE}-value with respect to time for all three Specimens

In Specimen T_X, there is a sudden increase in b_{AE}-value for a short duration. As the hypothesis predicted, this represents the microcracking and the dislocations during the early stages of yielding. This is followed by a gradual increase in the b_{AE}-value until around 220s. At this point, there is a sudden drop in the b_{AE}-value representing major significant damage. This could possibly be the region where the crack started to propagate through one or several of the larger surface/volumetric pores. The reason why it is believed to be the initial site of crack propagation because beyond this point, there still is a gradual increase in the b_{AE}-value. The specimen T_X retains its strength even after this point. However, around 240s, the b_{AE}-value drops suddenly once again. The percentage of drop compared to the previous instance is quite high, representing a major failure in the specimen. Beyond this point, the b_{AE}-value value almost remains constant representing that the material is progressing towards failure.

In Specimen T_Y, however, there is a drop in the b_{AE}-value at a very early stage after the acoustic gap, which precedes with a sudden increase. This also coincides with the previous observation that the porosity of the specimen T_Y possibly could be higher due to the built direction, direction of melt pool boundaries and its lower elongation at break. This means that even during the microcracking stages, the presence of large pores on the volume near the melt pool boundaries resulted in the crack growth. This is followed by several stages of sudden increases and drops in the b_{AE}-value until around 205s. This instability in the b_{AE}-value represents the presence of severe pores in the volume of specimen T_Y, only in comparison with the specimen T_6. It is well known that this porosity can be reduced and controlled by optimizing the process parameters of SLM and by post processing. Nonetheless, the aim of this research work is to predict the material characteristics through the AE technique. So, the point is not considered for this research work. At the point 205s, there is a steep drop in the b_{AE}-value and beyond that point, the material starts to progress towards failure.

In Specimen T_{45}, similar to Specimen T_Y, there is a drop in b_{AE}-value at a very early stage. Nevertheless, it is followed by a gradual increase in the b_{AE}-value representing the yielding stage of the material. It must be noted that unlike Specimen T_Y, T_{45} is not affected by its defects under yielding. Around 240s however, the specimen experiences a drop in b_{AE}-value, representing major damage. This damage is severe enough, despite the low energy of AE activity, forces the material to progress towards failure. A series of sudden drops and constant b_{AE}-value can be viewed. Each of the drops represents significant major damage, which is crack propagating through the material defects.

The b_{AE}-value clearly distinguishes the different damage modes under loading of the specimen. Although the results clearly show the different damage modes, a supporting evidence to clearly identify the damage mode can be of added advantage. For this reason, the waveforms of the AE signals taken from the different damage modes of the specimen are taken and analysed in their time-frequency domain. The details are explained in the subsequent sections.

6.4.3   Validation of the AE results

For validating the AE results, the waveforms are studied in their Hilbert spectrum. The details about the Hilbert Spectrum and the various other waveform analysing techniques are provided in the Chapter 3.

In this study, the waveforms are first denoised by using Empirical Mode Decomposition (EMD): by decomposing the signals into different Intrinsic Mode Function (IMF) and reconstructing them. Details about EMD and IMF are also provided in the previous chapters. Then these signals are analysed in Hilbert Spectrum.

For each specimen group, one signal from the initial stages of load response, one from the critical point of failure and one random signal is studied. The association of frequency spectrum of the AE signals with the damage progression in metals has been a central point of debate over the years. The reason behind this debate is due to the inability to identify exactly the source of the acoustic events during a material deformation under loading. For instance, Raj et. al (1989) investigated the deformation of AISI 316 Steel at different strain rates to understand the frequency spectrum of different damage modes. Some authors have tried to identify the primary source of acoustic events, whether it is due to the dislocation motions, movement of grain boundaries or local yielding around inclusions (Vinogradov et al. (2000), Akbari and Ahmadi (2010), Rouby and Flieschmann (1978), Kiesewetter and Schiller (1976)). Abkari and Ahmadi (2010) associated the plastic deformation with the 280 kHz – 310 kHz frequency band. Raj et. al (1989) associated crack growth through micro-void coalescences to 140 kHz frequency band and yielding from 470 kHz – 660 kHz. However, these research works have used Fast Fourier Transform (FFT) for analysing the frequency band, which is a major limitation. The reason is that the AE signals are transient, unstable, nonstationary and decomposing in nature. They are not strictly sinusoidal. So, using the FFT will not provide accurate information about the frequency spectrum. For this reason, EMD is used in this research work and the HHT results are used for analysing the instantaneous frequency band.

The Hilbert Spectrum of specimens built along X-direction T_X is provided in Figures 6.8, 6.9 and 6.10. Figure 6.8 shows the Hilbert Spectrum of the AE signal taken from the initial

stages of loading, Figure 6.9 the Hilbert Spectrum of AE signal from the critical failure point/final stage and Figure 6.10 couples of random signals. The magnitude identification is indicated in the right-hand side of all the figures and the line covering the shaded mountains indicates the instantaneous frequency results.
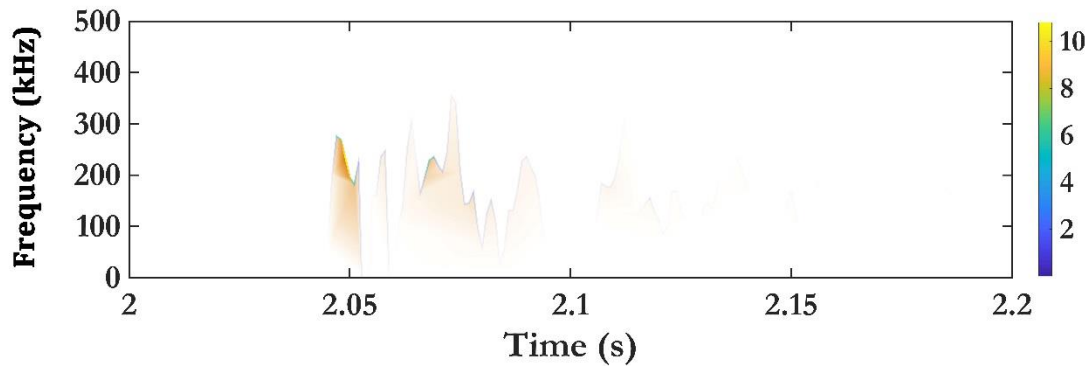
Figure 6.7. Instantaneous Frequency from Hilbert Spectrum of the Specimen T_X: Initial loading stage which has 200 kHz

The AE signals from the initial stages (Figure 6.7) represents the grain boundary movement and dislocations since it is the major damage progression mode at the early stages of loading. Thus, the AE signals generated due to the grain boundary movement and dislocations may be associated with 200 kHz. The frequency band between 150 kHz – 200 kHz is very important because it is associated with the crack growth or damage progression through micro-voids, as indicated by Raj et. al. That frequency band is observed only in the signals taken from the final stages of loading (Figure 6.8). This means that the signals with higher amplitude and has the instantaneous frequency centred at 150 kHz – 200 kHz can very possibly represent void opening.
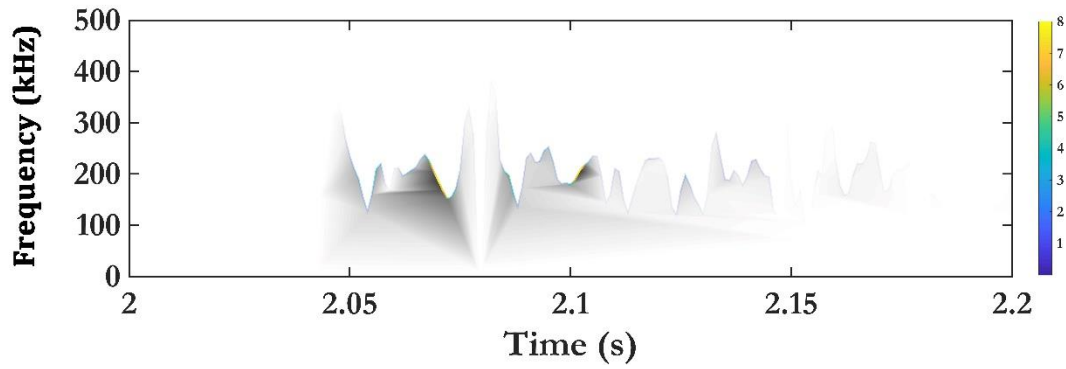
Figure 6.8. Instantaneous Frequency from Hilbert Spectrum of the Specimen T$_X$: Final Stages/Critical point of loading shows 150 kHz - 200 kHz

While studying the results of the random signals in Figure 6.9, the 150 kHz – 200 kHz frequency band can be associated with crack growth and the 200 kHz can be associated with the yielding of the material. This is very difficult to concur with since there is no previous research work which can be used for comparison. However, while comparing with the available research works, these results are compelling.
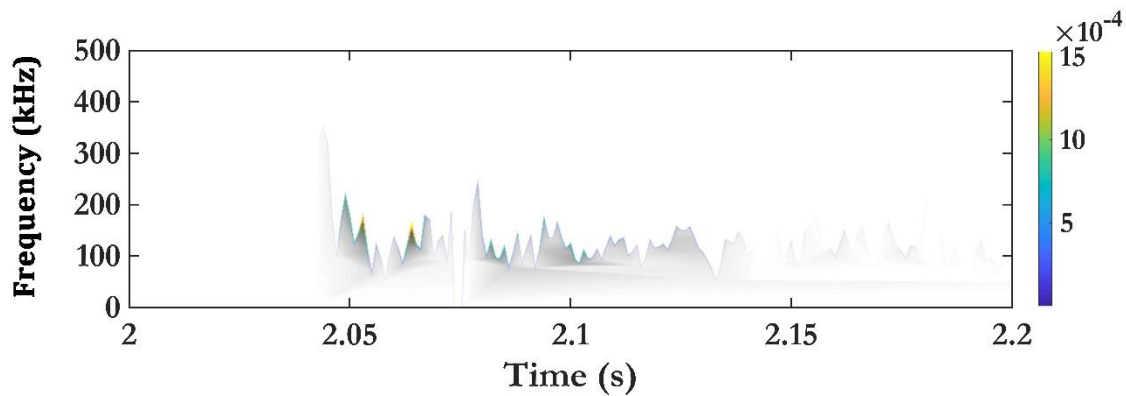
Figure 6.9. Instantaneous Frequency from Hilbert Spectrum of the Specimen T$_X$: Random Signal shows 150 kHz - 200 kHz
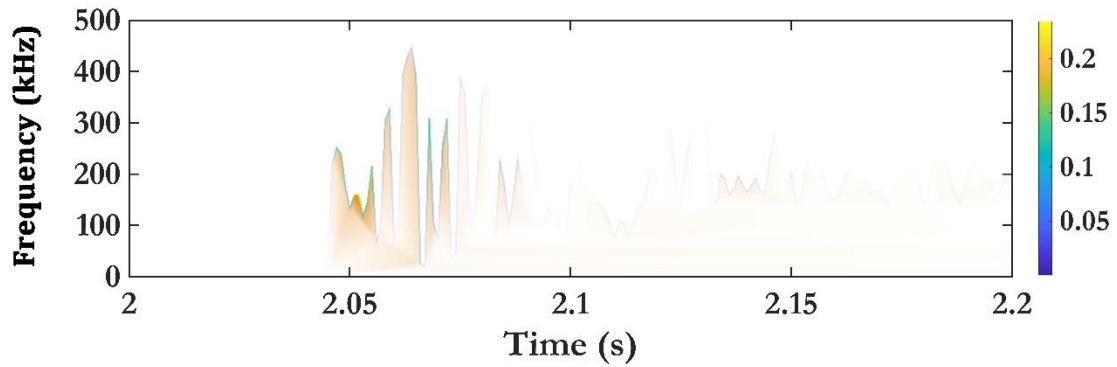
Figure 6.10. Instantaneous Frequency from Hilbert Spectrum of the Specimen T_Y: Initial Stages of loading shows 150 kHz - 200 kHz

Similarly, for specimen T_Y, the Hilbert Spectrums are presented in Figures 6.10, 6.11 and 6.12. The results of specimen T_Y are very intriguing because the frequency band 150 kHz – 200 kHz is observed in signal from the initial stages of loading in Figure 6.11. Does this mean this signal still represents the crack growth or micro-void opening? If so, why is it occurring in the very early stage (in the first cluster)? Fortunately, the answer has already been established in the previous sections. The high porosity in specimen T_Y, with respect to the other specimens, due to the melt pool boundaries distributed normally to the loading direction.
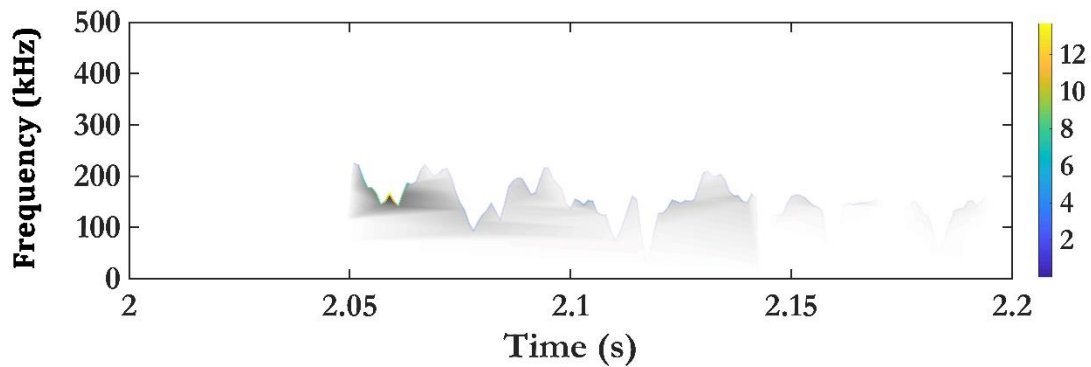
Figure 6.11. Instantaneous Frequency from Hilbert Spectrum of the Specimen T_Y: Final stages/Critical Points of Loading shows 150 kHz - 200 kHz

135

In Figure 6.11, the frequency bands are also associated with 150 kHz – 200 kHz frequency band. This necessarily means that most of the AE signals recorded in the specimen T_Y represent the opening of micro-voids. This again proves the high porosity in specimen T_Y. The random signals of Figure 6.12 represent the frequency bands 200 kHz and 250 kHz which most probably represents the yielding or grain boundary movements.
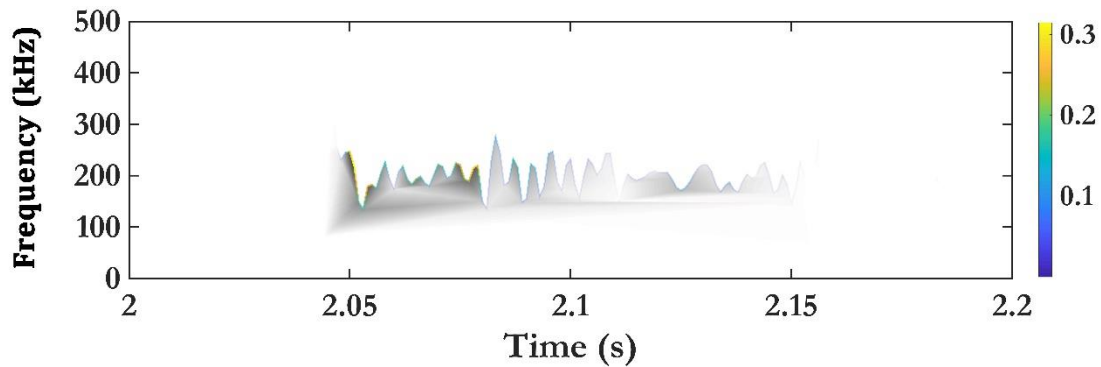
Figure 6.12. Instantaneous Frequency from Hilbert Spectrum of the Specimen T_Y: Random Signal shows 200 kHz - 250 kHz

Similarly, the frequency analysis of specimen T_{45} is presented in Figures 6.13, 6.14 and 6.15. The Hilbert spectrum results of specimen T_{45} are almost identical to the specimen T_X proving that the association of damage progression with the different frequency bands is agreeable with the available research activities. The grain boundary movement or dislocations can be identified at 200 kHz and 250 kHz in Figure 6.13 and Figure 6.15. The micro-void opening can be observed in Figure 6.14. This again agrees with the previously issued statements.
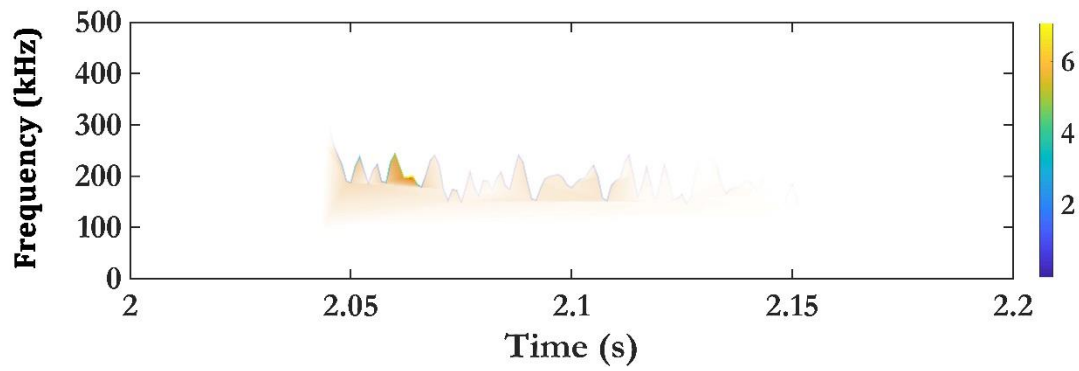
Figure 6.13. Instantaneous Frequency from Hilbert Spectrum of the Specimen T$_{45}$: Initial Stages of Loading shows 200 kHz - 250 kHz
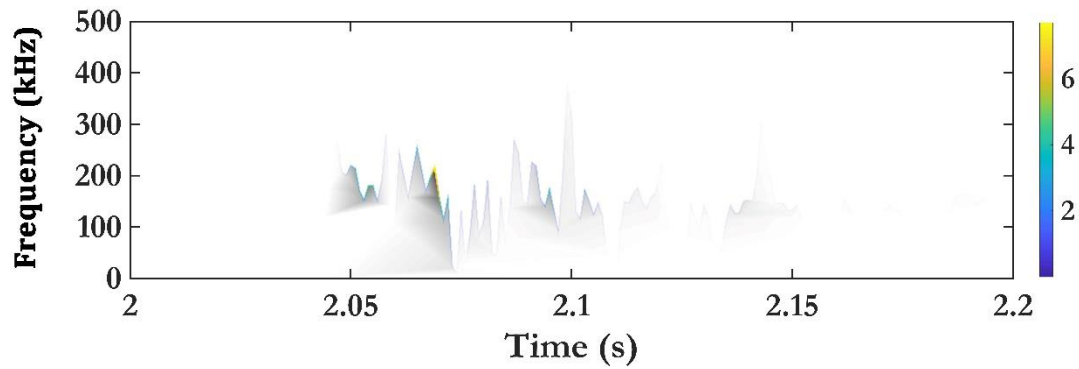
Figure 6.14. Instantaneous Frequency from Hilbert Spectrum of the Specimen T$_{45}$: Final Stages/Critical Stages of loading shows 200 kHz - 250 kHz
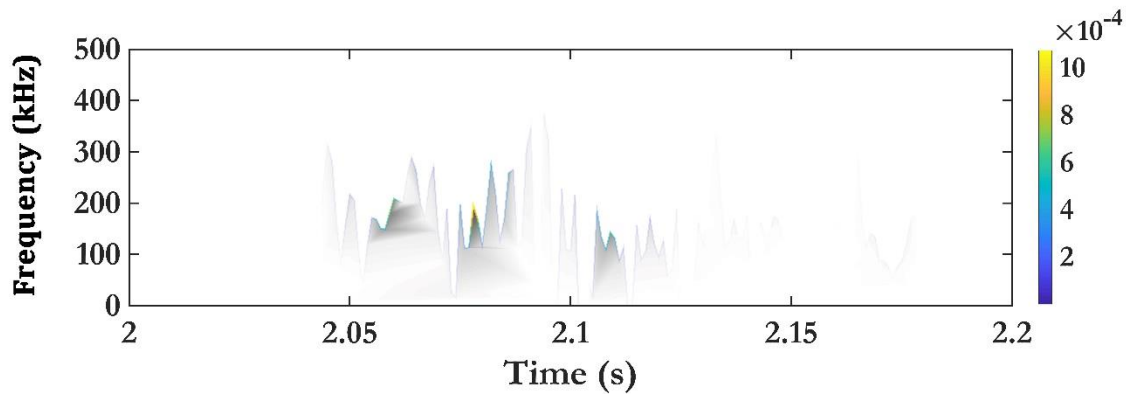
Figure 6.15. Instantaneous Frequency from Hilbert Spectrum of the Specimen T_{45}: Random Signal shows 150 kHz - 200 kHz

To summarize, the frequency band associated with grain boundary movement is around 200 kHz, yielding of material and dislocations motion or development of new dislocation motions are associated with 200 kHz and 250 kHz frequency bands. Finally, the crack growth or micro-void opening are associated with 150 kHz – 200 kHz.

This validates the b_{AE}-value at different damage modes, which can also be verified by the instantaneous frequencies of the AE waveforms recorded from each of the AE signal. Nonetheless, analysing all the AE signals in their Hilbert spectrum will be time consuming and also consumes a tremendous amount of data, the b_{AE}-value provides a global identification of the damage modes.

6.5 CONCLUSION

A new parameter, which relates the cumulative energy and cumulative counts of the recorded AE signals during an entire loading stage has been presented. The parameter is named as b_{AE}-value, the name which is given since it is comparable with the traditional b-value used in the concrete structures. A set of hypotheses has been created for comparing the b_{AE}-value trend with the different damage modes in metallic specimens. For validating the hypotheses, a series of tests are performed on SLM specimens built with AlSi10Mg as a raw material. The specimens are tested under static tensile loading and the acoustic signals are recorded during the entire loading history of the tests. The b_{AE}-value can distinguish the different damage modes in the different stages of the

138

loading. This is validated by comparing the results with the signal-based analysis of the AE signals in their Hilbert spectrum. The results show that the b_{AE}-value is powerful in identifying the damage modes. It has an advantage over the Hilbert spectrum, which is time and data space consuming. On the other hand, this newly developed b_{AE}-value can provide instantaneous results with very less necessity of data storing time.

The future scope of this newly developed parameter is to analyse it with different materials and also with different types of testing. Besides, analysing them with more in-situ damage monitoring tools can also enhance its reliability.

CHAPTER 7
NEW ACOUSTIC ENERGY BASED PARAMETER: ENERGY PER COUNT

Acoustic energy represents the total energy of an acoustic waveform above the acquisition threshold. Since its significance was introduced by Harris and Bell (1977), the acoustic energy has been used by several researchers over the years for the mechanical characterization of materials. This chapter highlights the importance of acoustic energy in mechanical characterization and identification of critical points of failure. Experimental validation is provided for the same. But the main objective of this chapter is to introduce a new parameter called Energy per Count, which is used for two purposes in this research work. The new parameter Energy per Count is used for characterizing the damage modes in structural materials and it is also used as an indicator for selecting representative acoustic emission events for waveform analysis. This chapter presents experimental results for verifying the application of this newly developed parameter.

7.1 INTRODUCTION

For a continuous acoustic waveform, the acoustic energy can be described as the square of the amplitude of the continuous signal. It is necessary to highlight how the acoustic energy is measured in the data acquisition system. A schematic representing how the acoustic energy is measured is presented in Figure 7.1. Firstly, the acoustic signal is squared using a squaring circuit, which is then followed by measuring the area under the curve of the squared signal. It is important to emphasize at this point that the acoustic energy is only the measure of the area under the curve above the acquisition threshold.

For a continuous signal with a frequency f and a constant amplitude V_0, the amplitude of the signal can be expressed as,

$$V_t = V_0 \sin 2\pi f t \tag{7.1}$$

where, t is the total duration of the signal. The energy rate of the signal $\dot{U}$ can be expressed as,

$$\dot{U} = \int_0^t V^2(t)dt = V_0^2 \int_0^t \sin 2\pi ft \, dt \propto V_0^2 \propto (\text{RMS Voltage})^2 \qquad (7.2)$$

If the signal is similar to the burst type signals, as in AE signals, it is assumed that the signal is a damped sinusoid. The voltage to the counter can be expressed as,

$$V_c = V \, e^{-t/r} \sin 2\pi ft = G_n C e^{-t/r} \sin 2\pi ft \qquad (7.3)$$

where, r is the decay time of the acoustic emission signal, C is constant and G_n is the gain of the amplifier chain to the counter.
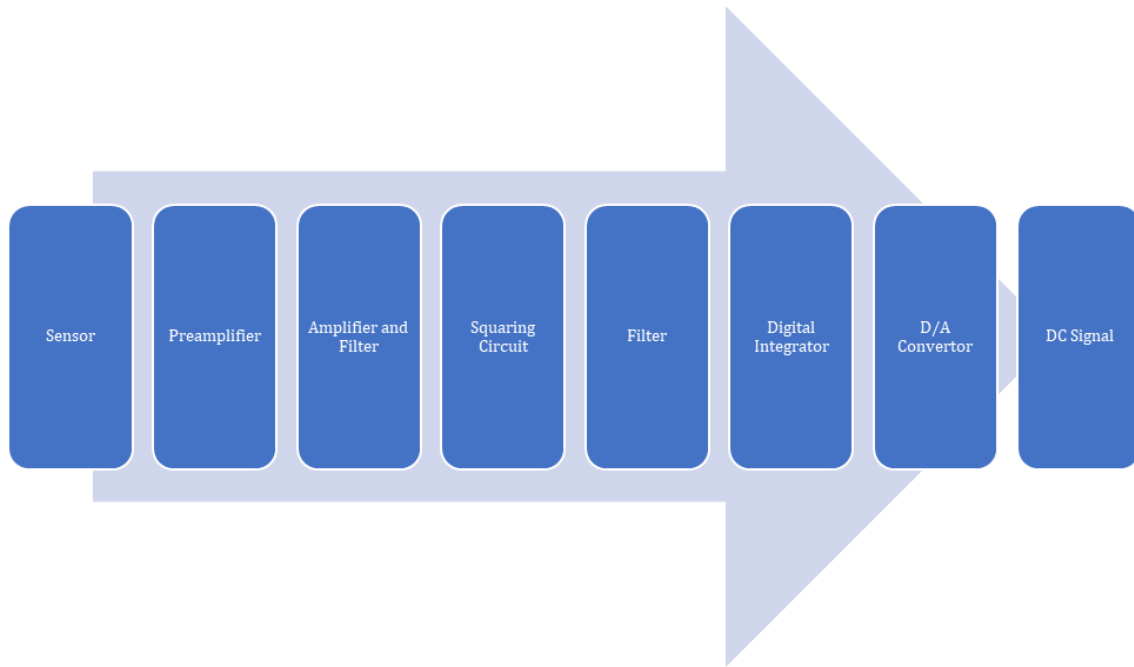
Figure 7.1. Schematic Representation of measuring Acoustic Energy

The acoustic energy of the waveform which is calculated is normally used as cumulative energy. Many researchers have found a strong relationship between the cumulative energy of the recorded acoustic events over a loading history with the cumulative counts. This has been explored to identify the critical points of failure, crack growth rate and residual life of the material. In the recent years, some researchers have attempted to establish a relationship between the acoustic energy and the strain energy of the material. In Chapter 6 of this thesis, a relationship between the acoustic parameters, cumulative

141

counts and energy has been used for mechanical characterization. Before introducing the new parameter in this Chapter, it is essential to highlight the available methods of using acoustic energy and how it has been experimentally used in this thesis work.

In the next section, the most common way of using acoustic energy is experimentally validated. The cumulative acoustic energy is used for identifying the critical points of failure in Carbon Fiber Reinforced Plastic (CFRP) composites. Following that, the sentry function, which relates the acoustic energy with the strain energy has been explained and the function is validated for mode I delamination in CFRP composites. After these two sections, the new parameter named Energy per Count has been introduced. This parameter is used for two purposes: damage mode assessment and selection criterion for waveform analysis. This concludes this chapter.

7.2   CUMULATIVE ENERGY FOR IDENTIFYING CRITICAL POINTS OF FAILURE

In quasi-brittle materials such as concrete structures, the Acoustic Emission (AE) signals are accumulated during the loading. During this period of accumulation, there will be a period of idle time where there will be no acoustic activities recorded. This period of no acoustic activity is called Acoustic Gap. Once this accumulation reaches a certain level, when the material is strained/deformed beyond a certain limit, the sudden burst of AE signals is generated. These signals are high-level AE signals with larger amplitude and greater acoustic energy.

In other structural materials such as metals or Fiber Reinforced Plastics (FRP), the acoustic gap is very narrow or almost non-existing. Nonetheless, there will be a period of time where the straining of the material occurs and very low-level AE signals are generated. These signals carry very little energy. This forms the basis for analysing the critical points of failure using cumulative acoustic energy. By measuring the total acoustic energy liberated during each stages of loading, the critical points of failure such as crack initiation, interlaminar crack growth, void nucleation and other critical failures can be identified.

For validating the usefulness of the critical points of failure, the cumulative acoustic energy along with the cumulative counts are used in this work.

7.2.1 Experimental Validation of the usefulness of Cumulative Acoustic energy

Two different configurations of CFRP specimens are used for this study: Single Lap Shear (SLS) and Joggled Lap Shear (JLS). Three specimens of each configurations are used for this study. Tensile loading is applied to the specimens and the acoustic activities are recorded through a pair of piezoelectric sensors.

For preparing the specimens, a prepreg fabric laminate with ER450 epoxy matrix (SAATI CIT CC206 ER450 43%) is used. The carbon fiber configuration is stitched with layers of fibers overlapping one other. The nominal ply thickness is 0.244 mm. The composite laminates for both JLS and SLS specimens (Figure 7.2) are cured by the autoclave method. Other details such as number of plies and geometry of the adherends of JLS and SLS can be found in Table 7.1 and Table 7.2, respectively. The specimens are prepared by following the ASTM D5868–Standard Test Method for Lap Shear Adhesion for Fiber-Reinforced Plastic (FRP) Bonding. The adhesive used for this study has a shear strength of 25 MPa and a peel strength of 65 MPa. The thickness of the adhesive coated and the area of the adhesive coated are also provided in Tables 7.1 and 7.2. The adhesive is cured at temperature of 65 °C for 1 hour, then the specimens are tested after 5 days.
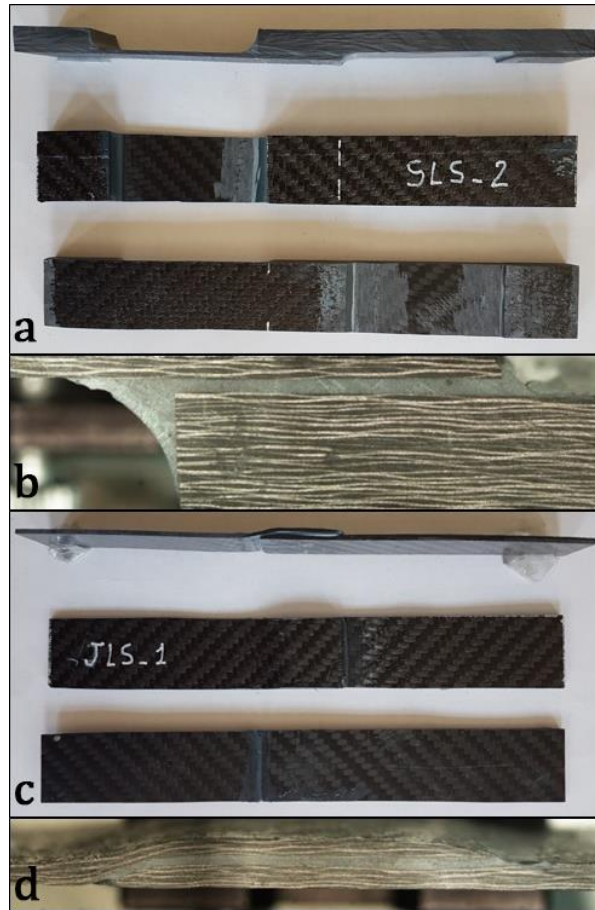
Figure 7.2. Configuration of (**a**) SLS specimen, (**b**) joint overlap of SLS specimen, (**c**) JLS specimen, (**d**) joint overlap of JLS specimen

Table 7.1. JLS specimens Geometry and Characteristics

Flat Adherend			
Length	**Width**	**Thickness**	**No. of Plies**
Mm	*mm*	*mm*	
101.6	26.09	2.0	8
Curved Adherend			
Length	**Width**	**Thickness**	**No. of Plies**
Mm	*mm*	*mm*	
101.6	26.09	1.5	6
Overlapping Region (Adhesive)			
Length	**Width**	**Thickness**	
Mm	*mm*	*mm*	
26	26.09	3.67	

Table 7.2. SLS specimens Geometry and Characteristics

Upper Adherend			
Length	**Width**	**Thickness**	**No. of Plies**
mm	*mm*	*mm*	
101.6	25.33	1.3	5
Lower Adherend			
Length	**Width**	**Thickness**	**No. of Plies**
mm	*mm*	*mm*	
101.6	25.33	6.4	26
Overlapping Region (Adhesive)			
Length	**Width**	**Thickness**	
mm	*mm*	*mm*	
26	25.33	8.5	

The tension is applied to the specimens under displacement-controlled mode at a speed of 13 mm/min, in accordance with the ASTM D5868 standard. The tests are carried out in the INSTRON servo-hydraulic testing machine with a maximum load capacity of 100 kN. For recording the acoustic activities under loading, two narrow-band general purpose AE sensors are used: R30a (Physical Acoustics, MISTRAS Group, NJ, USA). The sensor has an operating range of 150 kHz to 400 kHz and a resonant frequency of 300 kHz. The reason for selecting the narrow band sensor is because in CFRPs, the recorded AE signals mostly are under the frequency band of 400 kHz. To avoid unnecessary noise, the narrow-band sensor is selected. For the same purpose, the sampling rate was set as 1 MSPS (mega samples per second). The threshold of AE acquisition was set at 35 dB and the recorded signals were amplified by 40 dB through a 2/4/6 AE (Acoustic Emission) preamplifier.

The sensors are placed at 40 mm either side from the centre of the adhesive overlapping region. Silica gel is interposed between the surface of the sensor and the specimens, in order to improve the coupling of the elements. This location is selected based on the length of the overlapping region and to record the AE signals produced within the overlapping region. The AE signals recorded beyond the adhesive overlapping region are discarded. In the fractured specimen, not many damages are observed except in the area covering the overlapping adhesive layer. The surface of the specimen post rupture has been analysed by means of an optical microscope NIKON SMZ800. Moreover, the region

of the adhesive and the fractured surfaces have also been studied after the shearing failure.

Table 7.3. Calibration table for the propagation of signals in JLS and SLS specimens

Distance from the sensor (mm)	JLS Specimen	SLS Specimen
	Amplitude (dB)	
1	98	98
2	98	98
3	98	98
4	98	97
5	98	96
6	97	94
7	97	92
8	96	91
9	95	89
10	95	88
11	93	87
12	93	87
13	92	87
14	92	87
15	90	86

The distance from the sensor to the acoustic source affects the propagation of the AE signals. This can result in the attenuation of the recorded AE signals. To avoid this attenuation, the AE sensors are calibrated for the attenuation in signal with respect to the distance from the sensor. A pencil break tests are performed, which normally produces a peak amplitude of 95 dB to 99 dB at varying distances from the sensor on the SLS and JLS specimens. The table of this calibration was then fed to the PAC PCI 2 data acquisition system, which automatically calibrated the attenuation of the signal. The calibration table for JLS and SLS specimens are presented in Table 7.3.

7.2.2 Results and Discussions

7.2.2.1 Mechanical Test Results

The bonding characteristics of the JLS and SLS specimens are tested by applying tensile load under displacement-controlled mode as per the ASTM D5868 standard. When the tensile load is applied, the entire load is distributed through the adhesive region. It has

been reported by several researchers with solid evidences that the thickness of the adherend does not have a significant role in the distribution of load under shearing. There could also be more than one peak load value, with each of them contributing to the damage characteristics or the bonding characteristics of the specimen.

Table 7.4. Damage Characteristics in JLS and SLS specimens

Specimen	Peak Load *(kN)*		Specimen	Peak Load *(kN)*	
	Initial Rupture	Final Rupture		Initial Rupture	Final Rupture
JLS 1	6.02	4.09	SLS 1	7.05	7.75
JLS 2	2.67	3.89	SLS 2	7.06	5.96
JLS 3	3.86	5.57	SLS 3	5.93	7.36
Mean	*4.18*	*4.52*	*Mean*	*6.78*	*7.02*
Std. Dev.	*1.70*	*0.92*	*Std. Dev.*	*0.75*	*0.94*

Figure 7.3 shows the load vs. time curve for the specimens. In this work, more than one peak can be observed in the load vs. time curve for both specimens. It must be noted that although there are several small peaks observed in both JLS and SLS specimens in Figure 7.4, the initial peak load is considered as the initial rupture point and the final peak load is considered as the final rupture point. Since these mechanical results provide only a limited amount of information on the damage characteristics, the acoustic emission results have been used in the subsequent sections. Table 7.4 shows the mechanical characteristics of both JLS and SLS specimens.

The first major observation from the mechanical test results is the varying peak load values of the same specimen group, both in JLS and SLS. This is common when it comes to the practice of adhesive bonded specimens because the bond quality is not only determined by the curing characteristics, the thickness of the adhesive and other mechanical characteristics, but also on the efficiency of the user who handles the adhesives. The adhesives are normally mixed using a hand mixer rather than a mechanical controller owing to its high viscosity and requirements. Thus, it is inevitable that a considerable amount of difference can be observed between the adhesive bonded specimens of the same group. This is the reason why there is a difference in both the peak loads at initial and final ruptures and they are not similar between the same specimen

group (refer to Figure 7.3 and Table 7.4). Furthermore, under this view, an increase in the number of test specimens would increase the accuracy of the evaluation of the scattering but it will not reduce the latter.
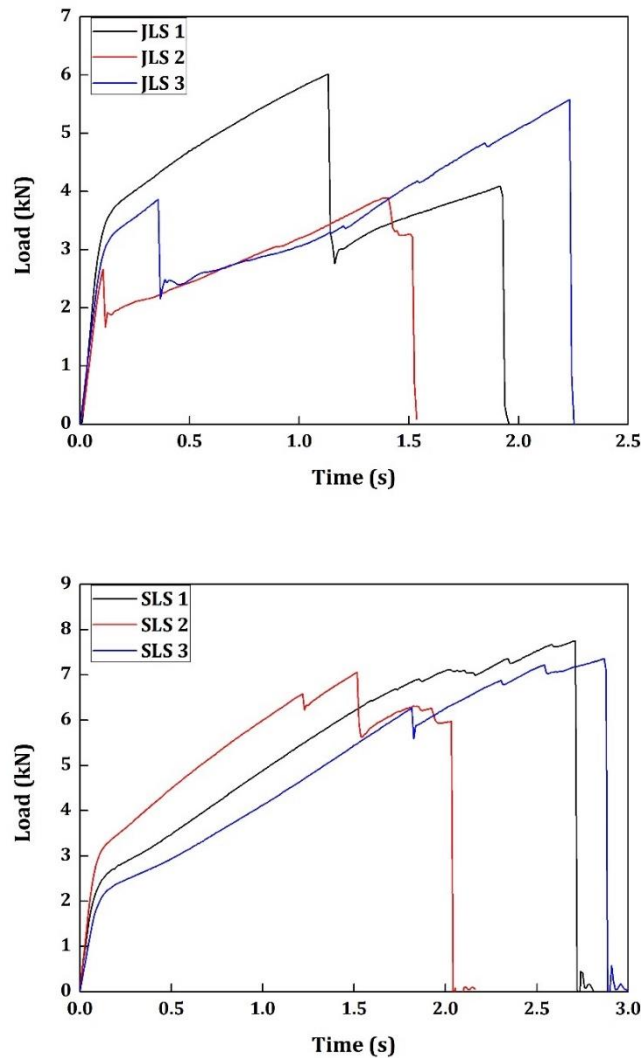
Figure 7.3. Load vs. time curve: (**a**) JLS Specimens; (**b**) SLS Specimens

The thickness of the adhesive carries the majority, if not all the load. In the SLS specimens, owing to their larger thickness than JLS specimens, higher peak loads are accounted for. The average peak load at the initial rupture in SLS specimens is 6.78 kN, while the JLS specimens have an average peak load of 4.18 kN. Similarly, at the final rupture stage, SLS specimens have an average peak load of 7.02 kN, while JLS specimens have 4.52 kN. In

148

SLS specimens, the load is carried along the cross-sectional area of the adhesive region. However, in the JLS specimens, the shear strength of the specimen is also governed by the end curvature effect. This is explained by Taib et. al. (2006) in their research work. Single lap joints, when loaded, transfer most of the load in shearing. Joggled lap joints, however, transfer most of the load in peeling. This is also the reason why the joggled lap joints have lower displacement when compared to the single lap joint specimens. The joggled joints suffer lateral deflections rather than shearing, which result in inducing high peel stress on the neutral axis. This results in the crack initiating at the joggled knee of the curvature region. This will result in low peak loads, which are observed in the presented results (see Table 7.4 and Figure 7.3). Similar results have been presented by Kishore and Prasad (2012), who also addressed the effect of the eccentricity of the joggle in the strength of the joggled lap specimens. It has been addressed by both Taib et. al (2012) and Kishore and Prasad (2012) that the joggled lap specimens will have lower strength in comparison with the single lap joints. The same has been observed in this work as well.

7.2.2.2   *Acoustic Emission Results: Cumulative Energy*

The damage characteristics or the mode of failure in the adhesive bonded specimens cannot be explained through the mechanical characteristics. Furthermore, predicting the failure at an early stage is also not easy by studying only the mechanical characteristics. It can be explained by the acoustic emission characteristics. The load vs. time curve of the JLS specimens is plotted over the cumulative counts and the cumulative energy of the AE recorded. It is presented in Figure 7.4. Similarly, the SLS specimens are presented in Figure 7.5.
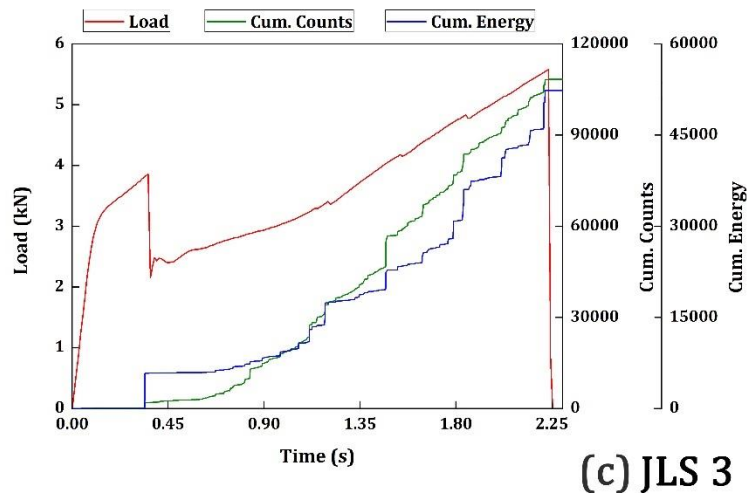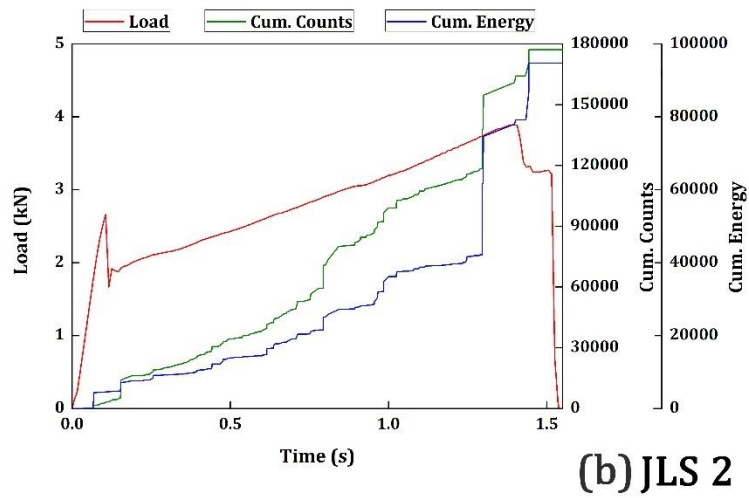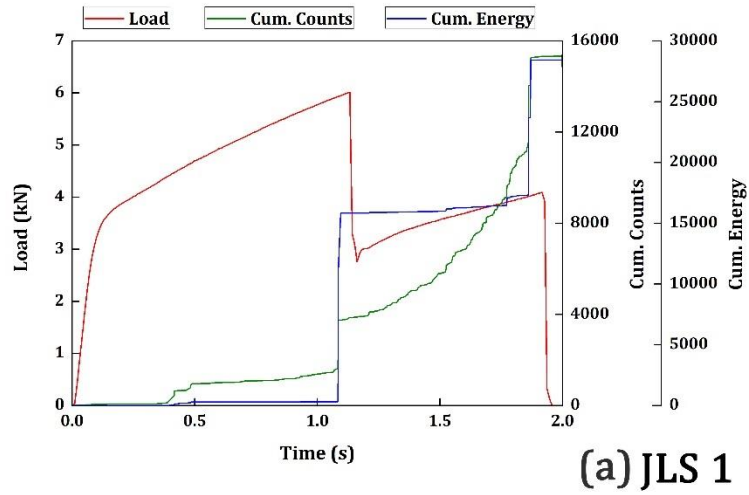
Figure 7.4. Load, cumulative counts, cumulative energy vs. time: (**a**) JLS 1; (**b**) JLS 2; (**c**) JLS 3

In Figure 7.4, it can be observed that whenever there is a load peak in the load vs. time curve in any of the JLS specimens, the cumulative counts and cumulative energy show a steep increase. The initial load drops in all JLS 1, JLS 2 and JLS 3 at 1.1 s, 0.1 s and 0.35 s, respectively, have been associated with the increase in cumulative counts and cumulative energy. Similarly, at the final stages of loading prior to failure 1.8 s, 1.35 s and 2.25 s, respectively, for JLS 1, JLS 2 and JLS 3 are also associated with the increase in cumulative counts and energy. However, there are some instances, particularly around 1.2 s in the JLS 2 specimen, where the cumulative counts and energy increased unexpectedly without any change in the load vs. time curve.

In JLS 1 specimen, the cumulative energy increases steeply around 1.1 s duration and it remains almost constant until the specimen reaches its final rupture region. Nonetheless, the cumulative counts kept increasing gradually beyond the 1.1 s duration and the slope took a steep increase as the material reaches failure. This means that a large number of counts have been recorded with very low energy from 1.1 s duration to the final failure. In a non-linear material, such as plastics or composite materials, the large counts with low energy represent the matrix cracking. The ratio between the cumulative energy and the cumulative count varies at different damage modes in a material. When this ratio exhibits a very low value, it can be said that the energy is low with large counts. On that basis, this can be attributed to the matrix cracking. Brittle fractures such as interlaminar crack growth and fiber breakage release large energy acoustic events, which are responsible for the initial and final ruptures. Between the stages of the initial failure and the final failure in the JLS 1 specimen, the material has experienced only matrix cracking. This indicates that shearing has occurred in the adhesive region rather than peeling which attributes to the low-energy acoustic events. This indicates that the JLS 1 specimen has carried more load before failure than the JLS 2 and JLS 3 specimens due to the shearing mode of failure. This could be one of the reasons why the JLS 1 specimen has a higher peak load when compared to JLS 2 and JLS 3.

In the cases of JLS 2 and JLS 3, they have similar load vs. time, cumulative counts and energy patterns. Both these specimens experienced the initial rupture at a very early stage, 0.1 s for JLS 2 and 0.35 s for JLS 3. The cumulative counts and energy have also

increased steeply at these time periods. Beyond that point, the cumulative counts and the cumulative energy increase almost linearly with one another. This represents the delamination in the adhesive bonded region. The adhesive peeling is occurring at this stage, which is the reason for the simultaneous increase in the counts and energy. While reaching the final stage of failure, JLS 2 and JLS 3 have probably experienced fiber breakage which is indicated by the sudden increase in counts and energy near the final rupture region.
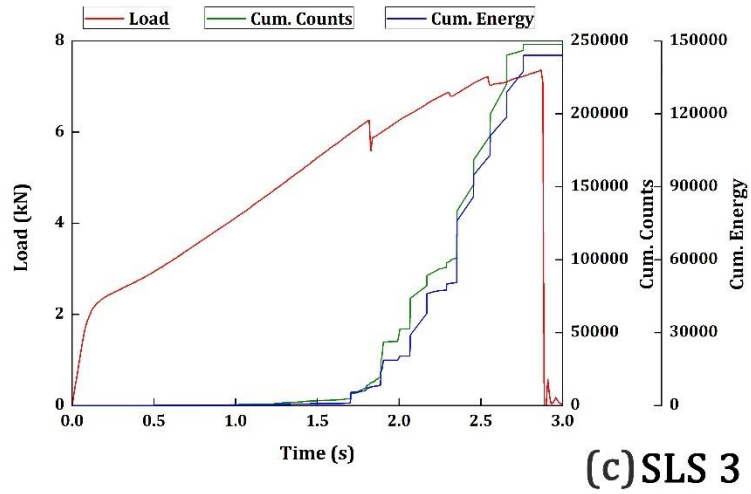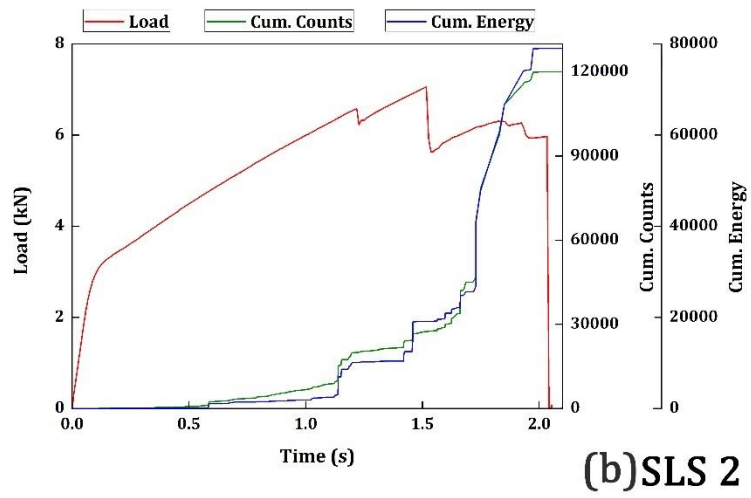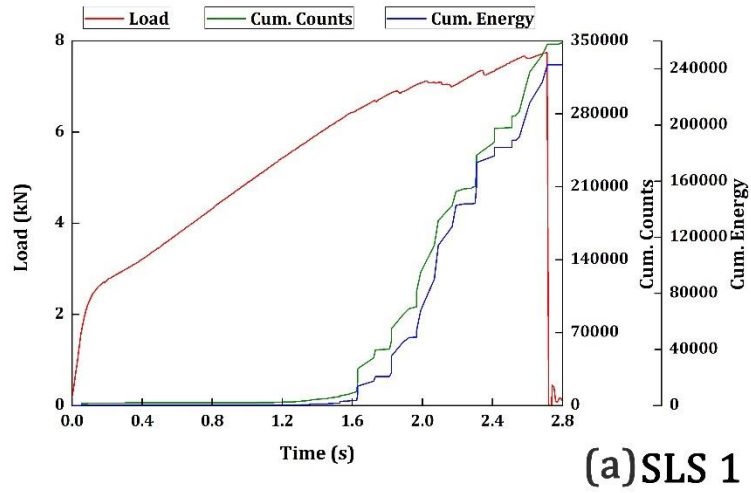
Figure 7.5. Load, cumulative counts, cumulative energy vs. time: (**a**) SLS 1; (**b**) SLS 2; (**c**) SLS 3

153

While looking at Figure 7.5, all the three specimens have almost similar patterns in terms of load vs. time, cumulative counts and energy. However, the simultaneous increase in the counts and energy of the SLS specimens must not be compared or to be confused with the JLS specimens. Although in both the cases the cumulative counts and cumulative energy increased linearly, the slope of the increment is entirely different. The slope of the increment in SLS specimens is higher than the JLS specimens. Therefore, they do not represent the same damage mode although it looks similar. In the SLS specimens, the cumulative counts and energy are very low during the initial stages of loading until the specimens have suffered their initial rupture. In the SLS specimens, most of the load is distributed in shearing and these low-energy and low-count AE signals indicate the shearing occurring in the adhesive region. AE signals connecting to fiber breakages and transverse cracks growth release acoustic data with higher energy and lower counts, owing to their lower order symmetric nature. Since the energy and counts recorded are low during these stages, these signals are higher order asymmetric in nature that could be connected only to shearing phenomena. Beyond the region of the initial rupture, in all three SLS specimens, the cumulative counts and energy start to increase simultaneously until they reach the final failure. This indicates that the cumulative counts and energy were very low until the crack opens in the adhesive. Generally, the crack opens at the adhesive and adherend interface, which is governed by the geometry of the overlapping area. Once the crack had opened, due to the brittle nature of the adhesive, it progressed faster through the thickness of the adhesive. This interlaminar crack growth always generates higher counts and higher energy. This pattern continued until the specimens failed at the final rupture.

7.2.2.3   *Fractographic Analysis*

The different damage modes are theoretically explained in the previous section using the cumulative acoustic energy and counts. For a definite proof, the ruptured surfaces of the JLS and SLS specimens are analyzed fractographically. To confirm the brittle failure of the adhesives in the SLS specimens and to identify the peeling and fiber breakage failure in JLS specimens, the fractured surfaces are observed under optical microscope. The fractographic results of specimen JLS is presented in Figure 7.6.

154
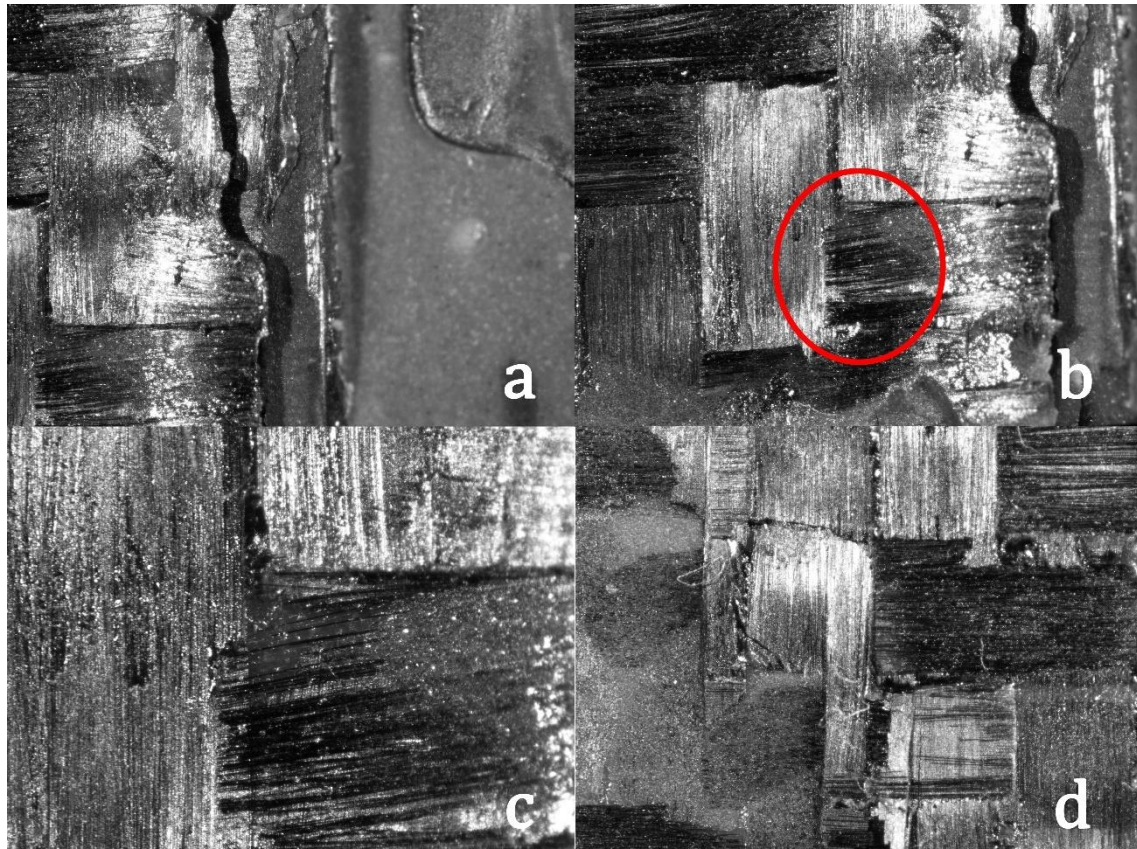
Figure 7.6. Fractographic analysis of JLS specimens. (**a**) Peeling at the knee of adhesive; (**b**) Debonding of laminates; (**c**) Ruptured Fiber; (**d**) Fiber/Matric Debonding

In Figure 7.6(a), the adhesive layer peeling off at the knee of the curvature in the joggled overlapping region can be observed. The debonding of the laminates along the applied adhesive layers can be viewed in Figure 7.6(b). The adhesive not only peeled off from the lamina but also inflicted fiber/matrix debonding in the same lamina. Figure 7.6(c) is the zoomed view of the circled region in Figure 7.6(b). From Figure 7.6(c), the ruptured fiber at the end of the lamina can be observed. Figure 7.6(d) shows the presence of more fiber/matrix debonding and fiber breakage near the knee of the adhesive joint. This consolidates the explanations provided in the previous section regarding the failure modes by acoustic emission parameters.

Similarly, the optical images of SLS specimens are presented in Figure 7.7. Figure 7.7(a) shows the complete lack of matrix/fiber debonding in the area where the adhesive is applied. The fibers are left unharmed in the fractured region of the adhesive. The

adhesive has delaminated from the outermost ply, but it did not affect the fiber/matrix integrity. Figure 7.7(b) shows the brittle fracture and the direction of the crack grew along the width of the adhesive under loading. Figure 7.7(c) shows the fiber breakage at the end of the specimen. Figure 7.7(d) is the zoomed image of the ruptured fibers. So, the fiber breakage has occurred in the SLS specimens, nonetheless, only at the edge of the lamina.
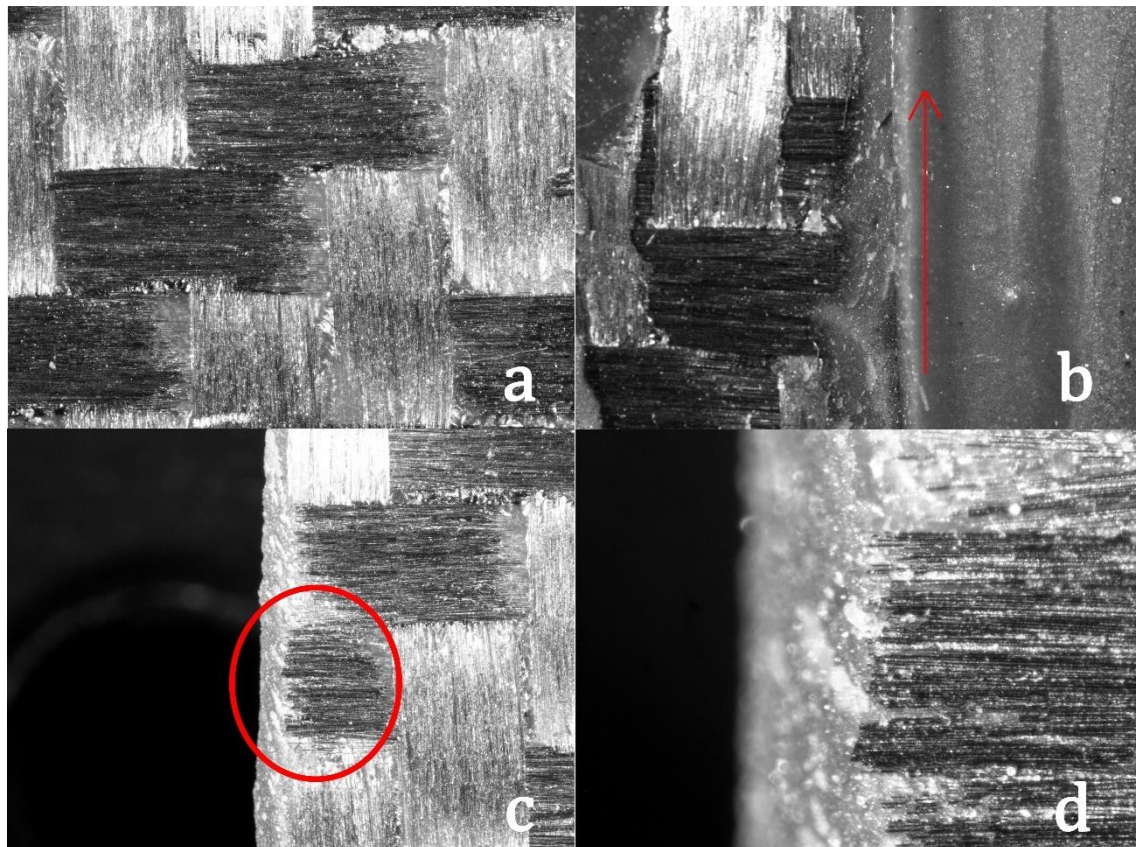
Figure 7.7. Fractographic analysis of SLS specimens. (**a**) Lack of Fiber/Matrix debonding; (**b**) Direction of cracking growth along the length of adhesive; (**c**) Fiber breakage; (**d**) Close in view of fiber breakage

Therefore, by comparing Figures 7.6 and 7.7, it can be concluded that the crack growth initiated at the knee of the joggled lap in the JLS specimens, which in turn results in the peeling. The peeling also has induced the debonding between the fiber and matrix in the area where the adhesive is applied. However, in SLS specimens, the crack opened in the

adhesive region and travelled through the width of the specimen resulting in a brittle failure.

The fractographic results are sufficient to prove the damage modes explained in the acoustic emission result sections. This shows the efficiency of the acoustic energy, particularly the cumulative acoustic energy, for characterizing the damage modes and efficiently identifying the critical points of failure.

In the next section, a function which relates the acoustic energy with the strain energy is explained along with the experimental validation of the function.

7.3   SENTRY FUNCTION: ACOUSTIC ENERGY AND STRAIN ENERGY

One of the most challenging tasks is to relate the acoustic energy with the fracture process, especially in FRP. The AE technique is very intricate due to the transient nature of the waves that are analyzed. The number of factors affecting the generation and propagation of these AE waves are numerous. It is very difficult to relate the fracture process in a structural material with the acoustic emission. One of the successful attempts in relating these two is the Sentry function. Zucchelli and Dal (2004) had considered the ratio of strain energy produced in the material under loading and the cumulative acoustic energy to deeply analyse the relation between the material properties and the energy released by the acoustic events. Similar research work was carried out by Cesari et al. (2007) in CFRP specimens. However, it was Minak and Zucchelli (2008) who standardised this relation by giving it a name 'Sentry Function'.

Sentry function relates the Acoustic and Mechanical Information of the material under loading. It is the logarithm of the ratio between the Cumulative Acoustic Energy (E_a) released to the Strain Energy (E_s) stored by the material under loading. The Sentry function $S(x)$ is given by the equation,

$$S(x) = \ln \frac{E_s(x)}{E_a(x)} \tag{7.4}$$

where, x usually represents the test-driving variable, displacement or strain.

When the sentry function is plotted against the displacement, the resulting curve is mostly discontinuous and having different patterns. These patterns can be termed as acoustic emission domains. Each domain constitutes a curve of a unique function, from which the relation between the strain energy and the cumulative acoustic energy can be established. The different functions/acoustic sub-domains are presented in Figure 7.8.

In Figure 7.8, the function P_I has an increasing trend, albeit with a decreasing slope owing to the fact that the stored strain energy will be limited with the increase in damage progression. This leads to the increase in E_a. Thus, the function P_I represents the damage progression in the material within which the material can store strain energy despite the damage progression. This trend will last long until the stored energy attains its limits.
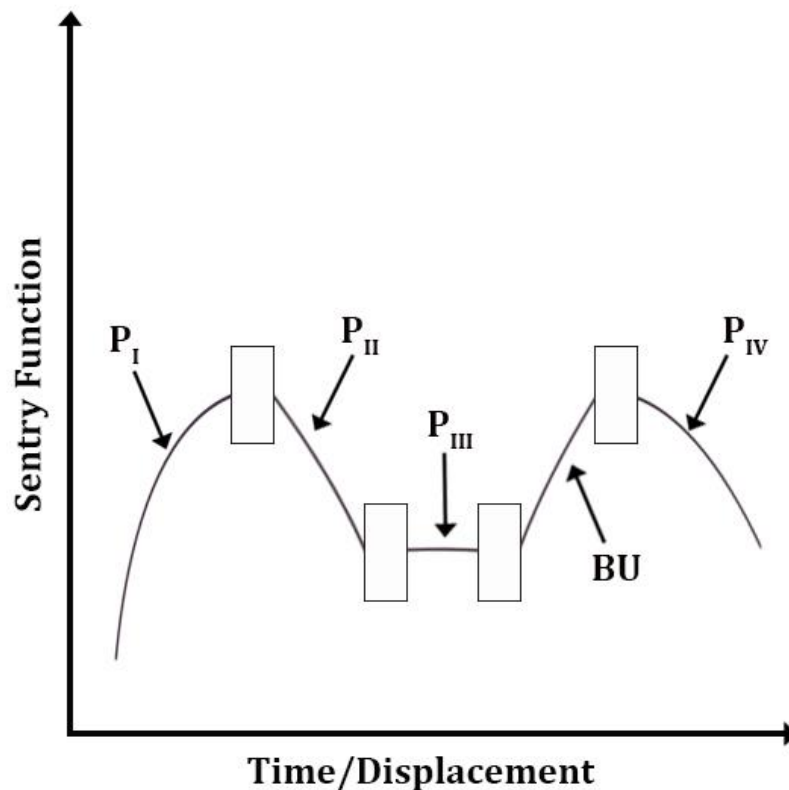
Figure 7.8. Sentry function domains

During a major damage progression, which will result in the sudden increase in E_a, the sentry function drops suddenly. The function P_{II} represents a sudden and transient

158

damage progression in the material. However, it still is possible to observe the P_I function following this sudden drop in sentry function. Because, not all the sudden damage in the material will lead to a catastrophic failure.

The function P_{III} indicates a progressive phase in which the strain energy is stored in the material, nonetheless, is equivalent to the continuous damage progression. This is the reason for the linearity in the P_{III} function. It is possible to observe the P_{II} function following the P_{III} but not the P_I function. Because when the material starts to experience a continuous damage progression, the strain energy has already reached its limits and the material starts to reach the inevitable failure.

The function P_{IV} is a gradual decrease in the sentry function. This indicates that the material had lost its capability to store strain energy and is about to failure. This function does not necessarily need to have any sudden drop as the progressive failure is occurring in the material. This function may follow either P_{II} or P_{III} and indicating the material beyond conserving energy.

This method successfully relates the mechanical information with the AE results as it avoids the necessity of essential processing or an in-situ monitoring.

7.3.1   Experimental Validation of Sentry Function

For validating the efficiency of the Sentry function, the AE data recorded from the mode I delamination test on DCB specimens are used. The materials and the testing methods are the same as the DCB tests explained in Chapter 3, Section 3.6.2.1. The cumulative acoustic energy is measured from the recorded AE data and the strain energy is calculated from the load-displacement curve. From this information, the Sentry function $S(x)$ is calculated using the Equation (7.4).
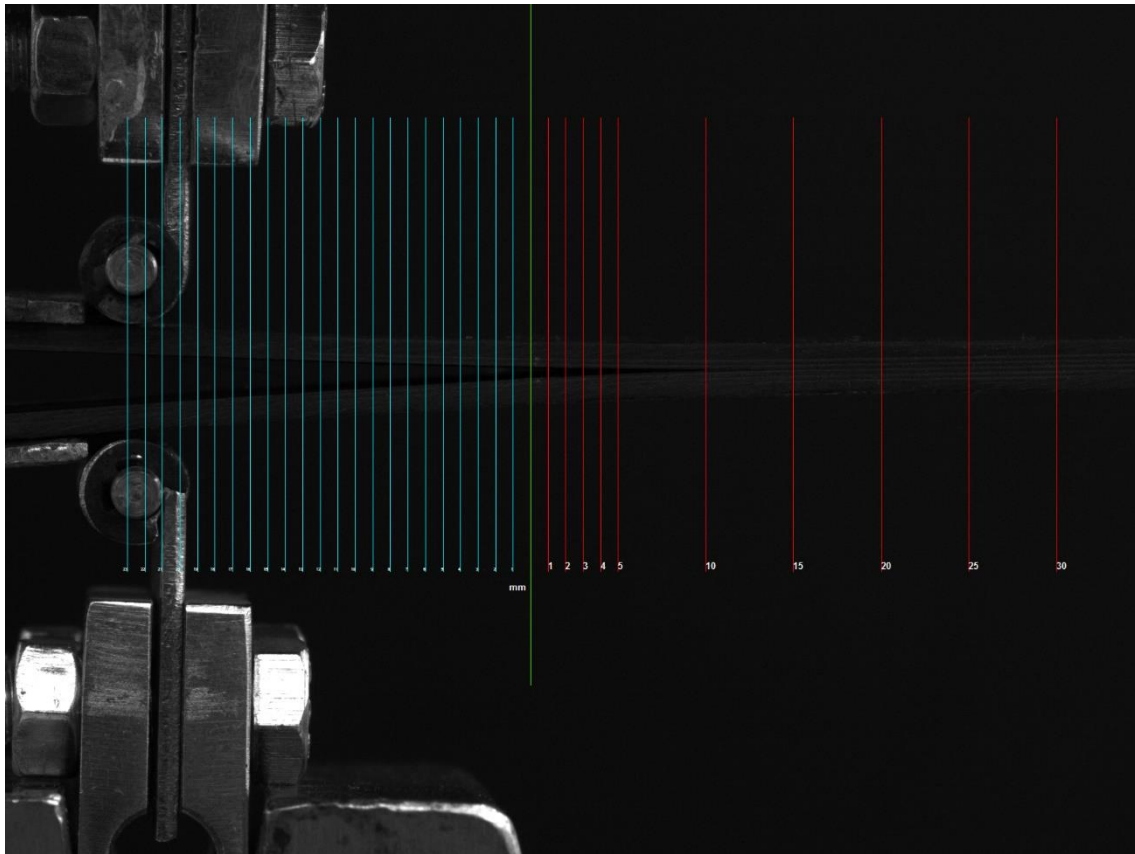
Figure 7.9. Delaminated DCB specimen with digital grid

The information which is not provided in Chapter 3, Section 3.6.2.1 about the materials and testing methods is the measurement of crack length, which is explained below. The CCD Marlin AVT is a black and white fire-wire camera, which can record images at a resolution of 1636x1252 pixels and a speed of 12.75 frames per second. The images are recorded at the highest resolution and frame rate during the test. The data acquisition system of the camera allows the overlapping of a calibrated digital grid over the recorded images. The digital grid has two parts of calibrated sections: the first section represents the pre-delaminated crack length, which represents the length from the piano hinges to the end of the non-adhesive insert and the second section represents the true crack opening. For better understanding Figure 7.9 is provided, which shows an image recorded by the CCD camera containing the delaminated sample with the digital grid overlapped over it.

7.3.2　　　　Sentry Function Results and Discussions

As indicated in Chapter 3, Section 3.6.2.1, three DCB specimens named MI-1, MI-2 and MI-3 are tested. For the purpose of comparison, the load-displacement curves of specimens MI-I, MI-2 and MI-3 are presented in Figure 7.10. In Figures 7.11, 7.12 and 7.13, the Sentry Function over the crosshead displacement has been compared with the Crack Length of specimens MI-1, MI-2 and MI-3, respectively.
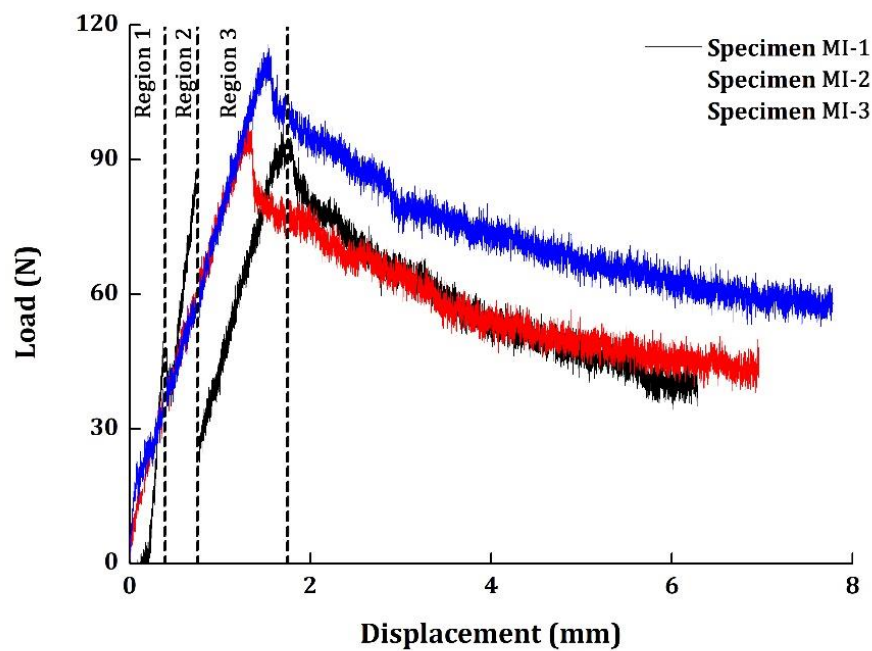
Figure 7.10. Load-displacement for specimens MI-1, MI-2 and MI-3
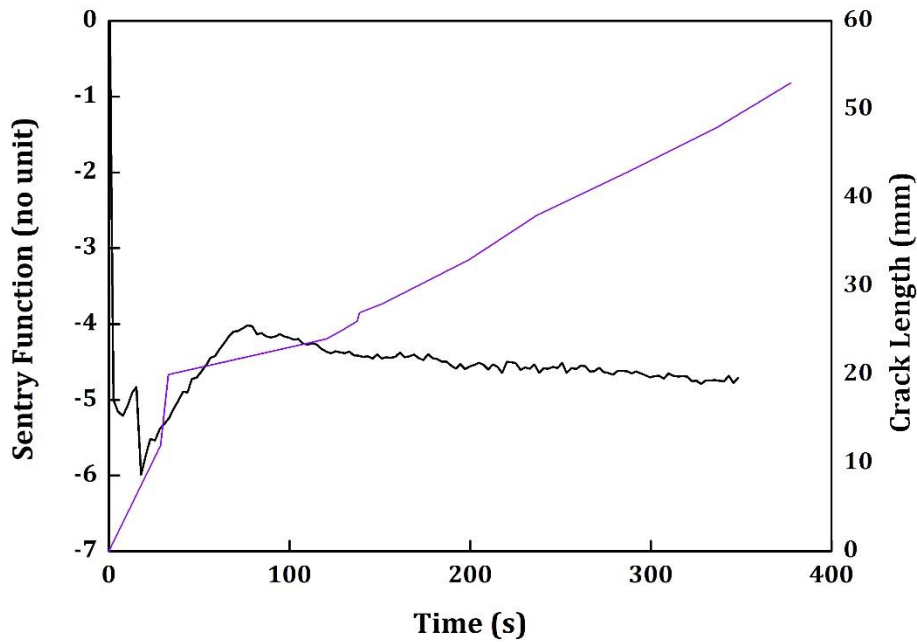
Figure 7.11. Sentry function and crack length progression for specimen MI-1

For Specimen MI-1, three Load Peaks, each in one Region can be observed in Figure 7.10, with the Peak with the Maximum Load is on Region 3 around 100 s duration. The crack length at the duration of 90 s is close to 25 mm. The crack length 25 mm represents the 2 mm opening of the delaminating crack beyond the length of the insert (the true length of the insert is 45 mm but only 23 mm is included in the calibrated grid for observation; Refer Figure 7.9). Despite the maximum peak load is at Region 3 around 90 s duration, a steep drop in Sentry function can be observed around 20 s duration (Figure 7.11). Beyond that point, the Sentry Function gradually increases implying that the material is trying to retain its property. The probably is the reason for the load drop in Region 1 and Region 2 is the unhinging of the piano hinges due to the improper curing. The acoustic signal does not represent the mechanical failure of material at 20 s duration which is why the Sentry function gradually increased beyond the point.

Nonetheless in Specimen MI-2, a steep drop in the Sentry Function around 90 s duration (crack length of 24 mm) and its gradual decrease beyond that point (Figure 7.12). When it reaches the duration of 90 s, the Sentry Function starts decreasing gradually, again

162

indicating the deterioration of the Specimen to failure. It should be noted that both Specimen MI-1 and MI-2 have a lower peak load when compared to Specimen MI-3. Specimen MI-2 started losing it property at an earlier stage when compared to both Specimen MI-1 and MI-3. The duration at which the Peak load can be observed and also the point at which the sentry function gradually started to decrease indicates the same.
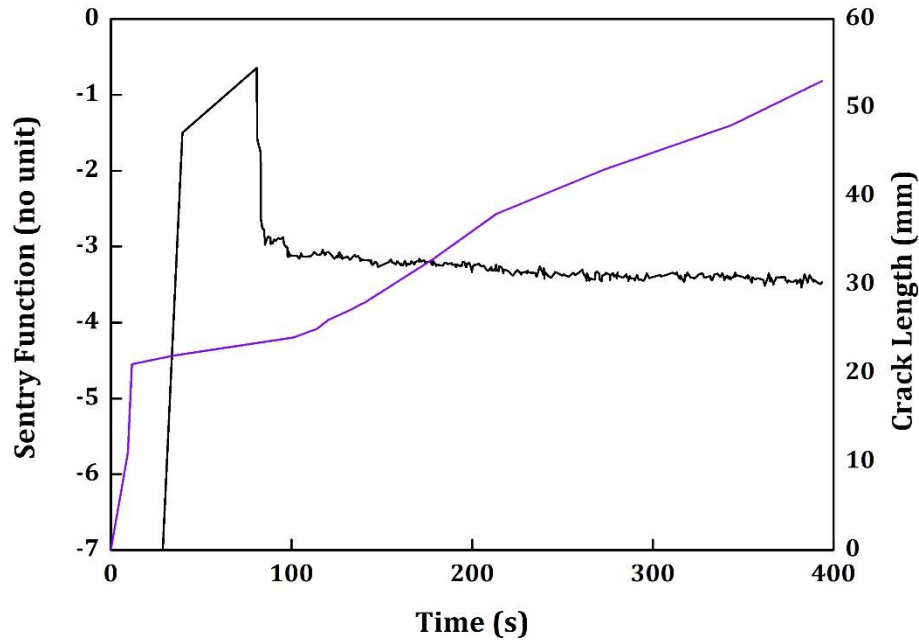
Figure 7.12. Sentry function and crack length progression for specimen MI-2

In both cases of Specimens MI-1 and MI-2, it is evident that by relating the Acoustic Parameter and Strain Energy, more useful and concealed information about the Material can be obtained. Specimen MI-3, by far the best specimen among the three, has a unique case while observing the Load-Displacement curve in Figure 7.10. It has only one Load Peak around 100 s duration and beyond that point, the load decreases. However, the Sentry Function in Figure 7.13 shows that after the steep drop at 100 s duration, there persist some sudden outbursts of Acoustic Energy, which can be identified by the subsequent drops in Sentry Function (at 105 s and 150 s). These can be attributed to the opening of the crack length and the propagation of crack length through the Specimen. The Crack Length at the point of the load drop in the Sentry Function is 24 mm.

163

From these observations, it is quite evident that the Sentry Function is a reliable tool to relate the Acoustic Activity with the Material Property under loading. One of the major questions that can arise from the Sentry Function is the lack of activity in the Sentry function beyond the point of 100 s duration in all the 3 Specimens. Upon studying the literature based on Sentry Function, normally, the Sentry Function is discontinuous with different domains. However, in case of the DCB Specimens MI-1, MI-2 and MI-3, there is no significant change in the Sentry Function beyond 100 s duration. The probable reason is that the Mode I delamination requires very less energy to occur and the material starts losing its load-carrying capability completely beyond that point, which is the reason only one steep drop in Sentry Function has been observed.
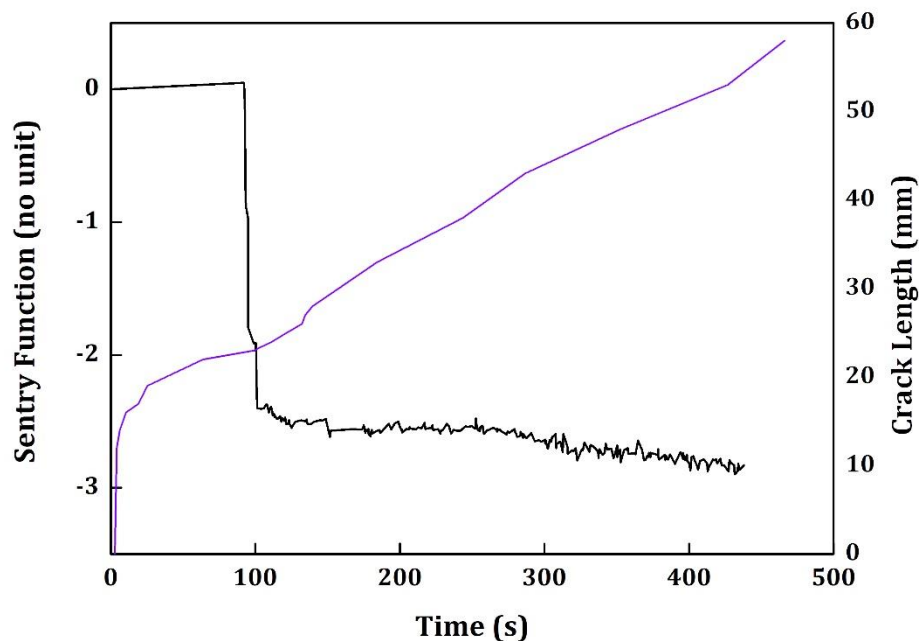
Figure 7.13. Sentry function and crack length progression for specimen MI-3

Davijani et. al (2011) has studied the Sentry Function on Glass Fiber Reinforced Plastic (GFRP) DCB Specimens and have observed discontinuous patterns in Sentry Function until failure. However, it should be understood that the Glass Fibers have significantly lower strength when compared to the Carbon Fibers and the energy required for Fiber Breakage or Fiber Pullout is low as well. Moreover, the specimen Davijiani et. al (2011)

used has a woven mid ply compared to the unidirectional plies in the presented study. When the load is applied to the DCB specimen, the Mode I delamination progresses along the direction of the fiber and thus we have one major damage at around 100 s and no major significant damages beyond that point. Summarizing the results, it can be concluded that the material has lost its load-carrying capability around 100 s duration.

7.4　　　　　ACOUSTIC ENERGY BASED PARAMETER – ENERGY PER COUNT

A very simple, yet novel parameter has been introduced in this work, which is named as Energy per Count. It is the ratio of total energy of the acoustic signal recorded to the number of counts in each acoustic event. Normally, the AE signals are classified purely based on the energy, however, under certain circumstances, the results can be misleading. As indicated in Section 7.1, the squared signal is used for calculating the acoustic energy and the acoustic energy is the area of the curve under the squared waveform above the acquisition threshold. This means that the total counts in the acoustic event can also influence the acoustic energy. This is proved by the strong relationship between acoustic counts and acoustic energy on many occasions. For instance, fiber breakage in a FRP release AE waves with large acoustic energy, at the same time, fiber matrix debonding or matrix cracking can produce large number of counts. This is because the acoustic waves propagate in two different modes—lower order symmetric and higher order asymmetric. The higher order symmetric waves, originating from failures such as fiber breakage carries large energy and short duration, consequently, a lower number of counts. The lower order asymmetric waves originating from matrix cracking or debonding carries large number of counts with lower energy. In some cases, when the material has high stiffness/brittleness, the cumulative number of energy recorded from these two types of modes can be similar. This makes them hard to categorize and makes it difficult to identify the damage modes. In this work, this problem has been addressed through a very simple yet innovative approach—energy per count. Using this parameter, it is easy to categorize the different signals with their energy levels, which will be helpful in identifying the damage mode in the material. In simple terms, the energy per count (E_c) can be expressed as, for each acoustic event 'N_i',

$$E_c = \frac{E_a, i}{C_i} \tag{7.5}$$

where E_a is the acoustic energy, C_i is the count and i represents the number of the acoustic event N.

As indicated in Section 7.1, the E_c has been used in two different ways in this work. First, it is used as an identifier for the damage assessment in the CFRP composites. In Chapter 5, Section 5.5, it was mentioned that one AE descriptor cannot be used for damage assessment. Following that same rule, the peak amplitude distribution and cumulative energy is also used for supporting the E_c.

7.4.1　　Energy per Count for Damage Assessment

7.4.1.1　　Materials and Testing Methods

Two groups of specimens are used for this study. Both are Single Lap Shear (SLS) specimens but one of the specimen group is also uses a rivet, making it a hybrid bonding. The CFRP prepreg laminate is prepared by impregnating high strength carbon fibers in ER450 epoxy matrix (SATTI CIT CC206 ER460, CIT Composite Materials, Legnano, Italy). The resin percentage in the composite laminate is 43% and each ply has a nominal ply thickness of 0.244 mm. The carbon fibers are stitched in a woven configuration with the layers of fibers overlapping one another. The laminates are cured by autoclave method. The adhesive used for bonding the laminates is an epoxy adhesive EA9395 with a shear strength of 25 MPa and a peel strength of 65 MPa. The adhesive is applied to the laminates and are cured at an elevated temperature of 100 ℃ to 150 ℃ for 1 h. Two types of configuration of specimens are prepared for this study.

The adhesively bonded Single Lap Shear (SLS) and hybrid Single Lap Shear with Rivets (SLS-R) are prepared using the aforementioned methods. The geometry of the specimen groups SLS and SLS-R, respectively, the number of plies, orientations are given in Table 7.5 and Table 7.6.

Table 7.5. SLS Specimen Nomenclature, Geometry and Configurations

Upper Adherend				
Length l_u (mm)	Width b_u (mm)	Thickness h_u (mm)	No. of Plies	Stacking Sequence
101.6 ± 0.11	25.33 ± 0.12	1.3 ± 0.05	5	+45/+45/+45/-45/+45
Lower Adherend				
Length l_l (mm)	Width b_l (mm)	Thickness h_l (mm)	No. of Plies	Stacking Sequence
101.6 ± 0.09	25.33 ± 0.14	6.4 ± 0.12	26	+45/[+45/-45]$_{12}$/+45
Overlapping Region				
Length l_{or} (mm)		Width b_{or} (mm)		Thickness h_{or} (mm)
26 ± 0.12		25.33 ± 0.25		8.5 ± 0.11

Table 7.6. SLS-R Specimen Nomenclature, Geometry and Configurations

Upper Adherend				
Length l_u (mm)	Width b_u (mm)	Thickness h_u (mm)	No. of Plies	Stacking Sequence
101.6 ± 0.09	25.34 ± 0.10	1.3 ± 0.07	5	+45/+45/+45/-45/+45
Lower Adherend				
Length l_l (mm)	Width b_l (mm)	Thickness h_l (mm)	No. of Plies	Stacking Sequence
101.6 ± 0.14	25.32 ± 0.16	6.4 ± 0.10	26	+45/[+45/-45]$_{12}$/+45
Overlapping Region				
Length l_{or} (mm)		Width b_{or} (mm)		Thickness h_{or} (mm)
25.40 ± 0.06		23.32 ± 0.12		8.27 ± 0.08

For SLS-R specimens, a hole was drilled in the middle of the adhesive overlapping region. The self-piercing rivets (SPR) are not used for this study because the adhesive thickness makes the specimen more brittle and SPR is not suited for those joints. A flat-headed aluminum rivet with a radius (r_r) of 1.6 mm and a length of 14 mm is used for joining the SLS-R specimens. The configuration of the SLS and SLS-R specimens is presented in Figure 7.14.
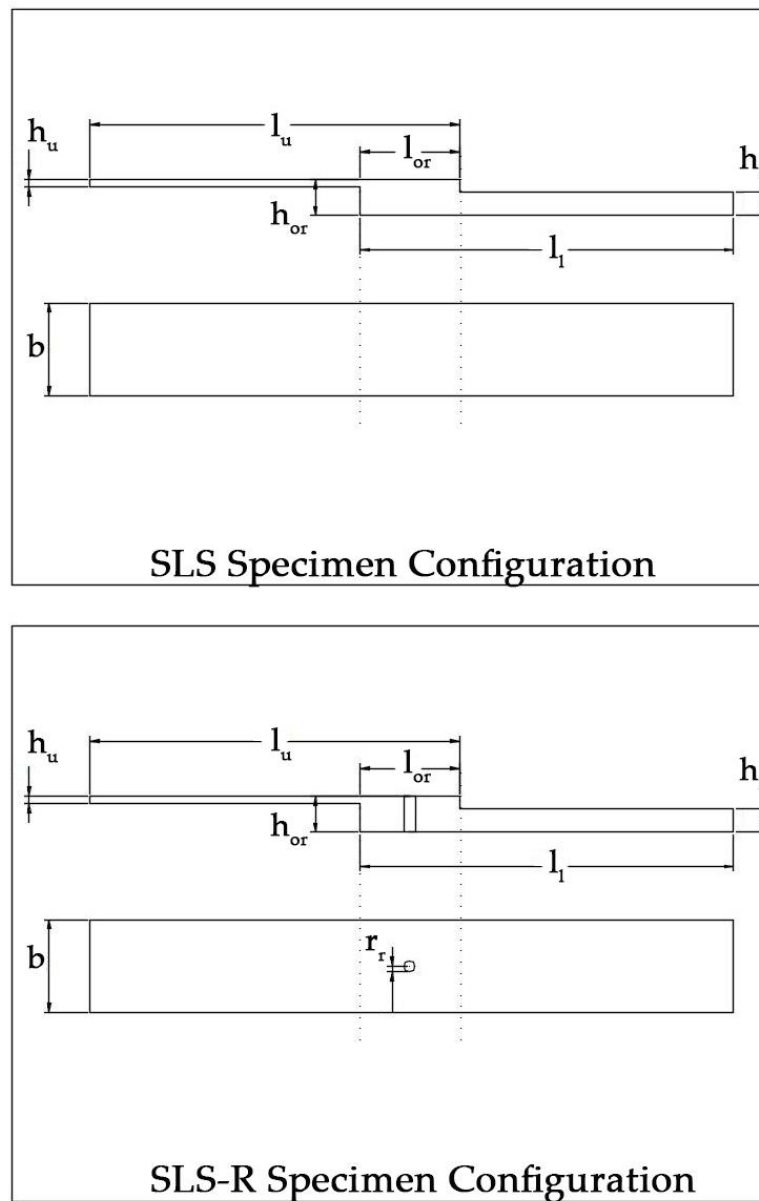
Figure 7.14. Configuration of SLS and SLS-R Specimens

The standard testing procedure for ASTM D5868—Standard Test Method for Lap Shear Adhesion for Fiber Reinforced Plastic (FRP) Bonding is followed for testing. The tests are carried out in INSTRON Servo-Hydraulic testing machine with a load capacity of 100 kN under displacement controlled mode at a rate of 13 mm/min. The tensile load is applied to the specimen.

For recording the acoustic signals emitted during loading, two narrowband sensors R30α (Physical Acoustics, MISTRAS Group, NJ, USA) are used. The sensors have an operating frequency range of 150 kHz to 400 kHz, with a resonant frequency of 300 kHz. It has been indicated in several reports that the AE signals will not be above 400 kHz in Fiber Reinforced Plastics (FRP). The narrowband sensor is selected based on that observation and to reduce the recording of noise signals. The sensor signals are amplified by 40 dB using a 2/4/6 AE preamplifier. The threshold for acquisition is set as 35 dB and the signals are recorded at a sampling rate of 1 mega samples per second (1 MSps).
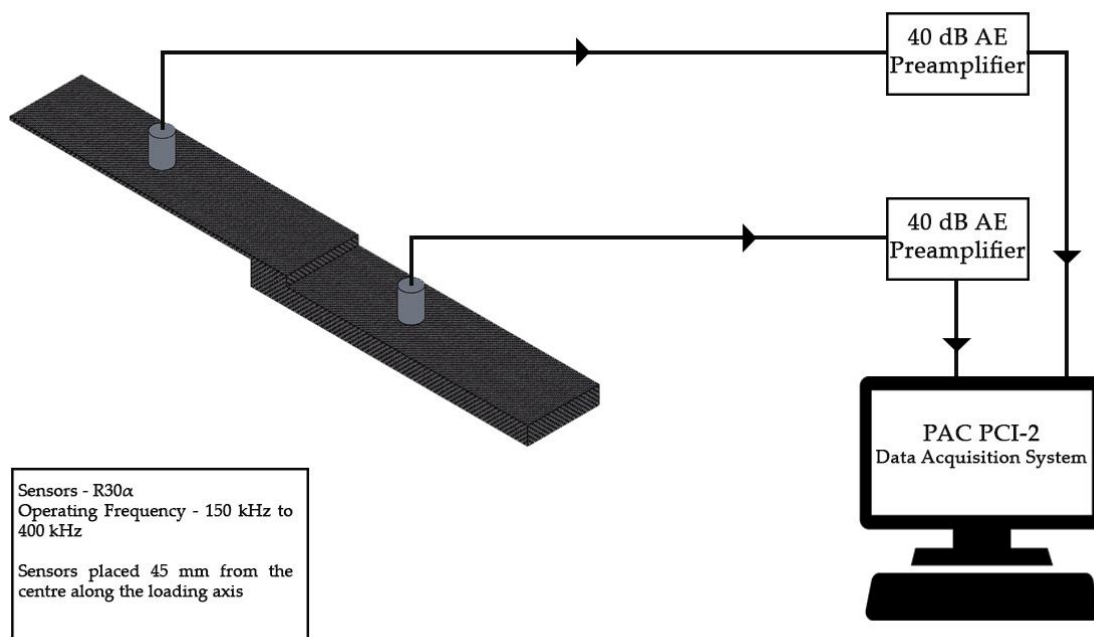
Figure 7.15. Schematic of Acoustic Emission Setup

The sensors are mounted on the specimen at 40 mm from its center. Silica gel is interposed between the sensor surface and the specimen surface to enhance the coupling between the two elements. The silica gel also reduces the recording of reverberated signals arising from the surface of the specimen.

The distance of the sensor from the acoustic source can affect the recorded AE signals. For this reason, the attenuation of AE signals along the length of the specimen is studied

using pencil lead break test and the attenuated values are fed to the PAC PCI-2 data acquisition system. The schematic of the AE setup is presented in Figure 7.15.

7.4.1.2   Data Processing

This section details the acoustic emission descriptors used for this study. The acoustic emission descriptors used for this study are peak amplitude, cumulative counts, cumulative energy and energy per counts.

Peak amplitude represents the largest voltage peak (U_{max}) in the recorded AE signal waveform with respect to the reference voltage (U_{ref}). The reference voltage is adjusted by the data acquisition system depending on the amplitude threshold provided.

Besides, the energy per count is clustered using k-means++ algorithm. The pattern recognition algorithm is used for classifying the energy per count calculated for all the specimens into 3 clusters.

The detailed explanation about the k-means++ algorithm, the procedure for selecting the optimal number of clusters and the procedure for classification of the data into the predefined numbers of cluster are provided in Chapter 5, Section 5.3.1.

7.4.1.3   Mechanical Test Results

For identifying the damage mechanisms involved in the fracture of the SLS and SLS-R specimens, it is essential to describe the mechanical results. For this study, three specimens each from SLS and SLS-R group are tested. The tensile load is applied on the specimens at a crosshead displacement of 13 mm/min and the load-time response is presented in Figure 7.16. The load response is plotted against time instead of crosshead displacement is for the ease of comparing the mechanical results with the acoustic results, which are plotted over time.

Both the group of specimens have multiple load peaks before failure. It can be observed that the SLS specimens have carried more load than the SLS-R specimen group. It has been indicated by Chowdhury et al. (2015 & 2016) that the riveted specimens do not necessarily have significant strength as the normally adhesively bonded specimen but

can reduce the propagation of internal failure within the adhesive. Typically, in an adhesively bonded joints, failure occurs in two modes. The first mode is interfacial failure or adhesive failure which occurs between the adhesive and the adherend. The second mode is the cohesive failure within the adhesive layer, which is due to the delamination of the composite adherend. The two most significant stresses that induce the failure modes are interlaminar stresses at the vicinity of the bond line edges which causes the interfacial failure and the normal stress acts on the adhesive, the peel stress, which is responsible for the cohesive failure. Generally, the peel stresses are higher compared to the interlaminar shear stresses and are responsible for the failure. Since the specimen groups SLS and SLS-R has significantly larger thickness (8.25 mm appro7.), most of the failure could be attributed to the interlaminar failure.
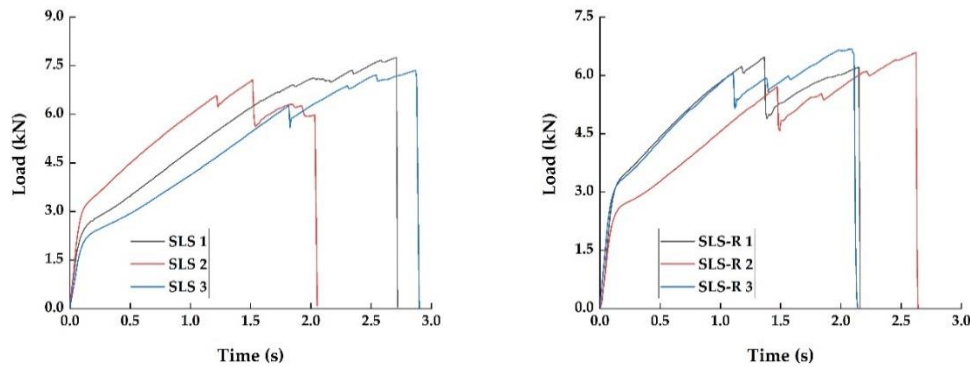
Figure 7.16. Load response plotted over time for the (**a**) SLS Specimens SLS 1, SLS 2 and SLS 3 and (**b**) SLS-R Specimens SLS-R 1, SLS-R 2 and SLS-R 3

The resulting peel stress probably has initiated the failure at the vicinity of the boundaries between the adhesive layer and the adherend at the edges. However, due to the high peel strength of the adhesive, the cohesive crack path is not very stable. This can be attributed to the multiple load peaks in both the specimen groups.

Moreover, the peel stress is typically larger at the center of the adhesive overlapping region and is lower near the boundary edges. The SLS-R specimens are riveted at the center, where the peel stress will be maximum. This probably had made the crack growth more unstable, resulting in multiple load peaks in the SLS-R specimens. From Figure 7.16, it can be observed that the load peaks in SLS-R specimens occur earlier and are also lower

171

than in SLS specimens. The average peak load of SLS group of specimens is 6.91 kN, whereas SLS-R specimens have an average peak load of 6.08 kN.

Generally, the yielding of the rivets is observed around 4 kN to 6 kN in many of the hybrid composites. Nonetheless, in all the previous studies, one of the adherend is a metal, which makes them a hybrid composite. In this study, both the adherends are CFRP, which are stiffer than their metal counterparts. This results in forming high stress concentration around the rivets which are propagated towards the boundary edges, leading to the failure. This could be another reason why the SLS-R group of specimens have lower peak load than SLS specimen group.

7.4.1.4 *Acoustic Emission Results*

The cumulative counts recorded for all the specimens are presented in Figure 7.17. In the specimen group SLS, for SLS 1, the cumulative count remains below 100 until it reaches the duration 0.5 s. For specimens SLS 2 and SLS 3, the cumulative count remains to be very low until the duration 1.5 s and 1.75 s, respectively. After that, it increases linearly. The point at which the cumulative count increases rapidly for SLS 1, SLS 2 and SLS 3 are 1.1 s, 1.65 s and 1.75 s, respectively. If the cumulative counts curve in Figure 7.17(a) is compared with the load responses in Figure 7.16(a), the first load drop can be observed after this rapid increase in the cumulative counts. The rapid increase in the cumulative count is an indication that a major damage is about to occur in the specimen.
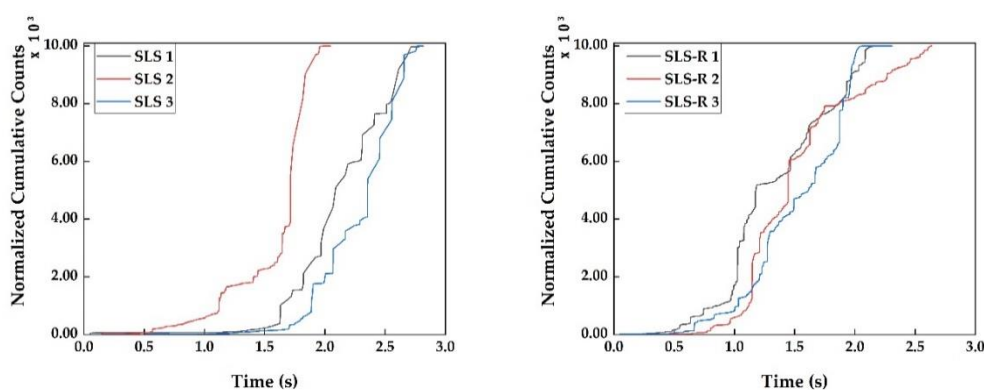
Figure 7.17. Normalized Cumulative Counts recorded for (**a**) SLS group of specimens, (**b**) SLS-R group of specimens

The acoustic waves generated during the straining and failure modes propagate in two different modes. The lower order symmetric AE signals, which represent the matrix cracking or interfacial failure normally has large number of counts. The accumulation of these damages before the specimens loses their load carrying capacity is the reason for the rapid increase in the cumulative counts before the failure. Thus, each time before a major failure is about to occur, the cumulative number of counts takes a steep increase indicating the occurrence of failure.

In Figure 7.17(b), the similar pattern can be observed. The first rapid increase in cumulative counts can be observed at 1.0 s, 1.275 s and 1.2 s for specimens SLS-R 1, SLS-R 2 and SLS-R 3, respectively. While comparing with the load responses in Figure 7.16(b), a pattern similar to the SLS group of specimens can be observed.

The major difference between the two group of specimens is the duration of the linear increase prior to the first rapid increase in the cumulative counts. The specimen group SLS has a longer duration of linear increase in the cumulative counts with respect to the SLS-R group of specimens. Moreover, before the rapid increase in SLS-R specimens, they also exhibit some small increases in the cumulative counts before the aforementioned duration of major failure occurrences. The differences in failure modes between the specimen groups SLS and SLS-R can be attributed for this phenomenon.

Both the specimen groups have larger thickness in the adhesive overlapping zone, close to 8.5 mm. As mentioned in the Section 7.4.1.3, the peel stress induced is significantly lower in both the specimen groups, which inhibit the cohesive failure of the composite. There will be more shearing of the adhesive layer before the cohesive failure starts to occur. In SLS-R group specimens; however, the presence of the rivets increases the stiffness of the specimen and induce more stress around them. This is the reason why there is less shearing, which is the reason for the shorter duration of linear increase in the cumulative counts in SLS-R group of specimens. This obvious stiffening effect is also evident from Figure 7.17, as there are more steps in the increase in cumulative counts in SLS-R group of specimens than SLS group.

As mentioned throughout this chapter and previous chapters, there is a strong linear relationship between the cumulative counts and cumulative energy of the recorded acoustic events. This is evident while comparing Figure 7.17 with the cumulative energy recorded during the acoustic events, which is presented in Figure 7.18.
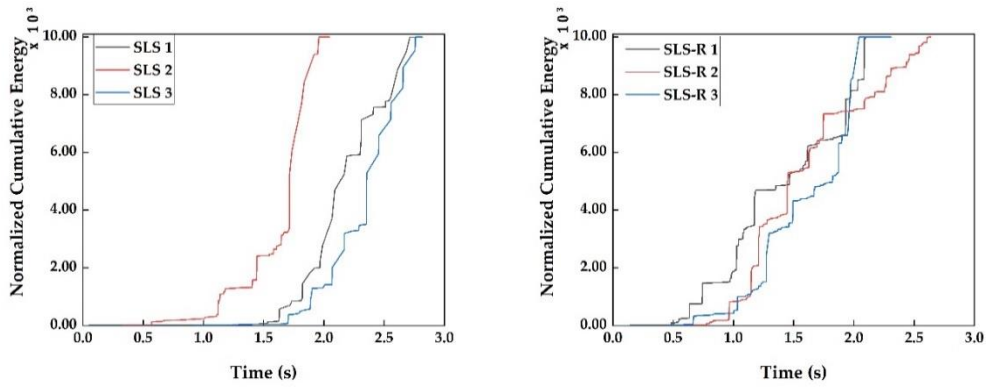
Figure 7.18. Normalized Cumulative Energy recorded for (**a**) SLS group of specimens, (**b**) SLS-R group of specimens

Both the cumulative counts and cumulative energy looks almost identical in comparison. However, while looking closely, some small differences can be observed. Particularly in the Figure 7.18(b), the cumulative energy for the specimen groups SLS-R.

There is no linear increase in the cumulative energy for specimen SLS-R 1 and SLS-R 3; the energy remains almost close to zero until the durations of 0.5 s and 0.65 s, respectively, followed by a sudden increase. Moreover, the increase in normalized cumulative energy is larger than the increase in normalized cumulative counts at the same duration. This indicates that there is more energy released during these acoustic events than the number of counts. This means that the acoustic wave propagated in higher order symmetric modes, indicating the interfacial failure or fiber breakage. This could be an indication that the induced stress by the rivets may have induced either interfacial failure or fiber breakage at that time.

Regardless of this one particular segment of the cumulative energy pattern, most of the segments and patterns in Figure 7.17 and Figure 7.18 are almost identical.

As indicated earlier, the utilization of cumulative counts, energy and the peak amplitude distribution are presented in this section is to support and validate the newly introduced parameter, the energy per count. The peak amplitude distribution recorded during the test of SLS and SLS-R groups of specimens are presented in Figure 7.19 and Figure 7.20, respectively.
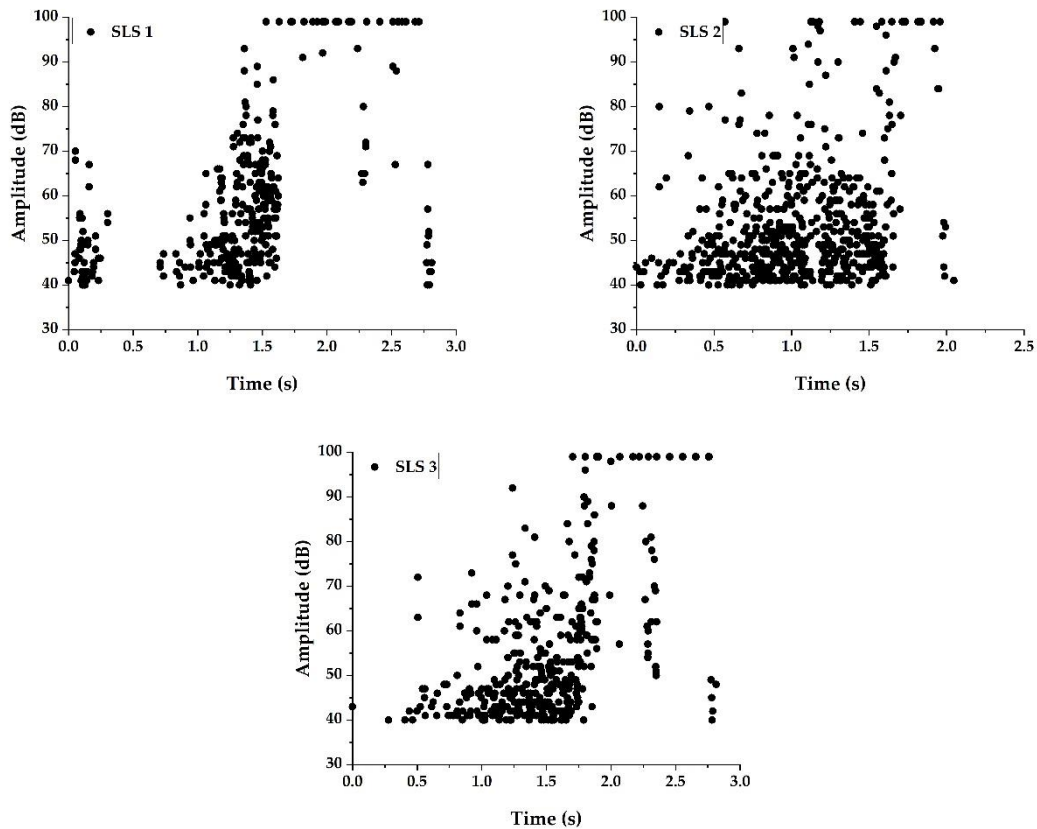
Figure 7.19. Peak Amplitude distribution for Specimens (**a**) SLS 1 (**b**) SLS 2 and (**c**) SLS 3

The peak amplitude distribution between the specimens SLS 1, SLS 2 and SLS 3 are not similar during the initial stages of loading. At the early stages of loading, the specimen SLS 1 released acoustic waves with a peak amplitude distributed between 40 dB and 70 dB, which is followed by a period of acoustic gap. This is followed by a surge of acoustic events distributed between 40 dB to 75 dB. Once the specimen reached the duration of the initial peak load, as indicated in Figure 7.16(a), acoustic events with an amplitude above 90 dB started to be observed. During the initial stages of loading, the SLS 1

specimen suffered severe matrix cracking and interfacial failure, which always releases AE energy below 65 dB to 70 dB. The acoustic gap indicates that the accumulated damage is about to cause a catastrophic failure. This can be observed by the sudden increase in AE events with amplitudes above 65 dB after the acoustic gap. This is also an indication why the SLS 1 specimen has suffered its initial failure at a very early stage, as seen in Figure 7.16(a). The number of AE events prior to the initial damage has resulted in the consequential failure of the specimen.
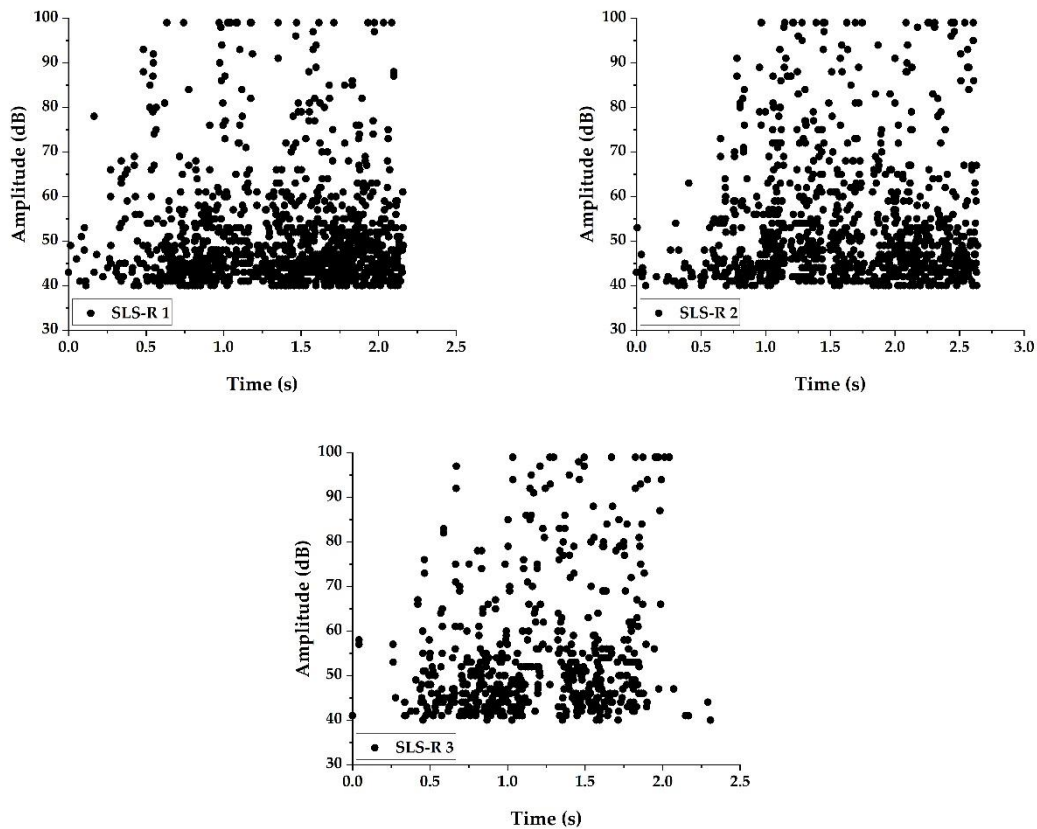
Figure 7.20. Peak Amplitude distribution for Specimens (**a**) SLS-R 1 (**b**) SLS-R 2 and (**c**) SLS-R 3

However, it is not the same for specimen SLS 2, which has only a limited number of AE events at the initial stages of loading. Moreover, those AE events are well below 50 dB; indicating that there are very few matrix cracking or interfacial failure in the specimen SLS 2. Nonetheless, the AE events are distributed between 40 dB and 65 dB throughout the entire loading history until the specimen started to lose its load bearing capability

176

completely. It must be understood that the matrix failure that occurred in the adhesive overlapping region, which is 8.5 mm thick may have released the AE waves with the distributed peak amplitude. But the specimen still transferred the load until the duration 1.2 s, where the major failure started to occur. It is from that instant, a higher number of AE events with amplitudes above 85 dB (or even 90 dB) can be observed.

Specimen SLS 3 has a unique trend as there are no AE events observed until 0.25 s duration. These differences in the failure modes can be attributed to the curing conditions of the adhesive applied. Moreover, the AE events above 85 dB normally represent fiber failure. However, in the present study, only a very few fiber failures are observed. Several researchers have indicated that the larger amplitude AE events can also represent the interlayer crack growth. Since these specimens have suffered significant damage due to the cohesive crack growth, the high amplitude events in all the specimens can be directly attributed to the cohesive failure of the specimens.

The peak amplitude distribution in SLS-R group of specimens are identical to one another; however, they are entirely different from the amplitude distribution of SLS group of specimens. The important reason for this is because of the failed matrix rubbing with the pivoted rivets, creating more frictional waves. This the reason why the AE amplitude is distributed between 40 dB to 75 dB throughout the loading duration. The final stages of loading, however, are similar to the SLS group of specimens where the failure occurred due to the cohesive crack growth. The induced peel stress probably has caused the cohesive crack growth to propagate from the middle of the specimen to the upper adherend boundary, inducing the final failure of the specimen.

One important observation that can be observed while comparing the peak amplitude distribution, the SLS group of specimens show different trends, however, the SLS-R group shows similar trend. This means that the crack growth is unstable due to the larger thickness in the SLS specimens but is controlled and propagated in a controlled manner by adding the rivets. This coincides with the observations of Chowdhury et al. Nonetheless, even at the final stages of loading, the AE events are distributed in a wide range of peak amplitude, which makes it quite difficult to easily identify the failure mode.

177

7.4.1.5   *Energy per Count*

The energy per count recorded for the SLS specimens are calculated using Equation (7.5) and are presented in Figure 7.21. The energy per count for all the specimens are clustered into 3 classes using k-means++ algorithm.

The clustered energy per count gives a clear indication of the failure modes in the specimen group SLS. The cluster 1 represent the AE signals with larger energy with lower number of counts, indicating the higher order symmetric AE signals. This means that the cluster 1 has AE signals representing the cohesive crack growth. The second cluster represents the AE signals released during the interfacial failure between the adhesive and the adherend. The cluster 3 possibly can represent the lower order asymmetric AE signals, which represent the matrix cracking.

In specimen SLS 1, a significant number of AE signals in cluster 1 can be observed even during the early stages of loading. This again coincides with the mechanical results from Figure 7.16 indicating why the specimen SLS 1 failed early and carried less load. The specimen SLS 2 and SLS 3, however, show a large number of events in cluster 2 and cluster 1. This means that the cohesive crack growth occurred in the SLS 2 and SLS 3 specimens probably have propagated along the thickness of the adhesive, resulting in the interfacial failure. This is the reason why many AE events above 90 dB can be identified in the later stages of loading in specimen group SLS 2 and SLS 3 in Figure 7.19 (b and c).
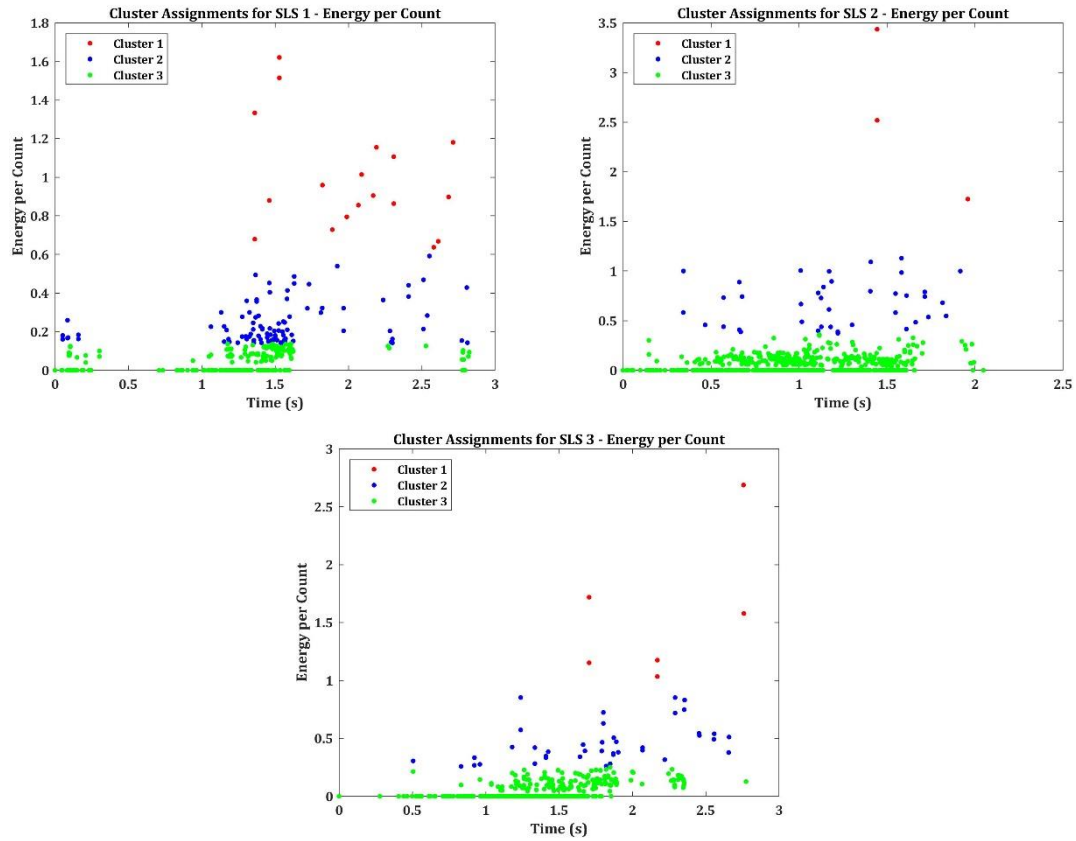
Figure 7.21. Clustered Energy per count for Specimens (**a**) SLS 1 (**b**) SLS 2 and (**c**) SLS 3

The energy per count results of SLS-R groups of specimens are presented in Figure 7.22. As indicated in Section 7.4.1.4, the distributed AE amplitudes in SLS-R group of specimens might represent the friction between the damaged matrix and the rivets. This is evidently proved while looking at Figure 7.21. For all the three specimen groups, most of the AE events have the energy per count distributed in the cluster 3. Only a selective number of events can be observed in cluster 1 and cluster 2. This indicates that the events in cluster 3 represents (1) matrix cracking and (2) friction between the rivets and the damaged matri7.
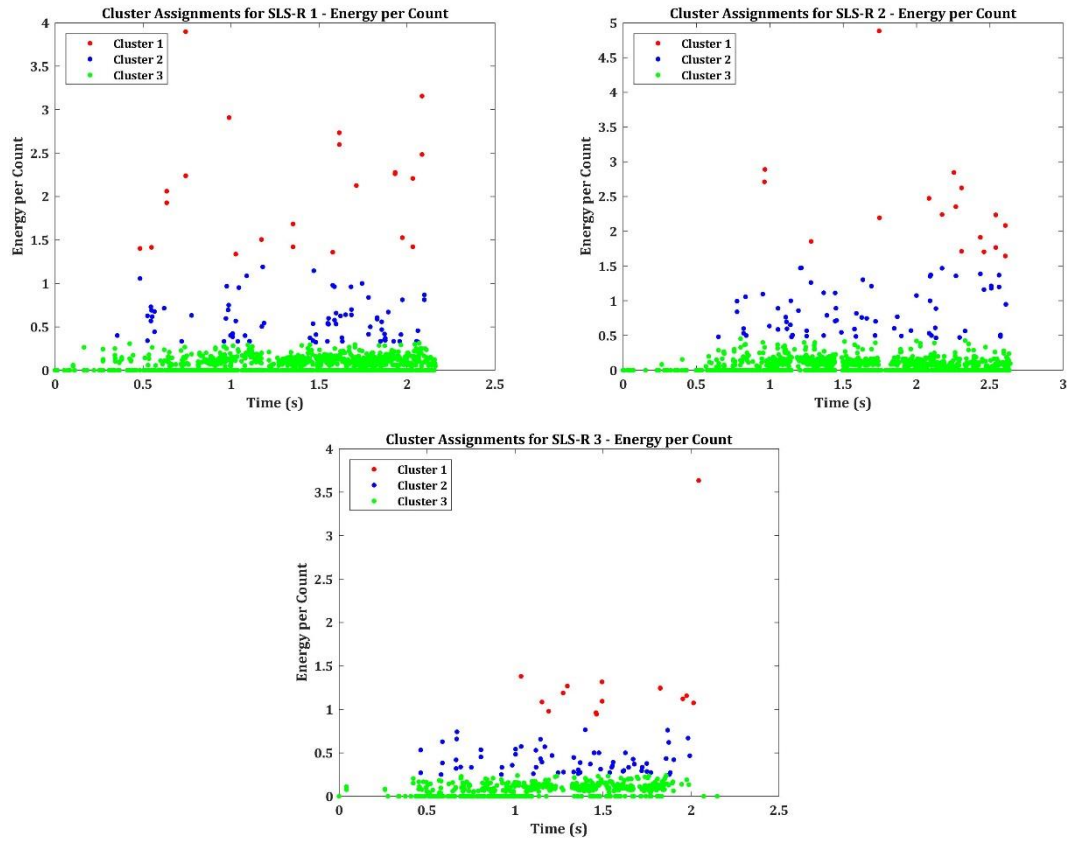
Figure 7.22. Clustered Energy per count for Specimens (**a**) SLS-R 1 (**b**) SLS-R 2 and (**c**) SLS-R 3

However, a lot of events in cluster 1 with a larger energy per count can be observed in SLS-R specimen group. This is because of the presence of rivets, which induce stresses around them which results in creating larger stiffness. When the material fails in the region of high stress, it releases AE events with larger energy per count.

One could easily be misled to the assumption that the events in cluster 1, 2 and 3 represents cohesive crack growth, through thickness crack growth and matrix cracking, respectively. This may be true only if more than one AE descriptor is used for analysis. This hypothesis is established by observing the results of normalized cumulative counts, energy and peak amplitude distribution and finally proved by the energy per count. Anyhow, this clearly shows that the new parameter introduced in this chapter, energy per count, is capable of identifying the damage modes in the material.

This concludes the first way of using energy per count, which is introduced in this thesis work. The second way of using this parameter is explained in the next section.

7.4.2   Energy per Count as the Selection Criterion for Waveform Analysis

The acoustic waveforms are selected from the set of AE events recorded in a specimen with the energy per count as the selection criteria. Then these waveforms are analyzed using Wavelet Packet Transform (WPT), which is explained in Chapter 3, Section 3.4. The waveform results and the WPT results are used for identifying the damage modes. As mentioned in the aforementioned chapters, it is not possible to perform waveform analysis on all the AE waveforms generated. It is a tedious task which consumes lots of memory and time. For that reason, a representative waveform from a group of AE events must be selected. So far, there are no tools that can perform this task. This work aims in using Energy per Count (E_c)as the selection criterion.

For this analysis, the specimen SLS-R 1 from Section 7.4.1 is selected for analysis. The load response of SLS-R 1 specimen can be separated into eight different stages and the acoustic emission results are analyzed in each of these stages (Refer Figure 7.23). The reason for categorizing the load response into different stages is because the stress distribution and corresponding damage propagation in this hybrid joint specimen vary from stage to stage owing to several factors. The larger thickness of the lower adherend, the thickness of the adhesive and the aluminium rivet are some of the reasons for the complex stress distribution in the specimen. Based on that, the load response is classified into stages:

i)   Linear elastic response – 1
ii)   Linear elastic response – 2
iii)   Sudden load drop – 1
iv)   Linear plastic response – 3
v)   Sudden load drop – 2
vi)   Nonlinear plastic response
vii)   Linear response – 4
viii)   Final fracture
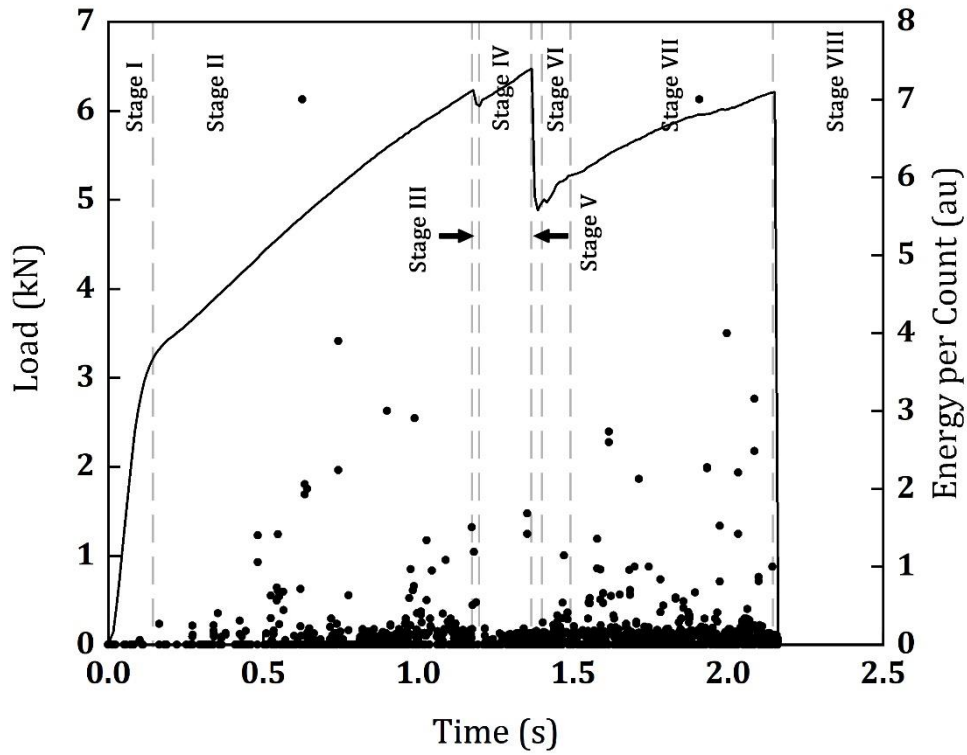
Figure 7.23. Load vs Time for the CFRP Hybrid Joint Specimen over plotted with Energy per Count calculated from the acoustic results

From each stage (except Stages i, iv and viii), two acoustic events are selected for the WPT analysis. The selection is based on the E_c. In each stage, the E_c value ranges from close to 0 to 7 au, with the majority of the AE events distributed below E_c value of 1. For this reason, two acoustic events, one between $0 < E_c < 1$ (level 1) and another $E_c > 1$ (level 2) is taken for this study. Since the stages i, iv and viii do not have any AE events with $E_c > 1$, only one acoustic event is taken from this stage.

From the WPT, the energy percentage distributed in each frequency band is calculated for all the signals taken from the eight stages. The results are presented in Table 7.7.

Table 7.7. Spectral Energy distributed in each frequency band from WPT results for all AE events

Stages	Levels	Frequency (kHz)							
		437.5-500	375-437.5	312.5-375	250-312.5	187.5-250	125-187.5	62.5-125	0-62.5
I	1	3.31	0.22	18.50	29.31	10.76	9.08	28.80	0.03
II	1	0.92	0.34	39.30	26.94	13.11	7.63	11.70	0.05
	2	0.83	0.93	7.09	7.13	10.56	54.46	17.97	1.03
III	1	3.29	1.46	37.82	25.25	8.85	10.67	12.13	0.52
	2	2.96	1.10	43.37	19.10	7.81	16.10	9.18	0.38
IV	1	0.84	0.22	44.16	21.05	8.92	15.18	7.18	2.45
	2	0.91	0.66	19.34	9.77	5.74	39.50	23.49	0.60
V	1	0.95	4.73	45.34	17.79	11.53	14.48	4.80	0.38
VI	1	0.26	0.38	21.27	29.20	13.65	28.18	6.88	0.19
	2	1.48	2.06	51.84	8.56	8.35	8.64	18.74	0.32
VII	1	0.63	0.63	12.44	14.82	4.54	24.88	41.90	0.16
	2	1.99	1.91	38.33	21.25	9.01	10.97	15.77	0.76
VIII	1	0.68	0.50	35.78	29.81	16.08	9.57	7.42	0.16

The waveform and the WPT results of the low E_c signal recorded during stage i is presented in Figure 7.24. First of all, the stage i lasts only for 0.16 s duration in the entire test. This suggests that it is a very short stage and consequently very few AE events are recorded during this stage. The AE event selected from this stage has a relatively high amplitude and count so that any noise signals can be avoided in the analysis. In Figure 7.24(a), it is evident that the maximum amplitude of the waveform is 0.7 µV. Comparing the results from Table 7.7 and Figure 7.24(b), the spectral energy is distributed in all frequency bands between 62.5 kHz and 437.5 kHz. There is no frequency band which has specifically carried any significant amount of energy. Moreover, while testing lap-shear specimens with wedge-shaped grips, during the initial loading, the specimen aligns itself to the axis of loading. That is why there are two linear elastic stages in the load response with the first region is very short (0 s – 0.16 s). Since there is no signal with any significant E_c, a conclusion can be drawn. During this region, the specimen aligns itself to the axis and the AE signals generated during this stage are a result of the friction between the specimen and the end grips of the loading setup.
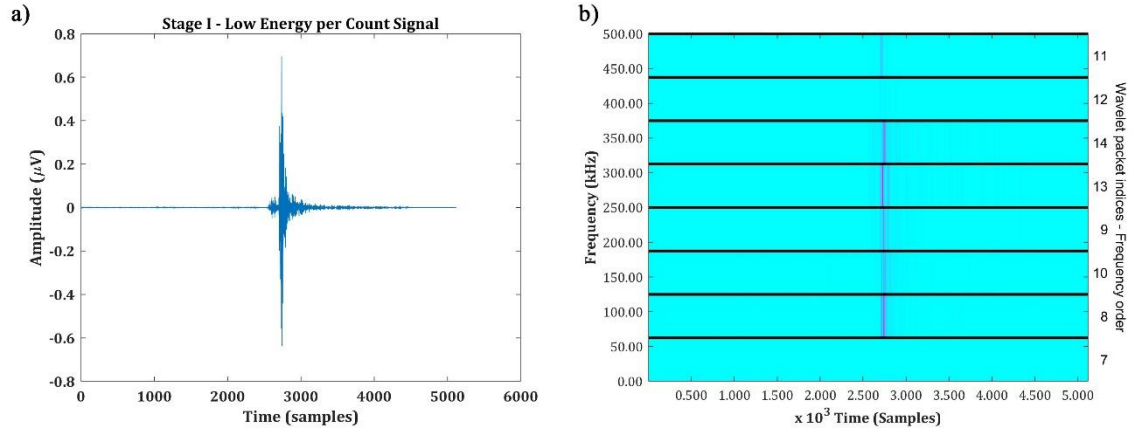
Figure 7.24. Low E_c signal recorded at Stage i a) Waveform Result b) WPT Result

The waveform and the WPT results of the low E_c signal in stage ii are presented in Figure 3. By comparing Figure 7.25(a) and 7.25(b), it can be seen that the waveform between time 2500 samples and 3000 samples in Figures 7.25(a) and 7.25(b) do not carry the majority of the spectral energy. So, the actual signal is shifted to the right in the time domain, indicating the delay in the acquisition. The maximum amplitude is around 0.85 µV and the maximum spectral energy is distributed in two bands: 26.94% in 250 kHz – 312.5 kHz and 39.30% in 312.5 kHz – 375 kHz. The delay in the acquisition, low amplitude and the energy distributed in high-frequency band suggests that the signal is generated due to the microcracking in the specimen or the friction between the specimen and the end grips. However, the results are inconclusive without any secondary damage monitoring capability for this stage.
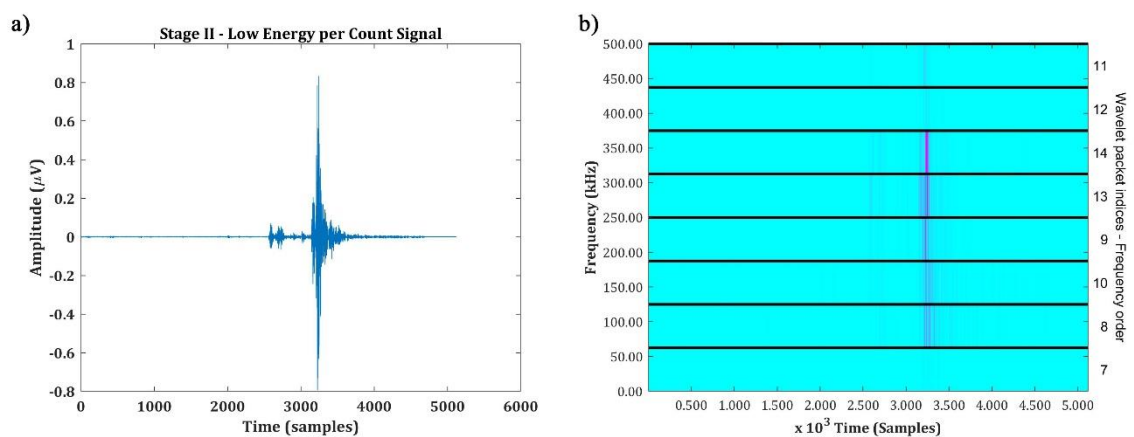
Figure 7.25. Low E_c signal recorded at Stage ii a) Waveform Result b) WPT Result

184

The waveform and the WPT results of the high E_c signal in stage ii are presented in Figure 7.26. The intensity of the signal between the time period 2500 and 3000 samples in Figure 7.26(b) suggests that the small decaying waveform at that time period is significant. In addition to that another similar signal with a very high amplitude of 8 μV can be observed in Figure 7.26(a). From Table 7.7, the maximum spectral energy is found to be centered around 125 kHz – 187.5 kHz with 54.46%. In this stage, the high E_c signal clearly distinguishes the signal generated from damage from the spurious signal associated with the friction in low E_c signal. Some shreds of evidence from other researchers can suggest that the low frequency can represent matrix cracking in FRP composites, however, the evidence are still inconclusive.
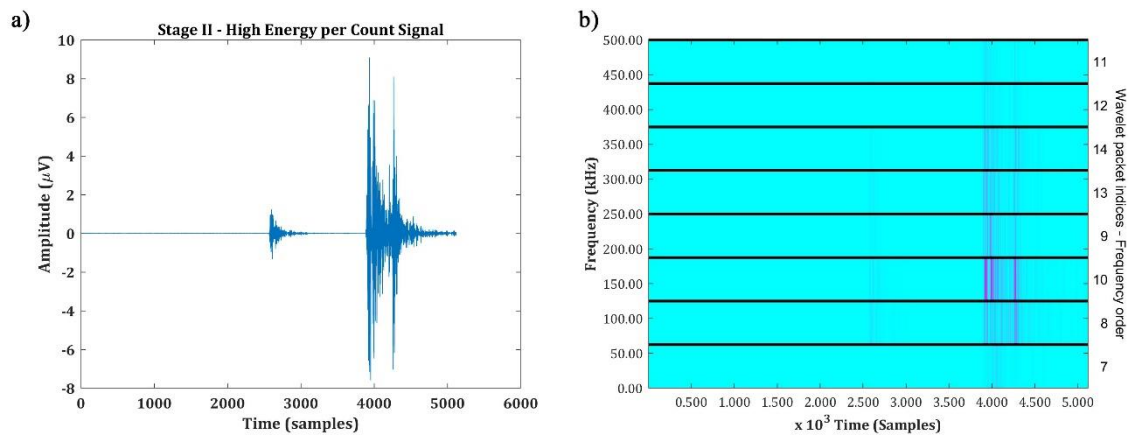
Figure 7.26. High E_c signal recorded at Stage ii a) Waveform Result b) WPT Result

The low E_c AE signal during stage iii – load drop is presented in Figure 7.27. It can be seen that the maximum amplitude of the signal is merely 0.07 μV and spectral energy is distributed in all frequency bands randomly (Table 7.7). Moreover, the spectral energy is spread out also in the time domain. This is a clear indication that this recorded signal is noise and does not represent any damage mode. It must be understood that this stage is also very short (1.17 s – 1.19 s) and very few AE signals can be found during this stage. Various signals, with low E_c value, are analyzed and repeatedly similar waveform and frequency spread is observed. This concludes that the low amplitude signals in stage iii are noise.
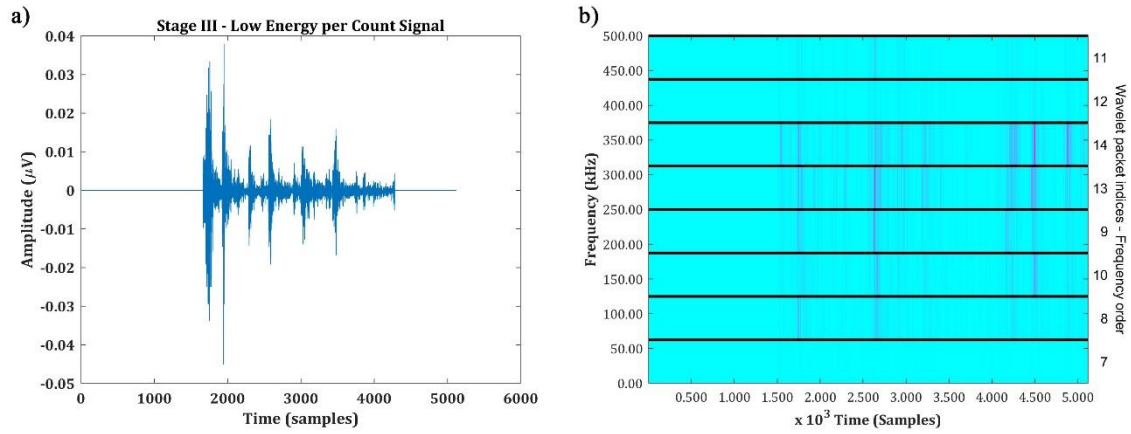
Figure 7.27. Low E_c signal recorded at Stage iii a) Waveform Result b) WPT Result

However, the high amplitude signal in stage iii is very peculiar. The signal is very narrow with a very short signal length and is shifted to the right in the time domain (Figure 7.28(a) and 7.28(b)). Moreover, the maximum spectral energy of this signal is distributed (about 43.37%) in the high-frequency band of 312.5 kHz – 375 kHz. This represents the lower order asymmetric AE signal, which carries high-frequency signal with a short duration and travels slowly before reaching the sensor. The lower order asymmetric signals are due to the interlaminar crack growth or delamination in the specimen. The load drop in Figure 1 also corroborates that significant damage occurred at this stage is the consequence of the load drop. However, the load drop is less than 0.25 kN (Figure 7.23). This means that the crack had initiated at one of the weakest ply but it could not propagate further. The material retains its load-bearing capability and moved to the linear elastic regime in stage iv.
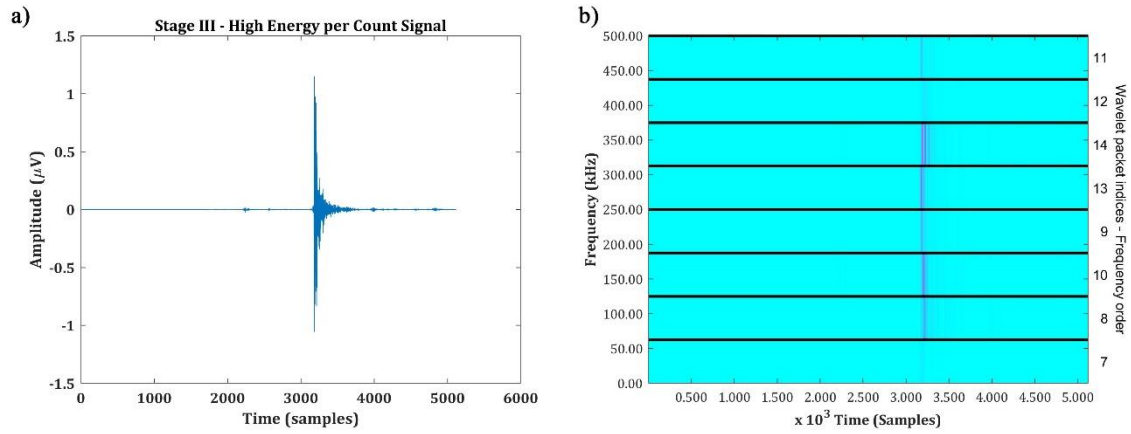
Figure 7.28. High E_c signal recorded at Stage iii a) Waveform Result b) WPT Result

The low E_c signal in stage iv – Linear plastic response is presented in Figure 7.29. The maximum amplitude of the signal in Figure 7.29(a) is very low, displaying a peak at 0.07 μV. The small decaying signals in the time domain before 2500 samples are all noise signals as they are insignificant due to their low amplitude. The spectral energy, however, is about 44.16% in the high-frequency band 312.5 kHz – 375 kHz. Once again, the signal recorded at low E_c turns out to be inconclusive as this frequency band and the low amplitude cannot be directly related to any of the damage modes.

Figure 7.29. Low E_c signal recorded at Stage iv a) Waveform Result b) WPT Result

The high amplitude signal in stage iv is very significant in the analysis. The signal is shifted to left in the time domain (Figure 7.30(a)) and the maximum of the energy content is distributed around 62.5 kHz – 135 kHz (Figure 7.30(b)). About 39.49% of energy is distributed in this frequency band (from Table 7.7). This represents the higher-order

187

symmetric AE signal, which is characterized by high speed and low frequency. This mostly is generated due to the consequence of matrix cracking and delamination. After the initial load drop in stage iii, the specimen started to damage through local matrix cracking and delamination, which can be characterized through this signal.

In stage v, there is a major load drop, accumulates for about 1.75 kN drop in the load before the material withheld its load-bearing capability. Only low E_c signals can be found in this region and are presented in Figure 7.31. The amplitude of the signal in Figure 7.31(a) is low, with the peak only at 0.125 µV. The narrow frequency band is associated with noise and has a maximum energy of about 45.34% centered around 312.5 kHz – 375 kHz (Figure 7.31(b) and Table 7.7). This signal represents the interlaminar crack growth during this load drop. Once again, very few signals can be found at this short stage which extends only for a time period of 1.36 s – 1.38 s and the presented waveform is the representative of most of the AE signals recorded at this stage.

Figure 7.30. High E_c signal recorded at Stage iv a) Waveform Result b) WPT Result
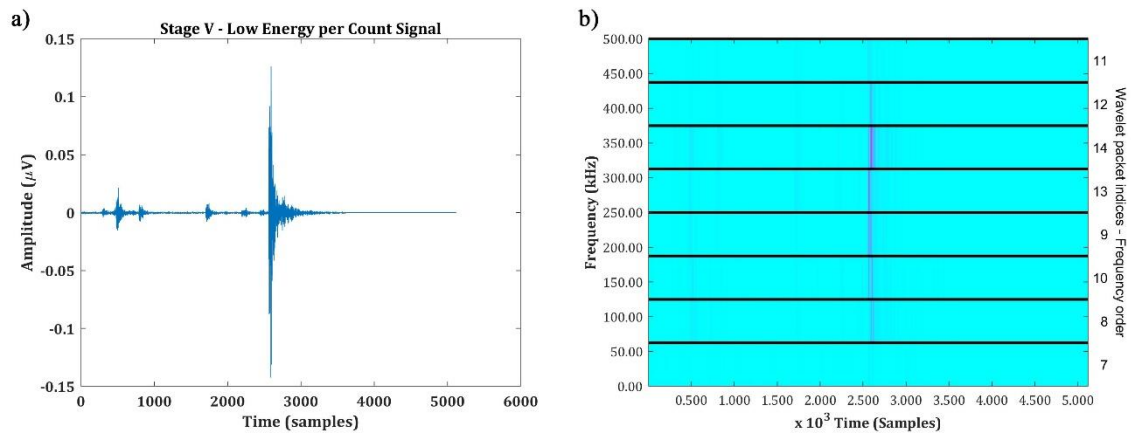
Figure 7.31. Low E_c signal recorded at Stage v a) Waveform Result b) WPT Result

Following this stage, the material shows a nonlinear response to the loading in stage vi for a period of 0.10 s (1.38 s to 1.48 s). Some researchers have reported that in riveted joints, sometimes, there will be the yielding of the rivets under loading before the crack starts to progress. The waveforms for the low E_c signal are presented in Figure 7.32. The signal is shifted to the left in the time domain and has a maximum amplitude of 0.225 µV in Figure 7.32(a). The spectral energy is distributed in all the bands except 0 – 132.5 kHz and 375 kHz – 500 kHz frequency bands (Figure 7.32(b) and Table 7.7). Once again, the low amplitude, random distribution of the frequency spectrum indicates that the signal with low E_c is inconclusive. Moreover, the reverberated signals can be found in Figure 7.32(a) after the initial waveform.
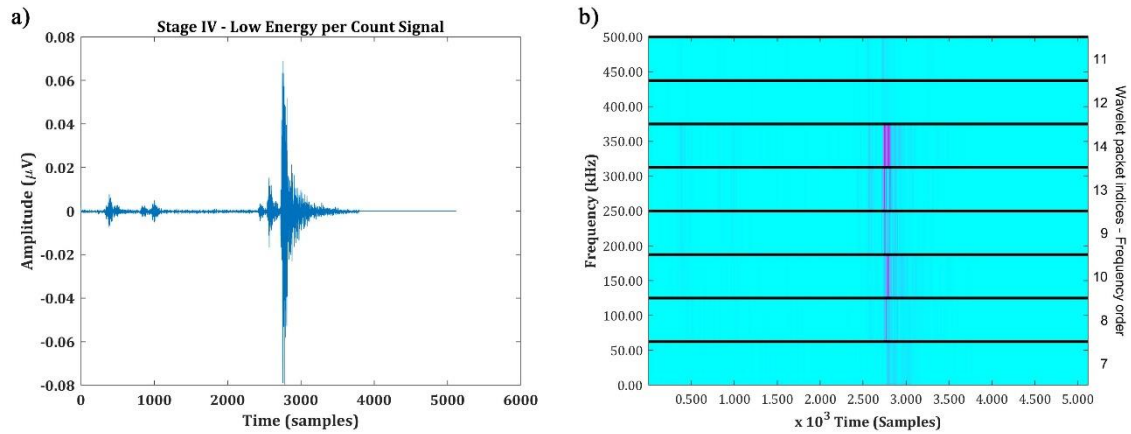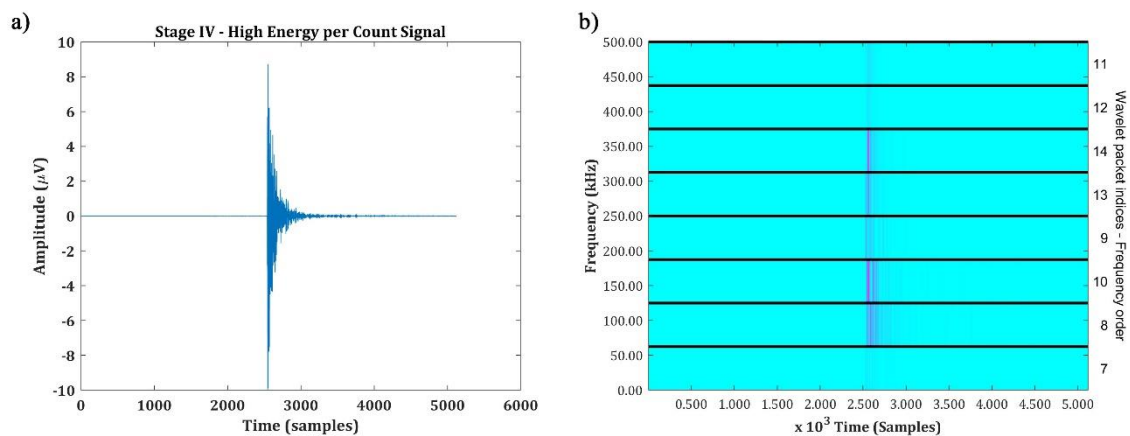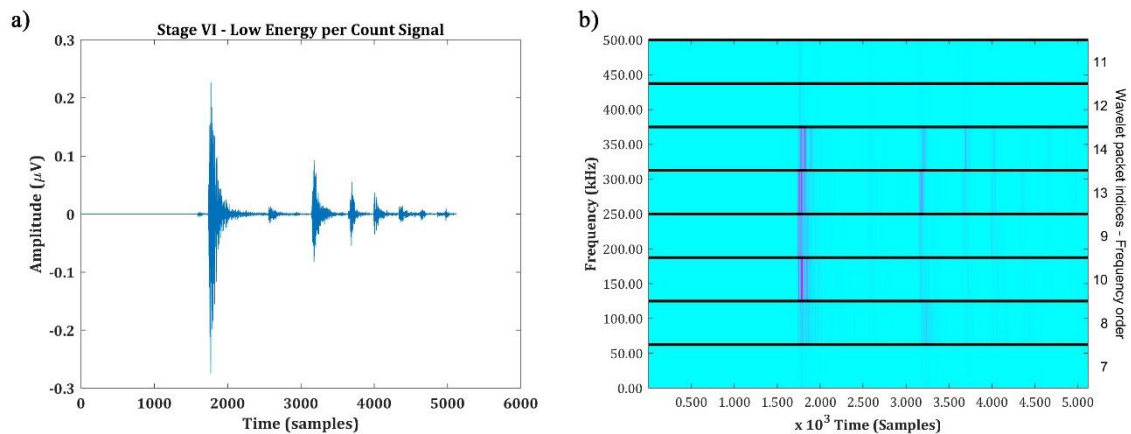

Figure 7.32. Low E_c signal recorded at Stage vi a) Waveform Result b) WPT Result

189

The high E_c signal in stage vi is presented in Figure 7.33. The signal is very short in its length and has a maximum amplitude of 10 μV (Figure 7.33(a)). From Figure 7.33(b), it can be seen that the frequency band is centered in the band 312.5 kHz – 375 kHz of about 51.84% (Table 7.7). The signal has high frequency and high amplitude indicating that this could possibly be the representative of the acoustic events generated by the rubbing of the rivet with the matrix and fiber bundles of the CFRP. However, conclusive evidence can be provided only by analyzing the damage mode using some other characterizing tool. Though a conclusion can be made from these results that the specimen had suffered some major damage in stage vi but owing to the presence of the rivet, it carries the load for a period of time before fracture.
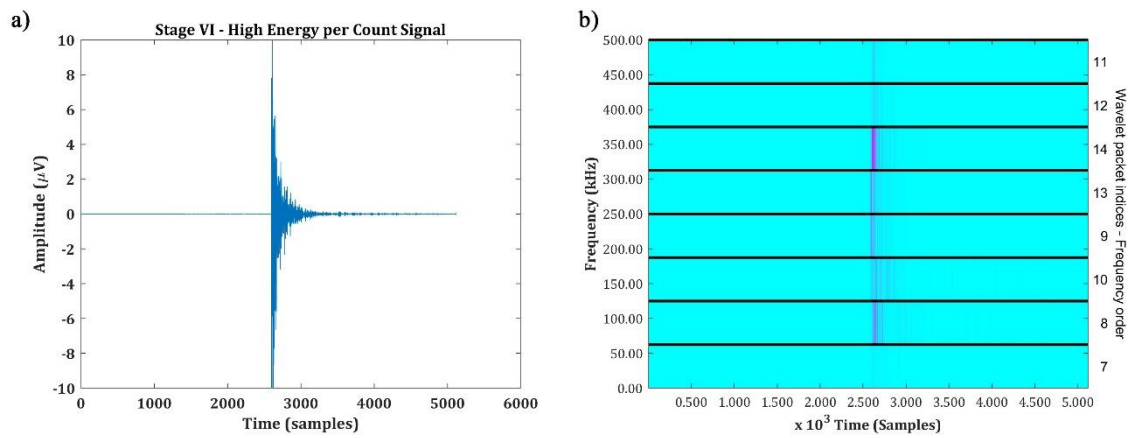
Figure 7.33. High E_c signal recorded at Stage vi a) Waveform Result b) WPT Result

In stage vii, the material shows a linear load response before failure. Thus, the signals must be the representations of the damage accumulation before failure. The low E_c signal is presented in Figure 7.34. The maximum amplitude is only 0.65 μV in Figure 7.34(a). The spectral energy in Figure 7.34(b) is distributed in two frequency bands: 41.90% of energy in 62.5 kHz – 135 kHz and 24.88% of energy in 125 kHz – 187.5 kHz (Table 7.7).
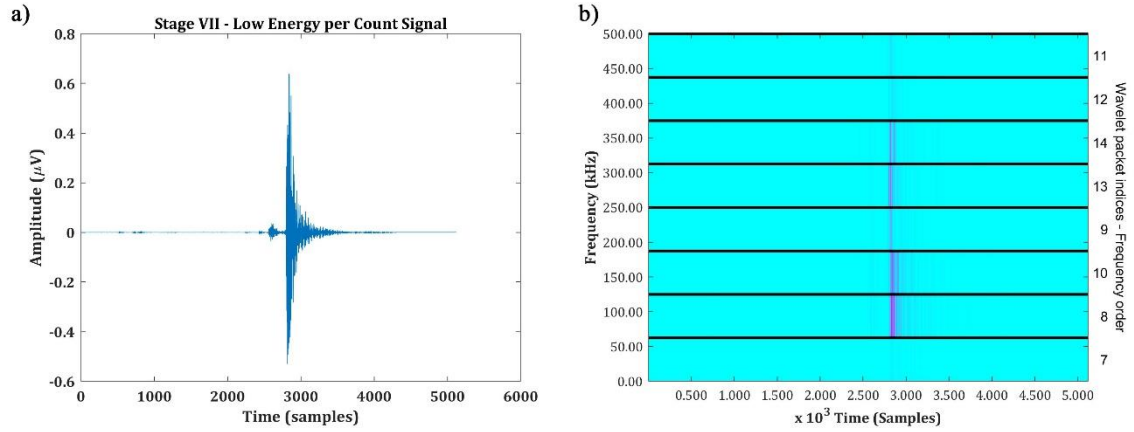
Figure 7.34. Low E_c signal recorded at Stage vii a) Waveform Result b) WPT Result

Similarly, the high E_c signal from stage vii shows two amplitude peaks in Figure 7.34(a) with one at 9.5 µV and another at 7.5 µV. In Figure 7.34(b), the maximum frequency band is also distributed in two frequency bands: 38.33% in 312.5 kHz – 375 kHz and 21.25% in 250 kHz – 312.5 kHz. Both these signals have one similarity that they have multiple load peaks in the amplitude of the waveform and the energy is distributed in two different frequency spectrums, although the frequency bands are different. The damage mode cannot be conclusively identified; however, a definite difference can be drawn between the linear responses in stage ii, stage iv and stage vii. The damage mode certainly did not generate lower-order asymmetric AE signal, which means that the damage mode is not matrix cracking. The material responded to several accumulated damage modes in stage vii before failure.
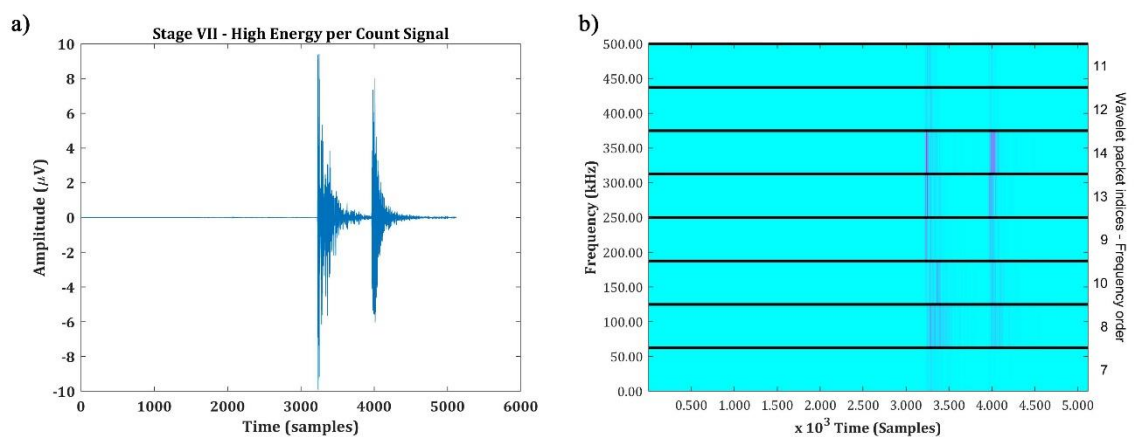
Figure 7.35. High E_c signal recorded at Stage vii a) Waveform Result b) WPT Result

During the final fracture stage at stage viii, only low amplitude signals can be found. The waveforms and the WPT results of the signal recorded from this stage are presented in Figure 7.36(a) and 7.36(b), respectively. During the fracture, two amplitude peaks can be observed in the two time domains and most of the spectral energy is distributed in the high-frequency band 250 kHz – 375 kHz. The signal observed from this load drop is entirely different from the signal observed from the load drops in stage iii and stage v.
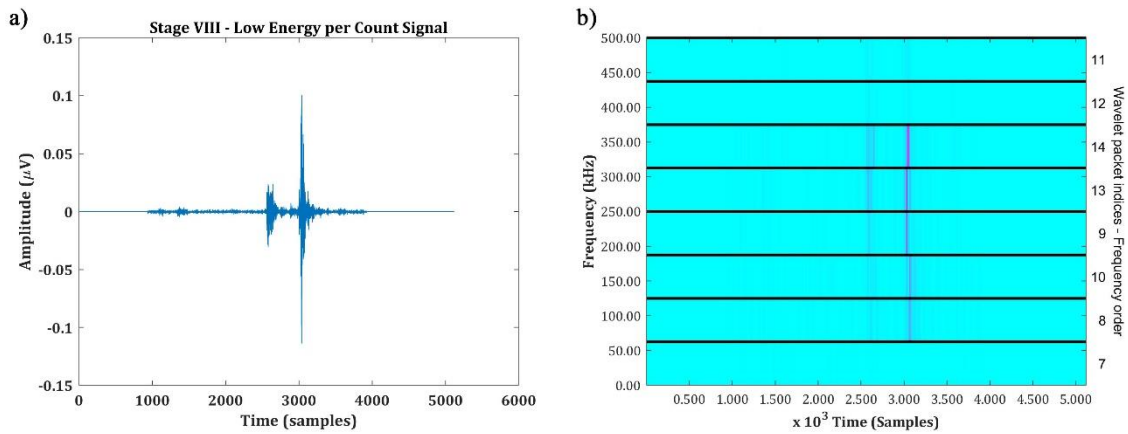
Figure 7.36. Low E_c signal recorded at Stage viii a) Waveform Result b) WPT Result

The following conclusions can be drawn from the observed results of all the waveforms and WPT results from different stages. The signals with low E_c always turn out to have inconclusive results. During a loading, a large number of AE signals are generated, each carrying their own distinct waveform. It is difficult to analyze all the waveforms in the time-frequency domain using WPT, due to the large time consumption and excessive data storage. Only a few signals can be chosen, and they can act the representative of that stage during loading. In that regard, the E_c serves the purpose that the signals selected from E_c > 1 always draw definite conclusions about the damage mode. This value is relative in the sense that it can vary from tests to tests. Nonetheless, signals with a considerably high value of E_c must be taken for the analysis. Through that, the damage modes can be assessed through the waveforms and wavelet transforms.

This concludes the section, which describes E_c as a powerful selection criterion for waveform analysis. These are the two methods of using this newly developed parameter for the damage assessment.

192

7.5 CONCLUSION

This chapter summarizes the basic methods of using acoustic energy for mechanical characterization and damage assessment of materials. This includes the usage of cumulative acoustic energy for identifying the critical points of failure, sentry function, which is the only logical relation between the acoustic and mechanical data. However, the core concept of this chapter is the introduction of a new parameter called Energy per Count. This parameter is used in two different ways: damage assessment as an independent parameter and selection criterion for waveform analysis. When the Energy per Count is used as an independent parameter, it is used co-independently with cumulative counts, cumulative energy and amplitude distribution. This is because these supporting parameters are used for validating the performance of the Energy per Count. Secondly, this parameter is used as a selection criterion for waveform analysis. It is concluded that the waveforms from each stage of damage mode must be selected only for the AE events with the Energy per Count value above certain limits. Then these selected waveforms clearly represent the characteristic damage state and the damage modes can be assessed.

CHAPTER 8
CONCLUSION

This chapter presents the concluding remarks of the research activities carried out in this presented thesis. This chapter also presents an overview of all the novel parameters and methods used throughout this research work, while also addressing the future scope for the topic discussed. All the key findings are also highlighted in this section.

The objective of this research work is to use Acoustic Emission (AE) technique for describing the structural materials' characteristics and their different damage modes under different types of loading. The structural materials focussed on this research work are based upon the requirements of aerospace industries. Two types of structural materials are characterized: Carbon Fiber Reinforced Polymer (CFRP) composites and Selective Laser Melted (SLM) materials.

Various experimental campaigns are organized for understanding the behaviour of these materials in their different configurations under different types of loadings. The configurations and the types are loadings are based upon the requirements of the industry, but the AE technique is used for a better understanding of the damage modes.

The first part of this research work is focussed on the acoustic waveforms. The different types of waveform processing techniques from the state of the art of signal processing are explored. The different waveform processing techniques used are Wavelet Transform (WT) and Empirical Mode Decomposition (EMD). While the WT can be categorized into several methods such as Continuous Wavelet Transform (CWT), Discrete Wavelet Transform (DWT) and Wavelet Packet Decomposition (WPT), the EMD is based upon the instantaneous frequency measured using Hilbert-Huang Transform (HHT). During the experimental campaign, the advantages and limitations of using these different waveform processing tools are explored. It is concluded that the WPT and EMD/HHT are supposedly very powerful in processing the waveform analysis, albeit each of them has their own advantage and limitations. The WPT can provide greater information about the damage

modes of materials in their time-frequency domain. It can clearly depict the spectral energy associated with each band of damage mode. The HHT, on the other hand, provides instantaneous frequency and not the details about the time-frequency domain. Some of the key findings using these two methods are as follows:

- The Double Cantilever Beam (DCB) specimens (prepared using CFRP) subjected to mode I delamination is analyzed in their time-frequency domain. The spectral energy content calculated using WPT is used for classifying the different damage modes. The frequency band of the AE signals recorded during the initial stages of loading is mostly around 100 kHz to 150 kHz, which represents the matrix cracking. Similarly, during the critical damage state of the DCB specimens, most of AE signals have frequency band centred around 200 kHz to 250 kHz, which represents debonding or delamination. Finally, during the ultimate failure of the materials, most of the AE signals have a frequency above 250 kHz, which is associated with the fiber breakage or interlaminar delamination.

- The SLM – additively manufactured specimens built with AlSi10Mg, is tested under static tensile loading. The damage modes are assessed by the EMD/HHT analysis. The AE signals released due to the grain boundary movements during the initial stages of loading have an instantaneous frequency of 200 kHz. The yielding of the material, dislocation motions release AE signals with an instantaneous frequency around 200 kHz to 250 kHz. Finally, the micro-void opening or the crack growth releases AE signals with an instantaneous frequency of 150 kHz to 200 kHz.

The EMD/HHT is chosen over WPT in the case of SLM materials is because the AE signals released from the metallic specimens are very narrow and have very short time domain. Thus, finding the instantaneous frequency is deemed better over analyzing the time-frequency domain.

The next part of the research work is the introduction of a new approach called Acousto-Ultrasonic. This method is based on the attenuation of the AE signals due to their dispersion behaviour owing to the propagating medium. The Acousto-Ultrasonic

approach is used for characterizing the interlaminar fracture toughness and the residual strength of CFRP composites subjected to drop-weight impact. The CFRP composite with and without the Barely Visible Impact Damage (BVID), as a consequence of the drop-weight impact event is studied using this method.

For studying the waveforms, a hybrid approach is introduced, which is based on the combination of the WPT and EMD. The AE signals are decomposed using EMD and are then reconstructed by removing the noise signal. This helps in lowering the noise level of the recorded signal. Then the spectral analysis using WPT is used for understanding the interlaminar strength and the residual strength of the material. The key findings of this research works are as follows:

- It is possible to identify the direction (longitudinal or transverse) along which the CFRP laminate composites have low interlaminar strength using Acousto-Ultrasonic approach. This is possible through the percentage of energy loss and the amplitude loss in the propagating acoustic wave along the particular direction. Besides, the experimental results show that the direction along which the material had low interlaminar strength suffered more damage.

- The extent of the BVID damage can be qualitatively assessed using the hybrid approach using WPT/EMD adopted. The spectral energies of different frequency bands are analyzed and the propagation of the AE signals along the fiber or the matrix can be identified from the spectral energies. Through that, the extent of damage, either on the matrix or the fiber, can be identified.

The next part of this research work focuses on the data clustering of the AE parameters. This is based on the observations that analyzing an AE parameter solitarily can lead to biased results as several factors affect the acquisition of AE parameters. For this reason, more than one AE parameter must be employed. The data clustering using an unsupervised pattern recognition approach called k-means++ data clustering method is used. Five different AE descriptors recorded from DCB test of CFRP specimens are analyzed. The five descriptors studied as amplitude, frequency centroid, counts, risetime

and duration. The different damage modes during the progress of the loading is assessed by using these multi-parameter approach.

A new parameter is introduced in the next part of the research work for the mechanical characterization of the SLM materials prepared using AlSi10Mg alloy. This new parameter is a slope coefficient, named as b_{AE}-value, which is based on the linear relationship between the cumulative counts and cumulative energy of AE events recorded during the loading history of a static tensile test. The key findings are indicated as follows:

- A set of hypotheses is formed for describing the material characteristics during the course of loading. The sudden increase in the b_{AE}-value represents the matrix cracking or the dislocation movements under straining during the loading. The gradual increase in the b_{AE}-value represents that the material is progressing through its yielding stage or the crack has started nucleating through the micro voids. The rapid increase in the b_{AE}-value represents the sudden liberation of energy, which can be related to the crack growth in the material. Finally, if the b_{AE}-value remains constant, the material is progressing towards the failure.
- The hypothesis is proved by comparing the results with the microscopic analysis and by testing different configurations of the SLM specimens tested. The results coincide also with the results obtained from the instantaneous frequency measured using EMD/HHT analysis.

The final part of the research work introduces another new parameter called energy per count. This parameter is based on the energy of an AE signal for a single count recorded in the hit. This new parameter is used in two different modes:

- The energy per count is used directly for understanding the damage behaviour in Single Lap Shear (SLS) specimens prepared using CFRP laminates. This parameter is then clustered using k-means++ data clustering technique and used for understanding the damage behaviour of the specimens.
- The energy per count is used as a parameter for selecting the representative waveform from the entire AE waveform dataset. This proves to be successful as

the AE signals with the energy per count value less than 1 mostly are noise, while the AE signals with energy per count value above 1 shows the characteristic damage state.

This concludes the research activities completed during the course of this thesis work. Several new parameters and new methodologies for optimizing the AE technique has been introduced. The methods used are aimed at breaking the limitation barrier of the AE technique.

The future scope of this work will focus on addressing the limitations of the AE technique and attempting to rectify them. A new parameter called Renyi's entropy will be introduced as a part of the future work, which will reduce the problem involving the AE noise to some extent. Besides, the validity of the new parameters and the new techniques will be tested against a large variety of structural materials. In addition to that, the numerical analysis and the finite element modelling will also be useful for understanding the wave propagation attenuation.

BIBLIOGRAPHY

Aggelis DJ, Barkoula NM, Matikas TE, Paipetis AS. Acoustic structural health monitoring of composite materials: Damage identification and evaluation in cross ply laminates using acoustic emission and ultrasonics. Compos Sci Tech 2012;72(10):1127-1133.

Akaike H. Markovian representation of stochastic processes and its application to the analysis of autoregressive moving average processes. Ann Inst Stat Math 1974;26:363-387.

Akbari M, Ahmadi M. The application of acoustic emission technique to plastic deformation of low carbon steel. Physics Proc 2010;3:795-801.

Alam SY, Loukilli A. Transition from energy dissipation to crack openings during continuum–discontinuum fracture of concrete. Int J Fract 2017;206:49–66.

Alia A, Fantozzi G, Godin N, Osmani H, Reynaud P. Mechanical behaviour of jute fibre-reinforced polyester composite: Characterization of damage mechanisms using acoustic emission and microstructural observations. J Compos Mater 2019 (published online) https://doi.org/10.1177%2F0021998318822128

Anastassopoulos A, Philippidis TP. Clustering methodology for evaluation of acoustic emission from composites. J Acoust Emiss 1995;13:11-22.

ASTM D5868-01(2014), Standard Test Method for Lap Shear Adhesion for Fiber Reinforced Plastic (FRP) Bonding, ASTM International, West Conshohocken, PA, 2014, www.astm.org

ASTM D7136 / D7136M-15, Standard Test Method for Measuring the Damage Resistance of a Fiber-Reinforced Polymer Matrix Composite to a Drop-Weight Impact Event, ASTM International, West Conshohocken, PA, 2015, www.astm.org

ASTM D7137 / D7137M-17, Standard Test Method for Compressive Residual Strength Properties of Damaged Polymer Matrix Composite Plates, ASTM International, West Conshohocken, PA, 2017, www.astm.org

ASTM E8 / E8M-16ae1, Standard Test Methods for Tension Testing of Metallic Materials, ASTM International, West Conshohocken, PA, 2016, www.astm.org

ASTM E976-15, Standard Guide for Determining the Reproducibility of Acoustic Emission Sensor Response, ASTM International, West Conshohocken, PA, 2015, www.astm.org

Awerbuch J, Ghaffari S. Monitoring Progression of Matrix Splitting During Fatigue Loading Through Acoustic Emission in Notched Unidirectional Graphite/Epoxy Composite. J Reinf Plast Comp 1988;7(3):245-264.

Awerbuch J, Madhukar M, Gorman MR. Monitoring Damage Accumulation in Filament-Wound Graphite/Epoxy Laminate Coupons During Fatigue Loading Through Acoustic Emission. J Reinf Plast Comp 1984;3(1):2-39.

Baker C, Morscher GN, Pujar VV, Lemanski JR. Transverse cracking in carbon fiber reinforced polymer composites: Modal acoustic emission and peak frequency analysis. Compo Sci Tech 2015;116:26-32.

Balázs GL, Grosse C, Koch R, Reinhardt HW. Damage accumulation on deformed steel bar to concrete interaction detected by acoustic emission technique. Mag of Concrete Research 1996;48:311-320.

Barile C, Casavola C, Pappalettera G, Vimalathithan P.K. Acousto-ultrasonic evaluation of interlaminar strength on CFRP laminates. Compos Struct 2019;280:796-805.

Barile C, Casavola C, Pappalettera G, Vimalathithan PK. Experimental wavelet analysis of acoustic emission signal propagation in CFRP. Eng Fract Mech 2019;210:400-407.

Barile C, Casavola C, Pappalettera G. Acoustic emission waveform analysis in CFRP under Mode I test. Eng Fract Mech 2019;210:408-413.

Baxter MG, Pullin R, Holford KM, Evans SL. Delta T source location for acoustic emission. Mech Syst Signal Process, 2007;21(3):1512-1520.

Beaumont PWR, Zweben CH. Polymer Matrix Composites: Applications. In: Beaumont PWR, Zweben CH. Comprehensive Composite Materials. Elsevier, 2018, Volume 3.

Beaumont PWR, Zweben CH. Polymer Matrix Composites: Fundamentals. In: Beaumont PWR, Zweben CH. Comprehensive Composite Materials. Elsevier, 2018, Volume 2.

Botvina LR, Tyutin MR, New acoustic parameter characterizing loading history effects. Eng Fract Mech 2019;210:358-366.

Botvina LR, Tyutin MR, Petersen TB, Levin VP, Soldatenkov AP, Prosvirnin DV, Residual Strength, Microhardness, and Acoustic Properties of Low-Carbon Steel after Cyclic Loading. J Mach Manuf Reliab 2018;47:516-524.

Broutman LJ, Krock RH. Modern Composite Materials. In: Krock, Editor. Reading, Mass: Addison-Wesley, 1967. p.266.

Campanelli SL, Casalino G, Contuzzi N, Angelastro A, Ludovico AD. Analysis of the molten/solidified zone in selective laser melted parts. In: Proceedings of SPIE - The International Society for Optical Engineering, San Francisco, CA, United States, 2014.

Carpinteri A, Lacidogna G, Paggi M. Acoustic emission monitoring and numerical modeling of FRP delamination in RC beams with non-rectangular cross-section. Mater Struct 2007;40:553-566.

Carpinteri A, Lacidogna G, Puzzi S. From criticality to final collapse: Evolution of the "b-value" from 1.5 to 1.0. Chaos Soliton Fract 2009;41(2):843-853.

Cesari F, Dal Re V, Minak G, Zucchelli A. Damage and residual strength of laminated graphite-epoxy composite circular plates loaded at the centre. Compos Part A-Appl S 2007;38(4):1163-1173.

Ceysson O, Salvia M, Vincent L. Damage mechanisms characterisation of carbon fibre/epoxy composite laminates by both electrical resistance measurements and acoustic emission analysis. Scr Mater 1996;34(8):1273–1280

Chandarana N, Sanchez DM, Soutis C, Gresil M. Early Damage Detection in Composites during Fabrication and Mechanical Testing. Materials 2017;10(7):685.

Chen O, Karandikar P, Takeda N, Rcast TK. Acoustic emission characterization of a glass–matrix composite. Nondestruct Test Eval 1992;8:869–878.

Chowdhury NM, Chiu WK, Wang J, Chang P. Static and fatigue testing thin riveted, bonded & hybrid carbon fiber double lap joints used in aircraft structures. Compos Struct 2015;121:315-323.

Chowdhury NM, Chiu WK, Wang J, Chang P. Experimental and finite element studies of thin bonded and hybrid carbon fibre double lap joints used in aircraft structures. Compos Part B-Eng 2016;85:233-242.

Davijani AA, Hajikhani M, Ahmadi M. Acoustic emission based on sentry function to monitor the initiation of delamination in composite materials. Mater Des 2011;32:3059–65.

de Groot PJ, Wijnen PAM, Janssen RBF. Real-time frequency determination of acoustic emission for different fracture mechanisms in carbon/epoxy composites. Compos Sci Tech 1995;55(4):405-412.

Downs KS, Hamstad MA. Acoustic emission from depressurization to detect/evaluate significance of impact damage to graphite/epoxy pressure vessels. J Compos Mater 1998;32(3):258-306.

El Batanouny MK, Larosche A, Mazzoleni P, Ziehl PH, Matta F, Zappa E. Identification of Cracking Mechanisms in Scaled FRP Reinforced Concrete Beams using Acoustic Emission. Exp Mech 2014;54(1):69-82.

Feynman P, Leighton R, Sands M. The feynman lectures on physics. Am J Phy 1965;33(9):750-752.

Finkel P, Mitchell JR, Carlos MF. Experimental study of 'Auto Sensor Test-Self Test Mode' for acoustic emission system performance verification. AIP Conf Proc 2000;509:1995–2002.

Fotouhi M, Pashmforoush F, Ahmadi M, Oskouei AR. Monitoring the initiation and growth of delamination in composite materials using acoustic emission under quasi-static three-point bending test. J Reinf Plast Compos 2011;30(17):1481–1493.

Fotouhi M, Sadeghi S, Jalalvand M, Ahmadi M. Analysis of the damage mechanisms in mixed-mode delamination of laminated composites using acoustic emission data clustering. J Thermoplast Compos 2017;30(3):318-340.

Fotouhi M, Saeedifar M, Sadeghi S, Najafabadi MA, Minak G. Investigation of the damage mechanisms for mode I delamination growth in foam core sandwich composites using acoustic emission. Struct Health Monit 2015;14(3):265–280.

Gillis PP. Dislocation motions and acoustic emissions. In: Liptai R, Harris D, Tatro C, Editors. Acoustic Emission, ASTM STP 505. West Conshohocken, PA: ASTM International, 1972. p.20-29.

Godin N, Huguet S, Gaertner R, Salmon L. Clustering of acoustic emission signals collected during tensile tests on unidirectional glass/polyester composite using supervised and unsupervised classifiers. NDT&E Int 2004;37(4):253-264.

Gong XL, Laksimi A, Benzeggagh M. Nouvelle approche de l'émission acoustique et son application à l'identification des mécanismes d'endommagement dans les matériaux composites. Rev Compos Matér Av 1998;8(1):179–205

Grosse C. Introduction. In: Grosse C., Ohtsu M. (eds) Acoustic Emission Testing. Springer, Berlin, Heidelberg, 2008.

Grosse C, Linzer L. Signal-Based AE Analysis. In: Grosse C., Ohtsu M. (eds) Acoustic Emission Testing. Springer, Berlin, Heidelberg, 2008.

Gutenberg B, Richter CF. Seismicity of the Earth and associated phenomena. Princeton University Press, 1949.

Gutkin R, Green CJ, Vangrattanachai S, Pinho ST, Robinson P, Curtis PT. On acoustic emission for failure investigation in CFRP: Pattern recognition and peak frequency analyses. Mech Sys Signal Pr 2011;25(4):1393-1407.

Habibi M, Lebrun G, Laperrière L. Experimental characterization of short flax fiber mat composites: tensile and flexural properties and damage analysis using acoustic emission. J Mater Sci 2017;52(11):6567-6580.

Hamstad MA. Thirty years of advances and some remaining challenges in the application of acoustic emission to composite materials. In: Kishi T, Ohtsu M, Yuyama S, Editors. Acoustic Emission - Beyond the Millennium, Elsevier, Oxford, UK, 2000. p.77-91.

Harris DO, Bell RL. The measurement and significance of energy in acoustic-emission testing. Exp Mech 1977;17:347-353.

Harris DO, Tetelman AS, Darwish FA. Detection of fiber cracking by acoustic emission. In: Liptai R, Harris D, Tatro C, Editors. Acoustic Emission, ASTM STP 505. West Conshohocken, PA: ASTM International, 1972. p.238-249.

Hotelling H. Analysis of a complex of statistical variables into principal components. Journal of educational psychology. 1933 Sep;24(6):417.

Huang NE, Shen Z, Long SR, Wu MC, Shih HH, Zheng Q, Yen N, Tung CC, Liu HH, The empirical mode decomposition and the Hilbert spectrum for nonlinear and non-stationary time series analysis. Proc R Soc Lond A 1998;454:903-995.

Jong HJ. Transverse cracking in a cross-ply composite laminate—Detection in acoustic emission and source characterization. J Compos Mater 2006;40:37–69.

Kalteremidou KA, Murray BR, Tsangouri E, Aggelis DG, Van Hemelrijck D, Pyl L. Multiaxial Damage Characterization of Carbon/Epoxy Angle-Ply Laminates under Static Tension by Combining In Situ Microscopy with Acoustic Emission. Appl Sci 2018;8(11):2021.

Kempen K, Thijs L, Van Humbeeck J, Kruth JP. Mechanical properties of AlSi10Mg produced by Selective Laser Melting. Physics Proc 2012;39:439–446.

Kempf M, Skrabala O, Alstädt V. Acoustic emission analysis for characterisation of damage mechanisms in fibre reinforced thermosetting polyurethane and epoxy. Compos Part B-Eng 2014;56:477-483.

Kiesewetter K, Schiller P. The acoustic emission from moving dislocations in aluminium. Phys Status Solidi A 1976;38(2):569-576.

Kharrat M, Ramasso E, Placet V, Boubakar ML. A signal processing approach for enhanced Acoustic Emission data analysis in high activity systems: Application to organic matrix composites. Mech Syst Signal Pr 2016;70-71:1038-1055.

Kim ST, Lee YT. Characteristics of damage and fracture process of carbon fiber reinforced plastic under loading-unloading test by using AE method. Mater Sci Eng A 1997;234-236: 322–326.

Kishore AN, Prasad NS. An experimental study of Flat-Joggle-Flat bonded joints in composite laminates. Int J Adhes Adhes 2012;35:55–58.

Komai K, Minoshima K, Shibutani T. Investigations of the fracture mechanism of carbon/epoxy composites by AE signal analyses. JSME Int J 1991;34:381–388.

Kotsikos G, Evans J, Gibson A, Hale J. Use of acoustic emission to characterize corrosion fatigue damage accumulation in glass fiber reinforced polyester laminates. Polym Compos 1999;20(5):689–696

Kotsikos G, Evans JT, Gibson AG, Hale J. Use of acoustic emission to characterize corrosion fatigue damage accumulation in glass fiber reinforced polyester laminates. Polym Compos 1999;20:689–696.

Li L, Lomov SV, Yan X, Carvelli, V. Cluster analysis of acoustic emission signals for 2D and 3D woven glass/epoxy composites. Compos Struct 2014;116:286–299.

Li L, Swolfs Y, Straumit I, Yan X, Lomov SV. Cluster analysis of acoustic emission signals for 2D and 3D woven carbon fiber/epoxy composites. J Compos Mater 2016;50(4):1921-1935.

Liptai RG. Acoustic emission from composite materials. In. Corten H, Editors. Composite Materials: Testing and Design, ASTM STP 497. West Conshohocken, PA: ASTM International, 1972. p.285-298.

Liptai RG, Harris DO, Tatro CA. An introduction to acoustic emission. In: Liptai R, Harris D, Tatro C, Editors. Acoustic Emission, ASTM STP 505. West Conshohocken, PA: ASTM International, 1972. p.3-10.

Lissek F, Haeger A, Knoblauch V, Hloch S, Pude F, Kaufeld M. Acoustic emission for interlaminar toughness testing of CFRP: Evaluation of the crack growth due to burst analysis. Compos Part B-Eng 2018;136:55-62.

Liu PF, Chu JK, Liu YL, Zheng JY. A study on the failure mechanisms of carbon fiber/epoxy composite laminates using acoustic emission. Mater Design 2012;37:228-235.

Maćkiewicz A, Ratajczak W. Principal components analysis (PCA). Computers & Geosciences. 1993 Mar 1;19(3):303-42.

Mailet E, Baker C, Morscher GN, Pujar VV, Lemanski JR. Feasibility and limitations of damage identification in composite materials using acoustic emission. Compos Part A-Appl S 2015;75:77-83.

Maillet E, Morscher GN. Waveform-based selection of acoustic emission events generated by damage in composite materials. Mech Sys Signal Process 2015;52:217-227.

McCrory JP, Al-Jumaili SK, Crivelli D, Pearson MR, Eaton MJ, Featherston CA, Guagliano M, Holford KM, Pullin R. Damage classification in carbon fibre composites using acoustic emission: A comparison of three techniques. Compos Part B-Eng 2015;68:424-430.

Meraghni F, Benzeggagh M. Micromechanical modelling of matrix degradation in randomly oriented discontinuous-fibre composites. Compos Sci Technol 1995;55:171–186

Minak G, Zucchelli A. Damage evaluation and residual strength prediction of CFRP laminates by means of acoustic emission techniques. In: Durand LP, editor. Composite Materials Research Progress. New York: Nova Science Publishers Inc, 2008. p.165-207

Mirmiran A, Philip S. Comparison of acoustic emission activity in steel-reinforced and FRP-reinforced concrete beams. Constr Build Mater 200;14:299-31.

Mohammadi R, Najafabadi MA, Saeedifar M, Yousefi J, Minak G. Correlation of acoustic emission with finite element predicted damages in open-hole tensile laminated composites. Compos Part B-Eng 2017;108:427-435.

Mohammadi R, Saeedifar M, Toudeshky HH, Najafabadi MA, Fotouhi M. Prediction of delamination growth in carbon/epoxy composites using a novel acoustic emission-based approach. J Reinf Plast Compos 2015;34(11):868–878.

Njuhovic E, Bräu M, Wolff-Fabris F, Starzynski K, Altstädt V. Identification of failure mechanisms of metallised glass fibre reinforced composites under tensile loading using acoustic emission analysis. Compos Part B-Eng 2015;81:1-13.

Oskouei AR, Zucchelli A, Ahmadi M, Minak G. An integrated approach based on acoustic emission and mechanical information to evaluate the delamination fracture toughness at mode I in composite laminate. Mater Design 2011;32(3):1444-1455.

Oz FE, Ersoy N, Lomov SV. Do high frequency acoustic emission events always represent fibre failure in CFRP laminates? Compos Part A-Appl S 2017;103:230-235.

Philippidis TP, Assimakopoulou TT. Using acoustic emission to assess shear strength degradation in FRP composites due to constant and variable amplitude fatigue loading. Compos Sci Tech 2008;68(3-4):840-847.

Pollock AA, Cook WJ. Technical Report DE 76-10, Dunegan/Enderco, San Juan Capistrano, CA, 1976.

Raj B, Jha BB, Rodriguez P, Frequency spectrum analysis of acoustic emission signal obtained during tensile deformation and fracture of an AISI 316 type stainless steel. Acta Metall 1989;37(8):2211-2215.

Ramirez-Jimenez CR, Papadakis N, Reynolds N, Gan TH, Purnell P, Pharaoh M. Identification of failure modes in glass/polypropylene composites by means of the

primary frequency content of the acoustic emission event. Compos Sci Tech 2004;64(12):1819-1827.

Reifsnider KL, Masters JE. Investigation of characteristic damage states in composite laminates. In: Reifsnider K, Editors. Damage in Composite Materials: Basic Mechanisms, Accumulation, Tolerance, and Characterization, ASTM STP 775. West Conshohocken, PA: ASTM International, 1972. p.40-62.

Romhány G, Szebényi G. Interlaminar fatigue crack growth behavior of MWCNT/carbon fiber reinforced hybrid composites monitored via newly developed acoustic emission method. Express Polym Lett 2012;6(7):572-580.

Rouby D, Flieschmann P. Spectral analysis of acoustic emission from aluminium single crystals undergoing plastic deformation. Phys Status Solidi 1978;48(2):439-445.

Roundi W, El Mahi A, El Gharad A, Rebiere J. Acoustic emission monitoring of damage progression in Glass/Epoxy composites during static and fatigue tensile tests. Appl Acoust 2018;132:124-134.

Saeedifar M, Fotouhi M, Najafabadi MA, Toudeshky HH, Minak G. Prediction of quasi-static delamination onset and growth in laminated composites by acoustic emission. Compos Part B-Eng 2016;85:112-122.

Saeedifar M, Fotouhi M, Najafabadi MA, Toudeshky HH. Prediction of delamination growth in laminated composites using acoustic emission and Cohesive Zone Modeling techniques. Compos Struct 2015;124:120-127.

Sause M, Hamstad M. Acoustic Emission Analysis. In: Beaumont PWR, Zweben CH, Editors, Comprehensive Composite Materials, Elsevier, 2018. Volume 7, p.291-326.

Sause MGR., Müller T, Horoschenkoff A, Horn S. Quantification of failure mechanisms in mode-I loading of fiber reinforced plastics utilizing acoustic emission analysis. Compos Sci Tech 2012;72(2):167-174.

Sedlak P, Hirose Y, Enoki M. Acoustic emission localization in thin multi-layer plates using first-arrival determination. Mech Sys Signal Process 2013;36:636-649.

Shigeishi M, Ohtsu M. Acoustic emission moment tensor analysis: development for crack identification in concrete materials. Constr Build Mater 2001;15:311-319.

Silversides I, Maslouhi A, La Plante G. Acoustic emission monitoring of interlaminar delamination onset in carbon fibre composites. Struct Health Monit 2013;12(2):126-140.

Sleeman R, van Eck T. Robust automatic P-phase picking: an on-line implementation in the analysis of broadband seismogram recordings. Phys Earth Planet Inter 1999;113:265-275.

Soulioti DV, Barkoula NM, Paipetis AS, Matikas TE, Shiotani T, Aggelis DJ. Acoustic emission behaviour of steel fiber reinforced concrete under bending. Constr Build Mater 2009;23:3532-3536.

Taib AA, Boukhili R, Achiou S, Gordon S, Boukehili H. Bonded joints with composite adherends. Part I. Effect of specimen configuration, adhesive thickness, spew filler and adherend stiffness on fracture. Int J Adhes Adhes 2006;26:226–236.

Tang J, Soua S, Mares C, Gan T. A Pattern Recognition Approach to Acoustic Emission Data Originating from Fatigue of Wind Turbine Blades. Sensors-Basel 2017;17(11):E2507.

Tridello A, Fiocchi J, Biffi CA, Chiandussi G, Rossetto M, Tuissi A, Paolino DS. VHCF response of Gaussian SLM AlSi10Mg specimens: Effect of a stress relief heat treatment. Int J Fatigue 2019;124:435-443.

Vary A, Bowles KJ. An ultrasonic-acoustic technique for nondestructive evaluation of fiber composite quality. Polym Eng Sci 1979;19(5):373–376.

Vary AA. Review of issues and strategies in nondestructive evaluation of fiber reinforced structural composites. "New Horizons -Materials and Processes for the Eighties", SAMPE, Azusa. 1979.

Vinogradov A, Patlan V, Hashimoto S. Spectral analysis of acoustic emission during cyclic deformation of copper single crystals. Philos Mag 2000;81(6):1427-1446.

Wenqin H, Ying L, Aijun G, Yuan F. Damage Modes Recognition and Hilbert-Huang Transform Analyses of CFRP Laminates Utilizing Acoustic Emission Technique. Appl Compos Mater 2016;23(2):155-178.

Yousefi J, Mohamadi R, Saeedifar M, Ahmadi M, Hosseini-Toudeshky H. Delamination characterization in composite laminates using acoustic emission features, micro visualization and finite element modelling. J Compos Mater 2016;50(22):3133–3145.

Yu F, Okabe Y, Wu Q, Shigeta N. A novel method of identifying damage types in carbon fiber-reinforced plastic cross-ply laminates based on acoustic emission detection using a fiber-optic sensor. Compos Sci Tech 2016;135:116-122.

Yu F, Okabe Y. Fiber-Optic Sensor-Based Remote Acoustic Emission Measurement in a 1000 °C Environment. Sensors 2017;(2):2908.

Zhuang X, Yan X. Investigation of damage mechanisms in self-reinforced polyethylene composites by acoustic emission. Compos Sci Tech 2006;66(3-4):444-449

Zucchelli A, Dal Re V. Experimental analysis of composite laminate progressive failure by AE monitoring. In: Proceedings of ICEM12 - 12th International Conference on Experimental Mechanics, Bari, Italy, 2004.

ADDENDUM

Selection of suitable AE parameter of analysis of the acoustic signals in parameter-based approach has remained a debate for several years. The research works, which focus on identifying the suitable AE parameter in the literature is very few to none. This section highlights the importance of parameter selection and its efficiency in identifying the damage modes in CFRP composites.

A.1   INTRODUCTION

In this section, additional work on the use of AE technique in damage characterization of adhesively bonded CFRP composites is presented. Although there are several parameters for damage characterization, which is aptly explained throughout this thesis work, a definite rule for selecting the best parameter always had remained a debate. In this section, principal component analysis (PCA) is used for identifying the suitable sets of parameters from a large dataset, for analysis. The initial parameter set that is considered are the peak amplitude, absolute signal level (ASL), initiation frequency (I-Frequency), peak frequency (P-Frequency), average frequency (A-Frequency), and reverberation frequency (R-Frequency). These parameters may represent the characteristic features of the waveform. Furthermore, in Chapter 3 and Chapter 7 the high asymmetric nature of the acoustic signals observed from different damage modes were identified. The propagation of the acoustic signals released from the different damage sources is responsible for the asymmetry of these signals. For this reason, the I-Frequency and R-Frequency, alongside other AE signals, are considered for this analysis.

The selected features are clustered using the fuzzy c-means data clustering technique into different classes. For implementing this methodology, the acoustic signals used are recorded from CFRP laminates bonded in the single-lap shear (SLS) configuration and then subjected to a static tensile load. An attempt is made to correlate the AE parameters (which were selected using PCA and clustered using fuzzy c-means) with the different damage modes.

A.2   MULTIPARAMETER APPROACH – FEATURE SELECTION

The CFRP composite adhesively bonded in Single-Lap-Shear (SLS) configuration is tested for this study. The SLS specimens used in this study are the same materials used in Section 7.2.1. Similarly, the acoustic signal acquisition setup is also the same as the aforementioned section.

The different AE features provide the characteristic representation of the acoustic waveform. Many of these AE features are closely related to one another. For example, the absolute energy of the AE signal and the ASL are in direct relationship with the RMS voltage. Absolute energy is directly proportional to the square of the RMS voltage, while ASL is analogous to RMS voltage, with the only difference being that RMS voltage is measured in millivolts or microvolts, whereas ASL is measured in decibels. As such, using both RMS voltage and ASL for analyzing the signal characteristics is redundant.

For this reason, the set of parameters used in this section are:

- Peak Amplitude
- Absolute Signal Level (ASL)
- Initiation Frequency
- Reverberation Frequency
- Average Frequency
- Peak Frequency

A.2.1   Principal Component Analysis for Data Reduction and Feature Selection

Principal Component Analysis (PCA) is a multivariable data reduction technique. This is introduced by Hotelling in 1933 and its procedure is explained in detail by Maćkiewicz and Ratajczak. The core idea of PCA is to reduce the dimensionally of a dataset that has a large number of interrelated variables, which is essentially the necessity in this case. The data reduction is done while retaining as much of the variation present in the dataset as possible. The data reduction is achieved by reducing the data dimensions into new correlated features called principal components, which are minimally correlated.

These principal components form a symmetric matrix, where the eigenvectors of the matrix form the elements of the matrix. These eigenvectors can be defined as the characteristic vectors of the matrix. They are unique in the sense that they remain directionally invariant under linear transformation by its parent matrix.

The AE data from testing the SLS specimens SLS 1, SLS 2, and SLS 3 are recorded using a pair of piezoelectric sensors. The input parameters of peak amplitude, ASL, I-Frequency, R-Frequency, P-Frequency, and A-Frequency are reduced into their eigenvector matrix using PCA. The variances of the eigenvalues of the eigenvector matrix or the different principal components are also calculated. The scree plots describing the variance of the different principal components are presented in Figure A.1. The set of principal components from 1 to 6 provides a representation of the reduced dataset.
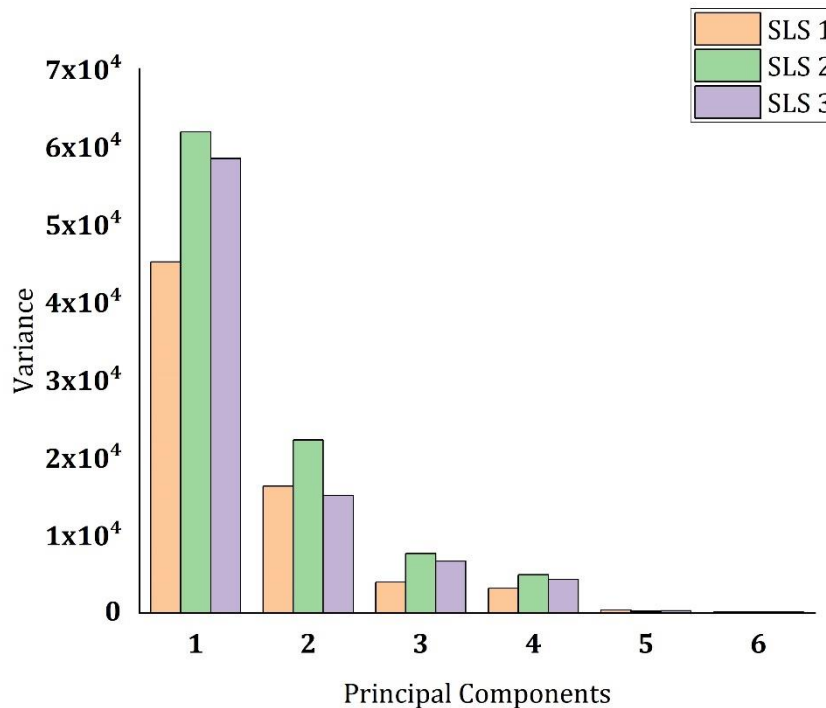
Figure A.1. Scree plot for the different principal components for SLS 1, SLS 2, and SLS 3

The variances of the first and second principal components are significantly larger than the remaining components combined in Figure A.1. Thus, the dataset was reduced to only the first two principal components PC 1 and PC 2.

For the reduced data, the eigenvalues of the principal components PC 1 and PC 2 of all the AE parameters are presented in Figure A.2. It can be observed that the peak amplitude, peak frequency, and amplitude formed a group with the eigenvalues of PC 1 and PC 2 close to each other. Therefore, a representative AE parameter from this group is selected for further analysis. The peak amplitude is selected as the representative from the group.

It can also be observed from Figure A.2 that the I-Frequency, R-Frequency, and A-Frequency have large variations in their eigenvalues for PC 1 and PC 2 and could not be constituted into a group. This means that there exists a large variation in these parameters. Therefore, the I-Frequency and R-Frequency are considered for the analysis.
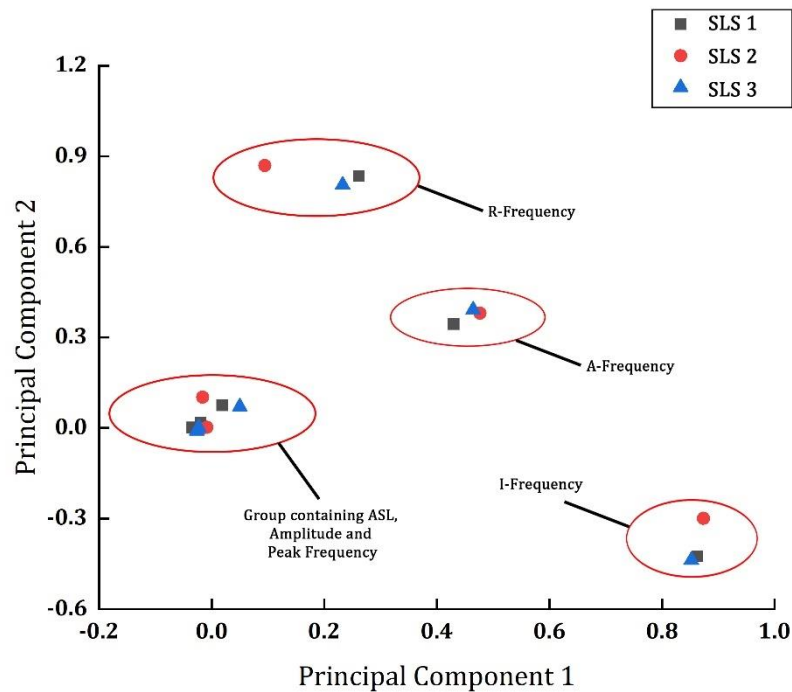
Figure A.2. Principal components PC 1 and PC 2 for all the parameters selected for all specimens

From the PCA results, three parameters from the initially assigned group of six parameters are selected: amplitude, I-Frequency, and R-Frequency. Instead of going through a rigorous process of analyzing all the parameters and finding the optimal parameters for analysis, the PCA reduced the dimensionality of the dataset into three

parameters. For comparison purposes, the amplitude from the ASL, amplitude, and P-Frequency group was compared with I-Frequency and R-Frequency.

There is a specific reason for comparing the amplitude with these two parameters. For damage assessments using AE, the peak amplitude values are directly related to the damage modes. It is explained in detail in Section 5.5 with experimental validation. For instance, the most general trend was that the AE signals with an amplitude above 60–70 dB represent fibers breakage, 35–50 dB represents matrix cracking, and 50–60 dB represents fibers debonding or delamination. There is no definite value for this correlation of the amplitude with damage modes.

The AE signals with high amplitudes not only represent fibers breakage but also interlaminar crack growth in many cases. This is because of the mode of propagation and the degree of absorption of the AE waveforms. The peak amplitude only corresponds to the largest voltage peak and the modes of propagation, while the degree of absorption in the propagation medium is ignored. For this reason, the I-Frequency and R-Frequency are considered for this study.

The decaying frequency of the AE signals can be defined using the R-Frequency, while the I-Frequency can define the characteristics of the initiation level before the largest amplitude is recorded. Hence, these two parameters, when compared with the peak amplitude of the signal, can provide information about the acoustic signal characteristics.

A.2.2 Fuzzy c-means for data clustering

In Section 5.3., nonparametric pattern recognition technique k-means++ is used for data clustering. In this section, however, Fuzzy c-means (FCM) data clustering is used. The FCM is a data clustering method for any two-dimensional data. The dataset is clustered into a predefined number of clusters in FCM, similar to k-means++. Unlike other data clustering methods, in which all the data points belong to only one cluster, in FCM, the data points belong to all the clusters to some degree. The degree of membership is based on the distance between the data point and the centroid of each cluster. The data point has a large degree of membership with the cluster that has the closest centroid, while it has a smaller degree of membership with the cluster that has the farthest centroid.

215

The assignment of the centroids and the data points to each cluster is determined by the objective function. By iterating, the distance from any given data point to a cluster center is weighted by the membership of that data point in the cluster.

The I-Frequency and R-Frequency with respect to the different amplitudes of the recorded AE events are clustered using the FCM clustering technique. Initially, for selecting the optimal number of clusters, the Davies–Bouldin Index (DBI) is calculated for the abovementioned data (Refer to Section 5.3.2 for details about DBI). The DBI with the minimum value for the different clusters N = 1, 2, …, 6 is supposed to be selected as the optimal number of clusters. For all sets of data recorded for SLS 1, SLS 2, and SLS 3, the DBI returned the lowest value for N = 3. The FCM is used for clustering I-Frequency and R-Frequency into three clusters. The clustered data of I-Frequency and R-Frequency with respect to amplitude is presented in Figure A.3 and Figure A.4, respectively, for all SLS specimens.

The clustered data in Figure A.3 shows that despite the peak amplitude level, the R-frequency of the recorded waveforms varied significantly. Similar results are also observed in Figure A.4 for the R-Frequency. Furthermore, the frequency levels for I-Frequency and R-Frequency in Figure A.3 and Figure A.4 are not very similar for all the AE signals. They differed significantly in several instances. For example, in Figure A.3 a and b, which shows the I-Frequency of the recorded signals, there were very few AE events recorded between the frequencies of 100 and 200 kHz in cluster 2, and even less AE signals between 100 and 300 kHz below 90 dB in cluster 3. However, in Figure A.4 a and b, which shows the R-Frequency, the number of AE signals in the frequency range of 100 to 300 kHz was significantly higher. This also meant that the frequency rate of absorption, which can be indicated by the R-Frequency, varied significantly from the I-Frequency. A question may arise: why did the I-Frequency range from 0 to 1000 kHz, while the R-Frequency was only below 500 kHz? The I-Frequency was calculated using Equation (2.7) in Chapter 2, which is the ratio of P.Counts to the rise time. If the second or third count of the AE waveform has the largest amplitude, then P.Counts is counted as 1 or 2, respectively. This also means that there was a huge possibility that the rise time could be very short during these instances. By considering the large differences between

the short duration of the rise time and the duration of the AE signal, the variation between the I-Frequency and R-Frequency is quite common. This was the reason for the wide range of I-Frequency compared to the R-Frequency.
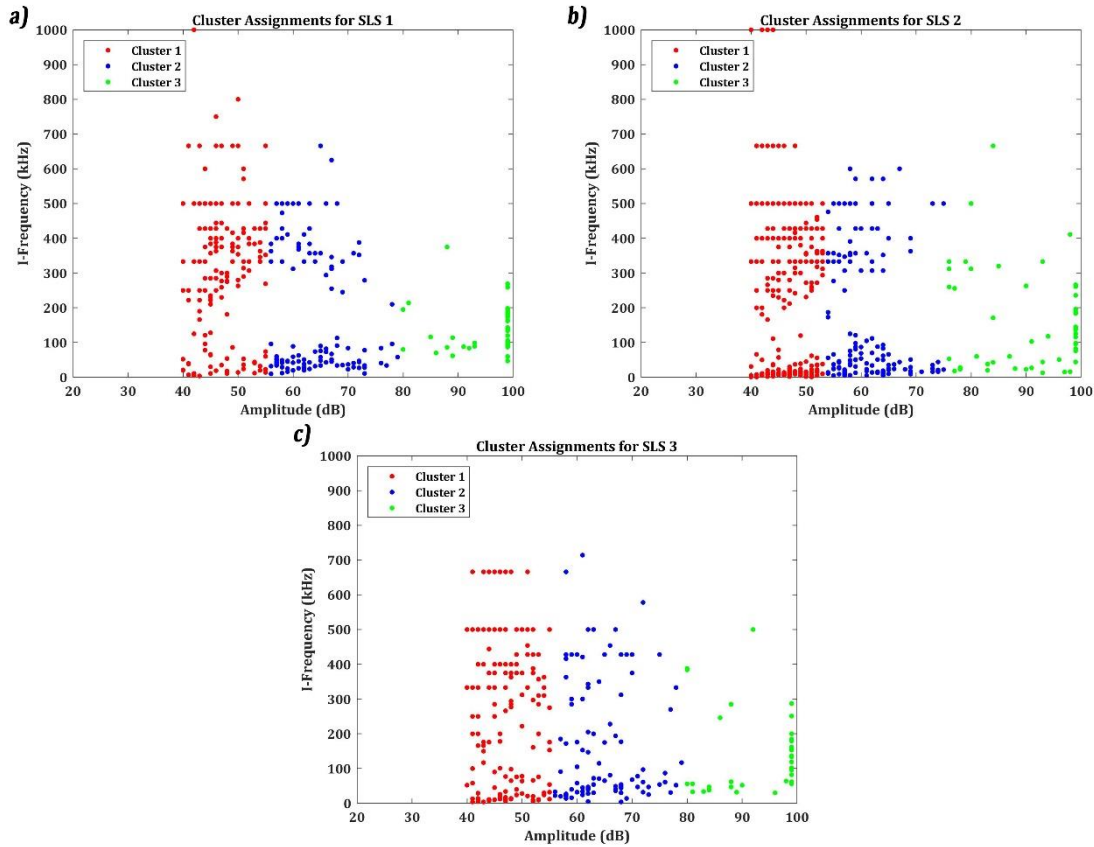
Figure A.3. I-Frequency vs. amplitude plotted as three clusters using FCM for the **a**) SLS 1, **b**) SLS 2, and **c**) SLS 3 specimens

The I-Frequency clusters can be classified as follows: cluster 1 had AE signals with a low amplitude but with the I-Frequency spread between 0 and 1000 kHz; cluster 2 had AE signals with a moderate amplitude (mostly between 55 and 75/80 dB) with the I-Frequency spread between 0 and 700 kHz; cluster 3 had the signals with higher amplitude (>75/80 dB) but with the I-Frequency spread between 0 and 500 kHz, ignoring the outliers. Since I-Frequency is inversely proportional to the rise time, it can be used as a parameter for classifying the type of damage mode that the AE signals have as their source. The AE signals with a larger peak amplitude and a shorter rise time correspond to an interlaminar crack as the source, while the signals with a smaller peak amplitude

and a longer rise time may correspond to the shearing mode under tensile loading. Analogous with these observations, the differences between the shearing mode and the interlaminar crack can be identified. A detailed explanation of how to identify the damage sources is presented in the next section.
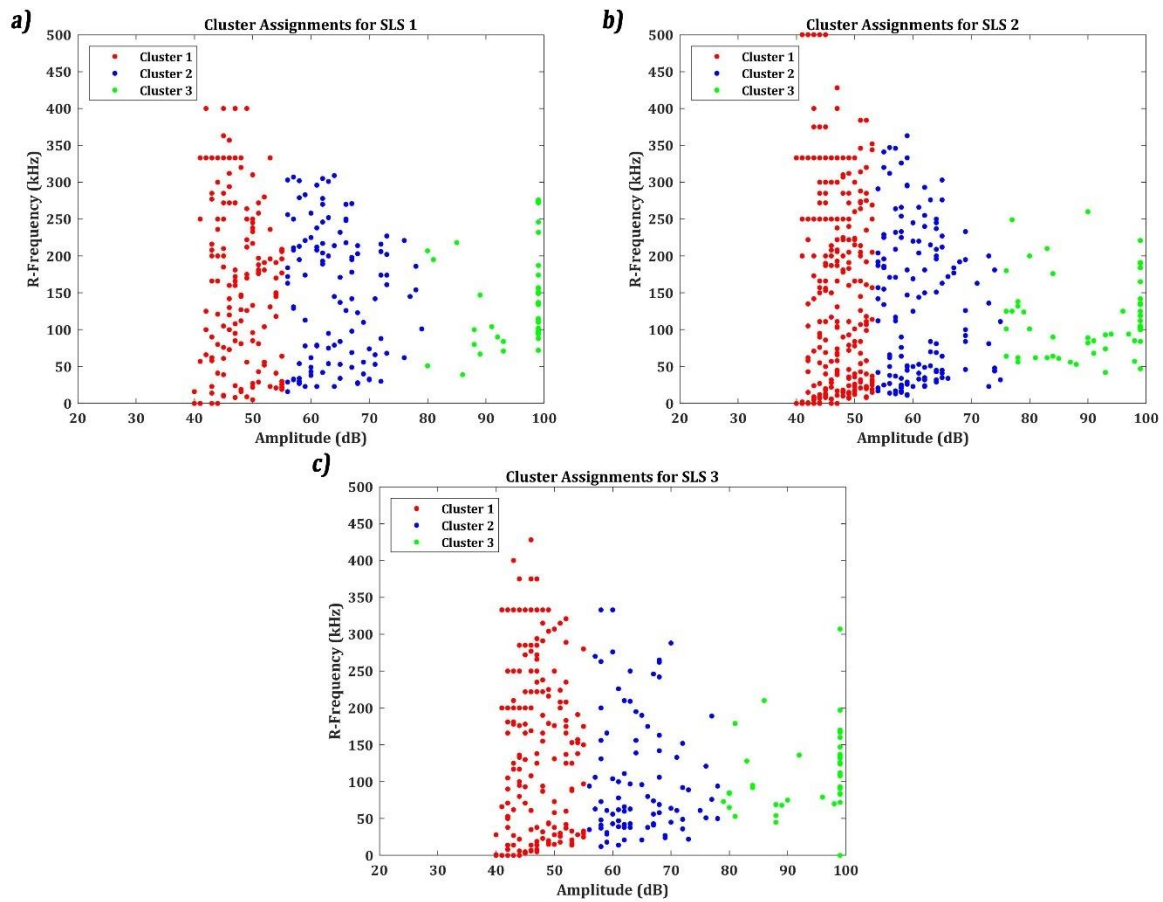
Figure A.4. R-Frequency vs. amplitude plotted as three clusters using FCM for the **a**) SLS 1, **b**) SLS 2, and **c**) SLS 3 specimens

The R-Frequency represents the amount of absorption of the AE signals. The AE signals generally propagate in two different modes: symmetrical and asymmetrical. The symmetrical mode AE signals carry a lower frequency component but have less dispersion in their energy during propagation. The low amount of dispersion means that the R-Frequency can be high for the symmetrical mode. This is because the signal duration in the symmetrical mode of propagation is very low, which leads to the higher R-Frequency. The AE signals generated from matrix cracking and delamination release

AE signals, which propagate in symmetric mode. In contrast, the AE signals, which are propagating in asymmetric mode, have a higher frequency and disperse more during propagation. The asymmetric mode AE signals can have a lower R-Frequency compared to the symmetric mode AE signals. These asymmetric AE signals mostly have fibers breakage or interlaminar crack growth as their AE source.

A.3 DAMAGE ASSESSMENT USING CLUSTERED I-FREQUENCY AND R-FREQUENCY

For assessing the damage modes properly, it is essential to map the AE descriptors with the load response of the SLS specimens. The clustered AE data are plotted with respect to the load response of the SLS specimens for detailed analysis. The SLS load response results with I-Frequency and amplitude are presented in Figure A.5 and the results with R-Frequency and amplitude are presented in Figure A.6.
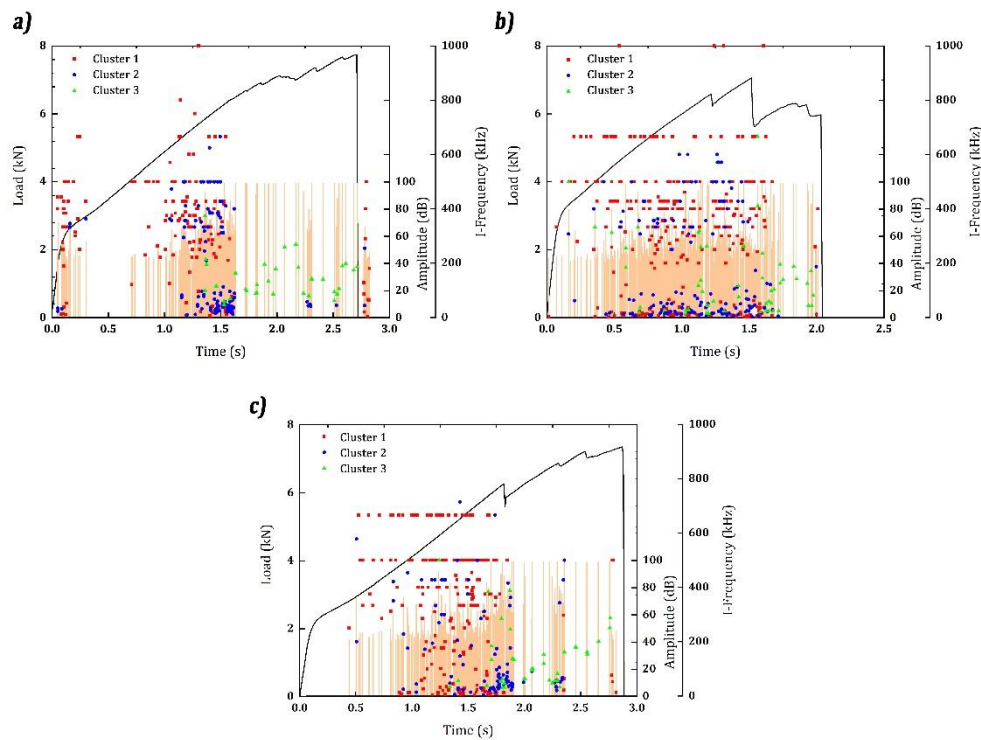
Figure A.5. Load, amplitude, and clustered I-Frequency vs. time for the **a**) SLS 1, **b**) SLS 2, and **c**) SLS 3 specimens

In Figure A.5 a, the amplitude and clustered I-Frequency are plotted with respect to the load response of the SLS 1 specimen. First of all, the load responses have multiple load peaks before the final fracture. In Section 7.2.2.1, these peaks as regions of initial rupture and final rupture (refer to Table 7.4). For SLS 1, the initial rupture occurred at 7.05 kN and the final rupture occurred at 7.75 kN. From the point of initial rupture to the final rupture (roughly between 1.75 s and 2.75 s, the majority of the I-Frequency components are in cluster 3. Comparing this observation with Figure A.3 a, it can be identified that these clusters belonged to the category of AE signals with a high amplitude and low I-Frequency (<200 kHz). Similarly, if the results are compared with Figure A.4 a and Figure A.6 a, again, the AE signals have a low R-Frequency (<200 kHz). This implies that the signals are highly symmetric since both I-Frequency and R-Frequency are below 200 kHz, and at the same time, the peak amplitude was higher. These types of AE signals normally have interlaminar crack growth as their source. If the same figures are compared for the initial stages of load response, say before 0.5 s, the I-Frequency and R-Frequency are highly asymmetric. The signals during this stage are deemed to be asymmetric in the sense that the I-Frequency and R-Frequency varies significantly in the very few AE signals recorded during that short duration. This initial loading stage may represent the sliding of the specimen inside the loading grips. The next important stage is the stage between the initial stage and the initial rupture (between 0.75 s and 1.75 s). In Figure A.5 a, most of the AE signals have I-Frequencies in clusters 1 and 2. A similar observation could be found for R-Frequency in Figure A.6 a. Owing to the absence of cluster 3 in I-Frequency and R-Frequency, the damage modes in these regions are probably due to the matrix cracking and delamination. In adhesive-bonded components, under static loading conditions, a majority of the load is carried by the adherends. The delamination, however, initiates at the vicinity of the adhesive layer and the adherend and extended through the thickness of the adhesive layer. The region before the initial rupture suffered extensive microcracking in the thick adhesive layer and the delamination is initiated. However, the specimen SLS 1 retained its load-carrying capability until it reached 7.75 kN. During this transition stage, the crack has grown through the thickness, releasing AE signals with a high symmetry between I-Frequency and R-Frequency, resulting in the final fracture.
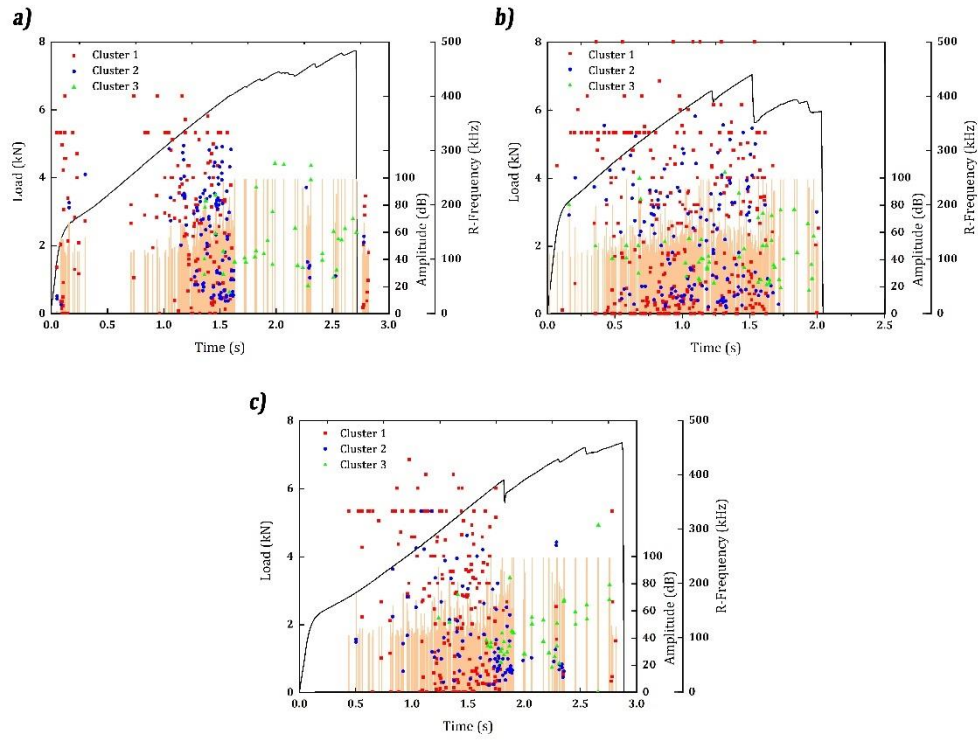
Figure A.6. Load, amplitude, and clustered R-Frequency vs. time for the **a**) SLS 1, **b**) SLS 2, and **c**) SLS 3 specimens

For specimen SLS 2 (Figure A.5 b and Figure A.6 b), more than one load peak can be observed. Nonetheless, the major initial rupture occurred at 1.5 s with the load peak of 7.05 kN and the final rupture at 2.25 s at 5.96 kN. It is clear from this observation that the damage modes of SLS 2 are different from those of SLS 1. However, there is an ambiguity in how this damage mode progressed. Comparing these results with the I-Frequency and R-Frequency clusters of Figure A.3 b and Figure A.4 b, the cluster 3 signals of I-Frequency and R-Frequency are distributed throughout the loading regions. Between the transition period of the initial and final ruptures, which lasted for only 0.75 s, a significant number of cluster 3 signals are observed. Even though this stage was shorter in duration, these signals still referred to the interlaminar crack growth. The distribution of cluster 3 throughout the loading stages indicates that the crack growth was initiated at a very early stage in SLS 2. This is probably the reason for the very low final rupture load (5.96 kN) compared to the SLS 1 specimen.

The results of the SLS 3 specimens are presented in Figure A.5 c and Figure A.6 c, which are almost identical to SLS 1. Interlaminar crack growth is observed between the initial and final rupture stages, which were at 5.93 kN (at 1.75 s) and 7.36 kN (at 2.75 s). The AE signals that corresponded to the matrix cracking and delamination are distributed after the duration of 0.5 s. Thus, the I-Frequency and R-Frequency clustered data can provide information about the damage modes.

A.4   CONCLUSION

From different AE features, the best features for analysis are selected by reducing their dimensions into principal components using PCA. From the scree plot of the variance for different principal components, it is concluded that the dataset can be reduced to two dimensions. Consequently, from the PCA analysis, the I-Frequency, R-Frequency, and peak amplitudes are chosen to be the best features for analysis. The selected features are clustered using the FCM algorithm into three clusters. Each cluster has I-Frequency and R-Frequency distributed over their peak amplitudes. Then, this clustered information is plotted over the load responses of the SLS specimens for identifying the damage modes. The different damage modes, such as matrix cracking, interlaminar crack growth, and the initial/final stages of rupture are identified by comparing the clustered I-Frequency and R-Frequency of the AE signals plotted over the load responses of the specimens under loading.

CURRICULUM VITAE

1992   Born in Tirunelveli, Tamil Nadu – India

2009   Graduated from PKN Higher Secondary School in Thirumangalam, Tamil Nadu – India

2009 – 2013   Bachelor Degree in Mechanical Engineering – Maharaja Engineering College/affiliated with Anna University – Chennai, Tamil Nadu – India

2013 – 2015   Master Degree in Manufacturing Engineering – Kamaraj College of Engineering and Technology/affiliated with Anna University – Chennai, Tamil Nadu – India

2015 – 2017   Assistant Professor at Department of Mechanical Engineering – Kamaraj College of Engineering and Technology – India

2017 – 2020   PhD in Ingegneria Meccanica e Gestionale – Dipartimento di Meccanica Matematica e Management, Politecnico di Bari, Bari – Italy

2020   Guest Researcher at Department of Engineering, Aarhus University, Aarhus – Denmark

Publications

2020   C. Barile, C. Casavola, G. Pappalettera, C. Pappalettere & **P.K. Vimalathithan**. Detection of Damage in CFRP by Wavelet Packet Transform and Empirical Mode Decomposition: an Hybrid Approach. *Applied Composite Materials 27(5): 641-655.*
https://doi.org/10.1007/s10443-020-09823-5

2020   C. Barile, C. Casavola, G. Pappalettera & **P.K. Vimalathithan**. Application of different acoustic emission descriptors in damage assessment of fiber reinforced plastics: A comprehensive review. *Engineering Fracture Mechanics*: 107083 (Published online).
https://doi.org/10.1016/j.engfracmech.2020.107083

2020   C. Barile, C. Casavola, G. Pappalettera & **P.K. Vimalathithan**. Acoustic emission descriptors for the mechanical behavior of selective laser melted samples: An innovative approach. *Mechanics of Materials*: 103448 (Published online).
https://doi.org/10.1016/j.mechmat.2020.103448

2020   C. Barile, C. Casavola, V. Moramarco & **P.K. Vimalathithan**. A comprehensive study of mechanical and acoustic properties of selective laser melting material. *Archives of Civil and Mechanical Engineering* 20(1): 3.
https://doi.org/10.1007/s43452-019-0005-9

2020   C. Barile, C. Casavola, G. Pappalettera & **P.K. Vimalathithan**. Damage Propagation Analysis in the Single Lap Shear and Single Lap Shear-Riveted CFRP Joints by Acoustic Emission and Pattern Recognition Approach. *Materials* 13(18): 3963.

https://doi.org/10.3390/ma13183963

2020   C. Barile, C. Casavola, G. Pappalettera & **P.K. Vimalathithan**. Damage assessment of carbon fibre reinforced plastic using acoustic emission technique: experimental and numerical approach. *Structural Health Monitoring*: 1475921720946438 (Published online).

https://doi.org/10.1177%2F1475921720946438

2020   C. Barile, C. Casavola, V. Moramarco, C. Pappalettere & **P.K. Vimalathithan**. Bonding Characteristics of Single- and Joggled-Lap CFRP Specimens: Mechanical and Acoustic Investigations. *Applied Sciences* 10(5): 1782.

https://doi.org/10.3390/app10051782

2019   C. Barile, C. Casavola, G. Pappalettera & **P.K. Vimalathithan**. Damage characterization in composite materials using acoustic emission signal-based and parameter-based data. *Composites Part B: Engineering* 178: 107469 (Published online).

https://doi.org/10.1016/j.compositesb.2019.107469

2019   **P.K. Vimalathithan**, C. Barile, C. Casavola, S. Arunachalam, M.G. Battisti, W. Friesenbichler, C.T. Vijayakumar. Thermal degradation kinetics of polypropylene/clay nanocomposites prepared by injection molding compounder. *Polymer Composites* 40(9): 3634-3643.

https://doi.org/10.1002/pc.25226

2019 C. Barile, C. Casavola, G. Pappalettera & **P.K. Vimalathithan**. Experimental wavelet analysis of acoustic emission signal propagation in CFRP. *Engineering Fracture Mechanics* 210: 400-407.

https://doi.org/10.1016/j.engfracmech.2018.05.030

2019 C. Barile, C. Casavola, G. Pappalettera & **P.K. Vimalathithan**. Acousto-ultrasonic evaluation of interlaminar strength on CFRP laminates. *Composite Structures* 208: 796-805.

https://doi.org/10.1016/j.compstruct.2018.10.061

2019 C. Barile, C. Casavola, G. Pappalettera & **P.K. Vimalathithan**. Characterization of adhesive bonded CFRP laminates using full-field digital image stereo-correlation and finite element analysis. *Composites Science and Technology* 169: 16-25.

https://doi.org/10.1016/j.compscitech.2018.10.032

2019 C. Barile, C. Casavola, G. Pappalettera & **P.K. Vimalathithan**. Novel method of utilizing Acoustic Emission Parameters for Damage Characterization in Innovative Materials. *Procedia Structural Integrity* 24: 636-650.

https://doi.org/10.1016/j.prostr.2020.02.056

2019 C. Barile, C. Casavola, G. Pappalettera, C. Pappalettere & **P.K. Vimalathithan**. Investigation of Structural Integrity of Composite Materials using Wavelet Packet Transform. *Procedia Structural Integrity* 17: 582-588.

https://doi.org/10.1016/j.prostr.2019.08.078

2019   C. Barile, C. Casavola, **P.K. Vimalathithan**, M. Pugliese, V. Maiorano. Thermomechanical and Morphological Studies of CFRP Tested in Different Environmental Conditions. *Materials* 12(1): 63.

https://doi.org/10.3390/ma12010063

2018   **P.K. Vimalathithan**, C. Barile, C. Casavola, S. Arunachalam, M.G. Battisti, W. Friesenbichler, C.T. Vijayakumar. Investigation on the Thermal Degradation Kinetics of Polypropylene/Organically Modified Montmorillonite Nanocomposites with Different Levels of Compatibilizer. *Macromolecular Materials and Engineering* 303(12): 1800260.

https://doi.org/10.1002/mame.201800260

2018   **P.K. Vimalathithan**, C. Barile, C.T. Vijayakumar. Investigation of kinetic triplets for thermal degradation of thermally cured vinyl ester resin systems and lifetime predictions. *Journal of Thermal Analysis and Calorimetry* 133(2): 881-891.

https://doi.org/10.1007/s10973-018-7154-6

2018   **P.K. Vimalathithan**, C.T. Vijayakumar. Characterization of cenosphere-reinforced vinyl ester composites. *Journal of Elastomers & Plastics* 50(2) (2018): 95-106.

https://journals.sagepub.com/doi/abs/10.1177/0095244317708591

2020   C. Barile, C. Casavola, G. Pappalettera, C. Pappalettere & **P.K. Vimalathithan**. Evaluating bonding characteristics of Joggled Lap CFRP using Acoustic Emission Technique. *Proceedings of the Third International Conference on Theoretical, Applied and Experimental Mechanics*. Springer Nature.

https://doi.org/10.1007/978-3-030-47883-4_5

2020   C. Barile, C. Casavola, G. Pappalettera & **P.K. Vimalathithan**. Multiparameter Approach for Damage Propagation Analysis in Fiber Reinforced Polymer Composites. *Presented at 1st International Electronic Conference on Applied Sciences*. Vol. 10. 2020.

https://sciforum.net/manuscripts/7517/manuscript.pdf